Controlling mitochondrial dynamics: population genetics and networks

a thesis presented for the degree of

Doctor of Philosophy of Imperial College London

by

Hanne Hoitzing

Department of Mathematics

Imperial College London

September 2017

I certify that this thesis, and the research to which it refers, are the product of my own work, and that any ideas or quotations from the work of other people, published or otherwise, are fully acknowledged in accordance with the standard referencing practices of the discipline.

Copyright

The copyright of this thesis rests with the author and is made available under a Creative Commons Attribution Non-Commercial No Derivatives licence. Researchers are free to copy, distribute or transmit the thesis on the condition that they attribute it, that they do not use it for commercial purposes and that they do not alter, transform or build upon it. For any reuse or redistribution, researchers must make clear to others the licence terms of this work.

Controlling mitochondrial dynamics: population genetics and networks

Abstract

Mitochondria form an essential component of nearly all eukaryotic cells, are implicated in numerous diseases and may play important roles in ageing. Mitochondrial populations are dynamic, controlled and heterogeneous, with different types – both mutant and wildtype – potentially coexisting in single cells. This thesis will study the dynamics of both mitochondria and their genetic material (mtDNA) to improve our understanding of the role of these dynamics in pathology and ageing.

This study suggests, as well as critically evaluates, reasons for the existence of complex continuous mitochondrial networks using coarse-grained mathematical models, underlining a nonlinear relation between functionality and network structure. Understanding the link between morphology and function is important as disruption of the former is directly implicated in cellular dysfunction. We perform experiments in which we measure the influence of mitochondrial fusion and division events on integrated mitochondrial membrane potential, an indicator of functionality, and find evidence for its conservation.

The cellular homeostatic control acting on a mitochondrial population is poorly understood; to address this, we study the influence of general feedback control strategies on mutant and wildtype mtDNA dynamics. We introduce a simple linear control mechanism that captures a wide variety of biologically observed dynamics, and study optimal parameterisations through the construction of an energy-based mitochondrial cost function. Not only cellular control, but also gene-therapeutic control of mtDNA is studied, allowing us to investigate optimal treatment strategies to reduce mutant loads.

The cellular proportion of mutant mtDNA molecules, known as heteroplasmy, is crucial in mitochondrial disease and we study the influence of cellular mtDNA exchange on heteroplasmy dynamics and mutant expansion during ageing. We find that this exchange of genetic material can induce preferential mutant expansion during ageing (even in the face of selection against mutants) through a stochastically driven increase in cellular mean heteroplasmy levels.

To Resi,

Acknowledgments

Many thanks to my supervisors Nick and Iain for their support and for giving me the opportunity to pursue this PhD. Thanks to Gyorgy, for helping me perform some real-life experiments and taking care of my cells.

Thank you Payam, for giving me advice, for answering my many emails and always being enthusiastic. Jure, thanks for making the days more enjoyable through board games and conversations. Thanks to both Jure and Nadja for providing me with a place to sleep when I was in need of one.

Finally, thank you Juvid and Tom for helping me throughout these four long years, for providing me moral support and for making this PhD worthwhile. Tom, thanks for buying most of the coffee. Juvid, thanks for being there for me and for making most (but not all) of this period of my life a nicer experience.

Publications & Contributions

What is the function of mitochondrial networks? A theoretical assessment of hypotheses and proposal for future research, BioEssays 37(6), 687 - 700 (2015)
Hoitzing H., Johnston, I. G., and Jones, N. S.
Contribution: performed all simulations, analysis and wrote the manuscript.
Appearance in thesis: Chapter 2

Energetic costs of cellular and therapeutic control of stochastic mtDNA populations, (in preparation)
Hoitzing H., Gammage, P. A., Minczuk, M., Johnston, I. G., and Jones, N. S.
Contribution: performed all simulations, analysis and wrote the manuscript. Part of the experimental data was provided by Payam A. Gammage.
Appearance in thesis: Chapter 4.

Mitochondrial heterogeneity, metabolic scaling and cell death, BioEssays (2017)
Aryaman, J., Hoitzing, H., Burgstaller, J. P., Johnston, I. G. and Jones, N. S.
Contribution: suggested research directions and contributed to manuscript development.

Stochastic models of mitochondrial heterogeneity, Springer, (in press)
Hoitzing H., Johnston, I. G., and Jones, N. S.
Contribution: wrote the manuscript. This work concerns a review which will appear as a chapter in a book titled 'Stochastic Dynamical Systems, Multiscale Modeling, Asymptotics and Numerical Methods for Computational Cellular Biology'.
Appearance in thesis: parts of the thesis introduction are based on this review chapter which has been peer reviewed.

Glossary

mtDNA	Mitochondrial DNA
Carrying Capacity	The steady state copy number of a given species when present at homoplasmy in a single cell
Relaxed Replication	The continuous turnover of mtDNA molecules even in the absence of cellular turnover. The 'relaxed replication model' refers to a mathematical model of mtDNA dynamics [1, 2]
Clonal expansion	The expansion of a specific (clonal) mtDNA species over time, often referring to mutant mtDNA
Cellular mean heteroplasmy	The average heteroplasmy value of a population of cells, i.e. $\frac{1}{n}\sum_i \frac{m_i}{w_i+m_i}$ with n the number of cells in the population, and m_i and w_i denoting mutant and wildtype mtDNA copy numbers in cell i, respectively
Homogenate heteroplasmy	The level of heteroplasmy obtained when all mtDNAs of a population of cells are combined together, i.e. $\frac{\sum_i m_i}{\sum_i (w_i+m_i)}$ with m_i and w_i denoting mutant and wildtype mtDNA copy numbers in cell i, respectively
System Size Expansion	A technique to approximate Master equations, whereby the dynamics are split into a deterministic and a stochastic component. The larger the system size, the smaller the stochastic contributions to the dynamics
Linear Noise Approximation	The leading order term in the System Size Expansion
Gillespie algorithm	A stochastic modelling method using random numbers to simulate individual reaction events; it is often used in computational systems biology.

List of figures

1.1 Mitochondrial structure . . . 3

1.2 Mitochondrial modelling . . . 8

1.3 Steady states of linear feedback control . . . 13

2.1 Potential causes and types of mitochondrial network formation . . . 19

2.2 Selective fusion on its own leads to a healthier mitochondrial population . . . 27

2.3 Apparent diffusion coefficient depends nonlinearly on degree of fusion. An abrupt change in diffusion rate can occur with only small changes in fusion rate . . . 30

2.4 The effect of fusion on rate of ATP synthesis depends on the magnitude of the potentials of the pre-fusing mitochondria . . . 32

2.5 Fusion may increase controllability of TCA cycle activity and total energy production . . . 34

2.6 Fusion buffers fluctuations in membrane potential, and provides a mechanism of power cabling . . . 37

3.1 A size-weighted averaging model for changes in $\Delta\psi$ during mitochondrial dynamics 42

3.2 Example images of mitochondrial networks and fission events . . . 44

3.3 Membrane potential and area analysis . . . 45

3.4 A weighted average model is better able to predict measured pre-fission potentials 47

3.5 Phototoxicity and transient depolarization events . . . 48

4.1 A wide range of cellular control strategies can yield similar dynamics . . . 60

4.2 Intermediate heteroplasmies can be less efficient than either wildtype or mutant homoplasmy . . . 67

4.3 A control that senses no mutations shows an exponentially increasing cost, which is most noticeable in low copy number cells . . . 69

4.4 Locally optimal controls show nonlinear behaviours close to demand-satisfying regions, but linear optimal dynamics far away from these regions . . . 70

4.5 A simple model of treating cells with mitochondrially targeted endonucleases . . . 72

4.6 Knowledge of the heteroplasmy distribution is important in predicting how efficiently a tissue can be treated . . . 73

4.7 Bayesian confidence intervals for heteroplasmy and copy number dynamics . . . 76

4.8 Posterior mtZFN treatment parameter distributions 77

5.1 Difference in carrying capacity induces heteroplasmy assymetry 90
5.2 A nonlinear mapping between heteroplasmy and copy number space 91
5.3 A model of interacting cells, allowing mtDNA exchange 95
5.4 A deterministic setting predicts small changes in mean cellular heteroplasmy due to differences in carrying capacity 95
5.5 Stochastic dynamics can induce large increases in mean cellular heteroplasmy, even in the presence of negative mutant selection that otherwise acts to lower mean heteroplasmy 98
5.6 Stochastic heteroplasmy fluctuations induce changes in mean, which are larger when heteroplasmy variance is high 99
5.7 Investigating the dependence of heteroplasmy mean on model parameters 99
5.8 MtDNA exchange induces higher mean heteroplasmy and preferential mutant expansion during ageing 100
5.9 Mapping mtDNA mutations to values of δ 102
5.10 Visualisation of mutants spreading along muscle fibres with age 106
5.11 Significant effects of mtDNA exchange on heteroplasmy mean in physiological settings are plausible 110

A.1 Increased fusion leads to a relatively smaller unhealthy fragmented population . 121

B.1 Equal variances for different feedback control mechanisms 143
B.2 Relationship between resource consumption and energy output 153
B.3 Changing mutant efficiency (ϵ_2) does not lead to expensive intermediate heteroplasmies 154
B.4 Intermediate h values require more resources to satisfy demand, but only if mutants consume less resources 156
B.5 The existence of intermediate heteroplasmy values is a robust feature of the saturating output model 157
B.6 Wildtype, mutant and cost dynamics for four different control strategies. 159
B.7 At long times and high heteroplasmies, energy sensing control becomes suboptimal 160
B.8 Zinc Finger Nuclease concentrations for short and long treatments 161
B.9 High correlation between nuclease treatment strength and duration 162

C.1 Position-dependent diffusion yields asymmetric boundary fluxes 165
C.2 Exponential increases in mean mutant copy numbers can be approximated analytically 169

C.3 Wildtype steady state distributions are accurately approximated numerically . . 172
C.4 Fixation probabilities in the limit of slow hopping 185
C.5 The interplay between mtDNA turnover, feedback control and intercellular exchange determine the type of copy number dynamics seen 186
C.6 The emergence of drift along the steady state line 188
C.7 Estimating the feedback control strength 191
C.8 Estimating mtDNA diffusion coefficients using the spread of abnormal fibre regions 195

List of tables

2.1 An overview of hypotheses on the function of mitochondrial fusion including criticism . . . 22

2.2 Suggestions for future modelling and experiments for further analyses of the hypotheses on the function of mitochondrial fusion . . . 24

4.1 Key results . . . 59

4.2 Analytical expressions for the means and variances according to the linear noise approximation . . . 63

4.3 Parameters used in our mitochondrial cost function with their descriptions . . . 66

5.1 A breakdown of the different linear feedback regimes . . . 103

5.2 An overview of the effect of known mtDNA mutations on copy number levels . . . 104

5.3 Summary of studies measuring frequencies of deletion mutations in ageing muscle 107

5.4 Estimations of mutation rates in skeletal muscle fibres . . . 108

5.5 An overview of possible experiments to test model predictions and improve parameter estimates . . . 116

A.1 Occurrences and causes of hyperfusion in wildtype cells . . . 137

A.2 Typical mitochondrial morphology in a variety of cells . . . 138

A.3 Diffusion constants of several mitochondrial proteins . . . 139

A.4 Overview of various post-translational modifications of the GTPase Drp1 which mediates mitochondrial fission . . . 140

A.5 Functions of the mitochondrial fusion and fission proteins other than inducing mitochondrial fusion or fission . . . 141

B.1 Parameter values for the four different control mechanisms we employ . . . 158

Contents

1 Introduction **1**

1.1 Mitochondria - the vital organelles . . . 1

1.2 Mitochondrial structure and behaviour . . . 2

1.2.1 Mitochondrial fusion and fission dynamics . . . 3

1.3 Mitochondrial DNA, heteroplasmy and pathology . . . 4

1.4 Modelling mitochondria . . . 6

1.4.1 Models of mitochondria during development . . . 7

1.4.2 Models of mutant accumulation during ageing . . . 9

1.4.3 Models of mitochondrial fusion/fission dynamics . . . 10

1.4.4 A linear model of mitochondrial feedback control . . . 11

1.5 Challenges and Outline . . . 13

2 What is the function of mitochondrial networks? **17**

2.1 Introduction . . . 17

2.2 The main players involved in mitochondrial dynamics . . . 18

2.3 Quantitative definitions of micro, meso- and hyperfusion . . . 19

2.4 Hypothesised reasons for mitochondrial meso- and hyperfusion . . . 21

2.4.1 Selective fusion creates the possibility of quality control without needing selective mitophagy . . . 25

2.4.2 Small changes in fusion state can cause large changes in complementation rate . . . 28

2.4.3 Fusion increases ATP synthesis . . . 31

2.4.4 Fusion affects bioenergetic control and total energy production through calcium signalling . . . 33

2.4.5 Fusion provokes state changes protective against perturbations . . . 35

2.5 Discussion . . . 37

3 Experimental exploration of mitochondrial dynamics and membrane potential **39**

3.1 Introduction . . . 40

3.2 Results . . . 41
3.2.1 Hypotheses regarding changes in membrane potential during network events 41
3.2.2 Visualising and defining mitochondria . . . 42
3.2.3 Data analysis shows support for a model of weighted averaging . . . 43
3.2.4 Discussion . . . 49
3.2.5 Materials and Methods . . . 52

4 Control and energetic costs of stochastic mtDNA populations **57**
4.1 Introduction . . . 58
4.2 Results . . . 59
4.2.1 Control: general insights on the role of feedback control . . . 59
4.2.1.1 A wide range of control strategies induces similar mtDNA behaviour and admits quantitative analysis. . . . 60
4.2.1.2 Nonlinear cost functions predict changes in tissue maintenance . 62
4.2.2 Cost: an effective mitochondrial energy-based cost function . . . 62
4.2.2.1 General cost function structure . . . 63
4.2.2.2 Intermediate heteroplasmies may be inefficient and resource availability can dictate the cost of mtDNA states . . . 65
4.2.3 Combining cost and control: comparison and optimisation of both cellular control and treatment strategies . . . 68
4.2.3.1 Timescales and energy sensing in optimal control of mtDNA populations. . . . 68
4.2.3.2 A parameterised model of artificial mtDNA control for disease treatment . . . 71
4.3 Discussion . . . 78
4.4 Methods . . . 81

5 Apparent mtDNA selection in models of random drift **86**
5.1 Introduction . . . 87
5.2 Results . . . 88
5.2.1 A linear model of feedback control: non-trivial and skewed heteroplasmy dynamics . . . 88
5.2.1.1 A heteroplasmy-dependent diffusion coefficient leads to heteroplasmy skew . . . 88
5.2.1.2 Analytical methods can be used to probe small δ regimes . . . 92

5.2.1.3 MtDNA exchange: a deterministic setting predicts small changes in mean heteroplasmy . . . 94
5.2.1.4 MtDNA exchange: a stochastic setting introduces selection for low-δ mutants . . . 96
5.2.2 Connecting with reality: parameter estimations and biological interpretations . . . 101
5.2.2.1 Mapping known mtDNA mutations onto values of δ . . . 101
5.2.2.2 Providing a target mutant load: skeletal muscle data predict low mutant accumulation rates . . . 105
5.2.2.3 Estimating mtDNA exchange rate and control strength . . . 109
5.2.3 Clonal expansion and random drift - Challenges and perspectives . . . 111
5.3 Discussion . . . 113

Appendix A Supplemental information complementing Chapter 2 **118**
A.1 Quantitative and mathematical models . . . 119
A.1.1 Model for increased selection bias through selective fusion . . . 119
A.1.2 Model for diffusion on lattice with fluctuating bonds . . . 120
A.1.3 Fusion of charged spherical capacitors . . . 121
A.1.4 Energy output by calcium stimulation as function of the number of fused mitochondria . . . 123
A.1.5 Mechanisms of calcium uptake and amount of mitochondria-ER contact . 124
A.1.6 Increasing mitochondrial size buffers fluctuations in membrane potential 125
A.1.6.1 Changes in membrane potential upon changes in permeability of the inner mitochondrial membrane . . . 125
A.1.6.2 Ising-type model for mitochondrial robustness . . . 127
A.2 Additional hypotheses on the function of mitochondrial meso- and hyperfusion . 129
A.2.1 Fusion allows for the possibility of creating a genetic reservoir . . . 129
A.2.2 Fusion increases ATP synthesis; hypotheses (i), (ii) and (iii) . . . 130
A.2.2.1 Hypothesis (i): Higher [ATP] is caused by fusion-induced changes in inner membrane shape . . . 130
A.2.2.2 Hypothesis (ii): Higher [ATP] is caused by fusion-induced decreases in proton leak . . . 131
A.2.2.3 Hypothesis (iii): Higher [ATP] is caused by fusion-induced decreases in mitochondrial degradation . . . 131
A.2.3 Fusion creates distributional 'power cables' . . . 132

A.2.3.1 Order of magnitude increase in energy production using mitochondrial power cabling . . . 134
A.2.4 Meso- and hyperfusion have no function . . . 136
A.3 Tables . . . 137

Appendix B Supplemental information complementing Chapter 4 **142**
B.1 Feedback control of a heteroplasmic mtDNA population . . . 142
B.2 The relationship between resource consumption and energy production: $s_i(r_i)$ . . . 144
B.2.1 A linear output model . . . 144
B.2.2 A saturating output model . . . 144
B.3 Parameter values for the cost function . . . 146
B.3.1 Mitochondrial energy production and leak: ϕ and β . . . 146
B.3.2 Resource and supply and maintenance cost: r_{max}, r_n and s_n . . . 147
B.3.3 Maintaining, building and degrading: ρ_1, ρ_2 and ρ_3 . . . 148
B.3.4 Demand and resource availability: D and R . . . 150
B.3.5 Saturating model parameters: s_{max} and k . . . 150
B.3.6 The cost of resource consumption α . . . 151
B.3.7 Mutant parameters: ϵ_1, ϵ_2 . . . 151
B.3.8 Parameter units . . . 151
B.4 Cost function outputs . . . 152
B.4.1 Output visualisations . . . 152
B.4.2 Expensive intermediate heteroplasmies - explanation and robustness . . . 154
B.4.3 Comparison of the cost of different control mechanisms . . . 158
B.5 Zinc Finger nuclease treatment model . . . 160
B.5.1 Visualisation of Zinc Finger concentrations during treatment . . . 160
B.5.2 Heteroplasmy values can increase after nuclease treatments . . . 160
B.5.3 Bayesian inference model outputs . . . 162

Appendix C Supplemental information complementing Chapter 5 **163**
C.1 Analytical descriptions of mutant and wildtype dynamics under various simplifying conditions . . . 164
C.1.1 Heteroplasmy-dependent diffusion produces results qualitatively similar to heteroplasmy dynamics in our birth-death dynamics . . . 164
C.1.2 Exponential increase in mutant mean can be described analytically . . . 165
C.1.3 Approximating the wildtype steady state distribution . . . 170

C.1.4 Lotka Volterra model . . . 172
C.1.4.1 Solution for the mean and variance of a single species . . . 174
C.1.5 System Size Expansion . . . 175
C.1.5.1 Higher order terms . . . 178
C.2 Intercellular mtDNA exchange . . . 182
C.2.1 Fixation probabilities in the limit of slow mtDNA exchange . . . 182
C.2.2 Intuitions behind stochastic drive and copy number drift . . . 185
C.2.3 Estimation of control strength parameter c_1 . . . 189
C.2.4 Estimation of mtDNA exchange rate . . . 192
C.2.4.1 Estimating γ using mtDNA and protein diffusion coefficients . . . 192
C.2.4.2 Estimating γ using the spread of abnormal fibre regions . . . 193

References **231**

1

Introduction

1.1 Mitochondria - the vital organelles

Mitochondria are double membrane-bound organelles present in nearly all eukaryotic cells. Their acquisition occurred roughly 2 billion years ago perhaps when a bacterium was engulfed by another cell as an endosymbiont [3]. The relationship between bacterium and cell turned out to be a beneficial one, perhaps as the bacterium provided a new source of energy for the cell, which in turn provided protection from the environment. Over millions of years of evolution, the bacterium lost its independence and became an organelle of the cell: the mitochondrion.

Currently most cells in our body cannot survive without mitochondria which, besides being the main energy producers in the cell, are involved in various other processes including intracellular calcium signalling, iron-sulfur cluster biogenesis, and cell death [4–6]. The importance of studying and understanding mitochondria cannot be understated as they have been implicated in numerous diseases including Parkinson's [7], diabetes [8], cancer [9], and Alzheimer's [10], and are of central importance in various devastating mitochondrial diseases [8, 11, 12]. For many years, mitochondria have been linked to ageing [13–24] (recent reviews are provided in Refs. [23, 25–28]).

Because of the large number of different processes mitochondria are involved in, it is challenging to experimentally probe all of them which limits our ability to combat disease. Though

new technologies increasingly reduce these difficulties, mathematical and *in silico* models of mitochondria can provide useful additional insights and have been applied to many different mitochondrial research fields including development [29–33], ageing [2, 34–39], and mitochondrial dynamics [40–44].

1.2 Mitochondrial structure and behaviour

In this thesis, we first introduce some of the major mitochondrial components and functions, knowledge of which is required in the remainder of the thesis. Mitochondria have an outer and inner membrane, the latter containing many invaginations, called *cristae*, increasing surface area to accommodate a large number of proteins. The inner membrane is split between the inner boundary membrane and the crista membrane which, though connected, are populated by different proteins [45, 46]. Cristae have connections with the inner boundary membrane through tubules called crista junctions (Figure 1.1). A recent review on mitochondrial cristae structure is provided in Ref. [47]. An important feature of mitochondria is that they retain their own genetic material, *mitochondrial DNA (mtDNA)*, which is discussed in detail in Section 1.3.

In many cells, mitochondria are the main producers of ATP, the energy currency of the cell, whose synthesis is driven by an electrochemical potential gradient across the inner membrane. This gradient is maintained by pumping protons, H^+, from the matrix into the intracristal and intermembrane spaces (Figure 1.1), a process carried out by a set of large protein complexes. Ideas about the organization of these complexes have changed over time and it is now clear that they assemble into various supercomplexes [48] (e.g. Figure 1.1). They transfer electrons from donors to acceptors via reduction and oxidation reactions, and are therefore often referred to as the *electron transport chain*. Protons are allowed to flow down their gradient back into the matrix via the enzyme ATP synthase, thereby releasing their potential energy which is used to phosphorylate ADP to ATP (Figure 1.1). The entire process is known as *oxidative phosphorylation* because the final electron acceptor is oxygen.

Sometimes protons may leak across the inner membrane without being coupled to ATP production, thereby generating heat; this process is known as *uncoupling*. Uncoupling provides a mechanism of increasing an organism's temperature, used by e.g. hibernating animals [49]. However, it can also be the result of damage to the mitochondrial membrane caused by e.g. *Reactive Oxygen Species* (ROS), a source of mitochondrial damage induced by leakage of electrons from the electron transport chain. Damaged mitochondria may be removed by the cell through a process called *mitophagy* [50–53], though controversy exists over its ability to se-

lectively target damaged mitochondria [27, 54–56]. A recent study suggests that selectivity is relatively limited in physiological settings but can be greatly enhanced experimentally [57].

Mitochondria are heavily involved in programmed cell death, known as *apoptosis*. Apoptosis can be triggered by the release of an enzyme, called cytochrome c, in the cytoplasm. Normally, cytochrome c resides in the cristae with limited diffusion to the intermembrane space (for a review see Ref. [58]), but widening of the crista junctions enables cytochrome c to diffuse into the cytoplasm.

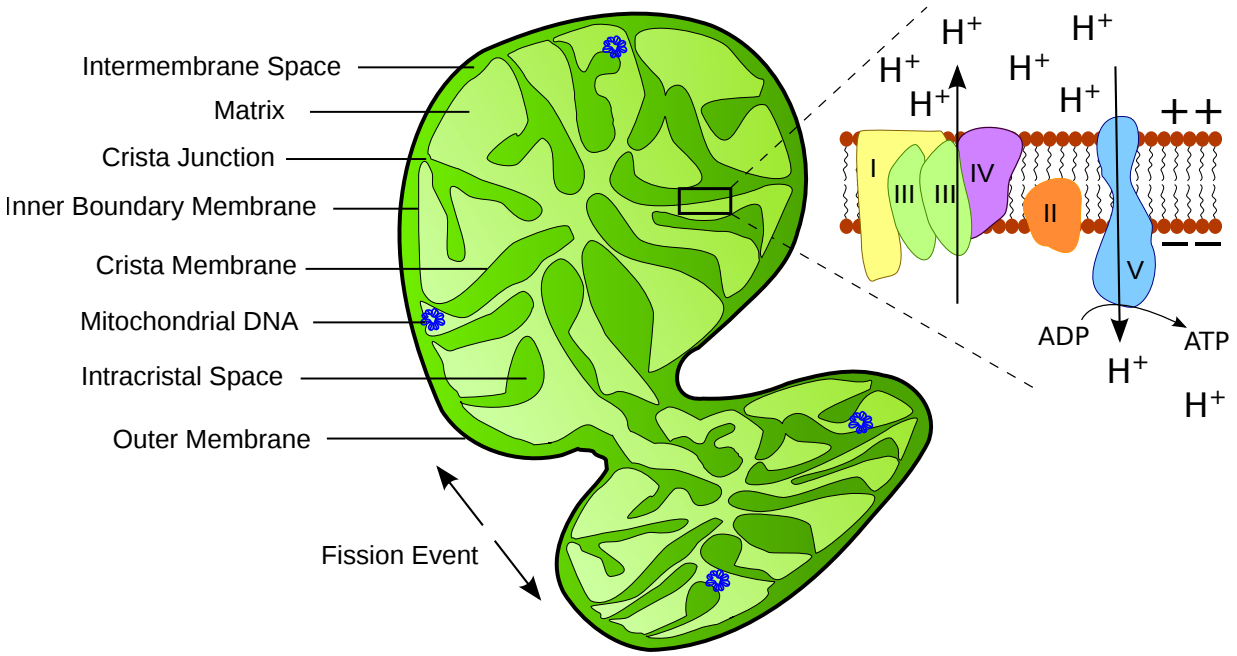


Figure 1.1: Mitochondrial structure. A simplified cartoon illustrating several main mitochondrial components. Left: mitochondrial membrane structure and compartmentalization. A fission event is illustrated. Right: respiratory chain complexes embedded in the mitochondrial inner membrane. As an example, the respirasome supercomplex is shown together with complex II (which is mainly found in free-floating form) and complex V (ATP synthase).

1.2.1 Mitochondrial fusion and fission dynamics

Mitochondria are highly dynamic organelles and they are observed to undergo fusion and fission events continuously (Figure 1.1), leading to a diverse range of mitochondrial morphologies, from fragmented states to continuous networks. Images of mitochondrial networks are provided in Chapters 2 and 3. Fusion events are known to be selective, and only involve mitochondria with a sufficiently high membrane potential [59]. This selectivity of fusion events will turn out to play an important role in the beneficial effects of highly fused states (Chapter 2). Cristae are also capable of undergoing fission and fusion events, thereby changing the morphology of the cristae-network inside the mitochondrion [60].

The morphological state of the network is itself directly implicated in a variety of diseases [61], and inhibiting fission or fusion can lead to severe cellular dysfunctions [62, 63]. Understanding why a network remodels itself and how exactly its structure impacts its function is of great importance but still unclear; we discuss this topic in detail in Chapter 2.

Mitochondrial fusion/fission dynamics do not merely change the shape of the network, they are able to isolate certain mitochondrial fragments which are then – due to their small size – susceptible to degradation. Because fusion with the network is selective, fragments containing mutant mitochondrial DNA may be less likely to join than others. Experimentally, disrupting the balance between fusion and fission has been shown to lead to loss of mtDNA [64], and increased mitochondrial fission is associated with reductions in lifespan [65–67]. Interestingly, a recent study showed that transient increases in fission in midlife can increase lifespan [68]. These findings indicate a close linking between mitochondrial fusion/fission dynamics, ageing, and mtDNA dynamics, the three main topics of this thesis.

1.3 Mitochondrial DNA, heteroplasmy and pathology

MtDNA is tiny compared to nuclear DNA and in humans comprises 16,569 base pairs, encoding only 37 genes. In healthy cells, the levels of mtDNA are controlled and remain fairly constant over time as we age [69], though there are indications that copy numbers drop with age in skeletal muscle [70–72] which is likely to be linked to muscle deterioration. The number of mtDNA molecules per cell ranges from about 100 to 10^5 and depends heavily on the type of cell, reflecting different cellular functions (e.g. mtDNA levels per cell have been measured to be 3650 ± 620 in skeletal muscle, 6970 ± 920 in heart [69], all the way up to 10^5 in mature human oocytes [73]). Note that due to the high mtDNA copy numbers, the total amount of mtDNA can comprise a macroscopic fraction of total cellular DNA (mtDNA and nuclear DNA combined). MtDNA molecules are packaged into protein structures called *nucleoids* which each contain $\sim 1-2$ mtDNAs [74].

Replication of mtDNA is linked to the cell cycle [75], as copy numbers must approximately double before a new cell division occurs. However, mtDNA turnover is still present in post-mitotic cells and is thus capable of occurring in the absence of cellular turnover [76]. Mutations in mtDNA can occur, and though it was previously thought that ROS damage was the main cause of mutations, it has now become clear they are mostly generated through errors during replication [77] (reviewed in Ref. [27]). Though machinery to repair mtDNA exists [78, 79], this machinery is possibly less efficient than nuclear DNA repair. Continuous mtDNA turnover in

post-mitotic cells is therefore desirable as otherwise mutations would accumulate without the possibility of their removal. However, mtDNA turnover, though it may be capable of eliminating mutations from the population, can itself lead to expansions of mutants as discussed in Chapters 4 and 5.

When mutations occur, they often coexist with wildtype mtDNA molecules, a situation which is called *heteroplasmy*. Denoting the number of wildtype and mutant mtDNA molecules in a cell by w and m respectively, the level of heteroplasmy is defined as

$$h = \frac{m}{w+m} \tag{1.1}$$

and can vary between cells in the same tissue, between different tissues, and between individuals. A state in which only a single type of mtDNA is present is known as *homoplasmy*.

Because of the large number of mtDNAs in a cell, the presence of a few mutants does not immediately cause major problems. The heteroplasmy value has to exceed a critical *heteroplasmy threshold*, typically 60-90%, before biochemical defects are observed [21, 80–85]. As mean heteroplasmy values do not completely specify threshold crossing probabilities, it is vital to have knowledge of how the heteroplasmy *distribution* changes over time. This requires stochastic treatments as opposed to deterministic ones which typically only describe mean behaviour. When mutation loads are sufficiently high they can have detrimental consequences, as is the case in mitochondrial diseases which affect $\sim$1 in 4300 of the adult human population (including mutations of both mtDNA and nuclear DNA) [86]. This again underlines the importance of studying mitochondrial behaviour.

Interestingly, the same pathogenic mutations that cause mtDNA diseases, are also found in healthy individuals but at much lower levels [87, 88]. These low-level mutations, both pathological and non-pathological, accumulate with age [27] and are typically seen in post-mitotic tissues (e.g. skeletal muscle, myocardium and brain). Often a cell contains very high fractions of a single mutation [89], which is said to have clonally expanded. Clonally expanded mutations are often *deletion mutations* which lack parts of the mtDNA (rendering them shorter) though point mutations can also expand [90, 91]. Mutation load only reaches high levels in a small fraction of cells, giving rise to a mosaic structure with patches of high-heteroplasmy cells distributed among low-heteroplasmy cells (e.g. [85, 92]).

How does this process of *clonal expansion* occur? Can we delay, or even prevent it? Despite ongoing active research, the answers to these questions are as yet unknown. Many hypotheses

on this topic involve a selection advantage for the mutant species such as: a shorter replication time for deletion mutants due to their smaller genomes [93, 94]; a lower degradation rate for certain mutants due to their reduced release of damaging superoxide molecules [95]; or, faster mutant replication which is stimulated by their microenvironment [96, 97]. Even though all of these hypotheses have some attractive features, they are not fully supported by data or only concern certain types of mutants [98, 99].

Rapid progress is being made, however, and various mathematical models incorporating these hypotheses and others are discussed in Section 1.4.2. The power of mathematical modelling becomes apparent when considering their useful insights and findings such as i) the discovery that many expanded mutants in aged individuals are likely to have occurred early in life [17, 20, 34], ii) two competing species cannot coexist indefinitely and one species will always outcompete the other [100], iii) before homoplasmy is reached the variance of at least one mtDNA species in a heteroplasmy cell always increases with time [101, 102]. We will adopt similar modelling approaches to add to this collection of interesting findings.

1.4 Modelling mitochondria

This thesis uses mathematical modelling as a tool to gain insights into mitochondrial biology and mitochondrial roles in ageing, disease, and cellular function. Therefore, having introduced various essential mitochondrial components in previous sections, we here turn towards summarising mathematical models currently existing in the literature, mainly focussing on stochastic models of ageing and mitochondrial dynamics as these topics are the main focus of this thesis.

We stress the crucial role of mathematical models in mitochondrial research. For example, they can generate new insights, lead to experimental suggestions, integrate and combine knowledge of different fields, enable sensitivity analyses, and deepen understanding. For a general discussion of the relevance of modelling in biology, we refer to Ref. [103]. Mitochondria and their mtDNAs form a stochastic system (e.g. the occurrence of mutations is random), the dynamics of which are hard to track experimentally without damaging the cell. Mathematically, one can readily simulate large populations of cells and, importantly, perform simulations over long timescales. Experimentally probing mtDNA dynamics over a lifetime will literally take a lifetime, whereas computer simulations can generate statistics within hours; modelling is thus a highly relevant tool in studying clonal expansion during ageing.

Examples of models describing mitochondrial and/or mtDNAs dynamics are illustrated in Figure 1.2. As mtDNA molecules replicate and degrade continuously, a mathematical approach known as a birth-death model [100] provides a natural way of describing their dynamics. In this class of models there are only two types of events: each individual of the population has a probability per unit time of increasing (birth) or decreasing (death) its copy number by one. In general, the birth and death rates may differ between mutant and wildtype and may depend on time or copy number (Figure 1.2(i)). These intracellular dynamics can be combined with any of the others shown in the figure.

One particular model to which we will often refer is the well-known 'relaxed replication model' which assumes continuous turnover of mtDNA in post-mitotic cells [1, 2]. Degradation rates are assumed to be constant, and replication rates are allowed to depend on wildtype and mutant copy numbers. The aim of the model was to see how the presence of mutant molecules affects the overall dynamics, and how heteroplasmy varies over time. A heteroplasmy threshold was predicted by assuming that wildtype copy numbers are being controlled towards a specific 'optimal' value. The model has since been used in a variety of other models [34, 36] and has obtained experimental support [104].

We split this section into four parts, each discussing mathematical models of different mitochondrial aspects: i) mitochondria during development, ii) mutant accumulation during ageing, iii) mitochondrial fusion/fission dynamics, and iv) a specific feedback control model we will use throughout this thesis.

1.4.1 Models of mitochondria during development

Unfertilised human eggs contain $\sim 10^5$ mtDNAs, some of which may be mutated. After fertilisation, the egg starts dividing, and with each division the mtDNAs are stochastically partitioned between the daughter cells. By chance, some daughter cells will inherit more mutants than others, introducing a variance in heteroplasmy across the population of cells (see e.g. [105]). A drastic drop in mtDNA copy number per cell in early development, known as the *bottleneck*, further increases stochasticity. There is evidence suggesting that different mtDNA mutations lead to different genetic bottlenecks which induces a variety of inheritance patterns [106].

The exact mechanism by which heteroplasmy variance increases through development is highly debated. It may be the result of a combination of random mtDNA copy number drift in between cell divisions and stochastic partitioning at cell divisions [101, 107–112], or additional mechanisms may be required such as restricting the ability to replicate to only a subpopulation

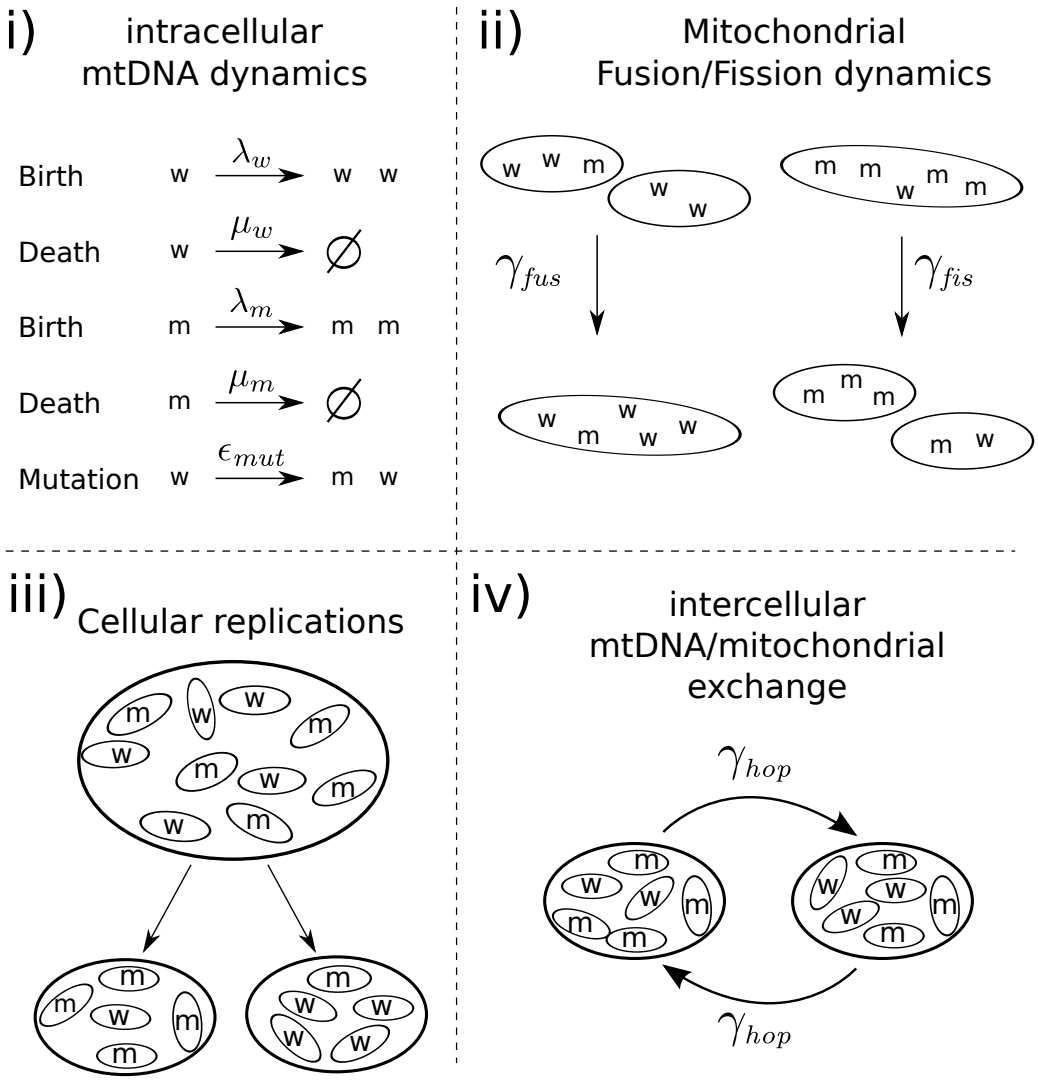


Figure 1.2: Mitochondrial modelling. Various kinds of mitochondrial models have been developed, focussing on different aspects. Four examples of the main ingredients often included in mitochondrial modelling are shown: i) mtDNA turnover within cells (with possible mutation events), ii) mitochondrial fusion/fission dynamics, which may or may not be selective processes (instead of redistribution of mtDNAs, more abstract 'health units' are often considered [40–42]), iii) cellular turnover with stochastic partitioning of mitochondria, and iv) intercellular mtDNA or mitochondrial exchange. Extension, variations and combinations of any of these basic models are possible.

of mtDNAs [113], or clustering of mtDNAs during cell divisions [114]. Recently, a general model was developed which was able to reproduce all of these mechanisms and, importantly, provides a statistical framework to compare them given experimental observations [32]. Using Approximate Bayesian Computation [115, 116] it was found that most support is found for a mechanism involving a combination of random mtDNA turnover and binomial partitioning at cell division [32].

Analytical treatments of heteroplasmy dynamics through development use results from population genetics such as the Wright formula [30] (providing information on heteroplasmy mean and variance) and the Kimura distribution [29] (allowing for descriptions of the entire heteroplasmy

probability distribution after any number of cell divisions). Recently, a model was developed that includes mtDNA dynamics in-between cell divisions [31, 32], suggesting a modification to the Wright formula [101].

Cellular turnover during development clearly plays a role in mtDNA and heteroplasmy dynamics, yet few models exist combining embryonic phases with post-natal mtDNA turnover during ageing [108]. This is likely due to an uncertainty in the contribution of embryonic mutations to end-of-life mutation levels, especially in long-lived organisms. Stochastic modelling suggested that inclusion of embryonic turnover in wildtype mice had little influence on mean mutant loads at older ages, but did increase heteroplasmy variance and led to long-tailed heteroplasmy distributions [108].

1.4.2 Models of mutant accumulation during ageing

Mutant accumulation during ageing can be modelled by assuming a certain mtDNA mutation rate. As most mutations occur during replication [117] a probability of mutation upon replication, P_{mut}, is often used [34, 36–38]. The aim is to construct a model that can explain the experimentally observed levels of clonal expansion in aged individuals, thereby generating an understanding of both the mechanisms behind the expansion and ways in which to reduce its rate.

Stochastic simulations were used to model whether shorter deletion mutant replication times – due to their smaller genome – could account for observed levels of clonal expansion in aged mammals [37, 118]. If the mtDNA population can be considered well-mixed, then predictions of this *survival-of-the-tiny* hypothesis agree with experimental data, but only under the assumption that mutation rate increases with heteroplasmy [118]. A more recent study by the same authors argues against the hypothesis in the context of short-lived mammals such as mice and rats [37]. Their results, however, seem to suggest that survival-of-the-tiny *can* account for clonal expansion in short-lived animals under the assumption that mtDNA half-lives are $\sim 2-4$ days. Though studies in mice and rats suggest half-lives on the order of $\sim 1-3$ weeks [119–121], these studies are both sparse and old [37]. Shorter replication times in deletion mutations may therefore, according to their treatment, still contribute to their expansion, though cannot explain expansion of point mutations.

A deterministic model employing slower mutant degradation and replication, correctly predicted a faster mutant accumulation rate in post-mitotic cells compared to dividing cells [99]. Recent evidence, however, suggests that mutants are degraded faster, rather than slower [59, 122]. A

recently proposed model, involving faster mutant replication due to altered transcription rates, is able to explain data in both short- and long-lived species [38]. However, the high level of positive mutant selection used (a 50% increase in replication rate) is likely to lead to much higher mutant levels – and therefore better agreement with data of short-lived species – in any model, without requiring the specific interpretation referring to transcription rates. Also, the model assumes a constant total population size which is unrealistic and misses out on implicit selection effects that become apparent when population size varies (Chapter 5).

Besides these selective models, various neutral models, without explicit mutant selection, were proposed to account for the observed data [34, 36, 123–125]. Mutants may generate more ROS, leading to even more mutants thereby creating a vicious cycle [123–125]. The vicious-cycle-hypothesis, however, predicts a plethora of distinct mutants, contrasting experiments. Moreover, it has become clear that ROS is not responsible for most mtDNA mutations [27, 77].

An alternative view is that, in theory, stochastic drift of mtDNA molecules over time can lead to a mutant taking over the entire mtDNA populations purely by chance because of the stochasticity of mtDNA replication and degradation, as well as cell divisions. Through stochastic simulations, using the relaxed replication model, it was found that no positive mutant selection is required to account for the observed levels of clonal expansion in aged humans [34]. However, a neutral model could not account for heteroplasmy data in short-lived mammals [36], which is due to a high level of P_{mut} being required to match the relatively high mutant levels in post-mitotic tissue of aged rodents. Any mutation event that occurs is assumed to generate a distinct type of mutant, and a high P_{mut} predicted a large number of such distinct mutants towards the end of life, disagreeing with experimental observations. These findings seem to suggest that neutral models cannot account for clonal expansion, though we revisit this question in Chapter 5.

1.4.3 Models of mitochondrial fusion/fission dynamics

Fusion and fission events can alter the rate of mutant mtDNA accumulation, and may thus be important processes to consider in modelling ageing. In many mathematical models the mtDNA molecules are assumed to be physically well-mixed and each mtDNA has a given probability per unit time of being replicated and degraded. However, through fusion and fission events, certain mitochondrial fragments may become separated from the network and can subsequently be degraded through mitophagy. The occurrence of mitophagy events, events involving the degradation of a whole mitochondrion, means that all the mtDNA molecules

within are simultaneously degraded. In this case, it becomes important to know which mtDNA resides in which mitochondrion. Moreover, mitochondria can only fuse with others when they are sufficiently close, meaning that spatial positions start to play a role in mtDNA dynamics.

Different kinds of models of fusion and fission dynamics exist, some of which focus on their role on heteroplasmy and clonal expansion [43, 44] whereas others focus not on mtDNA but rather the fusion and fission events themselves and how they affect the health of the overall mitochondrial population [40–42]. One model focussed on the different morphological structures of mitochondrial networks which arise from changing the relative rates of fusion and fission; it was suggested that the network contains a percolating phase transition [126].

Through stochastic Gillespie simulations [127] it was shown that slower mtDNA mixing increases the heteroplasmy variance between cells [43], which is only beneficial when mitophagy and fusion are sufficiently selective [44]. It was therefore suggested that the expansion of mutant mtDNA likely involves a decline in the selectivity of mitochondrial degradation and fusion with age [44]. Higher rates of fusion and fission tend to lead to more healthy mitochondria [40–42], though this may not be true if a damaged mitochondrion spreads this damage when fusing with others [42].

1.4.4 A linear model of mitochondrial feedback control

Having provided an overview of models in the literature on various mitochondrial aspects, we here focus on a specific model of mtDNA dynamics which will be used extensively throughout this thesis. This model, like many others discussed above, assumes that the mitochondrial population is under homeostatic control. Indeed, there is evidence of communication between the nucleus and mitochondria, known as *retrograde signalling* (mitochondrial signals to the nucleus) and *anterograde signalling* (nuclear signals to the mitochondria), which is used to regulate mtDNA content [128]. Different mutants accumulate preferentially in different tissues [129], again suggesting involvement of the cellular environment and the nucleus.

Our model belongs to the class of birth-death models, in which control can be incorporated by letting the mtDNA birth and death rates be functions of mutant and wildtype copy numbers themselves. We will mainly focus on a simple type of birth-death model, namely one in which the death rate is constant and the birth rate is a linear function of w and m. More precisely, referring to Figure 1.2(i), we assume a constant death rate $\mu_w = \mu_m \equiv \mu$ and a birth rate

$\lambda_w = \lambda_m \equiv \lambda(w, m)$ of the form

$$\lambda(w, m) = c_0 - c_1(w + \delta m) \tag{1.2}$$

where $c_0, c_1 > 0$ and δ are constants. We will occasionally include a small mutation rate.

We note that our model is neutral, a choice made due to the uncertainties surrounding the physiological relevance of possible selection mechanisms. We would argue that a neutral model forms an appropriate null model and can itself, remarkably, lead to selection effects (Chapter 5). A linear birth rate may seem limiting but it represents a first order approximation to many non-linear models, and can give rise to a surprisingly rich set of dynamics as shown in Chapters 4 and 5.

In steady state $\lambda(w, m) = \mu$, meaning we can rewrite the above equation into the more easily interpretable form

$$\lambda(w, m) = \mu + c_1(N_{ss} - (w + \delta m)) \tag{1.3}$$

where N_{ss} denotes the steady state value towards which the effective population, here defined as $w + \delta m$, is controlled. This equation states that replication rate will increase or decrease as the effective mtDNA population is decreased or increased with respect to its desired value, respectively. We note that assuming the existence of N_{ss} does not imply a control based on copy number; other quantities related to mitochondria (e.g. total ATP production, mtDNA mass or concentrations of specific mitochondrial proteins or transcripts) may be controlled instead, their desired values being reached at an effective population size of N_{ss}.

The parameter δ allows for differential feedback contributions of mutant and wildtype species, and the magnitude of c_1 determines how tightly the population is controlled. The deterministic steady state solution of Equation (1.3) is given by $(w_{ss} + \delta m_{ss}) = N_{ss}$ and represents a straight line in (w, m) space (Figure 1.3), whose slope depends on the value of δ. Similar lines of steady states are present in the relaxed replication model [1, 2]. Stochastic dynamics will fluctuate along this steady state line until fixation of either species has occurred.

For later convenience, we note that a population homoplasmic in wildtype or mutant has steady state $w_{ss} = N_{ss}$ and $m_{ss} = N_{ss}/\delta$, respectively. This difference in steady state copy numbers will lead to stochastic selection effects (Chapter 5).

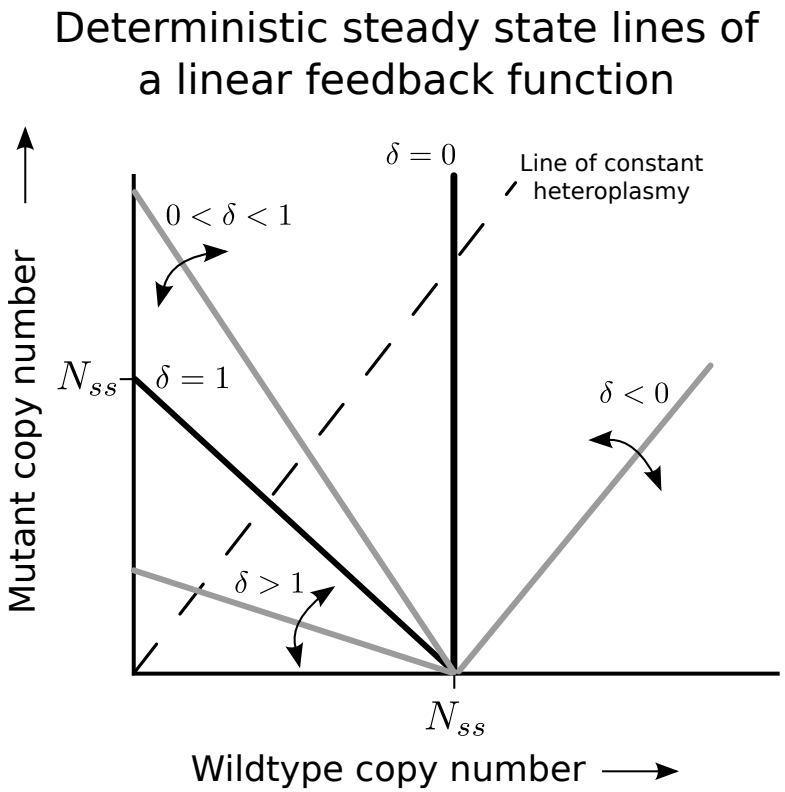


Figure 1.3: A linear feedback control has straight steady state lines. The deterministic steady state lines of the feedback control given in Equation 1.3 are shown in (w, m) space for various values of δ (grey lines show particular examples of ranges of δ). Constant heteroplasmy lines form straight lines through the origin.

1.5 Challenges and Outline

After decades of mitochondrial research, many challenges still exist. Here, we review some of the major outstanding challenges in mitochondrial research, before elaborating further on those challenges which we address in this thesis.

One major challenge is to understand the role of mitochondria in ageing. How and why do mutant mtDNA molecules accumulate during ageing? Why are the vast majority of clonally expanded mutations in aged individuals deletions, rather than point mutations? No consensus on these questions has been reached. Is there a causal link between mtDNA mutations and ageing? A homozygous 'mutator mouse', engineered to have two defective copies of the enzyme synthesising mtDNA (POLG), accumulates high levels of mtDNA mutations ($\sim$ 2500-fold higher than wildtype mice [130]) and shows premature ageing phenotypes [24, 131]. However, a heterozygous mutator mouse, showing mutation levels $\sim$ 500 times higher compared to wildtype mice, has a normal lifespan [130]. Another type of transgenic mouse, which accumulates deletion mutations in skeletal muscle and brain, also lacked premature ageing phenotypes (though mutations levels were relatively low) [132]. As of yet the existence of a causal link in physiological

conditions, though compelling, has not been proven (reviewed in Ref. [27]). If the accumulation of deletion mutations does cause ageing, can the removal of these mutations in middle-aged individuals reverse ageing phenotypes, or is the metabolic state of the cell irreversibly damaged by that point? Another point of discussion is the extent to which clonally expanded mutants are the result of somatic *de novo* mutations or mutations inherited at birth [17, 23, 133], as discussed in more detail in Chapter 5.

Another major challenge is to successfully treat patients with mtDNA diseases. No cure currently exists and treatment is often limited to treating or preventing the dysfunctions caused by the mutations (e.g. diabetes, myopathy and epilepsy) [134]. Mitochondrial disorders present themselves with large phenotypic heterogeneity, making it challenging to obtain correct diagnoses or predict disease progression. The same mtDNA mutation can affect different organs in different patients, the reason of which is currently unclear and a lack of animal models replicating human disease phenotypes means it is hard to make progress in this area [134]. Improved sequencing techniques have enabled better characterization of mtDNA diseases and the proteins and genes involved in mitochondrial function (e.g. Ref. [135]), and may provide answers to some of the currently open questions.

Mitochondria are maternally inherited and it was estimated that, on average, there are ~ 150 births per year in the United Kingdom among women at risk of transmitting mtDNA diseases [86]. Women carrying mtDNA mutations currently have several options including mitochondrial replacement therapy (MRT), in which nuclear DNA from an oocyte of the affected woman is transferred into enucleated donor oocytes containing healthy mitochondria [136, 137]. The method, however, raises ethical concerns and the long-term safety of the approach is yet to be established, as some mutated mtDNAs may be transferred together with the parent donor nucleus, possibly leading to complications arising from non-compatibility between nuclear and mitochondrial DNA as well as mitochondrial-mitochondrial DNA [138–141].

Fast progress is being made on designing methods to specifically cleave mutant molecules, thereby reducing heteroplasmy, using mitochondrially targeted nucleases [142–146]. However, these therapies are just beginning to develop and face many challenges themselves, e.g. high levels of off-target cleavage [142]. Designer nucleases are promising tools to treat patients using gene therapy, though the large size of some of these nuclease constructs may make it hard to package them into many vector systems [147]. Shorter nucleases were developed but showed lowered efficiency [147]. As of now, these therapies are designed to cleave specific mutant sequences. Though this may be suited for treating patients with a single type of deletion or

point mutation, it is less efficient for patients heteroplasmic in multiple pathogenic mutations or for combating ageing (which involves a wide variety of different mutations). Therefore, an interesting challenge is to design constructs that target short genomes, regardless of their sequence, to selectively degrade all deletion mutations at once.

Mitochondrial networks also impose challenges. The presence of large connected mitochondrial networks is associated with improved functionality (e.g. [148–151]). Many of the advantages of mitochondrial dynamics (such as sharing of components [83, 152]), however, could be obtained through frequent fusion/fission events, without requiring a large connected component. Are there beneficial effects associated with large continuous mitochondrial structures, which cannot be attained through small-scaled fusion/fission dynamics? Mitochondria tend to become more fragmented with age [153], and increased fission or fusion is associated with a decrease or increase in life-span, respectively [65, 66, 154]. How these effects are established, and whether mitochondrial fusion/fission dynamics play a causal role in ageing, remains unclear.

This thesis is centered on the theme 'mitochondrial dynamics' which refers both to fusion/fission dynamics as well as mtDNA dynamics. As discussed before, these two types of dynamics are closely linked (Sections 1.2.1 and 1.4.3). We use mathematical tools to address various specific challenges, as outlined below.

In Chapter 2, we address questions surrounding the advantages of large fused mitochondrial components (see above) by presenting an overview of existing hypotheses in the literature, as well as presenting some of our own, on this precise topic. We critically investigate each of these, provide coarse-grained mathematical models to probe their plausibility, and generate predictions and experimental tests for further validation. Overall, we find that large fused components can have a variety of advantages whose effect sizes depend nonlinearly on network state, being low or absent in relatively fragmented states and only becoming apparent in highly fused states. These insights stress the importance of fusion and may provide useful intuition on the consequences of impaired fusion. This chapter has appeared as a publication in Bioessays [155].

Chapter 3 forms a brief auxiliary chapter in which we perform one of the experimental tests suggested in Chapter 2. Specifically, we measure mitochondrial membrane potentials during fusion and fission events to test whether these events conserve total mitochondrial membrane potential (as defined in the chapter). We find evidence that this is indeed the case, which provides support for a novel mathematical model, presented in Chapter 2, relating fusion/fission events and ATP production rate.

In Chapter 4, we explore the role of nuclear control in mtDNA and heteroplasmy dynamics by considering a variety of control mechanisms to identify important aspects and general consequences of different strategies. Because it is unknown how the cell truly controls its mtDNA, this exercise provides useful insights and intuition (see also Ref. [101]). We continue by introducing a mitochondrial energy-based cost function enabling us to explore optimal control mechanisms. To our knowledge, no computational approaches have yet been considered for describing recently developed mitochondrial disease therapies. We provide such an approach by constructing a mathematical model of nuclease treatment using recent experimental data, allowing us to explore optimal treatment strategies. Some of our findings are: i) long, weak treatments are more efficient than short, strong treatments, and ii) heteroplasmy distribution (not mean alone) is crucial for the success of gene therapies. Chapter 4 corresponds to a preprint (Ref. [156]) which has been submitted to Cell Systems and been through one round of peer review; it is currently in preparation for resubmission.

Finally, in Chapter 5 we describe in detail the heteroplasmy dynamics resulting from the linear feedback model introduced in Section 1.4.4. We construct a model which includes intercellular mtDNA exchange, an approach which has not been considered before in the context of mtDNA dynamics. This novel approach leads to several interesting insights such as: i) the possibility of preferential mutant expansion without any selection advantage, and ii) a possible explanation as to why only certain types of mutants expand and why these often occur at high copy numbers. Finally, we provide new estimations of mutant loads in aged individuals which appear to be much lower than often assumed. The main finding of this chapter is that random drift models, in which all types of mtDNA have identical replication and degradation rates, can still give rise to stochastic selection effects. This means that experimental observations such as increases in mean heteroplasmy or faster mutant proliferation rates do not necessarily imply a mutant selection advantage. As such, we stress that random drift may play a larger role in ageing than previously assumed and can lead to non-intuitive behaviours.

2

What is the function of mitochondrial networks?

Summary

The cellular advantages underlying large mitochondrial fused networks are still incompletely understood. In this chapter, we describe and compare hypotheses as to the function of mitochondrial networks, we use mathematical and physical tools both to investigate existing hypotheses and to generate new ones, and we suggest experimental and modelling strategies. Among the novel insights we underline from this work are the possible functions that: selective mitophagy is not required for quality control because selective fusion is sufficient; increased connectivity may have nonlinear effects on the diffusion rate of proteins; and fused networks can act to dampen biochemical fluctuations. We hope to convey that quantitative approaches can drive advances in the understanding of the physiological advantage of these morphological changes.

2.1 Introduction

As mentioned in the thesis introduction, mitochondrial fusion/fission dynamics are directly implicated in a variety of diseases [61]. Understanding the benefits of adopting a certain

network morphology will help elucidate the consequences of disruption of this morphology. This illustrates the importance of studying mitochondrial dynamics and elucidating the functions that motivate form.

Various effects of fused mitochondrial states have been suggested, including an increase in ATP production [148, 149, 151, 157, 158], protection against apoptotic stresses [149, 159–162], an increase in cell proliferation ([163] and references therein), and regulation of various signalling pathways [164–167]. How exactly these effects are established through increased mitochondrial connectedness remains unclear. We try to provide more clarity by using physical reasoning to explore the mechanistic advantages of mitochondrial networks including increases in controllability, efficiency, robustness of mitochondria with respect to perturbations, and increases in the capacity to consume oxygen. To complement the mainly qualitative discussions that exist in the literature, we here use mathematical and physical arguments to probe the properties and bioenergetics of mitochondrial network formation, with the aim of gaining biological insights and suggesting research strategies.

In this chapter we discuss the function of mitochondrial networks, by which we mean large connected pieces of fused mitochondrial material. In the right-hand panel of Figure 2.1A, several of these functions are proposed. Some of them are novel; others have been suggested based on experimental results, and discussed qualitatively, largely in the absence of mathematical models to test them. We hope to show that quantitative approaches to the question of mitochondrial network formation can serve as a tool to critically analyse old hypotheses and motivate new ones.

2.2 The main players involved in mitochondrial dynamics

Though the focus of this chapter is not on the proteins involved in mitochondrial dynamics, we occasionally refer to them and therefore provide a brief overview. The three main proteins involved in the fusion of mammalian mitochondria are the enzymes Optic Atrophy 1 (Opa1) and the two mitofusins, Mfn1 and Mfn2. Opa1 is involved in inner membrane fusion, while Mfn1 and Mfn2 regulate fusion of the outer membrane [168]. The central protein in mitochondrial division is the highly conserved Dynamin-Related Protein 1 (Drp1), which can be recruited to mitochondria by the outer mitochondrial membrane protein Mff (mitochondrial fission factor). All these proteins are involved in other processes besides mitochondrial fusion and fission, some of which are summarised in Table A.5. Reviews on the proteins involved in mitochondrial dynamics and their role in disease are provided in Refs. [169–171].

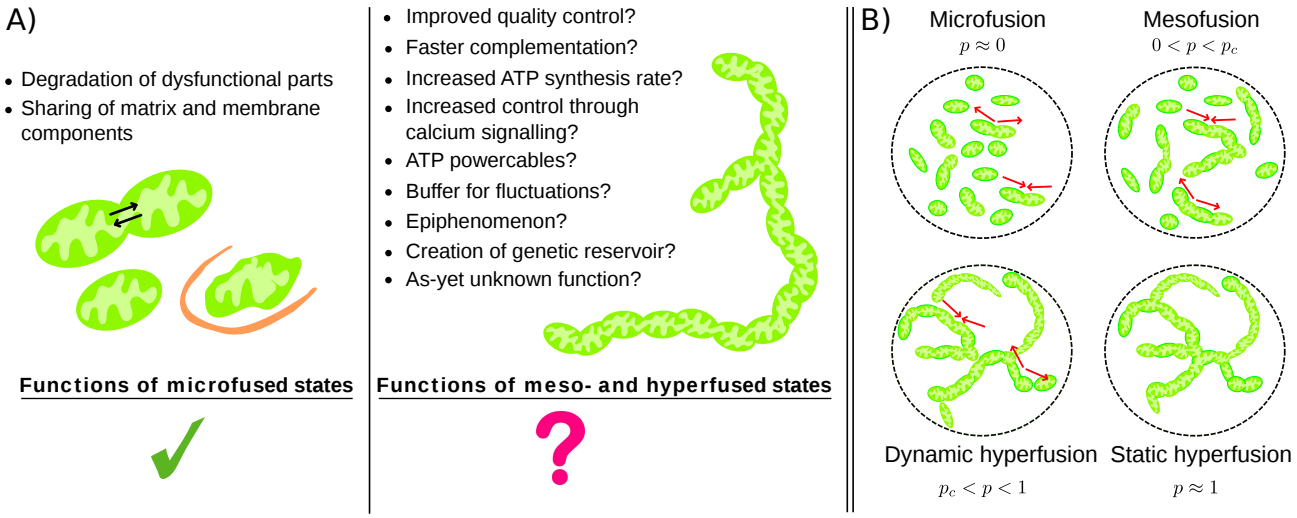


Figure 2.1: Potential causes and types of mitochondrial network formation. A) There are clear benefits of small scaled fusion events (microfusion) such as membrane- and matrix protein complementation (and possibly mtDNA complementation) and degradation of dysfunctional fragments (e.g. [59, 83]). However, to appreciate these advantages one does not require the formation of large extended networks, the functions of which remains to be elucidated. In this chapter we discuss the functions proposed on the right panel. **B)** The quantity p, defined as $\frac{\gamma_{fus}}{\gamma_{fis}+\gamma_{fus}}$, gives the probability that any two neighbouring mitochondrial units are fused. Note that different rates of fusion and fission can lead to the same connectivity of the network, as long as the ratio $\frac{\gamma_{fus}}{\gamma_{fis}+\gamma_{fus}}$ remains constant. In a static hyperfused state, virtually no fission events occur and therefore no quality control is possible. However, in a dynamic hyperfused state the fission rate is non-zero ($\gamma_{fis} > 0$) and quality control is present. The red arrows represent fusion or fission events and are absent in the static hyperfused state.

2.3 Quantitative definitions of micro, meso- and hyperfusion

In this section, we provide quantitative definitions of different mitochondrial morphologies. This approach facilitates further mathematical treatment and allows us to refer to the different morphologies in a clear and precise manner; the terms introduced in this section are used throughout the rest of the chapter.

We assume that there exists a smallest mitochondrial 'unit'. These units may be fused (when they are part of a lumenally continuous filament) or fragmented. This assumption is a mathematical convenience and does not affect our later findings or represent our belief in a quantised set of mitochondrial sizes. We define a fission rate γ_{fis} and a fusion rate γ_{fus}, which are considered to be the same for each mitochondrial unit*. The quantity $p \equiv \frac{\gamma_{fus}}{\gamma_{fis}+\gamma_{fus}}$ then gives the probability that a continuous link exists between any two neighbouring mitochondrial units (i.e. the probability that two neighbouring units are fused).

Percolation theory [172] suggests that as p increases, at some value of p a percolating path will exist (a chain of fused mitochondria extending from one end of the cell to the other, in the

*This automatically makes the total fission and fusion rates larger in a long mitochondrial filament compared to a small one because the larger filament consists of more units, each with fission rate γ_{fis} and fusion rate γ_{fus}.

limit of very large cells). This situation merits some special consideration in the context of several hypotheses, and so we refer to this percolating value as p_c. Roughly, at and above this critical value a mitochondrion at one extreme end of the network is expected to be continuously connected to a mitochondrion at the other end. We note that though simple percolation theory is of relatively limited use in describing mitochondria (which are dynamic, unlikely to lie on a lattice, and have connectivity properties dependent on membrane potential), it still provides a framework that can be used to gain intuition. The possibility of a phase-transition in mitochondrial network structure was raised previously in Ref. [126].

The different morphological states we introduce are: *fragmented* ($p = 0$; no fusion); *microfused* ($p \approx 0$; rare fusion); *mesofused* ($0 < p < p_c$; fission dominated); *dynamic hyperfused* ($p_c < p < 1$; fusion dominated); and *static hyperfused* ($p \approx 1$; rare fission). These states are illustrated in Fig. 2.1B.

A high value of p means that the mitochondrial population is in a highly fused state, which can be the result of a high fusion rate, low fission rate, or both. The distinction between dynamic hyperfusion and static hyperfusion is important. For both hyperfused states a percolating continuous path exists ($p > p_c$). The difference is that in dynamic hyperfused states there can still be an appreciable rate of fission (e.g. if fusion proteins are overexpressed), whereas in static hyperfused states there are (almost) no fission events (e.g. if fission proteins are knocked out or heavily downregulated). Enforcing mitochondrial elongation leads to oxidative damage and decreased respiration [59], increased cell death [150], mtDNA loss [64] and chromosomal instability [173]. In many of these studies, the hyperfused state is induced by knockout of fission proteins, which creates a static hyperfused state. However, if physiological hyperfusion involves dynamic rather than static hyperfusion, fission events do occur and the afore-mentioned negative consequences may not be manifest.

We appreciate that our assumption of equal rates of fission and fusion for all mitochondrial units represents an oversimplification. In reality, fusion rate depends on membrane potential [59, 174, 175] and fission and fusion events are not independent [59, 176]. We nonetheless believe that using a simplified approach can help make testable predictions and it provides a framework for more sophisticated models. We note that there is a disconnect between an idealised mathematical description of network structure and experimental measurements that are currently possible (including average mitochondrial length and form factors), although new approaches are narrowing this gap [177, 178]. Useful insights may still be gained by considering these mathematical abstractions. The exact value of the parameter p_c depends on

the underlying network structure, and it is not easy to find this value for real mitochondrial networks. Similarly, it is hard to say how connected the network is for a given value of p, without knowing the network structure.

Physiological circumstances in which meso- and hyperfusion occur, as well as the 'typical' morphological state of mitochondria, are summarised in Tables A.1 and A.2 in the appendix: it is unclear whether meso- and hyperfusion are a widespread cellular phenomenon or restricted to certain cell types and situations.

2.4 Hypothesised reasons for mitochondrial meso- and hyperfusion

In this section we list existing hypotheses as to the function of mitochondrial meso- and hyperfusion. Besides the hypotheses discussed here, additional ones are summarised in Section A.2 of the appendix. These are: meso- and hyperfusion i) create a genetic reservoir [179]; ii) increase ATP synthesis through a range of mechanisms in addition to the one described in this chapter; iii) enable faster energy transmission along mitochondrial cables [180–183]; and, iv) have no function. We note that the 'cabling hypothesis' (appendix Section A.2.3), which is illustrated in Figure 2.6B, has obtained some recent support in skeletal muscle fibres and cardiomyocytes [184–186]. All hypotheses, including the ones discussed in the appendix, are summarised in Table 2.1; critiques of each hypothesis are included in this table. In Table 2.2 we provide experimental tests and further modelling suggestions for all hypotheses discussed in this chapter.

One immediate consequence of a mathematical perspective on mitochondrial fusion is the observation that, for fused states to be physiologically beneficial, a nonlinear relationship between a mitochondrial property and cellular functionality must be involved. In other words, a fused mitochondrion must be of more use to the cell than the sum of the individual pre-fused mitochondria. Suppose x denotes some property of a mitochondrion (for example its membrane potential) and $f(x)$ describes how useful this mitochondrion is to the cell. Then, if there is another mitochondrion with property y and 'usefulness' $f(y)$, we expect:

$$\underbrace{f(x+y)}_{\text{'usefulness' of the fused mitochondrion}} > \underbrace{f(x)+f(y).}_{\text{sum of 'usefulness' of the individual mitochondria}}$$

In other words, the function $f(x)$, relating some aspect of mitochondrial size to 'usefulness', must be nonlinear. Somehow fusion into networks must create 'extra usefulness' to the cell; the network structure must allow for, or give rise to, options that were not available before.

In some of the hypotheses discussed each individual fusion event benefits the cell, in others, a benefit only arises once sufficiently many mitochondria have fused to form an interconnected network.

Hypothesis & references	Limitations/Criticism
Increased selection bias in quality control. ∗	The results of the model that is used depend on the rate of autophagy. If no autophagy is present, one needs to create additional assumptions to obtain the same results. If mitophagy is sufficiently functionally selective (meaning dysfunctional mitochondria are more likely to be degraded) then an increase in selection bias may be counteracted by a protection of dysfunctional fragments from degradation.
Faster or more effective complementation [187–192].	Matrix protein complementation through small fusion events is efficient [192], cells with low fusion levels show no major dysfunctions [62], and ongoing fission and fusion events can, according to one estimate, lead to better mixing after two hours than stress induced hyperfusion [190].
Increases in ATP production caused by:	
i) Changes in inner membrane shape (discussed in Section A.2.2.1) [45, 46, 193–196].	i) There is no obvious reason why cristal shape should be determined by overall state of mitochondrial organisation.
ii) Decreases in proton leak (discussed in Section A.2.2.2) [197].	ii) This may only be relevant in brown adipose tissue (because proton leak has a more important role in this tissue) it may not explain hyperfusion in other tissues.
iii) Decreases in mitophagy levels (discussed in Section A.2.2.3) [148, 158].	iii) The cell may keep total mitochondrial mass (or mitochondrial volume) at the same level; an absence of mitophagy may have other undesirable cellular consequences.
iv) nonlinear response of ATP synthesis rate to membrane potential. ∗	iv) The model discussed considers the role of $\Delta\psi$ in producing ATP, whereas actually the electrochemical potential $\Delta\mu_{H^+}$ drives ATP synthesis: extensions to the electrochemical potential are desirable.
Improved bioenergetic control and energy production through Ca^{2+} signalling [198–201].	Various studies suggest that calcium has no significant influence on rate of ATP synthesis *in vivo* [202]. Other modes of calcium uptake besides the mitochondrial uniporter that are more rapid exist [203].
Increased buffering against perturbations. ∗	It might seem just as natural that in a fragmented state the isolation of the different mitochondria is a form of robustness. Fluctuations in larger mitochondria will occur more frequently because of the larger surface area.
Enables energy transmission (power cabling) along mitochondria (discussed in Section A.2.3) [181–186].	Though experimental support for this hypothesis was found in skeletal muscle and heart tissue [184–186], it does not account for hyperfusion in tissues that are less dependent on oxygen and have lower ATP demand.
Creating a genetic reservoir (discussed in Section A.2.1) [179]. ∗	It is not clear whether large-scale fusion is necessary to maintain a genetic reservoir; modulating biogenesis and mitophagy might be sufficient. Some mitochondria with harmful mtDNA mutations may not be able to fuse, and are likely to be degraded regardless of increased fusion rates. If mtDNA mutations are not harmful, increased fusion is not required per se to create new mutations.
No function (discussed in Section A.2.4).	It seems coincidental that different kinds of stress lead to increases in fusion or decreases in fission activity with a hyperfused state as a result. Additionally, the main argument to support this hypothesis (many shaping proteins are involved in other processes) is also an argument for the importance of mitochondrial dynamics.

Table 2.1: An overview of hypotheses on the function of mitochondrial fusion discussed in this chapter including criticism. Asterisks denote hypotheses that, to our knowledge, have not been previously proposed.

Hypothesis	Further modelling	Experimental tests
Increased selection bias in quality control.	The ordinary differential equation model we describe in Section A.1.1 is deterministic and neglects the pronounced stochastic influences likely to affect mitochondrial quality control. More powerful models could be constructed by including these stochastic influences and relaxing some of the simplifying assumptions of our model.	One of the assumptions of our model is that only small mitochondrial fragments are degraded. It can be measured whether there exists a threshold size above which a mitochondrial filament is not degraded by mitophagy. Alternatively, construct two populations of cells, one wild-type and one with increased fusion rates. The rate of autophagy should be the same in both populations. Measure the average $\Delta\psi$ in cells from both populations. Our model predicts that the distribution of averages is more centered towards low values of $\Delta\psi$ in the wild-type population.
Faster or more effective complementation.	Mitochondria do not lie on a square lattice, so a better model can use randomly distributed nodes or use the microtubule network. A model that does not explicitly position nodes in space has been developed [126], but it does not consider diffusion on the network. This model of the mitochondrial network also shows percolation phenomena, and future work can extend the model by introducing a diffusing particle on the network and preferably introducing heterogeneity in fusion rates to represent heterogeneity in membrane potentials.	This hypothesis suggests that the root mean squared distance travelled by mitochondrial proteins depends nonlinearly on the connectedness of the network (network connectedness can e.g. be estimated by measuring the average length of a mitochondrial fragmented). Calculate the diffusion coefficient of proteins and the root mean squared distance travelled by these proteins while slowly changing fission or fusion rate.
Increased ATP production caused by nonlinear response of ATP synthesis rate to membrane potential.	Numerous biophysical models of the respiratory chain in mitochondria have been developed (e.g. [204–206]). Using this class of models to study respiratory chain and TCA cycle kinetics during fusion of two mitochondria can help in finding the existence and cause of increased ATP synthesis rate upon fusion.	Measure $\Delta\psi$ (and preferably simultaneously ΔpH) of mitochondria before, during and after fusion events. Measurements of $\Delta\psi$ during and after fission (but not fusion) events have been done before [59, 207], and an asymmetry in potential is seen after fissioning [59]. It would be interesting to see whether this asymmetry is simply a reversion to a pre-existing asymmetry in potential before the preceding fusion event (fusion events are usually followed quite soon by fission events [59]). We perform experiments along this line ourselves in the next chapter (Chapter 3). Alternatively, take snapshots of cells and quantify the amount of mitochondrial mass that is fused (by e.g. measuring the average mitochondrial size, which on average will be proportional to the level of connectivity in the cell) while also measuring [ATP]. Do this for many cells in order to search for a potential correlation between the amount of fused mitochondria and cellular [ATP]. Such correlations have been found before [148, 149, 151, 157] but not without perturbing the cell. We propose to take advantage of natural fluctuations in connectedness. Alternatively, look at passive fluctuations in network size of mitochondria in single cells, while reading out [ATP]. Alternatively, induce fragmentation while monitoring [ATP] and membrane potential during treatment.
Table 2.2 continued on next page		

Table continued from previous page

Improved bioenergetic control and energy production through Ca^{2+} signalling.	Metabolic Control Analysis (MCA) can be used to predict how sensitive ATP production is to changes in activities of mitochondrial enzymes (caused by changes in $[Ca^{2+}]$). MCA has been used to study OXPHOS and glycolysis [208–212] and the TCA cycle [213]. It was shown that α-ketoglutarate dehydrogenase and and isocitrate dehydrogenase (both stimulated by Ca^{2+}) had 70% and 23% control over respiration respectively [213]. This result, however, is only true for specific conditions. To make physiologically relevant predictions, these models can be integrated into biophysical models of the TCA cycle and respiratory chain. Ordinary differential equation based biophysical models linking calcium and mitochondrial physiology can also be probed to explore this relationship [202].	Prepare two populations of cells, one wild-type and one with more fused mitochondria. Then stimulate $[Ca^{2+}]_{\mathrm{cytoplasm}}$ while also measuring oxygen consumption of the populations. Compare the change in oxygen consumption induced by increased $[Ca^{2+}]_{\mathrm{cytoplasm}}$ between the two populations of cells, to find a relationship between connectedness of the mitochondrial network and calcium-stimulated respiration. Alternatively, look at the distribution of $[Ca^{2+}]_{\mathrm{matrix}}$ in single cells of both populations after stimulation of $[Ca^{2+}]_{\mathrm{cytoplasm}}$, to check whether this distribution is more homogeneous in cells with more fused mitochondria (see Figure 2.5).
Increased buffering against perturbations.	Biophysical models of the mitochondrion that already exist (many exist, e.g. [214–216]) can be used to check whether an increase in size indeed dampens fluctuations in membrane potential. However, one must be careful to use models that define the flux of ions into the mitochondrion to be proportional to surface area. The model presented in Ref. [204], for example, defines flux to be proportional to mitochondrial volume, and this model thus can not be used to check the hypothesis discussed here.	While looking at (and quantifying) natural fluctuations in the size of a mitochondrial filament, measure fluctuations in membrane potential (and preferably also fluctuations in ΔpH) of this filament to check whether larger filaments have smaller fluctuations. Alternatively, increase the permeability of the mitochondrial inner membrane in cells with fused mitochondria, and cells with fragmented mitochondria. Then measure the effect of this change in permeability on $\Delta\psi$ and ΔpH in both situations.

Table 2.2: Suggestions for future modelling and experiments for further analyses of the hypotheses on the function of mitochondrial fusion. For each hypothesis discussed in the main text, we suggest further modelling approaches and experiments that will help test the hypotheses. Most of the experimental tests suggested will be possible with the tools available today. We mentioned several hypotheses for an increase in [ATP] in highly fused mitochondrial states; in this table we only discuss hypothesis (iv): the others are discussed in Sections A.2.2.1 - A.2.2.3

2.4.1 Selective fusion creates the possibility of quality control without needing selective mitophagy

Summary. Mitochondrial quality control is the process that maintains a healthy mitochondrial population by identifying and degrading dysfunctional mitochondria [59, 217], degrading damaged mitochondrial components [218], and transporting damaged components out of the mitochondrion [219, 220]. Three mechanisms contributing to this control are fusion, fission and mitophagy. To ensure that a degradation bias is present, whereby dysfunctional mitochondria are more likely to be degraded than healthy mitochondria, selection occurring in one of these mechanisms is sufficient.

As mentioned in the thesis introduction, though mitophagy has been shown to be selective under various experimental perturbations [52, 53], it is currently still debated whether selection effects are significant in physiological settings [27, 54]. We argue that selective fusion combined with non-selective fission and non-selective mitophagy leads to the desired biased degradation and that in fact there are two levels of quality control: i) control on the level of the mitochondrial network (non-selective fission and selective fusion) that does not require mitophagy and which we call 'blind surveillance', and ii) control on the level of the cell using non-selective mitophagy. In this section, our terms 'selective' and 'non-selective' refer to selection based on mitochondrial function; we assume that mitophagy always selects on mitochondrial size [148, 158] (i.e. only small mitochondrial fragments are targeted for mitophagy). Size-dependent mitophagy is the source of nonlinearity in this model.

Blind surveillance consists of two parts. The first part involves random (blind) fission events. By random we mean that they are not selective, and therefore a functional mitochondrion is just as likely to become fragmented as a dysfunctional one. The second part is the surveillance, which involved selective fusion events: a functional mitochondrion is more likely to fuse [59]. As a consequence, a functional mitochondrion will, on average, stay fragmented for a shorter period of time than a dysfunctional mitochondrion. With blind surveillance present, mitophagy does not need to be selective *because any isolated mitochondrion is more likely to be dysfunctional than healthy and therefore even if mitophagy is non-selective, a bias towards degrading dysfunctional mitochondria is automatically established.* The strength of this effect is exacerbated the more fused the mitochondria are (as shown below).

Having dysfunctional mitochondria being separated from the fused network is an advantage on its own because a dysfunctional mitochondrion fusing with an already fused and functional network may have negative effects that are not present if the mitochondrion in question remains

isolated. Blind surveillance thus forms a first level of quality control (it separates dysfunctional mitochondria from the network by using non-selective fission and selective fusion), and mitophagy forms the second level by eliminating fragmented mitochondria (which are more likely to be dysfunctional).

Experimental support. Selection on the level of fusion (mitochondria with low $\Delta\psi$ are less likely to fuse [59, 174, 175]) has been discussed in the literature. Possible mechanisms for selective fusion are the increased processing of Opa1 by Oma1 [221, 222] or increased ubiquitination of Mfn1,2 by Parkin [223, 224] when $\Delta\psi$ is low, which then results in a lower fusion probability. Selective elimination of damaged mitochondria has been observed [50, 225–229], although the precise mechanisms are still incompletely understood [230] and, as mentioned before, the efficiency of selective mitophagy in physiological settings may be limited [57].

Coarse-grained quantitative model. Mathematical models of mitochondrial quality control have been constructed previously [40–42] and show that fission, selective fusion and selective autophagy together increase mitochondrial functionality. We here focus on the specific role of the network state itself, assuming non-selective mitophagy and varying fusion and fission rates. We construct a simple model of ordinary differential equations involving the following four mitochondrial populations: i) healthy fused, ii) healthy fragmented, iii) unhealthy fused, and iv) unhealthy fragmented. The concentrations of these populations are denoted by c_{hf}, c_{hs}, c_{uf} and c_{us}, respectively (the subscripts 'hf' and 'us' stand for 'healthy fused' and 'unhealthy singleton', where 'singleton' refers to a fragmented mitochondrion). In this context, mitochondria are considered unhealthy if they have decreased fusion probabilities caused by e.g. lowered membrane potential or mutant mtDNAs.

We denote the fusion rate of healthy and unhealthy mitochondria by γ_{hf} and γ_{uf}, respectively, where we encode selective fusion by assuming $\gamma_{hf} > \gamma_{uf}$. The rate of fission is set to be the same for all mitochondria and is denoted by γ_f. Mitochondria are created through biogenesis (occurring at a constant rate B) and removed through mitophagy (occurring at rate M). We assume that only fragmented mitochondria can be eliminated through mitophagy (as elongated mitochondria are protected from degradation [148, 158]). We also assume that a mitochondrion cannot change its status from healthy to dysfunctional or vice versa (this assumption is further discussed in Section A.1.1). Finally, as we solely focus on the role of network state, we impose a constraint to maintain constant total copy number, i.e. $B\cdot(c_{hf}+c_{uf}+c_{hs}+c_{us}) = M\cdot(c_{hs}+c_{us})$. The dynamics of this system, after eliminating M using the constraint, are given by the following equations (see Section A.1.1):

$$
\begin{aligned}
\dot{c}_{hs} &= -c_{hs}\left(\gamma_{hf} + B\frac{c_{hf}+c_{uf}}{c_{hs}+c_{us}}\right) + \gamma_f c_{hf} \\
\dot{c}_{us} &= -c_{us}\left(\gamma_{uf} + B\frac{c_{hf}+c_{uf}}{c_{hs}+c_{us}}\right) + \gamma_f c_{uf} \\
\dot{c}_{hf} &= c_{hf}(B-\gamma_f) + \gamma_{hf} c_{hs} \\
\dot{c}_{uf} &= c_{uf}(B-\gamma_f) + \gamma_{uf} c_{us}
\end{aligned} \tag{2.1}
$$

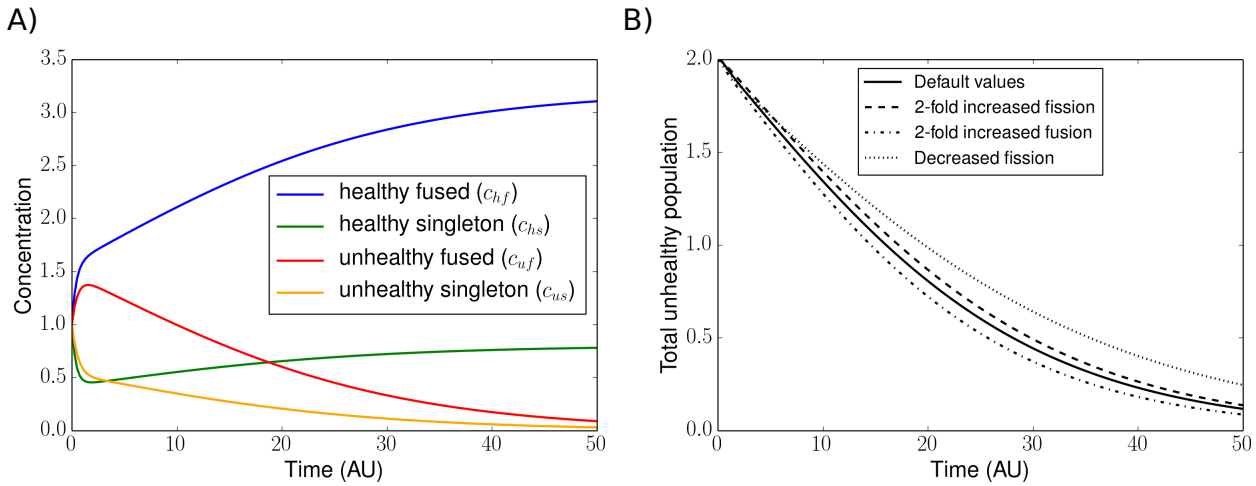


Figure 2.2: Selective fusion on its own leads to a healthier mitochondrial population. A) The trajectories of c_{hf}, c_{uf}, c_{hs} and c_{us} (all initialised at 1.0) are shown as a function of time. For long times, despite mitophagy being equal for healthy and unhealthy mitochondria, only healthy ones survive because of the combination of selective fusion and size-selective mitophagy. This behaviour does not depend on the initial conditions of the system. Parameters used are $\gamma_f = 0.8$, $\gamma_{hf} = 2$, $\gamma_{uf} = 1.3$ and $B = 0.3$. **B)** Here we observe the rate of decay of the unhealthy population ($c_{uf} + c_{us}$) for the following parameter settings: i) our 'default' parameters as used in figure (A) (solid), ii) setting $\gamma_f \to 2\gamma_f$ (dashed), iii) setting $\gamma_{hf} \to 2\gamma_{hf}$ and $\gamma_{uf} \to 2\gamma_{uf}$ (dash-dot), and iv) decreasing fission such that the total fraction of fused mitochondria is similar to case (iii) (which results in $\gamma_f = 0.55$, as shown in Section A.1.1).

Solving Equations (2.1) numerically, we find that *the population of dysfunctional mitochondria tends towards zero without selective mitophagy, due to the presence of selective fusion* (Figure 2.2A). This dysfunctional population decreases faster when fusion rate is increased (keeping the ratio γ_{hf}/γ_{uf} constant) and slower when fission rate is increased (Figure 2.2B). We also decreased fission rate to obtain a level of connectedness similar to the setting with increased fusion; this reduced the rate of decay of dysfunctional mitochondria[†] (Figure 2.2B). The total number of healthy mitochondria that are degraded, however, is largest in the case of increased fusion (as shown in Section A.1.1).

[†]Selective fusion is the factor in our model that drives dysfunctional mitochondria towards extinction, and increasing its rate increases this drive. Decreasing fission does not strengthen the selective drive and only slows down the rates of degradation as less mitochondria are fragmented.

In conclusion, an increased network connectivity can decrease the number of dysfunctional mitochondria solely through selective fusion. This decrease is faster at high levels of fusion, but not at low levels of fission (which has the effect of keeping dysfunctional mitochondria in the total population for a longer time). More details of the model are provided in Section A.1.1.

Limitations/Critique. Autophagy is required for this mechanism to function, although this assumption also underlies other quality control mechanisms. Our model makes several assumptions (mentioned above), which may be relaxed in future work. Though we observe an increase in the rate of removal of dysfunctional mitochondria at higher fusion levels, the effect size is small. Also, our deterministic model merely forms an approximation to the actual stochastic dynamics. It will be interesting to evaluate our model in a stochastic setting while investigating in more detail the size of the selection effect as a function of parameter values.

In our model we used non-selective mitophagy, an assumption which, as discussed in the thesis introduction, is controversial. However, we stress that the aim of the model is to illustrate that selective mitophagy is not required per se; as such, we do not claim it is not present at all. When mitophagy is selective, increased fusion will still contribute to a biased removal of dysfunctional mitochondria, but this beneficial effect is counteracted by the effect of protecting dysfunctional mitochondria from their selective degradation. A more detailed analysis is then required to establish whether increased connectedness still has an overall beneficial effect, and there will likely be a trade-off between the degree of functional selectivity of mitophagy and fusion.

2.4.2 Small changes in fusion state can cause large changes in complementation rate

Summary. Large-scale fusion facilitates sharing of mitochondrial machinery, as this machinery moves through the mitochondrial network. Increased sharing may equilibrate concentrations of nuclear encoded proteins to enable better control over mitochondria [188], promote co-ordinated behaviour between mitochondria to synchronise gene expression [61, 231], or improve the health of the mitochondrial population by allowing mitochondria to complement each other's deficiencies [83, 152] (functional complementation).

The effect of increased fusion (or decreased fission) on diffusion rate is most important for fast-diffusing species because they will have their diffusion rate capped by fission and fusion rates. By diffusion rate we mean the effective rate of diffusion through the mitochondrial network, which will depend on fission and fusion rates. As the network becomes more interconnected,

a fast-diffusing species will rapidly explore the new available spaces. Small increases in p (i.e. small increases in network connectivity, where these increases can be caused by an increase in fusion rate, a decrease in fission rate, or both) may lead to large, nonlinear, increases in diffusion rate. This is especially the case near the percolating value p_c, because when $p > p_c$ it suddenly becomes possible to diffuse from one extreme end of the network to the other end, whereas when $p < p_c$ the distance that can be travelled is much more restricted. A 'switch-like' response is thus present for fast-diffusing species. Slow-diffusing species will experience the network as being rapidly fluctuating, and their diffusion rate is likely to increase linearly with fusion level, lacking a 'switch-like' response.

Experimental support. Functional complementation through fusion has been observed in numerous experimental studies [83, 152, 189], indicating that fused mitochondria do exchange contents. As mentioned before, the effect of increased connectedness of mitochondria is likely to be largest for fast-diffusing species. We therefore compare diffusion constants of several mitochondrial proteins (and mtDNA) in Table S3. These diffusion coefficients are also used in Chapter 5, in which we consider mtDNA diffusion along skeletal muscle fibres.

Coarse-grained quantitative model. We can study the diffusion of species along mitochondrial networks by simulations in which the network is represented by a 2D or 3D lattice. Mitochondria are represented by nodes in the network, and can be connected through edges. The edges can flicker 'on' and 'off', representing fusion and fission events, respectively, with rates γ_{fus} and γ_{fis}. In this model, each mitochondrion has the potential to fuse with any of its direct neighbours independently, and does so with rate γ_{fus} (similarly for fission). The previously-defined value p determines how likely it is that an edge is 'on'. Given a hopping rate for molecules moving between adjacent points on the network, assuming particles are restricted to move only along 'on' edges, the average time it takes a particle to diffuse across a certain distance can be calculated in dynamic hyperfused ($p_c < p < 1$), mesofused ($0 < p < p_c$) and microfused ($p \approx 0$) states (see Section A.1.2). Our coarse-grained model makes several assumptions, including constant mitochondrial mass (corresponding to short timescales), an absence of mitophagy, and a lattice topology. Ref. [126] provides an alternative approach in which spatial structure is ignored but more realistic network morphologies are allowed; the authors do not consider diffusion on the network.

Figure 2.3A shows how the apparent diffusion coefficient varies with p for different values of τ, where τ is the relaxation time of the fluctuating bonds [232, 233] and is defined as $\tau = \frac{1}{\gamma_{fis}+\gamma_{fus}}$ (a lower τ means that bonds flicker more frequently between the states 'on' and 'off'). This

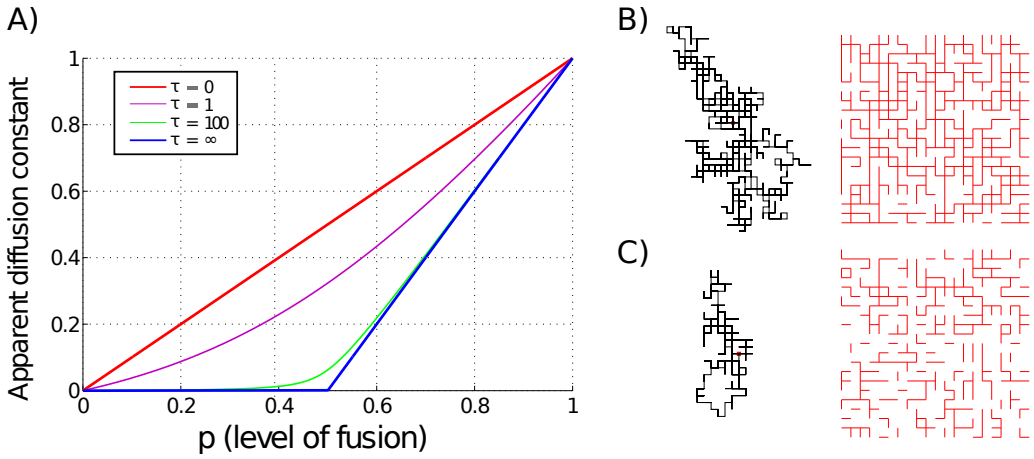


Figure 2.3: Apparent diffusion coefficient depends nonlinearly on degree of fusion. An abrupt change in diffusion rate can occur with only small changes in fusion rate. A) This figure shows the diffusion constant of a particle diffusing on a 2D fluctuating lattice as a function of p (the fraction of present bonds) and τ (the relaxation time of the fluctuating bonds). If $\tau = \infty$, bonds are static and in the limit of very fast fluctuating bonds, $\tau = 0$. **B)** We show the trajectory of a diffusing particle (left) and a lattice snapshot for $p = 0.6$ and $\tau = 100$ (right). The red dot marks the starting point of the particle. Existing bonds in the lattice snapshot are shown in red. **C)** Trajectory and lattice snapshot for $p = 0.4$ and $\tau = 100$. Figures B and C show that (for $\tau = 100$) increasing the value of p from 0.4 to 0.6, results in a more connected network and less restricted diffusion, as is also suggested in Figure A which indicates a rather abrupt increase in effective diffusion rate around $p = 0.5$.

figure is based on a mean field approximation, and similar results are produced by our stochastic model. In static percolation ($\tau = \infty$), an abrupt change in diffusion rate is present at $p = 0.5$ (in 2D, assuming a square lattice), but when bonds fluctuate in time, the diffusion rate changes less abruptly. For a given p, faster fluctuation has the effect of increasing diffusion rate; this effect is largest around $p = 0.5$. The simple model shows that a microfused state results in a smaller diffusion rate than a hyperfused state, even if the microfused state has very frequent fusion and fission events. Even slowly-varying hyperfused networks thus afford more facility to spread elements throughout the cell, confirming that a hyperfused morphology confers a mixing advantage for proteins.

Limitations/Critique. Complementation may be sufficiently achieved without a need for large-scale fusion: short 'kiss and run' events are claimed to be responsible for most mixing because of their high frequency [192]. In the spirit of 'back-of-the-envelope' calculations in biology [116], we use rough estimates to assess the feasibility of equilibration. The duration of association of these fusion events after exchange of content ranges from 4 s to 5 min, with a mean of 45 s [192]. The diffusion coefficient of Green Fluorescent Protein was measured to be 20-30 $\mu m^2/s$ [234, 235], meaning that in 45 seconds a distance of about $x \approx \sqrt{2Dt} \approx$ 40-50 μm can be travelled by a small protein, which is more than enough to accomplish equilibration. Even though complementation of matrix components is feasible, kiss and run events are likely to be too short to allow for sharing of membrane proteins and nucleoids.

2.4.3 Fusion increases ATP synthesis

Summary. Mitochondrial fusion may increase ATP production, through one or more of several possible mechanisms. We suggest the following mechanisms of particular interest: higher ATP production is caused by *(i) fusion-induced changes in inner membrane shape; (ii) fusion-induced decreases in proton leak; (iii) fusion-induced decreases in mitochondrial degradation; (iv) a nonlinear response of ATP synthesis rate to membrane potential.* (i)-(iii) are discussed in more detail in the appendix. We note that it is not entirely clear whether mitochondrial fusion is the cause of an observed increase in ATP production, or whether hyperfusion and high ATP production rates have a common cause, e.g. a recent study suggested that an increase in ATP production may precede mitochondrial fusion [236].

Experimental support. Several studies suggest that hyperfusion increases ATP levels and mitochondrial respiratory capacity [148, 149, 151, 157]. In nutrient-rich environments mitochondria tend to be fragmented, whereas under starvation they are observed to form elongated networks [148, 158], which can be interpreted as an attempt to enhance energy production in challenging environments. Hyperfusion is also observed at the G1/S transition, before energetically costly DNA replication [151]. It is worth noting that in hyperfused states, concentrations of cellular ATP – not just the rate of ATP production – were measured to be higher [149]. These increased concentrations suggest a physiological role for fusion beyond that of meeting extra ATP demand. This role could be to act as a cellular 'accelerator pedal', because an increase in ATP/ADP ratio in the cell has the consequence that many reactions will go faster [237, 238]. Further support for specific hypotheses is described in Sections A.2.2.1 - A.2.2.3.

Coarse-grained quantitative model. We focus mathematically on hypothesis (iv) which we have not seen discussed elsewhere. We first consider how the membrane potentials of two equally sized individual mitochondria $\Delta\psi_1$, $\Delta\psi_2$ are related to the overall membrane potential of their fused product, $\Delta\psi_{1+2}$. A simple model is that the fused product inherits the arithmetic average of the two individuals, i.e. $\Delta\psi_{1+2} = \frac{1}{2}(\Delta\psi_1 + \Delta\psi_2)$[‡]. We will show that this simple averaging of potentials can lead to increases of total ATP synthesis rates due to a sigmoidal dependence of ATP synthesis rate (r_{ATP}) on $\Delta\psi$ [239, 240] (Figure 2.4). We note that care must be taken in interpreting measured sigmoidal relations between $\Delta\psi$ and ATP synthesis rate [239]. The saturating behaviour observed at high $\Delta\psi$ may be an experimental artefact caused by the saturating relation between the ratio of ion concentrations at either side of the

[‡]Calculations based on considering charged capacitors show that it is possible that $\Delta\psi_{1+2} > \frac{1}{2}(\Delta\psi_1 + \Delta\psi_2)$ (Section A.1.3), though this capacitor model does not necessarily capture the behaviour of mitochondria fusing in chains. A simple averaging is the most natural null model to consider.

inner mitochondrial membrane and $\Delta\psi$ itself, as predicted by the Nernst equation. In the analysis below we assume the saturating relation depicted in Figure 2.4 exists and investigate the consequences of this relation.

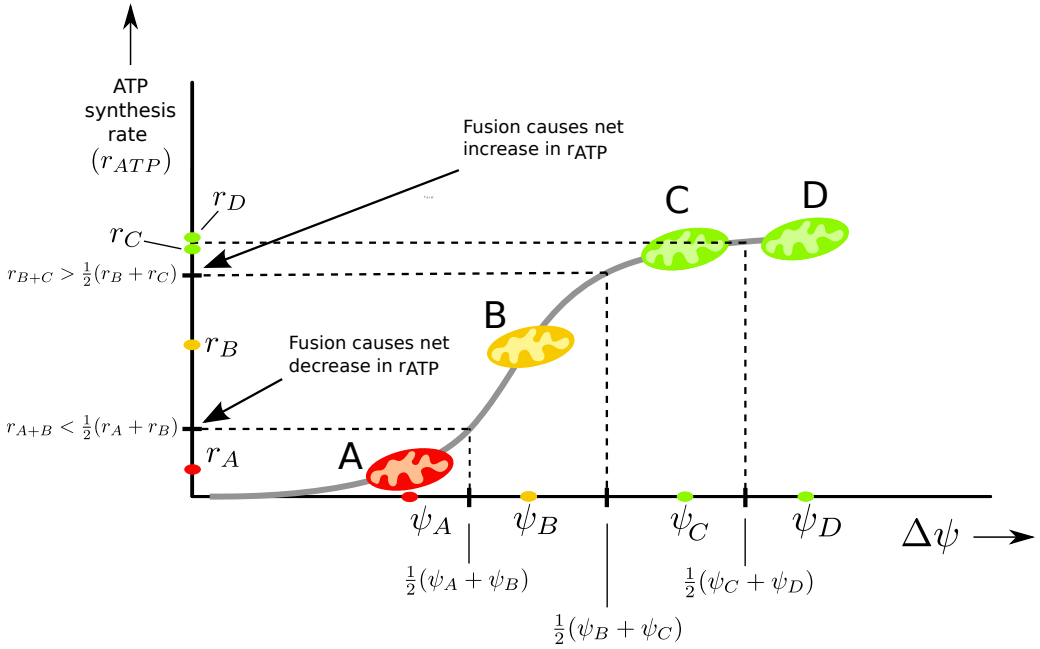


Figure 2.4: The effect of fusion on rate of ATP synthesis depends on the magnitude of the potentials of the pre-fusing mitochondria. In this figure, r_i denotes the ATP synthesis rate (r_{ATP}) per unit of mitochondrial size for mitochondrion i and r_{i+j} denotes the rate per unit size for the fused product of mitochondria i and j (a definition of mitochondrial size is provided in the next chapter). For simplicity we assume all pre-fusion mitochondria to have unit size; our results still hold when this assumption is relaxed. Because of the nonlinear dependence of r_{ATP} on $\Delta\psi$, if two mitochondria in the exponential regime fuse (i.e. mitochondria A and B), then averaging their potentials upon fusion causes the net ATP synthesis rate to decrease. This is because $2r_{A+B} < r_A + r_B$ (the fused mitochondrion is twice as large as the pre-fused mitochondria and the net post-fusion synthesis rate is therefore $2r_{A+B}$). In the plateau region, r_{ATP} does not depend on $\Delta\psi$ so there will most likely be no $\Delta\psi$-induced change in r_{ATP} if two mitochondria in this regime fuse (e.g. mitochondria C and D). Fusion of mitochondria in the saturating region (e.g. mitochondria B and C), induces net r_{ATP} increases because $2r_{B+C} > r_B + r_C$.

To explain this, consider Figure 2.4. As illustrated, fusion of mitochondria (B) and (C), while averaging their potentials, results in a net increase in ATP production rate. This is because the segment of the sigmoid connecting these two mitochondria is saturating[§]. Fusion of mitochondria (A) and (B), however, decreases net ATP production rates due to the strictly convex curve connecting them. Because fusion only occurs at sufficiently high membrane potential [59, 174, 175], we may expect events involving A-type mitochondria to be less common. Fusion then more often increases than decreases r_{ATP}, leading to an overall increase in cellular ATP production rates.

[§]A function $f(x)$ whose slope decreases with increasing x satisfies $f(\frac{1}{2}(x_1 + x_2)) > \frac{1}{2}(f(x_1) + f(x_2))$ where x_1, x_2 are any two points on the function. Similarly a decreasing slope with increasing x leads to $f(\frac{1}{2}(x_1+x_2)) < \frac{1}{2}(f(x_1) + f(x_2))$, a situation which occurs when fusing mitochondria (A) and (B) in Figure 2.4.

In the above, we assumed equally sized pre-fusion mitochondria and considered an averaging of potentials. This is equivalent to assuming a size-weighted averaging of potentials when fusion occurs between differently-sized mitochondria; the same argument as outlined above still hold. In the next chapter, we find some evidence for size-weighted averaging upon mitochondrial fusion/fission dynamics.

Limitations/Critique. The causal relationship between higher ATP levels and mitochondrial fusion is incompletely understood, and it may be possible that fusion is the effect of high [ATP] instead of the cause. A recent study showed that the rate of inner membrane fusion was closely correlated with oxygen consumption, and increased during OXPHOS stimulation as the result of increased Opa1 cleavage by Yme1l [236]. Also, in the model discussed above we have considered the role of $\Delta\psi$ in ATP synthesis rate, whereas actually the proton motive force (defined as $\Delta p = |\Delta\psi| + 2.3\frac{RT}{F}\Delta pH$) drives ATP production [239, 240]. The region of the ATP synthesis sigmoid at which mitochondria lie is not yet experimentally clear. Further critique of specific hypotheses is described in Sections A.2.2.1 - A.2.2.3.

2.4.4 Fusion affects bioenergetic control and total energy production through calcium signalling

Summary. Fusion averages out calcium concentrations across the mitochondrial network, giving rise to two advantages: 1) calcium concentrations are placed in an intermediate regime where small changes have pronounced effects on enzymatic rates, and thus tight bioenergetic control of the mitochondrial population is facilitated, and 2) the amount of mitochondrial volume that experiences a rise in $[Ca^{2+}]_{\text{matrix}}$ is increased, hence boosting total energy production.

Calcium is known to stimulate certain enzymes of the citric acid cycle (TCA cycle) [241–243], which in turn influences rates of ATP production. The dependence of TCA cycle activity on calcium is sigmoidal [244], meaning that the cell has maximal control over this activity when $[Ca^{2+}]_{\text{matrix}}$ is in the steeply rising part of the sigmoid, as indicated in Figure 2.5A. If $[Ca^{2+}]_{\text{matrix}}$ is high enough to reach the plateau region of the sigmoid, the enzymes are saturated. Only mitochondria located near microdomains of high $[Ca^{2+}]$ (e.g. calcium channels in the endoplasmic reticulum (ER)) are thought to take up calcium efficiently [245, 246]. The calcium concentration in these mitochondria rises significantly during ER depletion or calcium entry into the cell. This rise in $[Ca^{2+}]_{\text{matrix}}$ can be such that the saturation level is reached, and increasing $[Ca^{2+}]_{\text{matrix}}$ further has no effect on enzyme activity. Because fusion averages out concentrations inside the matrix, fusing a calcium-saturated mitochondrion with one with

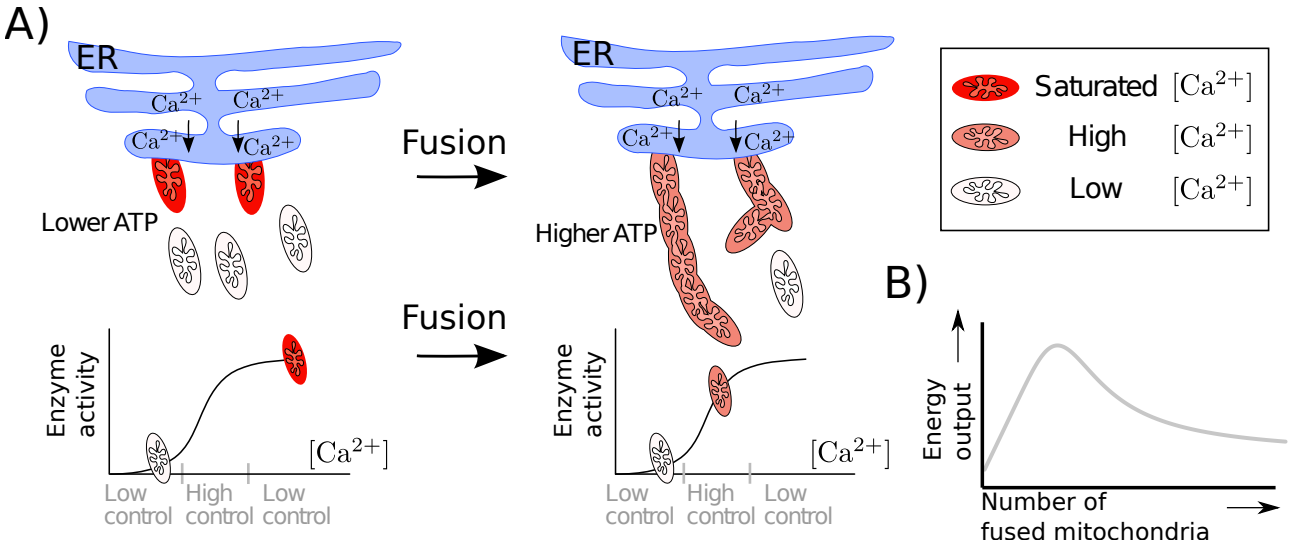


Figure 2.5: Fusion may increase controllability of TCA cycle activity and total energy production. A) If only mitochondria in contact with the ER easily take up calcium, then in a fragmented state only few mitochondria will have high (saturated) $[Ca^{2+}]_{matrix}$ and most will have low $[Ca^{2+}]_{matrix}$. The bottom figure indicates the position of the mitochondria on the sigmoid describing enzyme activity. If mitochondria fuse, $[Ca^{2+}]_{matrix}$ averages out, which moves the previously saturated mitochondria down the sigmoid and also moves the mitochondria which previously had very low $[Ca^{2+}]_{matrix}$ up the sigmoid with the result of increasing total enzyme stimulation. When even more mitochondria fuse, total enzyme stimulation will drop again because the mitochondria moved too far down the sigmoid. **B)** As the number of mitochondria fused to a mitochondrion close to the ER increases, total energy output will first increase and then decrease again because $[Ca^{2+}]_{matrix}$ is now so diluted as to reach the low enzyme activity regime. This plot is merely meant as a proof of principle, details are given in Section A.1.4.

low $[Ca^{2+}]_{matrix}$ has the effect of shifting $[Ca^{2+}]_{matrix}$ towards the more controllable region. Mitochondria far from high $[Ca^{2+}]$ microdomains with lower $[Ca^{2+}]_{matrix}$ increase stimulation of their TCA cycles by fusing with a mitochondrion with high $[Ca^{2+}]_{matrix}$. Fusion therefore increases the amount of mitochondrial volume affected by a calcium signal, which subsequently increases total energy production.

Experimental support. The idea that fusion increases the number of mitochondria that experiences a given calcium signal in the cell has been suggested before in Refs. [245, 247]. The existence of high $[Ca^{2+}]$ microdomains was suggested in Refs. [245, 246, 248], and it was found that only a small fraction of mitochondria were in close contact with the ER in various cell types [248].

Coarse-grained quantitative model. We focus on the uptake of calcium from the ER as the most important influence on mitochondrial calcium levels, assuming that without fusion, the mitochondria near ER calcium channels have saturated calcium-dependent TCA cycle enzymes, and the mitochondria far from the ER or plasma membrane have low $[Ca^{2+}]_{matrix}$ (as in Figure 2.5A). The first few fusion events will increase total enzyme stimulation (and therefore ATP production) because the mitochondria fusing to the calcium saturated ones experience a

significant increases in $[Ca^{2+}]_{matrix}$ and enzyme activation, whereas the saturated mitochondria experience little change in enzyme activation, despite their drop in $[Ca^{2+}]_{matrix}$ (because of the sigmoidal dependence of enzyme activity on $[Ca^{2+}]$). Adding more and more mitochondria to the fused chain will ultimately lead to a decrease in enzyme stimulation (because $[Ca^{2+}]_{matrix}$ will reach the lower part of the sigmoid), meaning that there exists a certain number of fused mitochondria that leads to maximal enzyme activation. This number depends on the amount of calcium released by the ER, the number of mitochondria near the ER, the basal $[Ca^{2+}]_{matrix}$ present in mitochondria far from the ER, the exact shape of the sigmoid, and, furthermore, relies on the assumption that when many mitochondria are fused, $[Ca^{2+}]_{matrix}$ becomes so diluted as to reach the low enzyme activity regime. There will of course be many other factors that influence this 'optimal number of fused mitochondria' (e.g. the ratio of phosphate-bound calcium to free calcium): we merely present the basic idea, which is also shown in Figure 2.5B (for details see Section A.1.4).

Limitations/Critique. This hypothesis is based on several assumptions that are debated in the literature. While various studies show that higher calcium concentrations lead to increases in NADH production and oxygen consumption [213, 249, 250], mathematical modelling [202] and uniporter studies [251] suggest that calcium perturbations may have little effect on respiration. Other studies observed calcium modulation only with elevated glucose [252] or only on a single TCA enzyme [244]. Which mechanisms of calcium uptake are mainly used, the dependence of these mechanisms on calcium concentrations, and the number of sites close to sources of calcium are also debated [245, 253] (for details, see Section A.1.5). Mitochondria have been observed to experience calcium transients, meaning that they extrude calcium quite after having absorbed it [199] and the simple model we discuss in Section A.1.4 may therefore only be valid on short timescales. Finally, calcium signalling linked to mitochondrial ultrastructure is by no means the only, or simplest, way in which the cell regulates its energy status.

2.4.5 Fusion provokes state changes protective against perturbations

Summary. By changing their morphological state, mitochondria can make themselves less susceptible to perturbations (for example, fluctuations in electrochemical membrane potential). The fused neighbours of a mitochondrial element can act as a buffer for biochemical or physical fluctuations. If failure of individual mitochondria has severe consequences for the cell, this increased robustness through fusion will be beneficial when mitochondria are subject to perturbations.

Experimental support. There are experimental indications that fused mitochondria are better protected against stress [254]. This hypothesis could account for why hyperfusion occurs during stress [149], and may explain why fusion protects the cell against apoptosis [149, 159–162] (or delays apoptosis [255]), because prior to cytochrome c release (which induces apoptosis) remodelling of cristae structure has been seen as a cause of changes in membrane potential [256]. If a larger network protects against fluctuations in membrane potential, it may be able to prevent cristae remodelling, thereby potentially delaying or preventing apoptosis.

In stressful conditions it may thus be disadvantageous for the cell to have its mitochondria fragmented because all of them are vulnerable to e.g. membrane potential fluctuations. If the cell fuses its mitochondria, they become more robust to the fluctuations, which may prevent the failure of many individual mitochondria, and subsequent cell death.

Coarse-grained quantitative model. A biophysical calculation considering the change in membrane potential upon changes in permeability of the inner mitochondrial membrane (see Section A.1.6.1) suggests $\frac{d\Delta\psi}{dt} \propto r^y$ where r is the radius of the mitochondrion and $y \in (-1, 0)$ depends on the structure of the membrane (the more invaginated the membrane, the larger y). This result suggests that for large mitochondria, fluctuations of $\Delta\psi$ will be of smaller magnitude. Fusing mitochondria thus protects them from perturbations, as illustrated in Figure 2.6A. This particular model assumes spherical mitochondrial geometry (as outlined in Section A.1.6.1). Small fragmented mitochondria are often seen to have a spherical shape and the fusion of two small spherical mitochondria may produce a mitochondrion that itself has an approximate spherical shape. The model discussed here may therefore be applied to fusion events involving small mitochondrial fragments.

We provide an alternative model that is independent of volume and surface area scaling and involves picturing mitochondria as individual agents coupled with spin-like interactions [257]. This model, in which a mitochondrion prefers to be in a similar state as its neighbours, shows that groups of mitochondria are less likely to undergo a catastrophic loss of function than individuals (see Section A.1.6.2).

Limitations/Critique. Even though fluctuations in larger mitochondria (fused mitochondria) may be of relatively smaller magnitude, they will occur more frequently because of the larger surface area which increases the probability that, for example, a pore opens or an ETC component fails. Stress does not always lead to a fused mitochondrial state, but can also lead to mitochondrial fragmentation [258, 259]. It can be that the level of stress is important, and that too much stress leads to fragmentation and subsequent apoptosis.

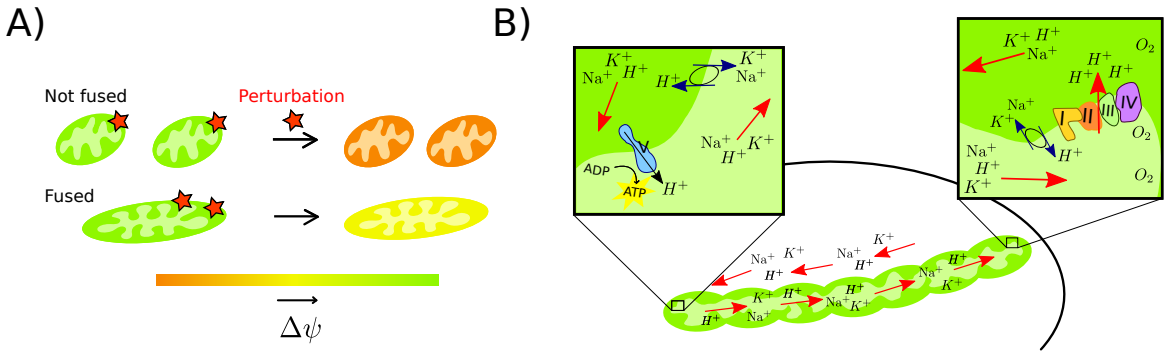


Figure 2.6: A) Mitochondrial fusion buffers fluctuations in membrane potential. Opening of the mitochondrial permeability transition pore or changes in leak can lead to depolarizations of mitochondria. These perturbations to the membrane potential will have less effect when mitochondria are fused because their bigger size makes them more robust. **B) The 'cable hypothesis': a mechanism of mitochondrial power cabling.** Oxygen concentrations are higher at the periphery of the cell and mitochondria positioned here are able to pump protons out of the matrix. If ATP is required in central regions of the cell, protons will flow into the matrix through ATP synthase. An electrochemical gradient establishes itself along the mitochondrial cable. Protons as well as K^+ and Na^+ cations (which can be exchanged for protons through Na^+/H^+ and K^+/H^+ antiporters) diffuse along the cable thereby transmitting electrochemical potential. This is the main idea of mitochondrial power cabling and it replaces diffusion of ATP or oxygen through the cytoplasm by cation movement along mitochondrial filaments, which may result in an increased speed of energy transmission.

2.5 Discussion

The function of mitochondrial networks is currently unclear, suggesting that new research strategies may be of use. We have shown that ideas from physics and mathematics provide a framework to suggest and critically evaluate hypothesised functions. Among the insights we underline from this work are the possibilities that 'blind surveillance' through selective fusion alone leads to an increase in mitochondrial quality control; that increased fusion may have nonlinear effects on the diffusion rate of proteins; that the effect on membrane potential of fusion may be more complicated than a simple averaging; and that fusion can act to dampen biochemical fluctuations. We note that selective fusion, being a key element of the hypotheses discussed in Section 2.4.1 and Section 2.4.3, is likely to be an important factor contributing to the benefits of fused networks. We stress again the observation that with increased fusion, ATP concentration, rather than merely the rate of production and consumption of ATP, changes. This implies an acceleration of cellular processes and suggests that fusion serves as a cellular accelerator pedal.

Which hypothesis is most likely to be true? Three hypotheses that we find attractive are (i) increased robustness; (ii) blind surveillance; and (iii) increased ATP production through nonlinear dependence of ATP flux on the properties of fusing mitochondria. Hypothesis (i) suggests a reason why mitochondrial morphology is dependent on cellular stress, which seems to be the main regulator of mitochondrial morphology. Hypothesis (ii) also links fusion with

oxidative stress, because in stress conditions improved quality control is beneficial. Hypothesis (iii) provides intuitive mechanisms by which fusion may improve the energetic status of the cell, compatible with a large amount of evidence that mitochondrial structure is correlated with bioenergetic capabilities of the cell. We cannot exclude the possibility that the central 'purpose' of network formation is not one of the currently considered hypotheses; but we anticipate that quantitative modelling approaches will also be powerful tools in analysing any future hypotheses.

As mentioned before, the 'cable hypothesis' (discussed in more detail in Section A.2.3 and summarised in Figure 2.6B) has obtained recent support in skeletal muscle and heart cells [184–186]. These cells have high energy requirements and mitochondrial movement is relatively limited [260, 261], meaning faster energy distribution through cabling may provide a significant advantage. However, as noted in Table 2.1, this hypothesis does not necessarily explain meso- and hyperfusion in other cell types.

We suggested experimental tests to further probe the hypotheses discussed in this chapter (Table 2.2), one of which (related to Section 2.4.3) we perform ourselves in the next chapter. Besides the future modelling strategies outlined in Table 2.2, which specifically address each of the discussed hypotheses, we stress that modelling the network dynamics themselves and their influence on mtDNA and heteroplasmy dynamics is of great interest. Network dynamics can be incorporated in the stochastic models of mtDNA dynamics introduced in Chapters 4 and 5; work along these lines is currently performed in our research group.

3

Experimental exploration of mitochondrial dynamics and membrane potential

Summary

Changes in mitochondrial membrane potential $\Delta\psi$ upon mitochondrial fusion and fission play an important role in determining how the state of the mitochondrial network influences cellular ATP production rates. We previously showed a mechanism by which a size-weighted averaging of membrane potentials during fusion can cause increased ATP synthesis rates in highly fused mitochondrial networks. In this chapter, we use confocal microscopy to track membrane potential during fusion and fission events in human primary fibroblasts. We find evidence that the pre-fission potential forms a size-weighted average of post-fission potentials, suggesting that total size-integrated mitochondrial potential is invariant under mitochondrial fusion/fission dynamics. This result, combined with i) a sigmoidal relation between $\Delta\psi$ and ATP synthesis and ii) $\Delta\psi$-dependent fusion, may form a potential explanation of observed increases in ATP production in highly fused networks.

3.1 Introduction

One of the hypotheses discussed in the previous chapter (Section 2.4.3) states that a highly connected mitochondrial network produces ATP at a faster rate than a fragmented network. The postulated underlying mechanism is that most fusion events cause a slight increase in ATP production rate, where we assumed the post-fusion membrane potential to form a weighted average (weighted by mitochondrial size) of the pre-fusion potentials (Figure 2.6). In this auxiliary chapter, we investigate whether this rule holds in human primary fibroblasts.

Several studies have experimentally measured changes in $\Delta\psi$ during mitochondrial dynamics by tracking mitochondrial network structure and membrane potential over time [59, 207, 262]. These studies mainly focus on the state of post-fission mitochondria, i.e. whether they are hyperpolarised or depolarised relative to the pre-fission mitochondrion. It was found that in 85% of 48 fission events studied, one daughter became hyperpolarised (by a maximal amplitude of -6.5 ± 3.8 mV) while the other became depolarised (by a maximal amplitude of 5.9 ± 3.7 mV) [59]; in 11% of cases no change was observed in potentials [59]. It was further found that the average difference in $\Delta\psi$ between two fusing mitochondria is 6.2 ± 4.3 and 7.2 ± 4.1 mV in INS1 and primary β cells, respectively [262].

However, from the existing studies it is unclear what the effect of a fusion or fission event is on 'cellular mitochondrial potential', a measure of the overall functionality of all mitochondria combined. This quantity cannot simply be defined as the mean value of $\Delta\psi$ (averaged over all mitochondrial fragments) as this does not distinguish between a single (small) mitochondrion with a certain potential or hundreds of mitochondria with the same potential. Obviously, a notion of size is required; no information on mitochondrial size was provided in the studies discussed above. If a large number of fission events were followed by a similar number fusion events to recover the initial network state, has there been a net change in overall mitochondrial potential?

In this chapter, we explore this question by performing similar experiments to those in Ref. [59] (i.e. we track mitochondrial membrane potential during fission events) with the addition of using data on mitochondrial size to test whether size-weighted average membrane potential is conserved during fusion and fission events. We find evidence that this is indeed the case, supporting the hypothesis discussed in the previous chapter stating that highly connected networks are associated with higher ATP production rates. Finally, we discuss limitations of our experiments and possible improvements for further research.

3.2 Results

3.2.1 Hypotheses regarding changes in membrane potential during network events

To test whether size-weighted averaging of potentials takes place, we first require a definition of mitochondrial 'size'. A natural candidate is the inner membrane area, as this is the site where the respiratory complexes and ATP synthases are situated, and therefore the site of $\Delta\psi$ generation; however, this quantity is hard to measure experimentally. The most straightforward measure of size is cross-sectional area (CSA), which we define as the area observed when cutting a mitochondrion longitudinally. Assuming mitochondrial width and thickness are roughly constant, a doubling of length corresponds to a doubling of both CSA and inner membrane length; this means that, under these assumptions, CSA provides a suitable measure of mitochondrial size.

We can now write down a definition of overall 'cellular mitochondrial potential', $\Delta\psi_T$, namely $\Delta\psi_T = \sum_i A_i \Delta\psi_i$, where i labels all mitochondrial fragments, and A_i and $\Delta\psi_i$ are the CSA and membrane potential of mitochondrion i, respectively. *Our hypothesis is that $\Delta\psi_T$, a notion of overall mitochondrial functionality, is invariant under mitochondrial fusion and fission events.* Note that, under the assumption that no mitochondrial mass is lost or gained during fusion or fission events, this statement corresponds to a conservation of integrated membrane potential. We stress that we investigate the effect on $\Delta\psi_T$ purely due to the fusion and fission events themselves. There will be many other processes (e.g. changes in proton leak or reverse ATP synthase activity) that influence $\Delta\psi_T$.

Specifically, we test the following identity:

$$\Delta\psi_{1+2} = \frac{1}{A_1 + A_2}(A_1\Delta\psi_1 + A_2\Delta\psi_2) \quad \text{(Model 1)} \tag{3.1}$$

where $\Delta\psi_{1+2}$ denotes the potential of the fused product which has a CSA of $(A_1 + A_2)$ (Figure 3.1). We test this model against an alternative model given by

$$\Delta\psi_{1+2} = \frac{1}{2}(\Delta\psi_1 + \Delta\psi_2) \qquad \text{(Model 2)} \tag{3.2}$$

Here, potential is simply averaged regardless of mitochondrial size and $\Delta\psi_T$ is not conserved. We will compute likelihoods for both models to test whether there is evidence to reject the simple averaging model in favour of the weighted average model.

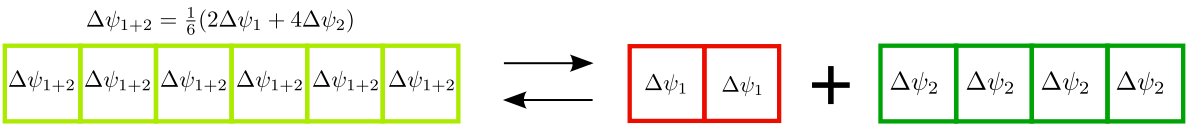


Figure 3.1: A size-weighted averaging model for changes in $\Delta\psi$ during mitochondrial dynamics. This cartoon illustrates the hypothesis we aim to test experimentally, namely that $\Delta\psi$ of the pre-fission (or post-fusion) mitochondrion forms the size-weighted average of the post-fission (or pre-fusion) potentials.

3.2.2 Visualising and defining mitochondria

We labelled mitochondria in intact human primary fibroblasts with two fluorescent dyes, enabling us to obtain qualitative information on changes in mitochondrial membrane potential while the mitochondria move around and undergo fusion and fission events. The two dyes used are the cationic dye Tetramethylrhodamine Methyl Ester (TMRM) and MitoTracker Green (MTG). Changes in the ratio of the fluorescent intensities of these dyes reflect changes in $\Delta\psi$ (see Materials and Methods) [59, 207]. Using the Nernstian fashion in which these dyes accumulate inside the negatively charged mitochondrial matrix (see Materials and Methods), information on changes in $\Delta\psi$ can be extracted and monitored over time.

To measure the membrane potential of a mitochondrion, we require a definition of its boundaries. Identifying the boundaries of a continuous fragment is complicated in itself and requires the use of photoactivatable fluorescent proteins. If activated, these proteins become fluorescent and spread throughout any mitochondrial sections continuously connected to the activated region, allowing for the boundaries to be easily visualised [207]. Because we had no access to such proteins, we identified boundaries by thresholding TMRM images (see Materials and Methods). Because of the uncertainty on whether a seemingly continuous mitochondrial fragment is actually fused, as well as uncertainty on the exact moment of fusion, we chose to focus solely on fission events which are more easily distinguishable.

To minimise misidentifications, we focussed our analysis on mitochondria physically separated from the bulk of the network (which usually surrounds the nucleus); these isolated mitochondria were assumed not to be connected to others elsewhere in the cell. Furthermore, we only analysed fission events which showed a clear physical separation of the two post-fission mitochondria. These kinds of events are likely to only represent a small fraction of all fission events, as many can occur without any physical separation [185, 207, 263]. Even with these precautions taken, we cannot be completely certain of whether our pre-fission mitochondrion is actually continuous, or whether any of our analysed mitochondria are connected to larger networks elsewhere in the cell; limitations of our analysis, together with suggestions for improvements, are discussed in Section 3.2.4.

3.2.3 Data analysis shows support for a model of weighted averaging

Figure 3.2A shows an example of a mitochondrial network labelled by TMRM and MTG obtained through confocal microscopy; merged and ratio images are also shown. A fission event occurred in this network involving the mitochondrion at the bottom of the image, as shown more clearly in Figure 3.2B. TMRM images were thresholded (Figure 3.2B) and subsequently used to identify mitochondrial outlines using the image processing program ImageJ (Figure 3.2C, Materials and Methods). These outlines were used as masks and applied to ratio images to obtain mean fluorescent intensities of individual mitochondria; changes in mean intensities of the TMRM-to-MTG ratio reflect changes in membrane potential (Materials and Methods).

Data was collected for $\sim$ 50 cells, though only 11 cells showed the particular type of fission event we focussed on (as discussed above). Time series data of changes in $\Delta\psi$ during 12 fission events (one cell showed 2 events) are shown in Figure 3.3. Each value of $\Delta\psi$ in this figure is calculated relative to the value in the very first frame of the series (using Equation 3.6), which is arbitrarily set to zero. Measurements of CSA of each mitochondrion are also shown and obtained from the number of pixels in the identified outlines (Figure 3.2C). Fluctuations in potential can be large (Figure 3.3), though this may reflect actual fluctuations in potential rather than large measurement errors.

Though we have several minutes' worth of data for each fission event (Figure 3.3), we chose to test our hypothesis using values of $\Delta\psi$ only at time points directly before and after fission*. The reasons for this are the following: i) we are interested in the immediate change in potential caused by the actual events themselves and try to avoid any compensations made by the mitochondria in response, and ii) we expect membrane potential values at later time points to be unphysiological (as explained below), and including this data will only introduce extra noise. The time interval between two consecutive frames in our experiments is usually $\sim$ 3 seconds, which we assume is larger than the response time of TMRM to changes in $\Delta\psi$. We do use all available data on mitochondrial size and define the CSA of a single mitochondrion as the time-averaged number of pixels contained in the outline defining the mitochondrion in question. Assuming that the 'true' mitochondrial area remains constant in the short time window of our experiment, using time-averaged values increases the accuracy of our estimations.

*This means we used only three data points of $\Delta\psi$ in each fission event, one before and two after the event.

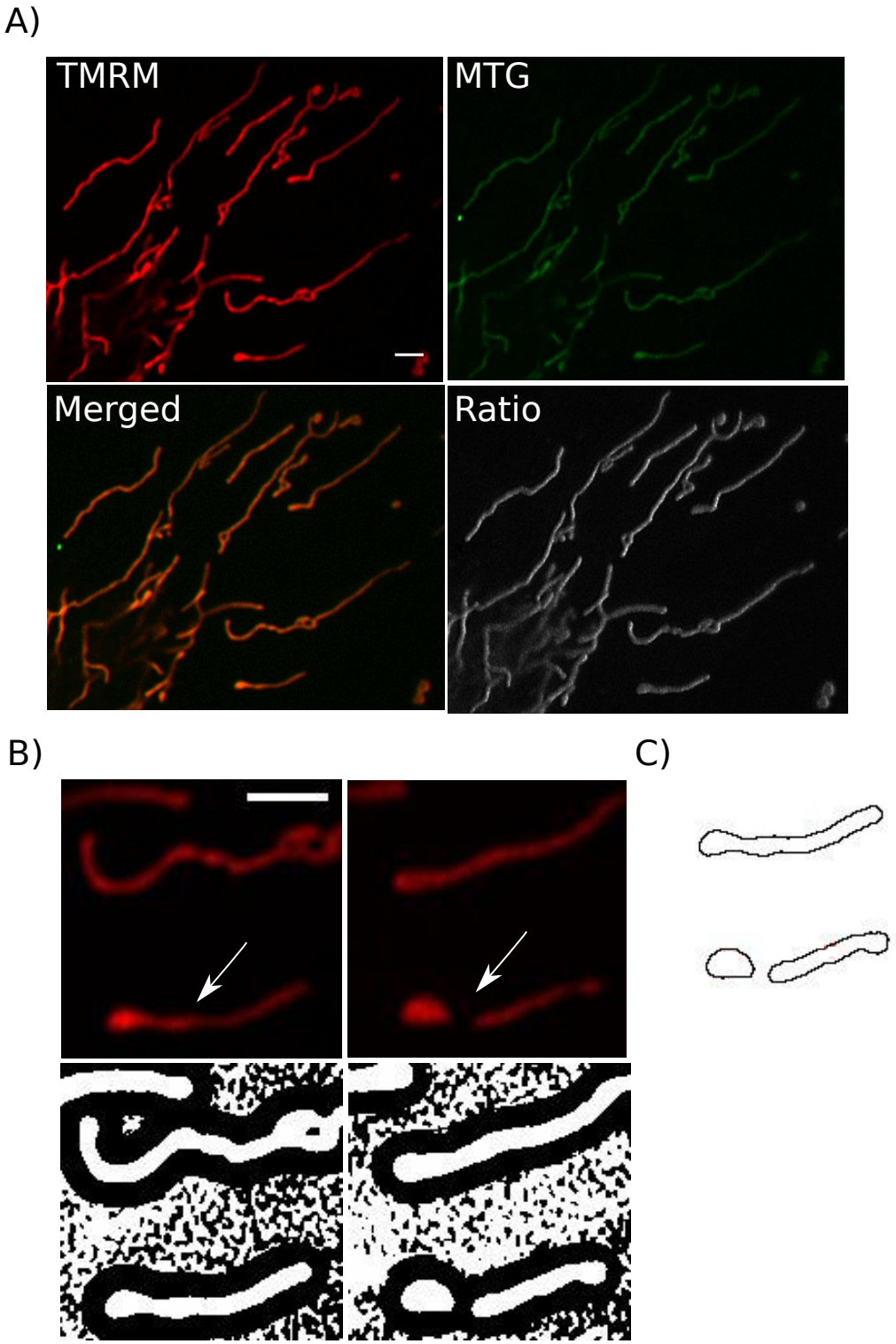


Figure 3.2: Example images of mitochondrial networks and fission events. A) A mitochondrial network is shown labelled by TMRM (red) and MTG (green). The merged and ratio images (TMRM-to-MTG) are also shown. Scale bar indicates 2μm. **B)** A mitochondrion undergoes fission at the location indicated by the white arrow. The black and white images are binary images obtained from thresholding the TMRM channel; identified objects have value '1' (white) while unidentified objects have value '0' (black). Because we use a local thresholding method, local fluorescent intensity maxima in the cytosol show up as white, but due to the often much higher mitochondrial intensity a black band appears around the mitochondria making them easily distinguishable from the cytosolic 'objects'. Scale bar indicates 2μm. **C)** Outlines of mitochondria identified in Figure (B) are obtained from the thresholded images, and are used as a mask to calculate statistics of the ratio image shown in Figure (A). The number of pixels in these outlines was used to define mitochondrial CSA.

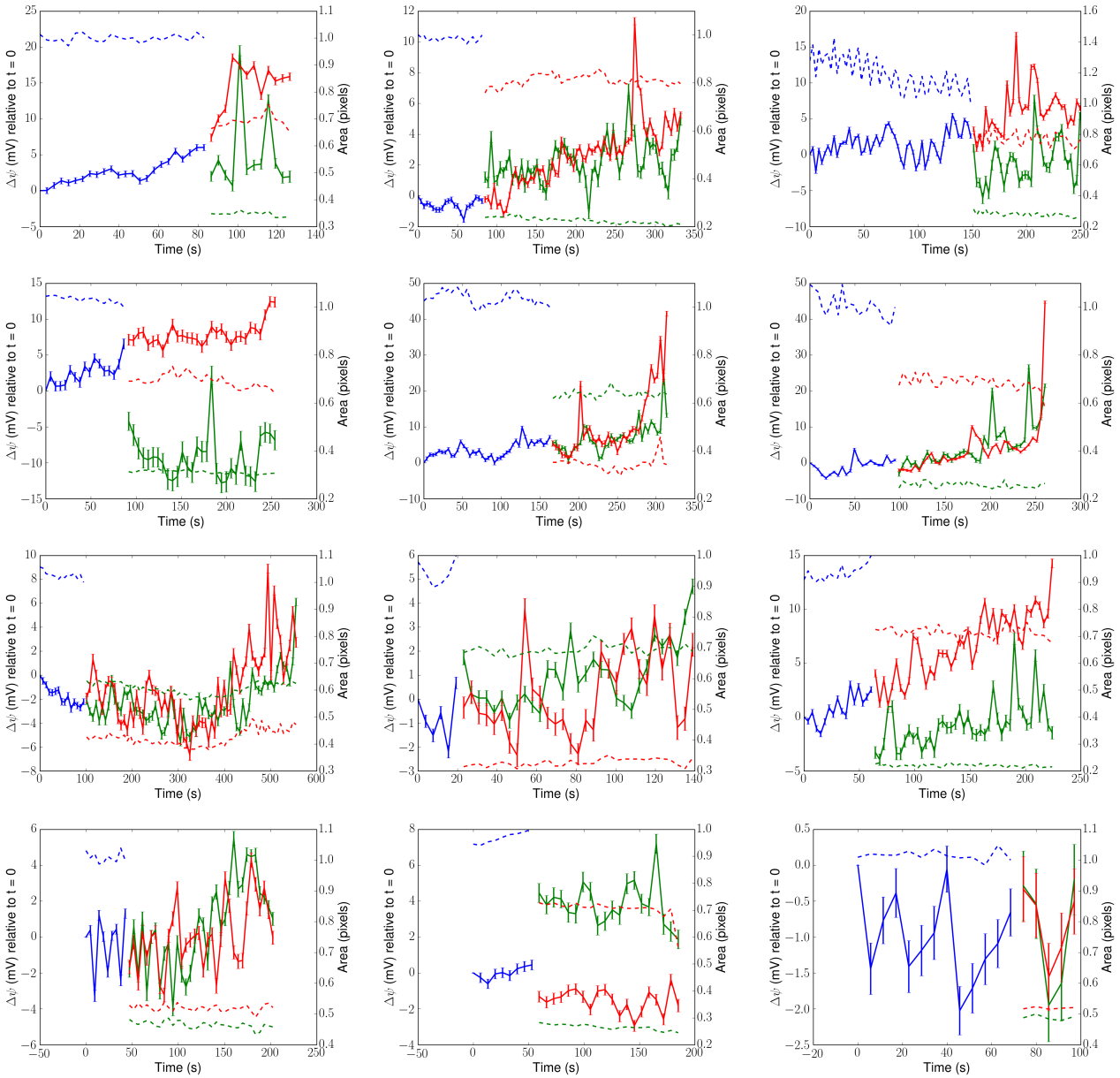


Figure 3.3: Membrane potential and area analysis. Here we show the results obtained from analysing the changes in membrane potential, using Equation (3.6); $\Delta\psi$ in every frame was calculate relative to the first frame, with cytosolic intensities assumed to be constant. Solid lines show $\Delta\psi$ for the pre-fission (blue) and post-fission (red and green) mitochondria, whereas dashed lines show the areas measured in number of pixels. Areas were normalised to the area of the pre-fission mitochondrion directly before fission. Error bars indicate standard deviations.

To test which of the two models defined in Equations (3.1) and (3.2) better accounts for the data, we compare the following quantities: i) experimentally measured values of $\Delta\psi_{1+2}$ directly before fission, and ii) values of $\Delta\psi_{1+2}$ as predicted by the models given experimentally measured values of $\Delta\psi_1$ and $\Delta\psi_2$ (directly after fission) as well as $\bar{A}_1$ and $\bar{A}_2$ (CSA averaged over time); correlations between these measured and predicted values are shown in Figure 3.4A. We then compute the likelihoods of both models using a Gaussian error model (Materials and Methods).

The log-likelihoods of models 1 and 2 given our data are $\mathcal{L}_1 \approx -20$ and $\mathcal{L}_2 \approx -37.0$, respectively (Section 3.2.5), confirming our prediction that the weighted average model is the one most likely to account for the data. Because the poorer fit of model 2 may be due to a few outliers (considering the small number of data points available), we used bootstrapping to obtain distributions of log-likelihoods. These distributions were then used to calculate differences in the Akaike information criterion (AIC), an estimator of the quality of a model relative to other models (Section 3.2.5). The model with the lowest AIC, which was found to be model 1 in 99.9% of our bootstrap samples, is the most likely to explain the data (Figure 3.4B). When model 1 was more likely, the relative likelihood of model 2 was less than 0.01 in 95% of cases (Section 3.2.5, Figure 3.4C). Therefore, *our experiments provide evidence for conservation of cellular mitochondrial potential upon fission events.* Does a similar result hold for fusion events? Though not proven, it seems plausible assuming that the same physical rules apply to both division and fusion. If so, then the nonlinear relation between ATP synthesis rate and $\Delta\psi$ as defined in Section 2.4.3 of Chapter 2, combined with selective fusion, means that fused mitochondrial networks produce ATP at a faster rate than fragmented networks.

One of the main limitations of our experiments is that the mitochondria we imaged showed signs of phototoxicity after $\sim$ 10 minutes and sometimes even after $<$ 5 minutes, as evidenced by their change in shape and fluorescent intensity (Figure 3.5A). Unfortunately, this introduces the possibility that effects due to cellular phototoxicity may influence our observations. However, we would argue that this has little influence on our conclusion because one might expect changes in $\Delta\psi$ to be governed by physics rather than physiology. Also, we only used potential values on a very short time-scale and all of our analysed events occurred within 3 minutes of starting the laser irradiation, at which point mitochondrial damage (if any) was limited. We thus argue that our results justify further testing of our hypothesis with more data and in a more physiological setting (as further discussed in the Discussion).

We briefly comment on other interesting behaviours that were observed. We found evidence for spontaneous transient mitochondrial depolarization events, which have been widely reported

in a variety of cell types [264–270]. On a time-scale of seconds, mitochondria can show a drop and subsequent recovery in TMRM fluorescence (Figure 3.5B). It was suggested that the mitochondrial permeability transition pore plays an important role in this phenomenon because opening of the pore, potentially a response to increased stress, can cause rapid depolarizations [269, 271, 272]. We observed transient depolarization events both at the start of experiments (without obvious signs of phototoxicity) as well as the end. We also observed that, unsurprisingly, mitochondrial CSA is well conserved.

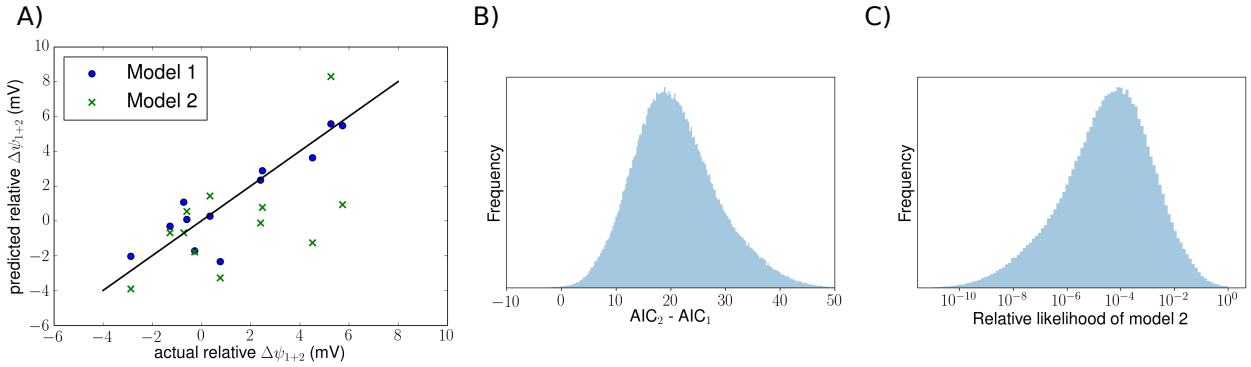


Figure 3.4: A weighted average model is better able to predict measured pre-fission potentials. A) Here we show the relation between the actual measured pre-fission potentials $\Delta\psi_{1+2}$, and the predicted values $\frac{1}{\bar{A}_1+\bar{A}_2}(\bar{A}_1\Delta\psi_1^0 + \bar{A}_2\Delta\psi_2^0)$ (Model 1) and $\frac{1}{2}(\Delta\psi_1^0 + \Delta\psi_2^0)$ (Model 2). Only potential values directly before and after the events are used. Through likelihood comparison (Equation 3.9), Model 1 is found to be more likely to account for the data. The straight line denotes identity. **B)** The distribution of the difference in AIC values between the two models is shown using bootstrapping (Materials and Methods, Equation (3.11)). At each bootstrap iteration (5×10^5 iterations were used), 12 data points are sampled with replacement from the set of all 12 data points. In 99.9% of cases, the AIC of model 1 (AIC_1) is lower than that of model 2 (AIC_2), meaning model 1 is more likely to explain the data. **C)** This figure denotes the relative likelihood of model 2 in the case that $AIC_1 < AIC_2$ (Equation (3.12)). For example, if this relatively likelihood is 0.01, then model 2 is 0.01 times as probable as model 1 to explain the data (Materials and Methods).

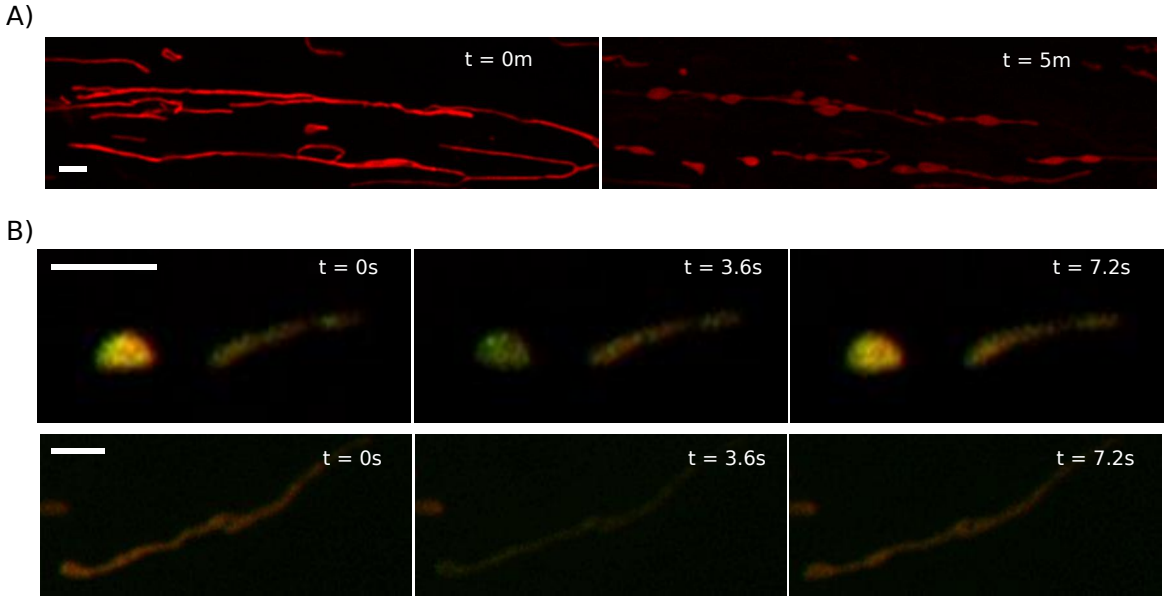


Figure 3.5: A) Phototoxic damage occurred during cell imaging. Here we show a fragment of a cell which appears healthy at the start of imaging, but shows damaged mitochondria at <5 minutes. This high level of laser-induced damage made it nearly impossible to track mitochondria for more than a few minutes. Scale bars indicate 2μm. **Transient mitochondrial depolarization events were observed in single mitochondria. B)** Depolarization event, lasting only a few seconds, were not uncommon; two examples are shown. Scale bar indicates 2μm.

3.2.4 Discussion

As discussed in Section 2.4.3 of the previous chapter, changes in mitochondrial membrane potential upon fusion and fission have important consequences for cellular ATP production rates. We tracked mitochondrial membrane potential and cross sectional area over time, and found evidence for conservation of total cellular mitochondrial potential $\Delta\psi_T$ during fission. If this conservation rule extends to fusion events, then highly connected mitochondrial states are expected to show increased rates of ATP synthesis as hypothesised in the previous chapter. We focussed our analysis entirely on fission, rather than fusion, events due to the difficulty in identifying the latter without photoactivatable fluorescent proteins. When such proteins are available, our analyses may be extended.

We note that our results imply that an asymmetry in potentials after fission, as observed in most events studied in Ref. [59], is not surprising if the two post-fission mitochondria are of different size (which is likely to be true in most cases). For example, a mitochondrial fragment may have a region with deficient ETC components or a damaged mitochondrial membrane, which causes this region to slightly lower the membrane potential of the entire segment. When fissioned off, the fragment containing the deficient region likely shows a lowered $\Delta\psi$, whereas the other post-fission fragment is likely to experience an increase; the larger the differences in size between the post-fission mitochondria, the larger the asymmetry in potentials can be. A mechanism like this was recently observed in cardiomyocytes [185]. The authors observed that local damage (due to experimental uncoupling) caused depolarization of an electrically continuous mitochondrial segment, after which electrical decoupling between different regions within the segment was seen. Following this decoupling was a physical separation of the different regions where the damaged region remained depolarised whereas the other region recovered its potential.

We will now discuss various limitations of our experiments and suggest improvements for future research. First, the mitochondria we imaged showed clear signs of phototoxicity, often at a timescale of $\sim$ 5 minutes. This made it impossible to track mitochondria for longer periods of time and, more importantly, means that our results cannot be considered to be valid for healthy cells. A careful analysis of the time and intensity limits of laser exposure which induce mitochondrial damage is therefore required. However, while phototoxicity limits the validity of our results, changes in $\Delta\psi$, as mentioned before, are likely to be governed by physics rather than physiology. Therefore, the preliminary results we present form important ground-work and, because of the positive evidence we found for our hypothesis, further testing is justified.

As mentioned before, we cannot be completely sure whether a fragment classified as a 'single mitochondrion' is actually continuous, or whether two seemingly fragmented mitochondria are still electrically coupled. The post-fission mitochondria in the event illustrated in the lower right corner of Figure 3.3 show a large degree of correlation, raising the possibility of an unobserved connection. Alternatively, the consistent large up and down fluctuations in $\Delta\psi$ observed throughout the imaging may indicate some external effect that dominates any natural fluctuations.

In calculating changes in $\Delta\psi$, we have implicitly assumed constant cytosolic dye concentrations throughout the experiments. Though this assumption may be reasonable in stable healthy cells, it may not be valid in our cells which increasingly accumulate irradiation damage. However, any changes in cytosolic concentrations are expected to be small in the very brief time interval of our analysed fission events.

There are various subtleties regarding the fluorescent dyes we used in our experiments. Before the cationic dyes accumulate inside the negatively charged mitochondrial matrix, they accumulate inside the cells themselves due to their negative charge relative to the surrounding medium. Changes in the potential across the plasma membrane of a cell ($\Delta\psi_P$) will in turn affect concentrations of TMRM in the cytoplasm. A change in TMRM fluorescence may therefore be caused by a change in $\Delta\psi_P$ rather than an actual change in mitochondrial potential $\Delta\psi$ [273]. Damages due to high phototoxicity may cause a drop in $\Delta\psi_P$, causing changes in TMRM fluorescent intensity to be unreliable predictors of $\Delta\psi$. Simultaneous measurements of $\Delta\psi$ and $\Delta\psi_P$ have been performed before [274, 275] and provide a more accurate estimate of $\Delta\psi$. Again, because we only use membrane potential data on a very short time interval, any changes in $\Delta\psi_P$ are expected to be small.

The fluorescent intensity of TMRM can only be used as a measure for membrane potential in a non-quench condition. At high dye concentrations, TMRM can form aggregates which do not fluoresce. This means that further increases in concentration do not lead to increases in fluorescent intensity, a phenomenon known as quenching. Therefore, dye concentrations must be sufficiently low to prevent this behaviour. The quench-limit of TMRM was estimated previously [274] and it was found that concentrations below $\sim$ 10-20nM cause very little quenching; concentrations of 50nM, however, which were used in these preliminary experiments, do cause quenching. Therefore, high values of $\Delta\psi$ may not have been picked up in our experiments; lower TMRM concentrations in any further experiment can prevent this problem. Absorption spectra are often skewed towards shorter wavelengths, while emission spectra tend to be skewed

towards longer wavelengths; it is therefore possible that emission from the green fluorophore MTG is detected through red emission filters. We measured levels of cross-talk between the dyes before starting our experiments; very little cross-talk was observed, making it unlikely to have caused any artificial changes in $\Delta\psi$.

To probe the influence on our results of the details of our thresholding method, we repeated our analyses using different parameters in the Niblack thresholding algorithm that was used (Materials and Methods). Often no large changes were seen but occasionally the exact moment of fission was altered, i.e. a physical separation of mitochondria was seen a few frames later or earlier[†]. This uncertainty in the exact moment of fission will affect predictions of changes in $\Delta\psi$. Ensuring full equilibration of both dyes across the mitochondrial inner membrane, subtracting cytosolic intensities, and carefully checking by hand threshold images may minimise, though not completely eliminate, this issue.

To summarise, we are of the opinion that this work presents useful insights and provides preliminary evidence for a model of weighted averaging of $\Delta\psi$ during fission. We suggest the following steps to be taken to continue this line of work with a similar but improved approach. Firstly, more data needs to be collected, while ensuring low phototoxicity by lowering laser power and checking whether cells still have a healthy mitochondrial network after ~ 30 minutes; this time window should be long enough to ensure healthy mitochondria during an entire fission event, and to be able to perform imaging for longer periods of time (thereby increasing the chance of observing fission or fusion events). Secondly, a lower concentration of TMRM should be used to avoid dye quenching. The combination of these two points will lead to a lower mitochondrial signal and some trial-and-error will be required to obtain data from healthy cells whose mitochondria are still distinguishable from background noise. If possible, fluorescent proteins may be used to allow for the study of fusion events. Though simultaneous measurements of both mitochondrial and plasma membrane potentials are desirable, this increases the complexity of the experiment and, given the short time-span between the data points actually used for analysis, may not yield significantly improved results.

[†]For example, consider a particular setting in which the mitochondria are, after thresholding, considered to be separated for the first time at time t (meaning that at this time, a set of pixels in between the mitochondria are below threshold). A different parameter setting which tends to reduce threshold values might still consider these pixels to be above threshold, meaning that the mitochondria will separate at a time $t' > t$.

3.2.5 Materials and Methods

Cell culture. Human primary fibroblasts were cultured in DMEM, high glucose, glutamine, pyruvate with phenol red; Gibco Catalog number:11995-073. For imaging, we used the following recording medium: DMEM A14430 with 1g/L glucose, 2 mM glutamine, 1 mM pyruvate, 10 mM HEPES, pH 7.4; no serum, no phenol red. Cells were stored at 37°C and 5% CO_2.

Mitochondrial membrane potential analysis. The fluorescent intensity of the cationic dye Tetramethylrhodamine Methyl Ester (TMRM) can be directly related (in a nonlinear fashion [275]) to the potential $\Delta\psi$ across the mitochondrial inner membrane; a loss of $\Delta\psi$ results in TMRM leakage from the mitochondria into the cytoplasm. Changes in fluorescent intensity of TMRM can occur because of changes in $\Delta\psi$ but also because of movement of a mitochondrion in and out of the focal plane. To correct for such movements, fluorescent intensity of the dye MitoTracker Green (MTG) was measured simultaneously. MTG is a dye that accumulates in mitochondria according to their membrane potential, but subsequently binds to mitochondrial proteins meaning that it is not released when mitochondria depolarise. The ratio of TMRM-to-MTG fluorescence is largely independent of mitochondrial movement (since intensity of both probes would decrease during an out-of-focus movement), and therefore reflects actual changes in $\Delta\psi$ [59, 207].

The membrane potential can be calculated by using the Nernst equation, which calculates the potential across a membrane due to a concentration difference of an ion of charge z and is given by

$$E = \frac{RT}{zF} \ln\left(\frac{C_i}{C_o}\right) \tag{3.3}$$

where R, T and F denote the ideal gas law constant, temperature and Faraday's constant, respectively, and C_i and C_o denote the ion concentrations on the inside and outside of the mitochondrion, respectively. It was shown previously that the fluorescent intensity of TMRM, here denoted by F^T, accumulates in a Nernstian fashion [264]. We thus obtain

$$\Delta\psi = -\frac{RT}{zF} \ln\left(\frac{F_i^T}{F_o^T}\right) \tag{3.4}$$

where the minus sign appears due to the fact that mitochondrial potential is defined with respect to the cytosol (leading to a negative mitochondrial potential). The difference in $\Delta\psi$

between two time points t and $t' > t$ is given by

$$\begin{aligned}\Delta\psi_{t'} - \Delta\psi_t &= \frac{RT}{zF}\Big[-\ln\left(\frac{F^T_{i,t'}}{F^T_{o,t'}}\right) + \ln\left(\frac{F^T_{i,t}}{F^T_{o,t}}\right)\Big] \\ &= \frac{RT}{zF}\ln\left(\frac{F^T_{i,t}}{F^T_{o,t}}\cdot\frac{F^T_{o,t'}}{F^T_{i,t'}}\right) \\ &\approx \frac{RT}{zF}\ln\left(\frac{F^T_{i,t}}{F^T_{i,t'}}\right) \end{aligned} \tag{3.5}$$

where in the last step it was assumed that the cytosolic TMRM concentration is constant between the two consecutive time points. We now adjust this equation to involve the ratio TMRM-to-MTG intensity, rather than TMRM alone, giving

$$\begin{aligned}\Delta\psi_{t'} - \Delta\psi_t &\approx \frac{RT}{zF}\ln\left(\frac{F^T_{i,t}}{F^T_{i,t'}}\frac{F^M_{i,t'}}{F^M_{i,t}}\right) \\ &= \frac{RT}{zF}\ln\left(\frac{F^T_{i,t}}{F^T_{i,t'}}\right) - \frac{RT}{zF}\ln\left(\frac{F^M_{i,t}}{F^M_{i,t'}}\right) \end{aligned} \tag{3.6}$$

where $F^M_{i,t}$ refers to the MTG fluorescent intensities inside the mitochondrion at time t. The correction term subtracts any contributions to $\Delta\psi$ caused by changes in MTG fluorescence due to out-of-focus movements. In an ideal situation, with no change in MTG fluorescence (and therefore TMRM fluorescence), this correction term is zero. Using $T = 37°\text{C}$ (though a recent study suggests mitochondria might be maintained at nearly 50°C [276]) and $z = 1$ [207], the proportionality constant has a value ~ 26.7 with $\Delta\psi$ measured in mV.

Loading with TMRM and MTG. Using a similar approach as in Ref. [59], mitochondria were labelled with both TMRM and MTG, and the fluorescent intensities of both dyes were measured. TMRM is a fluorescent indicator that accumulates in the negatively charged mitochondrial matrix. Before imaging, TMRM was freshly prepared at a concentration of 50 nM by diluting a stock of 50 μM which was stored at -20°C. MTG was prepared in the same way and used at the same concentration.

To prepare for imaging, 500 μL of recording media (defined under 'Cell culture') with both TMRM and MTG was added to cells and incubated for 20 minutes at 37°C. After incubation, the solution was removed and TMRM was added, removed (to wash out any remaining MTG), and added again. The final solution now contains recording media and TMRM (to keep its concentration equilibrated across the mitochondrial and plasma membrane), but not MTG (we want to prevent any additional uptake of MTG during the experiment).

Confocal microscopy. During imaging, live cells were maintained at 37°C. Cells were plated on glass coverslips an hour before imaging. Confocal microscopy was performed with a Zeiss LSM 880 with Airyscan using a ×63 oil immersion objective. TMRM was detected with excitation at 561 nm, and MTG with excitation at 488 nm. Each frame was scanned line by line and each line was scanned twice, first to detect TMRM emission and then MTG emission. Autofocus was used to prevent cells from drifting out of focus. A section of the cell not densely packed with mitochondria (for reasons discussed in Section 3.2.4) was chosen and was typically imaged for ∼5 minutes. In total, ∼ 50 cells were imaged.

Image analysis and processing. Image processing was performed with ImageJ. First, a ratio image (TMRM-to-MTG) was created. In previous analyses we subtracted background intensities for both channels using a rolling ball algorithm, but for the final results presented here no background subtraction was used in creating the ratio image. The reasons for this are i) the background subtraction itself induced noise and the ratio image contained very high pixel values due to very low values in the MTG image (these high pixel values then increased mean intensity values in the ratio image. A threshold value could have been used to exclude certain pixel values but this introduces another parameter); ii) the results without background subtraction were less noisy, and iii) part of our analysis assumes constant background intensities (Equation (3.5)) and therefore subtracting a different background value for each pixel (due to the local rolling ball algorithm) seemed inappropriate. Background subtraction *was* used to create threshold images (to be used as masks) using a rolling ball algorithm, as the increased contrast between mitochondria and background rendered the thresholding more accurate.

The $\Delta\psi$-independent channel identifies all mitochondria and this channel is usually used for image thresholding (see e.g. [207]). However, in our experiments the MTG channel showed a high level of noise which made thresholding based on this channel challenging, and thresholding was therefore performed using the TMRM channel; this may exclude depolarised mitochondria but for our purposes it suffices (in a few cases with less noisy MTG signals we compared results based on thresholding for either channel and no notable difference were found). Nine different local thresholding algorithms were compared and, after checking by hand the resulting images for a few different cells, the Niblack thresholding algorithm proved to be most accurate and was used for all further analyses [277]. All frames in the time series were checked by hand for correct identification of mitochondria. Finally, the thresholded image was used as a mask to obtain statistics of the ratio image.

Hypothesis testing. Let $\Delta\psi^f_{1+2}$, $\Delta\psi^0_1$ and $\Delta\psi^0_2$ denote membrane potentials of the pre-fission mitochondrion directly before, and the post-fission mitochondria directly after fission, respectively. For a perfect model, the difference between measured and predicted pre-fission potentials can be modelled by a random noise term with zero mean, where the noise is caused by a combination of e.g. measurement noise, natural mitochondrial fluctuations in $\Delta\psi$, and the discrete time lattice used to store information (which means our first measurement after fission may be several seconds after its actual occurrence). We use a Gaussian error model, giving

$$\text{Model 1:} \quad \Delta\psi^f_{1+2} = \frac{1}{\bar{A}_1 + \bar{A}_2}(\bar{A}_1\Delta\psi^0_1 + \bar{A}_2\Delta\psi^0_2) + N(0, \sigma_1^2) \tag{3.7}$$

$$\text{Model 2:} \quad \Delta\psi^f_{1+2} = \frac{1}{2}(\Delta\psi^0_1 + \Delta\psi^0_2) + N(0, \sigma_2^2) \tag{3.8}$$

where the bars indicate areas averaged over time, and $N(0, \sigma_1^2)$ and $N(0, \sigma_2^2)$ denote normally distributed noise terms with zero mean. The variance of the noise term is the only free parameter used in both models.

To compare the two proposed models (Equations (3.7) and (3.8)) we evaluate their likelihoods, i.e. the probability of observing the data given the model parameters. Denoting the measured values of $\Delta\psi^f_{1+2}$ by $(y_1, y_2, \cdots y_n)$, and introducing $X_1 = \frac{1}{\bar{A}_1+\bar{A}_2}(\bar{A}_1\Delta\psi^0_1 + \bar{A}_2\Delta\psi^0_2)$ and $X_2 = \frac{1}{2}(\Delta\psi^0_1 + \Delta\psi^0_2)$, the log-likelihoods of models 1 and 2 are given by

$$\begin{aligned}\mathcal{L}_1 &= \log\left(\prod_{i=1}^{n}\left(\frac{1}{\sqrt{2\pi\hat{\sigma}_1^2}}e^{-(y_i-x_{1,i})^2/2\hat{\sigma}_1^2}\right)\right) \\ &= -\frac{n}{2}\log(2\pi\hat{\sigma}_1^2) - \frac{1}{2\hat{\sigma}_1^2}\sum_{i=1}^{n}(y_i - x_{1,i})^2 \end{aligned} \tag{3.9}$$

$$\mathcal{L}_2 = -\frac{n}{2}\log(2\pi\hat{\sigma}_2^2) - \frac{1}{2\hat{\sigma}_2^2}\sum_{i=1}^{n}(y_i - x_{2,i})^2 \tag{3.10}$$

where n denotes the number of data points (corresponding to the number of events analysed), $\hat{\sigma}_1^2 = \frac{1}{n}\sum_{i=1}^{n}(y_i - x_{1,i})^2$ denotes the maximum likelihood estimate of the noise variance (and similar for $\hat{\sigma}_2^2$), and $x_{1,i} \in X_1$ and $x_{2,i} \in X_2$ denote the predictions of the two models.

The Akaike information criterion (AIC) is an estimator of the quality of a model relative to other models and is defined as

$$\text{AIC}_i = 2k_i - 2\mathcal{L}_i \tag{3.11}$$

where k_i and $\mathcal{L}_i$ denote the number of parameters and maximum log-likelihood of model i, respectively. In our models, $k_1 = k_2 = 1$ and $\mathcal{L}_i$ is given by equations (3.9) and (3.10). The

AIC provides a means of model selection and estimates the information lost when using a given model to represent the actual process generating the data. The model with the lowest AIC is most likely to minimize information loss (a low AIC corresponds to a large likelihood and a small number of parameters). The quantity

$$e^{(\mathrm{AIC}_{\min}-\mathrm{AIC}_i)/2} \tag{3.12}$$

denotes the relative likelihood of the ith model, with $\mathrm{ATC}_{\min}$ denoting the minimum of all AIC values. For example, if $\mathrm{AIC}_1 = 50$ and $\mathrm{AIC}_2 = 52$, the second model is $e^{(50-52)/2} \approx 0.37$ times as likely as the first model to minimize information loss. We used equation (3.12) with $i = 2$ to calculate the relative likelihood of model 2 when model 1 is more likely (Figure 3.4C). To create Figures 3.4B, C we used bootstrapping, i.e. we resampled with replacement the 12 data points shown in Figure 3.4A and calculated the log-likelihoods of both models for each of these resampled data sets. After 5×10^5 bootstrap iterations, the distributions of log-likelihoods obtained were used to calculate the distributions shown in Figures 3.4B, C.

4

Control and energetic costs of stochastic mtDNA populations

Summary

The cellular proportion of mutant mtDNA molecules is crucial in mitochondrial disease; understanding the dynamics of mtDNA populations inside cells and the way in which mutants accumulate over time is vital to understand these diseases. The mitochondrial population is under homeostatic control, but the details of the control mechanisms involved remain elusive. Here, we use stochastic modelling to derive general results for the impact of cellular control on mtDNA populations, the cost to the cell of different mtDNA states, and the optimisation of artifical, therapeutic control of mtDNA populations. We illustrate that an increasing mtDNA variance can increase the energetic cost of maintaining a tissue, that intermediate levels of heteroplasmy can be more detrimental than homoplasmy even for a dysfunctional mutant, that heteroplasmy distribution (not mean alone) is crucial for the success of gene therapies, and that long-term rather than short intense gene therapies are more likely to beneficially impact mtDNA populations.

4.1 Introduction

Mitochondrial biogenesis and maintenance require cellular resources, and mitochondria are key sources of ATP and play other important metabolic roles: a tradeoff of bioenergetic costs and benefits is thus involved in the interaction between the cell and its mitochondria. The particular 'effective cost' that cellular control acts to minimise remains poorly understood: for example, both decreases [104] and increases [104, 278] in wildtype copy numbers have been observed for different mutations as the mutant load increases. Some studies suggest that mtDNA density is controlled [279–281], others that total mtDNA mass [282, 283], or mtDNA transcription rate [38] is controlled. Understanding the dynamics of mtDNA populations inside cells, and how these populations react to clinical interventions, is crucial in understanding genetic diseases [141, 284]. However, experimental tracking of mtDNA populations over time is challenging, necessitating predictive mathematical modelling to provide a quantitative understanding of these systems.

In parallel with efforts to elucidate cell physiological control, protein engineering methods to control mtDNA heteroplasmy are making fast progress. Two recently developed methods for cleaving DNA at specific sites involve zinc finger nucleases (ZFNs) and Transcription Activator-like Effector Nucleases (TALENs) [285–291], which have been re-engineered to specifically cleave mutant mtDNA [142, 144, 145, 292, 293]. MitoTALENs have been successfully used to reduce mutant loads in cells containing disease-related mutations, but elimination of the target mutant mtDNA was not complete [144, 147]. Similarly, treating cells multiple times with mtZFNs led to near-complete elimination of mutant mtDNAs [142, 293]. As mentioned in the thesis introduction, quantitative theory for these promising therapeutic technologies has not yet been developed, leaving open questions about how these tools can be optimally deployed.

In this chapter, we develop theory from bottom-up bioenergetic principles which allows us to study the effects of distinct cellular mtDNA control strategies (Section 4.2.1), to analyse the bioenergetic cost of different mtDNA states (Section 4.2.2), and to combine mtDNA control and energy-based cost (Section 4.2.3.1) to identify optimal control strategies for the cell. Finally, we construct a model for artificial mtDNA control using recent experimental data [142] to propose optimised treatment strategies while highlighting challenges linked to heteroplasmy variance (Section 4.2.3.2).

	Key results presented in this chapter.
$\mathbb{I}$	If only one mtDNA species is controlled the variance of the controlled species reaches a constant value. When both species are controlled with equal strength their variances increase at identical rates, and, in general, the more tightly controlled species has a more slowly increasing variance (Figure 4.1, Section 4.2.1).
$\mathbb{II}$	The mean energetic cost of maintaining a tissue can increase over time due to the nonlinear influence of mtDNA variance, even if the energetic demand on the tissue stays the same and mean levels of mtDNA are constant (Section 4.4, Eq. 4.6).
$\mathbb{III}$	A control lacking any mutant contribution shows an exponentially increasing cost, and the effects of particular cellular control strategies are more pronounced in low copy number cells (Section 4.2.3.1, Figure 4.3A, B).
$\mathbb{IV}$	Control strategies based on the energy status of the cell will often outperform control based on mtDNA copy number or sensing mtDNA mass (which would work well for deficient deletion mutants, but would be suboptimal for deficient point mutations) (Section 4.2.3.1, Figure 4.3C).
$\mathbb{V}$	Even for pathological mutants, reduction of mutant mtDNA alone is not always the optimal control strategy for a cell to adopt (Section 4.2.3.1, Figure 4.4).
$\mathbb{VI}$	Tissues with high mean heteroplasmy levels will generally be harder to treat with mitochondrially targeted endonucleases if the heteroplasmy variance is high, especially if this high mean level is caused by a small percentage of cells (Section 4.2.3.2, Figure 4.5D).
$\mathbb{VII}$	Weak long-term rather than short intense endonuclease treatments are more likely to beneficially impact mtDNA populations (Section 4.2.3.2, Figure 4.5G, H).

Table 4.1: Key results. Here we present key results of this chapter, which hold under the assumptions used in our models. We model mtDNA dynamics using stochastic birth-death simulations and assume: cells are heteroplasmic (containing both wildtype and mutant mtDNA molecules); birth and death rates are identical for wildtype and mutant species; the mtDNA dynamics are subject to cellular feedback control. We introduce a mitochondrial energy-based cost function; results referring to optimal controls and costs depend on the structure of this cost function which is discussed in Section 4.4 and Section B.3.

4.2 Results

4.2.1 Control: general insights on the role of feedback control

We employ the linear model of feedback control presented in the thesis introduction in Eq. 1.3, which is a form of 'relaxed replication' as each mtDNA molecule replicates and degrades according to Poisson processes with rates $\lambda(w, m)$ and μ, respectively [1, 2]. We assumed only the replication rate to be a function of w and m because control of biogenesis or autophagy (i.e. degradation) yield similar behaviours [101]. To connect with experiments, we use $\mu \approx 0.07$ day^{-1} corresponding to a half-life of about 10 days [119]; this will be the default value of μ throughout this thesis unless specified otherwise. For clarity, the assumed deterministic dynamics of $w(t)$ and $m(t)$ are provided in Equation 4.5.

4.2.1.1 A wide range of control strategies induces similar mtDNA behaviour and admits quantitative analysis.

Whatever the quantity being controlled, in healthy cells the intuitive aim of homeostatic mtDNA control is to guarantee cell functionality by keeping wildtype copy numbers around a particular value and within certain bounds. Many possible control strategies can be parameterised to give rise to nearly identical means and variances for wildtype, mutant, and heteroplasmy dynamics up to long times (e.g. a human life-time) (Figure 4.1A,B,C, Figure B.1B,C,D). This is mainly true when mtDNA copy numbers fluctuate around their steady state values, in which case a linear control forms a good first order approximation to the complex 'true' feedback control function. In this case, *it is not the manner in which the controlled quantity is being controlled, but* which *quantity is controlled that is the most important.* For example, the extent to which mutants and wildtypes contribute to the replication feedback function (determined by the parameter δ) determines how their relative means and variances evolve (Figure 4.1D, and Chapter 5), and contains more information on the dynamics than the functional form of $\lambda(w, m)$ for fixed δ.

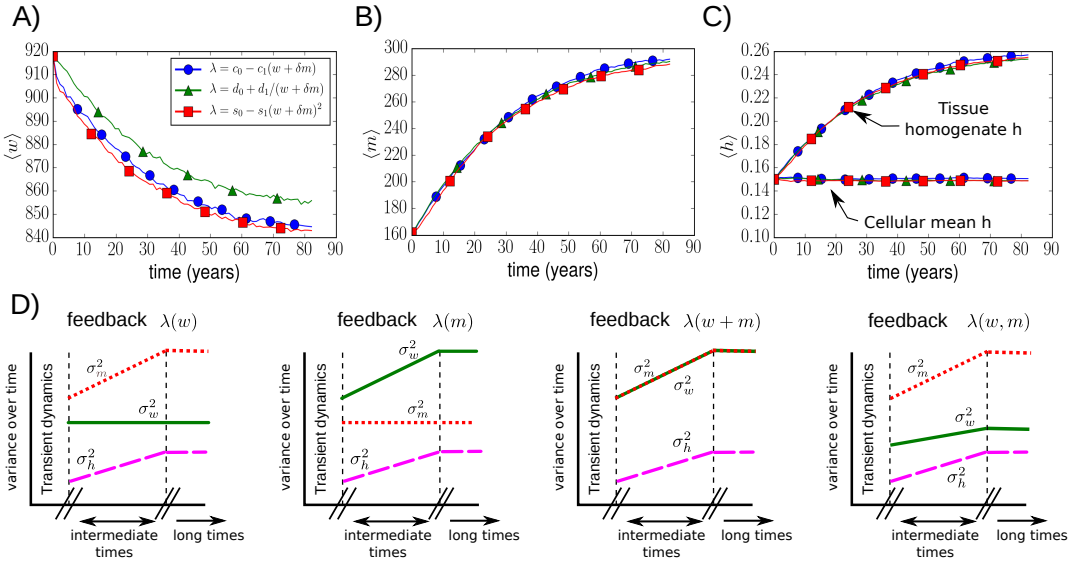


Figure 4.1: A) - C) A wide range of cellular control strategies can yield similar dynamics. Stochastic simulations were used to compare three structurally distinct cellular controls (see legend), each reflecting a different function of the underlying sensed quantity $w + \delta m$ with $\delta = 0.5$. All controls are set to have the same wildtype mean and variance in the absence of mutants (Section B.1). Figure (C) illustrates the difference between cellular mean and tissue homogenate heteroplasmy. **D) Control tradeoffs are required when multiple species are present.** The more strongly one species is controlled, the more control is lost over the other. Changes in variances as described by the linear noise approximation (Section C.1.5) are shown (intermediate times). For long times, fixation occurs and the variance of the surviving species saturates. In the most-right figure we depicted the case in which mutants contribute less to the control than wildtypes ($\delta < 1$).

We stress the difference between two types of average heteroplasmy, as was also stressed in Ref. [2]: the individual cellular mean heteroplasmy $\langle h \rangle_{cellular} = \frac{1}{n_{\text{cells}}} \sum_{\text{cells i}} \frac{m_i}{m_i+w_i}$ and the tissue homogenate heteroplasmy $\langle h \rangle_{homog} = (\sum_{\text{cells i}} m_i)/(\sum_{\text{cells i}} (m_i + w_i))$. The difference between individual and homogenate means is clearly seen in Figure 4.1C. When no explicit selection is present for either mtDNA species, the mean cellular heteroplasmy remains constant at its original value, i.e.

$$\langle h \rangle_{cellular} = \frac{m_0}{m_0 + w_0} \tag{4.1}$$

where w_0 and m_0 denote the initial wildtype and mutant copy numbers, respectively. These dynamics can be described by a random walk in heteroplasmy space (as there is no bias towards increasing or decreasing h) (see also Chapter 5). For long times, the percentage of cells that fixate on mutant species (i.e. $h = 1$) is then given by $m_0/(w_0 + m_0)$ and these cells have mean copy number N_{ss}/δ (see Section 1.4.4), whereas wildtype cells have mean copy number N_{ss}. We can now calculate the homogenate heteroplasmy at long times (i.e. times at which all cells have fixated) as*

$$\langle h \rangle_{homog,\, t\to\infty} = \frac{m_0}{m_0 + \delta w_0}. \tag{4.2}$$

It is clear that *when mutants contribute little to the feedback control (small δ), tissue homogenate heteroplasmy can reach high values, and even approach $\langle h \rangle_{homog} = 1$, without explicit selection.* A tissue can thus appear, when studying the homogenate heteroplasmy, to show selection for one type of mtDNA over another, whereas in fact mean cellular heteroplasmy is unaltered and both mutant and wild types have the same proliferation rates.

The observation of constant $\langle h \rangle_{cellular}$ despite a drop in $\langle w \rangle$ as well as an increase in $\langle m \rangle$ may seem unintuitive. However, this can be explained by the fact that cells with higher heteroplasmy levels have higher total mtDNA copy numbers when $\delta < 1$. For example, imagine 1000 cells all initialized at the state $(w, m) = (200, 200)$ which forms a deterministic steady state when $\delta = 0.1$ and $N_{ss} = 220$. Due to the lack of explicit selection, at long times we expect 50% of cells to fixate on mutant with mean copy number $N_{ss}/\delta = 2200$ and 50% to fixate on wildtypes with mean copy number $N_{ss} = 220$. We thus find that, for long times, $\langle m \rangle = 1100$ and $\langle w \rangle = 110$ whereas initially we had $\langle m \rangle = \langle w \rangle = 200$. In this example, $\langle w \rangle$ decreased, $\langle m \rangle$ increased, $\langle h \rangle_{homog}$ increased from 0.5 to ~ 0.91, and $\langle h \rangle_{cellular}$ remained constant at 0.5. The increase $\langle h \rangle_{homog}$ is caused by cells homoplasmic in mutant having a ten times higher copy number (due to $\delta = 0.1$) than cells homoplasmic in wildtype. Heteroplasmy distributions evolve asymmetrically if $\delta \neq 1$, examples of which are shown in Figure 5.1D,E.

*We note that Equation 4.2 only holds when $\delta > 0$.

4.2.1.2 Nonlinear cost functions predict changes in tissue maintenance

The model we use to describe mtDNA dynamics is an example of a birth-death model (see Section 1.4.4) which can be stochastically described by a master equation. Because the replication rate $\lambda(w, m)$ represents the birth rate of each individual mtDNA molecule, the total rate at which birth occurs is nonlinear, in which case the master equation often cannot be solved analytically. Approximation methods such as the van Kampen system size expansion (SSE) [294] can be used to predict mtDNA variances (Section C.1.5), showing good agreement with stochastic simulations up to hundreds of days [101]. Table 4.2 shows the first order solution of the SSE which is known as the linear noise approximation (LNA). Applying this approximation to a general form of mtDNA control (Section C.1.5), we find that *i) if only one species is controlled, the variance of the controlled species quickly reaches a constant value (see also [101]), ii) when both species are controlled with equal strength their variances increase at identical rates, iii) in general the more tightly controlled species has a more slowly increasing variance, and iv) the rate of increase of heteroplasmy variance depends, to first order, only on mtDNA copy number and turnover (as found in [101]).* (Figure 4.1, Table 4.1(𝕀)). Eventually, all variances reach a constant value due to complete fixation though this may take many years depending on initial heteroplasmy values and mtDNA turnover rates.

What are the biological implications of these findings? A given mtDNA state (w, m) will accrue a cost to the cell, denoted by $C(w, m)$, which can e.g. be an energetic cost or some other metric of tissue burden. If this cost function is nonlinear, increasing variances in w and m can lead to changes in mean cost $\langle C(w, m)\rangle$ even when mean cellular copy numbers $\langle w\rangle$, $\langle m\rangle$ remain constant (Methods) because the mean of a nonlinear function of random variables is not generally equal to the function of the mean of those variables (as seen above with cellular vs homogenate heteroplasmy). Therefore, *the mean cost of maintaining a tissue may increase over time, even if tissue demands stay the same and mean mtDNA levels are constant* (Table 4.1(𝕀𝕀)). However, these increases may be small and their significance depends on the details of the cost function: hence the need to consider explicit forms, as we do in the next section.

4.2.2 Cost: an effective mitochondrial energy-based cost function

Having compared various statistics of different functional forms of control, we want to investigate their different energetic burdens which requires the construction of a cost function. Therefore, we attempt to build a cost function that assigns a cost to a given mtDNA state (w, m) and allows a general quantitative investigation of the tradeoffs in maintaining cellular

	$\lambda(w)$	$\lambda(m)$	$\lambda(w,m)$ (including $\lambda(w+m)$)
$\sigma_w^2(t)$	$\frac{\mu}{\partial_w \lambda}\left(e^{2w_{ss}\partial_w \lambda t}-1\right)$	$2\frac{w_{ss}}{m_{ss}}\mu(w_{ss}+m_{ss})t+\cdots$	$\frac{2\mu m_{ss}w_{ss}(w_{ss}+m_{ss})}{(m_{ss}\partial_m\lambda+w_{ss}\partial_w\lambda)^2}(\partial_m\lambda)^2\,t+\cdots$
$\sigma_m^2(t)$	$2\frac{m_{ss}}{w_{ss}}\mu(w_{ss}+m_{ss})t+\cdots$	$\frac{\mu}{\partial_m \lambda}\left(e^{2m_{ss}\partial_m \lambda t}-1\right)$	$\frac{2\mu m_{ss}w_{ss}(w_{ss}+m_{ss})}{(m_{ss}\partial_m\lambda+w_{ss}\partial_w\lambda)^2}(\partial_w\lambda)^2\,t+\cdots$
$\sigma_h^2(t)$	$\frac{2m_{ss}w_{ss}\mu}{(m_{ss}+w_{ss})^3}t$		

Table 4.2: Analytical expressions for the means and variances according to the linear noise approximation. Solutions are shown for wildtype, mutant, and heteroplasmy variances for various types of control. Dots indicate constant or exponentially decaying terms; full solutions are given in Section C.1.5. Note that the initial rate of increase of heteroplasmy variance only depends on mtDNA copy number and turnover (see also [101]).

mtDNA populations. The 'true' energy budget of a cell with a given mitochondrial population is highly complex, involving many different metabolic processes in which mitochondria are involved [4–6]. We provide a simpler description, focussing on ATP production as a central mitochondrial function, and removing kinetic details in favour of a coarse-grained representation, to provide qualitative rather than quantitative results. We aimed to make most of our parameters biologically interpretable.

4.2.2.1 General cost function structure

Three important terms involved in the energy status of a cell are: i) the energy demand D, ii) the net energy supply S, and iii) the efficiency with which the energy is supplied. Here we define efficiency as the amount of energy that is produced per unit of resource consumed. For this study, we focus on mitochondria as the central bioenergetic actors in the cell, with wildtype and mutant mitochondria consuming resource and producing energy currency.

We express our effective cost function as:

$$C(w,m) = |D - S(w,m)| + \alpha(wr_w + mr_m) \tag{4.3}$$

where α is a constant, and r_i gives the rate of resource consumption of a mitochondrion of type i (w or m). The second term assigns a cost to the usage of resource. The terms in this cost function are expressed as rates: S and D then correspond to net energy production (supply) and demand per unit time. The demand can be considered to represent energy requirements of all cellular processes besides mitochondria (whose costs are incorporated in their net supply $S(w,m)$), which we assume to be constant. We are therefore modelling post-mitotic cells in stable environments, as demands are expected to change throughout the cell cycle. This cost

function assigns the lowest cost to a state that satisfies demand in the most efficient way, and both an excess or deficit of supply are penalised.

The net energy production of a state (w, m), $S(w, m)$, is modelled as

$$\begin{aligned} S(w,m) = w\Big(s_w(r_w) - \rho_1\Big) + m\Big(\epsilon_2 s_w(\epsilon_1 r_w) - \rho_1\Big) \\ - (w+m)\Big(\rho_2\lambda + \rho_3\mu\Big) \end{aligned} \tag{4.4}$$

where $\rho_{1,2,3}$ are mitochondrial maintenance, building, and degradation costs, $s_w(r_w)$ denotes the energy production rate (per second) for a single wildtype mitochondrion given a resource consumption rate r_w (Methods, Section B.3), and λ and μ (which can be functions of w and m) denote the birth and death rates in units per second. Mutant mtDNA molecules are distinguished by the parameters $\epsilon_1, \epsilon_2 \in [0, 1]$ describing the mutant resource uptake rate (ϵ_1) and efficiency (ϵ_2) relative to that of the wildtypes. A low ϵ_1 could represent reduced flow through the electron transport chain due to e.g. damaged respiratory complexes, whereas a low ϵ_2 could denote increased proton leakage.

The more detailed structure of our cost function, which has been very general so far, comes from specifying the relation $s_w(r_w)$. In other words, how does the energy output of a mitochondrion depend on its resource consumption rate? Various experimental studies find this relation to be linear [295–297]. However, we have several reasons to consider an additional relation. Firstly, a linear function $s_i(r_i)$ implies that mitochondrial energy production rate increases forever with increased resource consumptions rates, whereas it may seem more natural for $s_i(r_i)$ to saturate at high r_i. Secondly, a linear $s_i(r_i)$ means that the lowest cost is assigned to a state which satisfies demand with a minimally required number of mitochondria, all using their maximum resource consumption rates (Section B.2). Such a state, however, is not robust to fluctuations in both mitochondrial copy numbers and demand. Moreover, mitochondria are known to have large spare capacities [298, 299] indicating that in resting state they do not operate near their limits. A saturating function $s_i(r_i)$ solves these issues (Section B.2).

We thus consider two different types of cost function, which we refer to as the 'linear output model' and the 'saturating output model'. We compare these two models qualitatively, as we are mainly interested in how a saturating output function, which is arguably more natural, affects the qualitative structure of both the cost function as well as optimal control strategies. We fitted the parameters of the linear output model using data provided in Ref. [295] (Section B.2), and set the parameters of the saturating model such that the two models behave similarly at low r_i. Further details on the choice of parameter values, and their biochemical interpretations,

are given in Section B.3; default values are provided in Table 4.3.

We will assume that the cell acts to minimise cost, meaning that we consider the wildtype steady state copy number (in the absence of mutants) to be optimal. Throughout most of this chapter, we therefore refer to N_{ss} (introduced in the thesis introduction) as w_{opt}. We consider two different cost function parameterisations for both the linear and saturating output models, one for high and one for low copy number cells, meaning we investigate four different systems in total, each with their own value of w_{opt} (Table 4.3).

4.2.2.2 Intermediate heteroplasmies may be inefficient and resource availability can dictate the cost of mtDNA states

Figure 4.2 shows heatmaps of the cost function in (w, m) space for different mutant pathologies (here modelled as different values of ϵ_1). We observe clear qualitative differences in cost function structure between the saturating and linear output models. In the former, it is possible for intermediate heteroplasmy states to be more expensive than states homoplasmic for either species (Figure 4.2A, B). The linear output model, on the other hand, always shows higher costs at higher heteroplasmy (for fixed total copy number) (Figure 4.2C).

What is the reason behind expensive intermediate heteroplasmies? Increasing heteroplasmy while keeping total copy number constant can be interpreted as replacing a wildtype mitochondrion with a mutant, leading to a tradeoff. The changed mitochondrion (from wildtype to mutant) produces less energy than before; all other mitochondria need to consume more resource to maintain a constant total output, and so become less efficient due to output saturation. However, the changed mitochondrion itself has become more efficient because of its lower resource consumption rate. The tradeoff between these two factors depends on h itself; a more detailed discussion is given in Section B.4. The result is that *in the saturating output model, it is possible for intermediate heteroplasmies to be the least efficient and the most expensive* (Figures 4.2 and B.4).

How general is the existence of a state with $h \neq 1$ being more costly than a state with $h = 1$ or $h = 0$? When the relation $s_w(r_w)$ is saturating and mutants use (at any given time) a lower resource consumption rate than wildtypes, then the mutant species will effectively be more efficient, leading to the tradeoff discussed above. Therefore, under the above two assumptions we may expect an expensive intermediate heteroplasmy state to exist. In our specific cost function, the existence of a high-cost intermediate heteroplasmy value is a relatively general feature of the saturating output model. We calculated the value of h with maximum cost (at

Par.	Description	Default value
D	Mitochondrial energy demand in ATP/s. The default values given are in units of 2.6×10^5 ATP/s, as explained in Section B.3.8. We introduce two values of D, one for high and one for low copy number cells.	5110.7 (high) 1022.1 (low)
R	Maximum rate of resource supplied by the cell per second to be used by the mitochondria. We use the term 'resource' as an amalgamation of different mitochondrial resources, e.g. NAD(H), pyruvate, lactate, succinate, ADP, P_i, and oxygen. Two different values for R are used, corresponding to high and low copy number cells.	3800 (high) 760 (low)
ϕ	ϕ is related to the effective P/O ratio of a wildtype mtDNA molecule, it represents the slope of the linear relationship between r_w and s_w given in equation (B.1).	2.0
β	β denotes the resource consumption rate (in 'resource' per second) at zero energy production, and is therefore a measure of proton leak. Because we fix the maximum resource consumption rate to be 1 (Section B.3.1), β provides the fraction of resource consumption that is destined for 'futile' leakage.	0.1
k	Parameter describing the saturation of the saturating model.	3
s_{max}	An indication of the aximum energy supplied by a wildtype mtDNA molecule in the linear model in ATP/s.	1.54
r_{max}	Maximum rate of resource uptake by an mtDNA molecule (i.e. by a mitochondrion containing the mtDNA molecule). This can be interpreted as the maximum flow through the respiratory chain.	0.95
ρ_1	The mitochondrial maintenance cost in units of 2.6×10^5 ATP/s.	0.04
ρ_2	The mitochondrial building cost in units of 2.6×10^5 ATP.	3828
ρ_3	The mitochondrial degradation cost in units of 2.6×10^5 ATP.	383
ϵ_1	The mutant energy production efficiency (the energy produced per unit of resource consumed) relative to that of wildtype mtDNA molecules. A low value of ϵ_1 can be caused by a high proton leak or a deficient ATP synthase.	free parameter $\epsilon_1 \in [0, 1]$
ϵ_2	The mutant resource uptake rate relative to that of wildtype mtDNA molecules. We will mainly use $\epsilon_1 = 1$ and $\epsilon_2 < 1$ because mtDNA mutations usually affect the proton pumping electron transport chain complexes. A defect in e.g. complex I will reduce its activity and therefore also the rate of consumption of NADH.	free parameter $\epsilon_2 \in [0, 1]$
α	Scaling parameter in the cost function in front of resource consumption term.	0.1
w_{opt}	The cheapest value for w when $m = 0$, using all of the above parameter values. We have four values for w_{opt}, corresponding to the linear and saturating output models at low and high copy number.	1524 (sat. low) 7616 (sat. high) 638 (lin. low) 3129 (lin. high)

Table 4.3: Parameters used in our mitochondrial cost function with their descriptions. Parameter values are derived and motivated in Section B.3. In this table, 'high' and 'low' refer to high and low copy numbers, respectively, and the abbreviations 'sat.' and 'lin.' are used to indicate our saturating and linear output models.

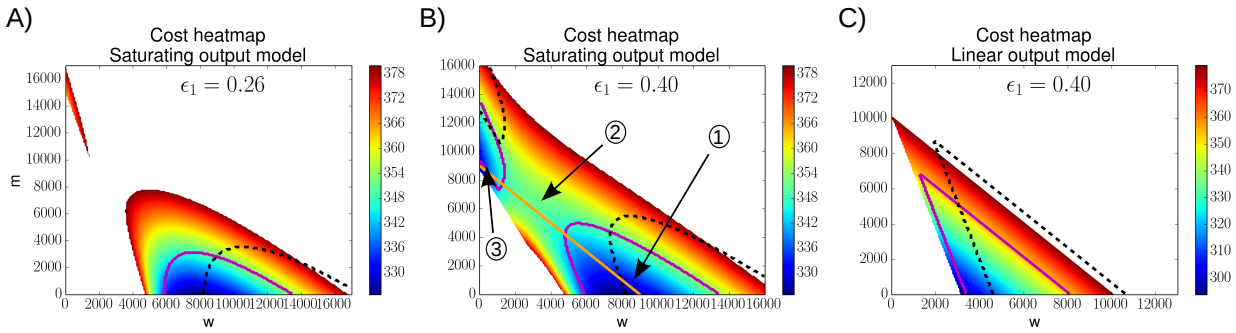


Figure 4.2: Intermediate heteroplasmies can be less efficient than either wildtype or mutant homoplasmy. A visualization of the cost function in (w, m) space is shown for both saturating and linear output models, for various mutant pathologies (described by ϵ_1). White regions correspond to states in which cellular demand is not satisfied though cells may still survive by e.g. increasing glycolysis (effectively reducing mitochondrial demand). This figure assumes high copy numbers, results are qualitatively similar for low copy numbers. **A)** The magenta (solid) and black (dashed) lines show the contour of the demand-satisfying region when demand is increased by 10%, or demand is increased by 50% and cellular resource availability is increased by 35%, respectively. **B)** The orange line corresponds to constant total copy number; moving up along this line increases heteroplasmy. Cells in region 1 or region 3 are more efficient, and show a lower cost, than cells in region 2. **C)** The linear mitochondrial output model does not show a decreased efficiency at intermediate heteroplasmy values.

constant total copy number), denoted by h_{max}, as a function of several model parameters. We find that $h_{max} = 1$ at values $\epsilon_1 \lesssim 0.3$ due to very low mutant functionality. However, at higher values of ϵ_1 ($\epsilon_1 \gtrsim 0.5$) we find $h_{max} \sim (0.5 - 0.8)$ over a large range of several of our cost function parameters (Section B.4.2). The size of the effect, however, may be small.

It was previously found that it possible for two mtDNA variants in mice to function normally at homoplasmy, but show deficiencies in heteroplasmic states [140]. We do not claim that our model is the reason behind these observations, we merely show that it can account for them in a relatively simple manner. The insights we obtained are that different resource consumption rates between distinct mtDNA species may play an important role in causing cells heteroplasmic in two different species (which are functional at homoplasmy) to show dysfunctions. We do not make any quantitative claims as we appreciate our cost function is phenomenological and the more detailed aspects of our outputs will depend on the exact structure we have imposed. It will be interesting to see whether the two mtDNA variants show different levels of oxygen consumption in heteroplasmic cells, as predicted by our model, though this may be difficult to measure experimentally.

4.2.3 Combining cost and control: comparison and optimisation of both cellular control and treatment strategies

4.2.3.1 Timescales and energy sensing in optimal control of mtDNA populations.

Here we compare the mean cost over time of four different plausible cellular control strategies. The first two consist of the linear feedback model $\lambda(w,m) = \mu + c_1(w_{opt} - (w + \delta m))$ with (I) $\delta = 0$ (only wildtypes are sensed) and (II) $\delta = 1$ (total mtDNA copy number is controlled without differentiating between mutant and wildtype). We further consider two control strategies that are optimised under our imposed cost function. We identify the optimal parameterisations that minimise steady-state cost for (III) a linear feedback control and (IV) the 'relaxed replication model' [1, 2]†.

First, we need to choose the parameter values that are not being optimised. We are mainly interested in how the different controls influence changes in mtDNA dynamics due to the presence of mutants, and therefore demand that they induce similar dynamics when only wildtypes are present. We do this by setting the wildtype mean and variance (in the absence of mutants) to be identical under all controls. The mean is chosen to be w_{opt} and the variance is set by fixing the parameter α_R in the relaxed replication model (see footnote) to $\alpha_R = 10$, as its value was originally estimated to lie in the range $(5 - 17)$ [1]. Setting $\alpha_R = 10$ then fixes the value for c_1, which is identical for models (I)-(III) (Table B.1). We optimise the parameters δ and η in models (III) and (IV), respectively.

To optimise a control, both an optimization time-scale T and a set of initial conditions are required. Here we use $T = \infty$, corresponding to the steady state limit, and a set of initial conditions with heteroplasmies in the range $h_0 \in [0, 0.2]$; we later consider finite values of T.

Figure 4.3 shows the mean cost of our four controls up to ~ 80 years resulting from stochastic simulations; cost variance, as well as mutant and wildtype dynamics, were also computed (Figure B.6). The relaxed replication rate control and our linear feedback function behave very similarly when δ and η take their optimal values. A control with $\delta = 0$ shows an exponential increase in cost (due to an exponential increase in mean mutant copy number (Chapter 5)),

†The relaxed replication model assumes a constant death rate μ and a birth rate of the form $\lambda(w,m) = \frac{\mu}{w+m}\Big(\alpha_R\Big[w_{opt} - (w + \eta m)\Big] + w + \eta m\Big)$ with $\alpha_R > 1$ and η constants [1, 2]. We have renamed the parameters of the original model for convenience. Note that both α_R and η influence the mutant contribution to $\lambda(w,m)$ (rather than a single parameter in our linear model).

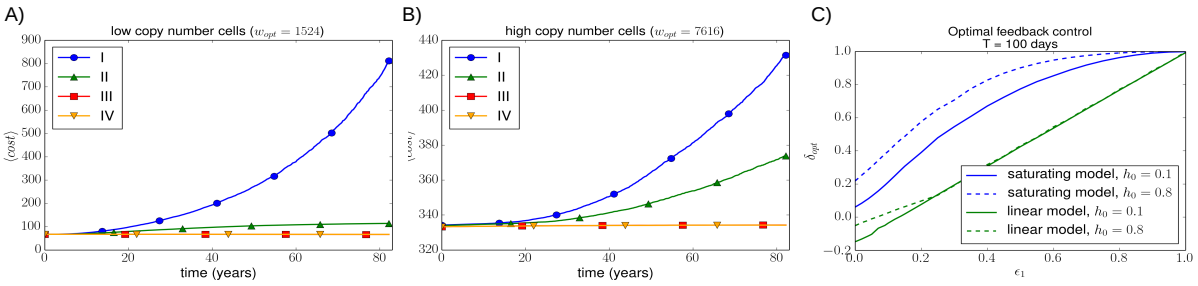


Figure 4.3: A control that senses no mutations shows an exponentially increasing cost, which is most noticeable in low copy number cells. A) + B) Here we show the mean cost (3×10^4 repeats) for the following four controls: linear feedback controls $\lambda(w, m) = \mu + c_1(w_{opt} - (w + \delta m))$ with I) $\delta = 0$, II) $\delta = 1$, and III) $\delta = \delta_{opt}$, and IV) the optimised 'relaxed replication control' [1, 2]. Controls were initialised in steady state at $h_0 = 0.15$. Both figures used the saturating output model; figures (A) and (B) correspond to low and high copy number cells, respectively. We used $\epsilon_1 = 0.3$; other control parameters used are specified in Section B.4.3. **C) A control based on sensing mitochondrial energy output may be generally a good strategy.** This plot shows the optimal value of δ in our linear control as a function of ϵ_1, for the linear and saturating model and for both low ($h_0 = 0.1$, solid line) and high ($h_0 = 0.8$, dashed line) initial heteroplasmies. Here we used $T = 100$ and high copy number values for both models. Similar plots for $T = 10^4$ are shown in Figure B.7, Section B.4.3.

though it still takes ~ 12 years and ~ 65 years for this control to become 10% more expensive than the others in our low and high copy number cells, respectively. We conclude that: *i) a control lacking any mutant contribution only becomes notably costly on the order of 10 years, and ii) effects of particular control strategies are more pronounced in low copy number cells* (Table 4.1(IIII)).

We now investigate how the optimal value of mutant sensing for the linear control (δ_{opt}) depends on timescale T, initial heteroplasmy h_0 and the 'mutant pathology level' described by parameter ϵ_1. Biologically, this question reflects how the cell should optimise its processing of mtDNA state as the mutant load and severity changes. Intuitively, values of $\epsilon_1 \simeq 1$ have $\delta_{opt} \approx 1$: when wildtypes and mutants are equivalent, having a steady state with $w + m = w_{opt}$ is desirable.

Values for δ_{opt} were found for the linear and saturating model, with low and high initial heteroplasmy values, for $T = 100$ days (Figure 4.3C). Having $\delta \approx 1$ means wildtypes and mutants are fed back similarly, whereas $\delta \ll 1$ means mutants are fed back much less. For very deficient mutants (low ϵ_1), a low δ_{opt} ensures that wildtype copy number remains close to its optimal value to compensate for the mutants. Generally, as ϵ_1 decreases, δ_{opt} decreases. In the linear model δ_{opt} becomes negative for low ϵ_1 values; as mutant copy number increases, a negative δ leads to an increase in wildtype to compensate for the deficient mutants. Similar results are found for longer timescales T (Section B.4.3).

When mitochondrial energy outputs are sensed, the quantity '$w + \delta m$' can be considered to represent the cellular energy production rate. A mutant with a low value of ϵ_1 is less able to produce energy, and would automatically obtain a low value of δ as it contributes less to the total

energy production rate. This means that in the setting of energy sensing, the relation between ϵ_1 and δ automatically obeys the trend shown in Figure 4.3C (i.e. δ decreases as ϵ_1 decreases). Therefore, *control strategies based on the energy status of the cell will often outperform controls based on mtDNA copy number (which always have $\delta = 1$) or sensing mtDNA mass (which would work well for deficient deletion mutants, but would be suboptimal for deficient point mutations)* (Table 4.1(IV)).

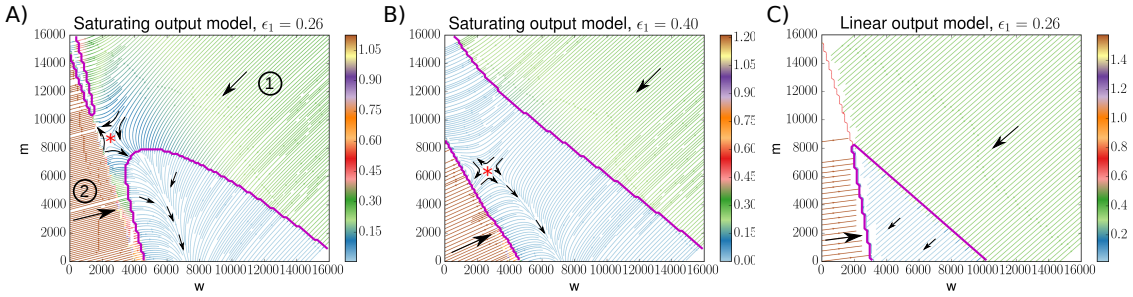


Figure 4.4: Locally optimal controls show nonlinear behaviours close to demand-satisfying regions, but linear optimal dynamics far away from these regions. We used streamplots in (w, m)-space to visualise the dynamics resulting from a locally optimal control, for various parameters of ϵ_1. At each point, arrows show the direction corresponding to the largest decrease in cost. Regions are coloured according to the magnitude of the decrease in cost when moving in the optimal direction. Black arrows illustrate general trends in these regions. **A)** Region (1) shows that at high copy numbers, both mutant and wildtype mtDNAs should be decreased in an evenhanded manner; region (2) shows the possibility that the optimal control involves an increase in mutant copy number. **B)** A higher value for the parameter ϵ_1 is used, meaning mutants are less pathological. **C)** the locally optimal control for the linear output model more closely resembles a linear control. In both (A) and (B) we see a divergence point (red asterisk) illustrating the fact that both high mutant and high wildtype states constitute local attractors of low cost (as in Figure 4.2).

Locally optimal control strategies map the control space of mtDNA populations.

With the use of our cost function it is possible to identify *locally optimal controls*: controls that, for each state (w, m), move the system in the direction of the largest decrease in cost. The dynamics resulting from these locally optimal controls are shown in Figure 4.4.

When heteroplasmy is high, the main priority is not always to decrease mutant copy number, but to increase wildtype copy number even if this means an increase in mutant load (region 2 in Figure 4.4A). It is only after wildtype copy number has sufficiently increased that the focus should be on decreasing m. At high copy numbers the optimal dynamics are to decrease all mtDNA in an evenhanded manner (region 1) rather than decreasing m at a faster rate than w. For the saturating model, we also observe a divergence point in the space of local optimal strategies, reflecting the two local cost minima (high wildtype and high mutant) observed earlier (Figure 4.2). Hence, there are several regions of state space where *even for pathological mutants,*

reduction of mutant mtDNA alone is not always the optimal control strategy (Table 4.1(𝕍)). Finally, the less pathological the mutants become (e.g. Figure 4.4B), the more the locally optimal control starts to resemble a linear control. In the linear output model, the optimal control always shows linear behaviour (Figure 4.4C).

4.2.3.2 A parameterised model of artificial mtDNA control for disease treatment

While the locally optimal controls identified above may not be achievable by the cell (for example, the cell may not be able to decouple biogenesis of wildtype and mutant mtDNA), genetic technology gives us the ability to artificially exploit these optimal strategies. Mitochondrially targeted Zinc Finger Nucleases (mtZFNs) [142, 143, 293, 300, 301] and mitoTALENs [144, 292] are able to produce shifts in heteroplasmy by specifically cutting mutant mtDNA; these technologies thus offer the prospect of gene therapeutic treatments for some mitochondrial diseases. Though results are promising, treatments with endonucleases are not perfect and can have substantial dose-dependent off-target effects [142].

To develop predictive quantitative theory to understand and tune the effects of these interventions, we model nuclease transfection as inducing selective increases in mtDNA degradation, on the background of the linear cellular feedback control used throughout this chapter. Our transfection model introduces three new parameters describing strength (I_0), duration (b), and selectivity (ξ) of nuclease treatment. We assume that for every mutant that is cleaved by the endonucleases, ξ wildtypes are cleaved. For example, when $\xi = 1$ there is no distinction between mutants and wildtypes, and when $\xi = 0$ there is no off-target cleavage. We fit these treatment parameters, as well as our feedback control strength parameter c_1, to recently obtained experimental data [142]. These data involve heteroplasmy and mtDNA copy number measurements during iterative treatments with mtZFNs of 80% heteroplasmic human osteosarcoma 143B cybrid cells. Four sequential cycles of transfection and recovery were performed, where each recovery period lasted 28 days [142].

Our nuclease treatment model is a work in progress. We initially fitted our parameters using simulated annealing, an approach which provides an approximation to the global optimum of a function but does not provide information on parameter uncertainties. We decided to improve our parameter estimates by using a Metropolis sampler, thereby obtaining posterior parameter distributions. One limitation of our analysis is the little amount of data we currently have. At this moment, more data is being collected (for details see below) to improve future model fits.

Simulated annealing provides good point parameter estimates

Here we use simulated annealing to produce a point estimate of the parameters I_0, b, ξ, and c_1 (Methods). Results are shown in Figure 4.5A, B, illustrating the ability of this simple model to capture the dynamics resulting from nuclease activity. The first mtZFN treatment experimentally shifted heteroplasmy from approximately 0.8 to 0.6 [142], meaning we expect the selectivity parameter ξ to be about $\xi \sim 0.6/0.8 = 0.75$, agreeing with our predicted value of $\xi \approx 0.76$. We note that we imposed a periodicity of 28 days in our model (Equation (4.11)), representing the experimental protocol.

Nuclease treatment and a subsequent recovery phase will have the net effect of mapping an initial heteroplasmy value h_i to a mean final heteroplasmy value, h_f. We simulated this mapping of initial to final heteroplasmy values in the presence of cellular feedback control (Figure 4.5), and observed that the *heteroplasmy shifts are similar in low and high mtDNA copy number cells (the variance of the shift is slightly lower for high copy number cells), and that the shift is largest for intermediate heteroplasmies.* Interestingly, *for high h values, it is possible to end up with a* higher *heteroplasmy value after treatment, especially if $\xi \simeq 1$ (Figure B.8).*

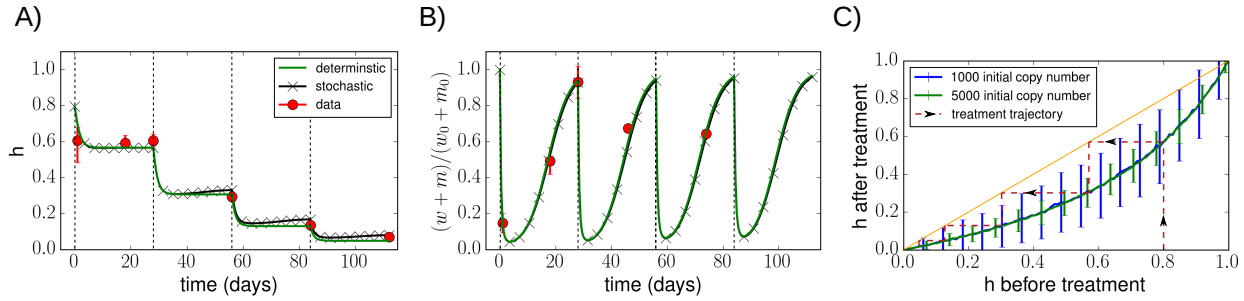


Figure 4.5: A simple model of treating cells with mitochondrially targeted endonucleases captures experimental observations of cellular mtDNA statistics. A, B) Our treatment model was used to fit recent experimental data [142], good agreement was found for both deterministic and stochastic simulations; details about the fitting produce are given in Methods. The periodicity of our model is fixed to represent experimental protocols of sequential rounds of transfection and recovery (Methods). Vertical dashed lines indicate transfection events (once every 28 days). **C)** A given initial mean heteroplasmy value maps to a final mean value after a round of treatment and recovery. Stochastic simulations were performed for both low (blue, 1000) and high (green, 5000) copy number cells. The orange line denotes identity, and the purple trajectory shows heteroplasmy shifts for multiple treatments starting at $h = 0.8$. Further details of the fitting procedure are given in Methods.

Knowledge of the heteroplasmy distribution of a tissue is important in determinining how effciently the tissue can be treated.

To explore the effect of the heteroplasmy distribution on treatment efficacy, we consider three different initial h distributions with different heteroplasmy variances, but identical homogenate

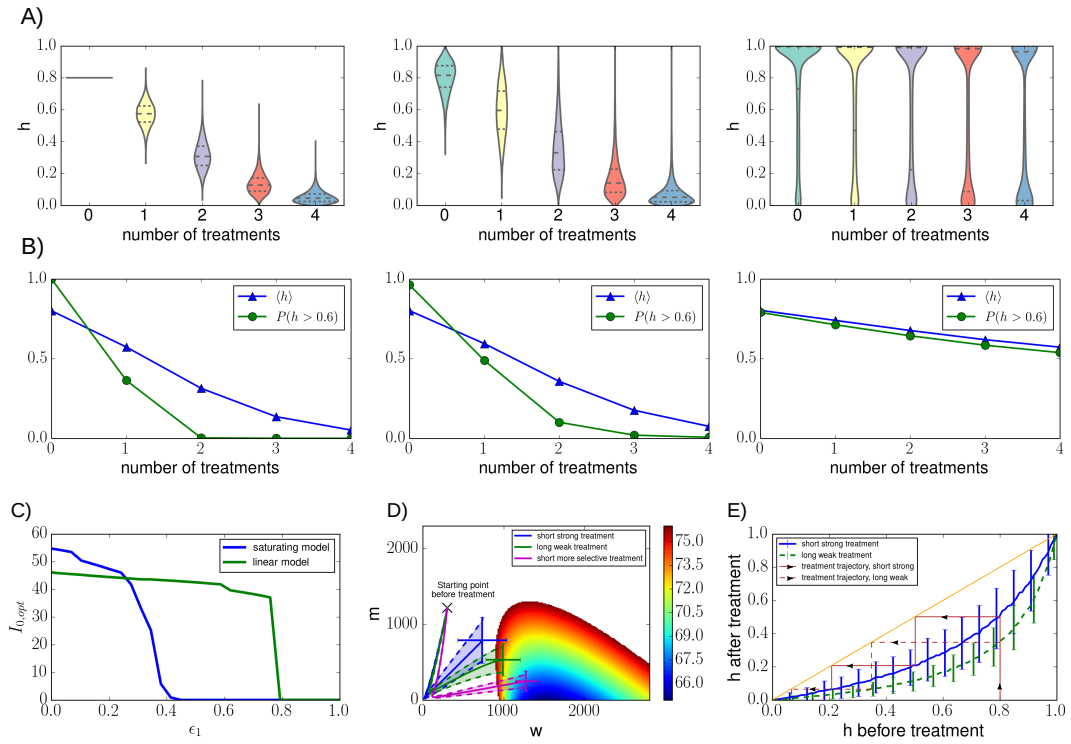


Figure 4.6: Knowledge of the heteroplasmy distribution is important in predicting how efficiently a tissue can be treated. A, B) The effect of four consecutive treatments on three different initial heteroplasmy distributions is shown; all initial distributions have identical means ($\langle h \rangle = 0.8$) but different variances (increasing from left to right). The higher the variance of the initial population, the harder to shift mean heteroplasmy values; mean values after each treatment as well as $P(h > 0.6)$ are shown more clearly in figure (B). In these simulations we assumed that every cell gets transfected. **Gentle but sustained treatments induce larger heteroplasmy shifts than hard and brief treatments. C)** Both the linear and saturating model show a sharp drop in the optimal treatment strength $I_{0,opt}$ as the mutants become more functional (i.e. as ϵ_1 increases). **D)** Means and variances of mutant and wildtype copy numbers were simulated during a round of treatment and recovery, using: i) fitted parameters (blue), ii) a longer treatment duration (smaller b, green) and iii) a higher selectivity (smaller ξ, magenta). The longer weaker treatment induces higher heteroplasmy shifts than the shorter stronger treatment. Not surprisingly, a higher selectivity also leads to an improved heteroplasmy shift. Note that the variance of the final values is lower for more selective treatments. Error bars show standard deviations (based on 10^4 stochastic simulations), further detailed are given in Methods. **E)** This figure again illustrates that gentle sustained treatments lead to larger heteroplasmy shifts. Examples of treatment trajectories are shown; after a single treatment, an initial heteroplasmy of 0.8 is mapped to 0.53 (short strong treatment) or 0.39 (long weak treatment).

means. We treat these populations multiple times using the parameters fitted through simulated annealing in the previous section, and observe the shift in heteroplasmy distribution as well as the change in heteroplasmy mean and the probability of crossing a pathogenic heteroplasmy threshold $P(h > 0.6)$ (Figure 4.6A, B).

High heteroplasmy variances require many cells close to the two extremes $h = 0$ and $h = 1$, which are challenging to shift. A striking reduction in treatment efficacy is predicted as heteroplasmy variance increases while mean heteroplasmy stays constant (Figure 4.6A, B). Threshold crossing probability (for example, $P(h > 0.6)$) also becomes harder to shift at higher heteroplasmy variance. These differences in treatment efficacy depend on the value of δ (mutant

sensing) in our model: lower δ will decrease the difference in efficacies. We conclude that *tissues with a high mean heteroplasmy levels will generally be harder to treat if the heteroplasmy variance is high, especially if this high mean level is caused by a small percentage of cells*, with the strength of this effect dependent on mutant sensing (Table 4.1(VII)).

We can use our parameterised theory to find optimal treatment strengths $I_{0,opt}$ for a given system. Figure 4.6C shows $I_{0,opt}$ as a function of ϵ_1. Intuitively, the strongest treatment should be given to the least functional mutants, and when mutants are almost as functional as wildtypes it is preferable not to treat at all. The optimal treatment strength drops rather sharply as ϵ_1 increases, and does so sooner for the saturating model. This last observation may be because at some point reducing heteroplasmy becomes more expensive as can be seen in Figure 4.2B. Optimal treatment strengths for longer treatments (higher b) show similar qualitative behaviour.

Figure 4.6D shows, using the identified values for $I_{0,opt}$, the trajectories in (w, m) space throughout a single treatment and recovery phase; we used $\epsilon_1 = 0.3$ and the corresponding cost heatmap is also shown. The three trajectories shown correspond to: i) a short and strong treatment (using the fitted parameter values), ii) a long and weak treatment, and iii) a short but more selective treatment. It can be seen that *treating longer but weaker results in a lower final heteroplasmy value than treating short and strong* (Table 4.1(VIII)). A weaker treatment also reduces the chance of a cell losing all its mtDNA molecules. Intuitively, a more selective treatment leads to larger heteroplasmy shifts. The difference in treatment results for long compared to short treatments is also illustrated in Figure 4.6E. We note that in finding $I_{0,opt}$, we initialised all cells at identical states. When a distributions of initial states is used, the variance that is now present is likely to affect the optimal treatment strength.

A Bayesian model of nuclease treatment

To obtain knowledge of the uncertainty in our parameter estimates, we here use a Markov Chain Monte Carlo (MCMC) model to fit our parameters (Methods). We note that this work is motivated by reviewer comments obtained after submission to Cell Systems and is still a work in progress. New data is currently being collected by our collaborator Payam A. Gammage which will be incorporated in future versions of the model. This new data consists of: i) total copy number measurements in the original 80% heteroplasmy cells, and ii) heteroplasmy measurements at a finer time lattice compared to earlier measurements (which were taken at 1, 18 and 28 days post-treatment).

The data shown in Figure 4.5A, B was obtained from cells transfected with mtZFNs without any sorting based on mtZFN concentration ([mtZFN]) [142]. The authors collected similar data from cells sorted for either low or high [mtZFN] [142], which we did not include in our previous approach but which we will include in our MCMC model in an attempt to reduce parameter uncertainty. Instead of a single mtZFN treatment strength I_0, we now have a set of strengths $I_0^{(\mathrm{N})}$, $I_0^{(\mathrm{H})}$ and $I_0^{(\mathrm{L})}$ referring to 'normal' (i.e. unsorted), high and low initial mtZFN concentrations. Because treatment efficiency was observed to depend on [mtZFN] [142], we also assume three different selectivities: $\xi^{(\mathrm{N})}$, $\xi^{(\mathrm{H})}$, and $\xi^{(\mathrm{L})}$. The treatment duration b as well as the cell's feedback control parameter c_1 are assumed to be shared between the three data sets.

Our posterior parameter estimates, obtained using a Metropolis algorithm (Methods), are shown in Figure 4.8. It is clear that our MCMC model is not mixing properly (reasons for which are discussed below), meaning our model is not efficiently sampling the available parameter space and the obtained posterior distributions do not represent the 'true' posteriors. We show (approximate) Bayesian confidence intervals for heteroplasmy and total copy number during treatment, illustrating that the posterior mean prediction of copy number dynamics is slightly different from the prediction found through simulated annealing (Figure 4.7); this is likely due to poor mixing.

From the sample values shown in Figure 4.8 we suspect a high correlation between the treatment duration parameter b and the treatment strength parameters $I_0^{(\mathrm{N})}$, $I_0^{(\mathrm{H})}$ and $I_0^{(\mathrm{L})}$, which is confirmed in Figure B.9A. This high correlation is due to a degeneracy in our model when $b \gg \mu_z$, in which case Equation (4.10), describing mtZFN concentrations over time, reduces to $[ZFN](t) = I_0/b \cdot e^{-\mu_z t}$. In this regime, mtZFNs enter the cell in a pulse-like fashion, being present at concentration I_0/b at time $t = 0$ and exponentially decaying afterwards at rate μ_z. A constant ratio I_0/b will provide identical mtZFN concentration profiles (and therefore heteroplasmy and copy number predictions), meaning the parameters I_0 and b can be arbitrarily large under our model as long as their ratio is conserved[‡]. The ratio I_0/b, as expected, is higher in the case of higher mtZFN concentrations (Figure B.9B).

The poor mixing of our MCMC model can be due to a variety of reasons. Firstly, we might not have performed enough iterations. Iterations of our model are expensive because at each iteration we numerically solve three ODE systems corresponding to the normal, high and low parameter sets (Section 4.4). Due to a lack of time we have currently only performed 3×10^5 iterations (requiring ~ 1.5 days), but this number can be increased by an order of magnitude

[‡]The parameter I_0 and b cannot become arbitrarily small because in this case the condition $b \gg \mu_z$ fails to hold, meaning that changing b (and I_0) influences the mtZFN dynamics and therefore our model predictions.

in the future. Secondly, the degeneracy in our model (discussed above) is likely to reduce the mixing efficiency. We may need to redefine our parameters or reconsider our nuclease model to eliminate the degeneracy. Further improvement may be obtained by including the new data that is currently being collected.

In conclusion, we have performed Bayesian inference to learn about the uncertainties in our parameter values. As the current status of this model is not final, and our obtained posteriors are only approximate, we cannot draw definite conclusions from our inference yet. However, we were still able to predict some expected results, including a higher selectivity (Figure 4.8) and lower treatment strength (Figure B.9B) for the low nuclease concentration setting compared to the high concentration setting. Furthermore, we discovered a high (unsurprising) correlation between treatment strength and duration (Figure B.9A).

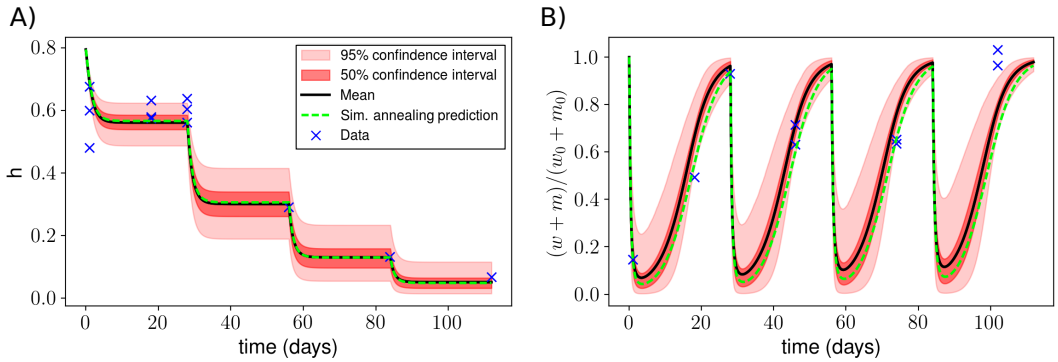


Figure 4.7: Bayesian confidence intervals for heteroplasmy and copy number dynamics. We inferred our model parameters using recently observed experimental data [142] (Section 4.4) and use posterior samples to observe data fits. We note that four extra data points on total copy number (which are not shown in Figure 4.5B) were provided by Payam A. Gammage. **A)** Drawing from our posterior distributions, we show the mean and 50% and 95% confidence intervals of our heteroplasmy dynamics predictions during four rounds of treatment and recovery. Deterministic simulations were used. The dashed green line indicates predictions made through simulated annealing (i.e. this line is identical to the deterministic trajectories shown in Figures 4.5A,B). Crosses indicate data points. **B)** Similar to figure (A), but showing relative total copy numbers.

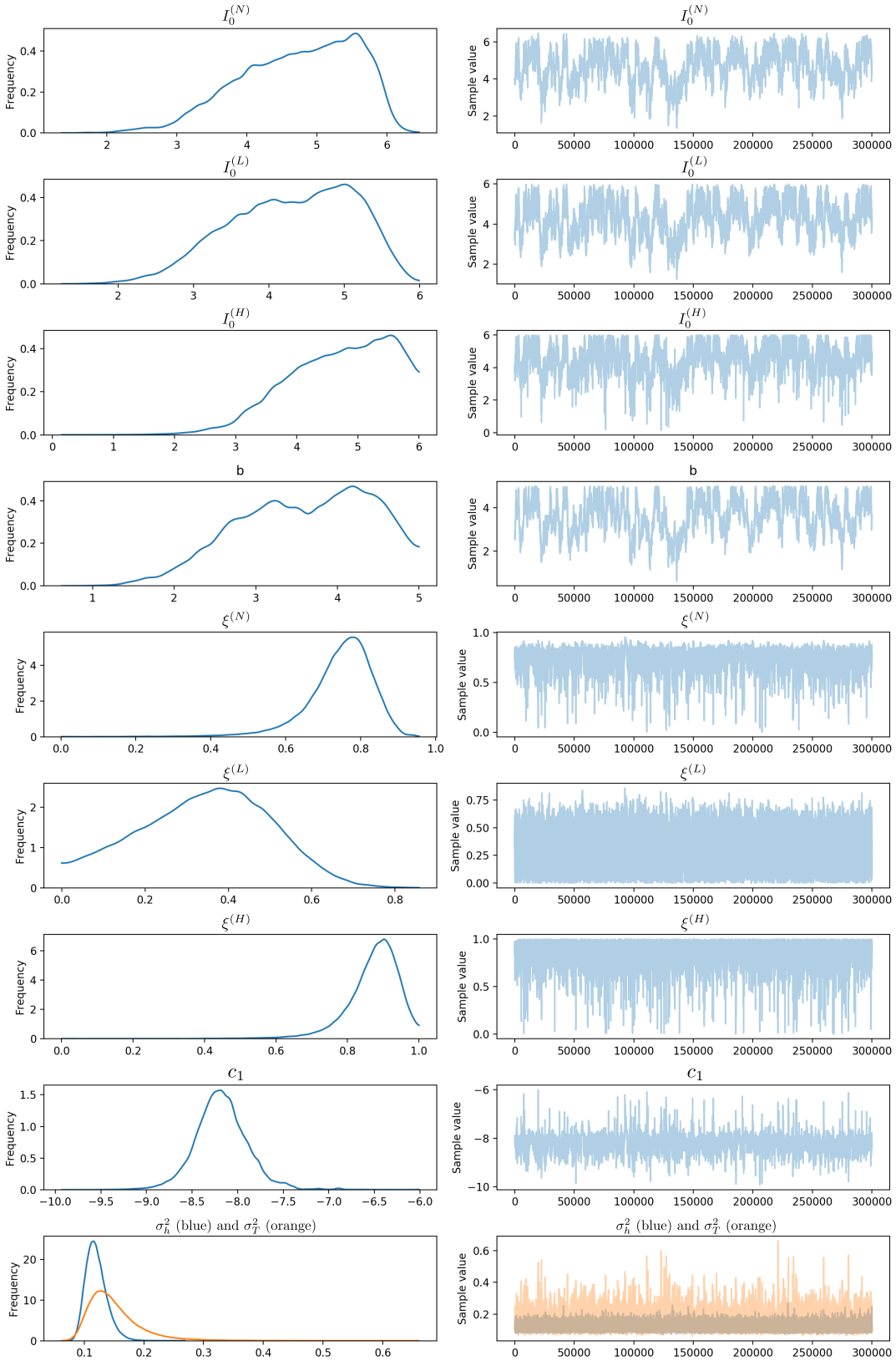


Figure 4.8: Posterior mtZFN treatment parameter distributions. Here we show our posterior distributions obtained after running our MCMC algorithm for 3×10^5 iterations (left) as well as the corresponding sample values (right). Our chains mix poorly, especially for the parameters $I_0^{(\mathrm{N})}$, $I_0^{(\mathrm{H})}$, $I_0^{(\mathrm{L})}$ and b, which show high correlations. Priors distributions are provided in Methods.

4.3 Discussion

In this work, we have built a quantitative theory bridging stochastic optimal control, costs of mtDNA populations, and gene therapies. Our results contribute to a growing body of evidence [32, 107, 302, 303] that the variance of mtDNA populations has important physiological and therapeutic implications independently of mean heteroplasmy, and underline that stochastic theory is required to understand this biologically and medically important quantity. We compared different cellular strategies of regulating the mtDNA population by studying wildtype and mutant mean and variance. We found that there exists a tradeoff between controlling one species, or controlling the other. We introduced a mitochondrial energy-based cost function enabling us to compare distinct control mechanisms and found that a control based on the energetic status of the cell forms a good strategy in many situations. Recent experimental data [142] was used to fit a therapeutic treatment model in which cells are transfected with mitochondrially targeted endonucleases. We showed that long gentle treatments induce higher heteroplasmy shifts than brief strong treatments, and that tissues with high heteroplasmy variances can be particularly hard to treat.

We appreciate that our cost function is phenomenological and contains many parameters. We would argue, however, that most of these are biologically interpretable meaning their values can be obtained or estimated from the literature. The main elements in our cost function are quite general: terms involving supply, demand, and resource. We stress that we do not make any quantitative predictions based on our cost function, but merely comment on its general qualitative features. One interesting insight we obtained is that intermediate heteroplasmy states may be the most expensive due to a combination of output saturation and lower resource consumption rates of one of the mtDNA species. Experimental evidence for dysfunctional heteroplasmic states (with normal functioning at homoplasmy) was found in mice [140]. As mentioned before, we do not claim to have explained this effect, we only conclude that mutant resource consumption rates may play important roles.

If the parameter δ is low, i.e. mutants are sensed less, mutant copy numbers at high heteroplasmies will be higher than wildtype copy numbers at low heteroplasmies. Experimentally, it has been observed that heteroplasmic cells can have total mtDNA copy number values that are 5-17-fold higher compared to cells homoplasmic in wildtype [97, 304–306]. The cell has somehow allowed these mutants to expand, which may mean that they are less tightly controlled; controls based on total energy output or mtDNA mass (which can result in $\delta < 1$) may lead to such behaviours. A control on mtDNA mass could explain why deletion mutants

are often seen to expand [307, 308] and would also predict normal copy number levels in cells harbouring mtDNA point mutations. Recently, it was found that samples with mtDNA indels had very high mtDNA copy number levels, but single nucleotide variants did not [309]. The cellular control mechanism could also be a mixture of copy number control, mtDNA mass control and energy sensing, meaning that mutations with different functionalities and masses all have different values for δ and expand to different extents. In the next chapter, we continue the discussion on the influence of δ and show that low-δ mutants can preferentially expand during ageing.

We showed that heteroplasmy distributions in cell populations can provide important information about the possibility of successfully treating these cells with endonucleases. A tissue may be harder to treat if its high mean heteroplasmy level is caused by a small percentage of dysfunctional cells. Experimental values of mean homogenate heteroplasmy in heart tissue of patients with the 3243A>G mutation are roughly around 0.8 (though ranges can be large [310–313]) and muscle tissue often shows mosaic structures, with deficient patches of cells adjacent to healthy cells. These examples show that it may be that, at least in some cases, high mean levels are indeed caused by a relatively low percentage of cells, meaning that there are still challenges ahead for efficiently treating these tissues.

One of the features of our cost function is that resource limitations play an important role in shaping the cost landscape. There are indications that cellular levels of NAD (a coenzyme involved in OXPHOS) are limiting, and that a sufficient supply of NAD to mitochondria becomes critical [314–317]. An increase of intracellular NAD can lead to an increase in oxygen consumption and ATP production [317] indicating that resource limitation may, at least in some cases, be a genuine constraint. Adding various kinds of resources can significantly change mitochondrial basal respiration rate [318–320].

We found that, under our model, it is more optimal to sense mutants to a lesser extent if the mutants have a lower energy output. In this way, their presence has little influence on wildtype copy number dynamics which then allows the wildtype mtDNA molecules to remain close to their 'natural' (and assumed to be close to optimal) levels. This makes a control directly based on the energetic status of the cell a good strategy. Measurements of mutant as well as wildtype copy number values for different types of mutants, together with their energetic functionality, are helpful for improving our understanding of the cell's control mechanisms.

In modelling gene therapies, our fit to endonuclease data obtained through simulated annealing yielded a high off-target cutting estimate, $\xi = 0.76$, which may be a result of a relatively

high nuclease concentration in experiments: lower or even higher mtZFN concentrations were experimentally observed to produce larger or smaller heteroplasmy shifts, respectively [142]. If the parameter ξ is a function of the treatment strength I_0, the values for $I_{0,opt}$ we found in Figure 4.5F will be different. We note that the value of ξ itself does not necessarily determine how effective a treatment will be. For example, even if $\xi = 0.95$ a long enough treatment is likely to eliminate all mutant species (unless the initial heteroplasmy was so high that wildtypes reach extinction during treatment) because a slight selection against mutants can, for long times, still lead to their extinction. Further work on the relationship between I_0 and ξ will elucidate more clearly the tradeoff between treating with a high strength and cleaving more mutants in the process, and having a high selectivity and therefore low off-target cleavage.

Besides our simulated annealing approach, we used a Metropolis algorithm to fit the endonuclease data [142]. Using this model we were able to demonstrate an expected high correlation between treatment duration and strength, introducing a degeneracy in our model which potentially led to the poor mixing of our MCMC chains. The current status of this model is not final and may be improved by increasing the number of MCMC runs, reconsidering our mtZFN concentration model, and including new data.

Like any other model, our models have a defined range of applicability. A key baseline assumption was using identical replication and degradation rates for mutants and wildtypes. As discussed in the thesis introduction, various possibilities of distinct rates have been offered in the literature, including faster mutant replication rates [38, 93, 94, 96, 97, 321], lower mutant degradation rates [99], and higher mutant degradation rates [59, 191]. Including such differences, and other features such as *de novo* mutations, degradation control, and cell divisions [31, 32, 101, 108], constitute natural extensions to our theory.

Wildtype and mutant mtDNA evolution equations Wildtype and mutant mtDNA copy numbers are considered to have birth rate $\lambda(w,m) = \mu + c_1(N_{ss} - (w + \delta m))$ and death rate μ, leading to the following evolution equations:

$$\begin{aligned}\frac{dw}{dt} &= w(\lambda(w,m) - \mu)\\ \frac{dm}{dt} &= m(\lambda(w,m) - \mu)\end{aligned} \tag{4.5}$$

We refer to N_{ss} as w_{opt}, the 'optimal' wildtype steady state which is present in the absence of mutants. Though these deterministic equations are analytically solvable, the corresponding stochastic system does not have an explicit solution due to nonlinearities. All stochastic simulations in this chapter use the Gillespie algorithm [127].

Expected cost per unit time. Let the cost per unit time of state (w,m) be denoted by Λ, and the cost corresponding to the steady state (w_{ss}, m_{ss}) by $\bar{\Lambda}$. Even if steady state copy numbers are constant over time (i.e. the mean values of w and m are always equal to w_{ss} and m_{ss}) the mean cost per unit time is generally not equal to $\bar{\Lambda}$. By performing a Taylor expansion, the mean cost per unit time can be written as follows:

$$\begin{aligned}E[\Lambda](t) \approx\ & \bar{\Lambda}\\ &+ \frac{1}{2}\Big(\mathrm{var}(w(t))\frac{\partial^2\Lambda}{\partial w^2} + \mathrm{var}(m(t))\frac{\partial^2\Lambda}{\partial m^2}\\ &+ 2\mathrm{cov}(w(t),m(t))\frac{\partial^2\Lambda}{\partial w \partial m}\Big)\end{aligned} \tag{4.6}$$

where $E[\Lambda](t)$ is the expected cost per unit time given that the trajectory starts in state (w_{ss}, m_{ss}), and all partial derivatives are evaluated at steady state.

Cost function structure. We assume that the net energy supply per unit time in a state (w,m), called $S(w,m)$, involves the following four terms: (i) the *energy output* per unit time (s_i) produced by the mitochondria; (ii) a *maintenance cost* per unit time (ρ_1) to maintain the mitochondria, as their presence imposes some energetic cost (e.g. mRNA and protein synthesis); (iii) a *building cost* (ρ_2) for the biogenesis of new mitochondria; and (iv) a *degradation cost* (ρ_3) to degrade mitochondria. We will assume that every mtDNA molecule is associated to a particular amount of mitochondrial volume which we refer to as a 'mitochondrion' (Section B.3).

At any time, mitochondria experience a certain energy demand and to meet this demand they need to have a certain resource consumption rate r_i (where $i = w, m$ refers to wildtype or mutant). Here we use the term 'resource' as an amalgamation of the substrates used for the oxidation system. We need to specify the relationship between the power supply (s_i) and the rate of resources consumed (r_i) by mitochondria. We use two different models $s_i(r_i)$ which are justified in Section B.2:

$$\begin{aligned} s_w(r_w) &= \phi(r_w - \beta) \\ s_w(r_w) &= 2\frac{s_{max}}{1 + e^{-kr_w}} - 1.1s_{max} \end{aligned} \tag{4.7}$$

where ϕ, β, k and s_{max} are constants respectively describing the mitochondrial efficiency, a basal proton leak-like term, the saturation rate of the efficiency, and the maximum energy production rate (Section B.3).

We assume that pathological mutants can have a deficient electron transport chain (which may support a smaller flux leading to a lower resource consumption rate for mutants and therefore a lower ATP production rate) and a lower energy production efficiency:

$$s_m(r_m) = \epsilon_2 s_w(\epsilon_1 r_w) \tag{4.8}$$

Here, $\epsilon_1, \epsilon_2 \in [0, 1]$ describe the mutant resource uptake rate and the mutant energy production efficiency relative to that of a wildtype, respectively. In the main text we set $\epsilon_2 = 1$; other values of ϵ_2 are discussed in Section B.3.7.

The mitochondrial maintenance cost is denoted by ρ_1 and corresponds to the energetic cost required to maintain the mitochondrion that contains the mtDNA. This energetic costs involves factors like the synthesis and degradation of mitochondrial proteins and enzymes. We assume the maintenance cost is the same for wildtype and mutant mitochondria (though for some mutations this is quite possibly not the case). The net energy supply per unit time, $S(w, m)$, then follows as Equation 4.4.

To determine the value of r_w for a given state (w, m), we first check whether the demand D (which we assume is a constant) can be satisfied in this state. If it can, we set equation (4.4) equal to D and solve for r_w, i.e. we assume that if possible, the mitochondria will exactly satisfy demand. It may, however, not be possible to satisfy demand, which can be because of two reasons: i) there are not enough mitochondria present to produce enough energy, or ii) there is not enough resource available to meet demand. In the former case, we set $r_w = r_{max}$;

the mitochondria work as hard as possible to keep their energy output closest to demand. In the latter case, we assume that the total available amount of resource, R (which we consider to be constant), is shared equally between the mitochondria: $r_w = \frac{R}{w+\epsilon_1 m}$. Cellular energy demand will naturally fluctuate over time, and because of excess capacity of mitochondria [322], there is no need to immediately increase mitochondrial biogenesis. In our model, a given state (w, m) may be able to satisfy a range of demands by changing its resource uptake rate. Further details of the cost function are given in Sections B.2 - B.4.

The parameters used in our cost function are summarised in Table 4.3 and motivated in Section B.3. Despite our model being simple, most parameters are biologically interpretable.

Modelling control through mitochondrially targeted endonucleases. Experimentally, cells are transfected with two mtZFN monomers: one which binds selectively to mutant mtDNAs, and one that binds mutants and wildtypes with equal strength [301]. We simplify this picture by assuming an 'effective' mtZFN pool and use $[ZFN]$ to denote its concentration. The increase in mtDNA degradation rate is then assumed to be proportional to $[ZFN]$.

Nucleases are imported into the cell and then degrade over time, meaning that their concentration in the cell (and in the mitochondria) may be approximated by an immigration-death model. This leads us to the following equation:

$$\frac{d[ZFN](t)}{dt} = I(t) - \mu_z[ZFN](t) \tag{4.9}$$

where $I(t)$ and μ_Z are the immigration and death rates of the effective mtZFN pool, respectively. In the recent experiments [142], nucleases are expressed for short times meaning that the immigration rate will increase sharply at the start of the treatment after which it decreases over time, and we have chosen to model $I(t)$ as an exponentially decaying function, $I(t) = I_0 e^{-bt}$, where I_0 is the initial rate right after the treatment is started and b is a constant describing the duration of the treatment. The mtZFN concentration now becomes

$$[ZFN](t) = \frac{I_0}{\mu_z - b}\left(e^{-bt} - e^{-\mu_z t}\right) \tag{4.10}$$

which is shown for various parameter values in Figure B.8A. The data we use to fit our models concerns heteroplasmy and total copy number measurements over four rounds of treatment, each treatment consisting of mtZFN transfection followed by a 28-day recovery period. During this recovery period, total copy numbers recover their initial values due to cellular feedback control. We assume our mutant and wildtype mtDNA death rates at any time t (measured in

days) to be given by

$$\mu(t)_m = \mu + \frac{I_0}{\mu_z - b}\left(e^{-b(t \bmod 28)} - e^{-\mu_z(t \bmod 28)}\right)$$
$$\mu(t)_w = \mu + \xi\frac{I_0}{\mu_z - b}\left(e^{-b(t \bmod 28)} - e^{-\mu_z(t \bmod 28)}\right) \tag{4.11}$$

where μ denotes the normal baseline mtDNA degradation rate, $0 < \xi < 1$ indicates how selective the treatment is (if $\xi = 1$ no distinction is made between w and m, if $\xi = 0$ no extra wildtype cleavage occurs during treatment), and 'mod' refers to the modulo operator.

Model fits using simulated annealing. To fit our nuclease model to recently obtained experimental data [142] we use Equations (4.5) with our linear feedback control to model mutant and wildtype dynamics, where the constant death rate μ is now replaced by the time-dependent death rates $\mu(t)_w$ or $\mu(t)_m$ (Equations (4.11)) for wildtype or mutant molecules, respectively. These new evolution equations incorporate the cellular feedback control as well as the nuclease treatment which occurs in cycles of 28 days. We assume $\delta = 1$ because total mtDNA copy numbers were observed to be independent of heteroplasmy [142]. The mtZFN degradation rate was assumed to be $\mu_z = \ln(2)$ day^{-1}, corresponding to a half-life of 1 day. This roughly matches the experimental observation that almost no mtZFN was present 4 days post-transfection (with a half-life of 1 day, only 6% of initial copy numbers remain after 4 days). We fitted four parameters in total: I_0, b, ξ and c_1.

Given a set of parameters, we numerically solve the ODEs describing mutant and wildtype dynamics over a period of 112 days (i.e. four treatments), and calculate the mean-squared-error between the observed data y_i and our model predictions $\hat{y}_i$, which is given by $\sum_i (y_i - \hat{y}_i)^2$. This error is then minimized through simulated annealing, provided an approximate global optimal parameter set. Because mtDNA copy number in the cells used in the experiment is not known we performed parameter fits using both low (1000) and high (5000) steady state copy numbers, modelled as $N_{ss} = 1000$ or $N_{ss} = 5000$. The obtained parameter fits are: $(I_0, b, \xi, c_1) \approx (38, 12, 0.76, 3 \times 10^{-4})$ and $(I_0, b, \xi, c_1) \approx (40, 12, 0.76, 5 \times 10^{-5})$ for cells with copy number 1000 and 5000, respectively.

Model fits using Metropolis sampling. We performed our MCMC inference using the Python package Pymc3, a package designed for Bayesian statistical modelling and probabilistic machine learning. The data we use concerns three experimental conditions (treatments with 'normal', high and low mtZFN concentrations), each of which involves measurements of heteroplasmy and total mtDNA copy number [142]. We assumed our nuclease model parame-

ter b (indicating the duration of treatment) as well ast he cellular control parameter c_1 to be shared between all three conditions, but allowed the parameters I_0 (treatment strength) and ξ (treatment selectivity) to vary. This leads to three sets of parameters, used to predict heteroplasmy and copy number dynamics in the three experimental conditions: $(b, c_1, I_0^{(\mathrm{N})}, \xi^{(\mathrm{N})})$, $(b, c_1, I_0^{(\mathrm{H})}, \xi^{(\mathrm{H})})$ and $(b, c_1, I_0^{(\mathrm{L})}, \xi^{(\mathrm{L})})$ where N, H and L refer to normal, high and low mtZFN concentrations. The parameter ξ is assumed to vary because it was experimentally observed that treatment with lower mtZFN concentrations were more effective [142].

Like in the simulated annealing approach, we solve the evolution equations (Equations 4.5) with μ replaced by $\mu(t)_w$ or $\mu(t)_m$, but now we solve them three times using our three different parameter sets as defined above. This provides us with three sets of heteroplasmy predictions (all together denoted by $\hat{y}_i^{(h)}$) and total copy number predictions (all together denoted by $\hat{y}_i^{(T)}$). We use a Gaussian error model, i.e. we assume that the observed heteroplasmy $y_i^{(h)}$ and total copy number $y_i^{(T)}$ data are given by

$$\begin{aligned} y_i^{(h)} &= \hat{y}_i^{(h)} + N(0, \sigma_h^2) \\ y_i^{(T)} &= \hat{y}_i^{(T)} + N(0, \sigma_T^2) \end{aligned} \tag{4.12}$$

where we allow for different noise variances for h and T (in general, different experimental errors are expected as different methods are used to measure h and T). A metropolis sampler is then used for parameter estimation. The total number of parameters we infer is 10: $b, I_0^{(\mathrm{N})}, I_0^{(\mathrm{H})}, I_0^{(\mathrm{L})}, \xi^{(\mathrm{N})}, \xi^{(\mathrm{H})}, \xi^{(\mathrm{L})}, c_1, \sigma_h^2$ and σ_T^2. Assuming an mtDNA copy number of $N_{ss} = 1000$ in all the cells, our maximum a posteriori (MAP) estimation is $(b, c1, I_0^{(\mathrm{N})}, I_0^{(\mathrm{H})}, I_0^{(\mathrm{L})}, \xi^{(\mathrm{N})}, \xi^{(\mathrm{H})}, \xi^{(\mathrm{L})}) = (15.4, 3.1 \times 10^{-4}, 55.4, 55.8, 36.1, 0.79, 0.88, 0.45)$. When comparing the estimates in the 'normal' setting with the ones found through simulated annealing (with $N_{ss} = 1000$), we see that ξ and c_1 are very similar and, though both I_0 and b were estimated to be higher according to the MAP, their ratio is similar.

We used the following prior distributions: log-uniform priors for parameters $I_0^{(\mathrm{N})}$ (between 0 and 6.5), $I_0^{(\mathrm{H})}$ (between 0 and 6), $I_0^{(\mathrm{L})}$ (between 0 and 6), b (between 0 and 5) and c_1 (between -11 and -6); uniform priors (between 0 and 1) for the parameters $\xi^{(\mathrm{N})}, \xi^{(\mathrm{H})}, \xi^{(\mathrm{L})}$; and half-normal priors for the noise variances σ_h^2 and σ_T^2 (with standard deviation 1.0).

5

Apparent mtDNA selection in models of random drift

Summary

Mutant mtDNA molecules expand during ageing, reaching high levels in a small fraction of cells thereby inducing pathology. Understanding how mutant clonal expansion arises is important in understanding the ageing process as well as disease progression. We deploy a random drift model of mtDNA dynamics and show that, interestingly, it can give rise to changes in mean cellular heteroplasmy without explicit selection. We investigate a setting of mtDNA exchange between cells, relevant in skeletal muscle fibres, which can induce preferential mutant expansion during ageing even if there is an active process selecting against the mutants. Using experimental data from skeletal muscle fibres, we estimate that mutant load in aged tissue may be lower than often assumed in model simulations. Finally, we provide a discussion on the role of random drift in clonal expansion and suggest experiments to test our model and improve parameter estimates.

5.1 Introduction

Mitochondrial diseases are associated with a wide range of phenotypes [323], disorders can present at any age, and they can involve a single organ or multiple organ systems. This wide phenotypic variety is partly reflected in the heterogeneous behaviours of different mutant species. For example, some mutations lead to increases (which can be 2-fold, 3-fold [324], or even 21-fold [22]) while others lead to decreases in total mtDNA copy numbers [325]. As mentioned in the thesis introduction, a good understanding of what causes the phenotypic variety and why certain types are more likely to expand, is lacking.

MtDNA dynamics form a stochastic process and it is well known that models showing neutral dynamics under a deterministic description can show non-neutral drifts when stochastic noise is included (see e.g. [326–332]). When multiple species co-exist and have identical birth-to-death ratios, deterministic treatments lack selection effects whereas a stochastic treatment shows selection in favour of the slow species which, being less noisy, is more robust to invasions of other species [327]. In this chapter, we find evidence for stochastic drift in neutral models of mtDNA dynamics induced by a difference in carrying capacity between mutant and wildtype species*. This copy number difference introduces a drift (even with identical birth and death rates for all species), this time in favour of the species with the highest carrying capacity. Just like a low-turnover species, a high copy number species has lower variance and is less susceptible to invasions.

We note that a recent paper studied population dynamics for a more general system (of which ours is a subset) [328] in a similar setting of different carrying capacities between species. We confirm some of their observations in our mitochondrial system, and use some of their analytical results to gain intuition. One of the more interesting results observed by the authors, however, was not accounted for; we provide a more thorough discussion of this, and expand upon their work, in Section 5.2.1.4.

In this chapter, we show that, remarkably, the simple linear feedback model introduced in the thesis introduction can account for a large variety of behaviours observed to be associated with different types of mtDNA, by changing only the value of δ. We show that a skew in heteroplasmy dynamics, caused by a nonlinear mapping between (w, m) space and heteroplasmy space due to different mutant and wildtype carrying capacities, can be reproduced by a diffusion model

*In this chapter we define the carrying capacity of a species as its steady state copy number in the absence of any other species. Note that this is slightly different from the more common use of term as a maximum population size.

with a heteroplasmy-dependent diffusion coefficient. We investigate the possibility of mtDNA exchange between cells, a behaviour which has recently been shown to occur across a variety of cell types [333–335] and arguably forms a natural setting in skeletal muscle fibres (Section 5.2.1.3). Finally, we comment on how our results influence the rate of mutant accumulation and ageing in skeletal muscle cells. We critique previous mathematical models of mtDNA dynamics during ageing and discuss how these models can be improved upon by using the insights developed in this chapter.

5.2 Results

5.2.1 A linear model of feedback control: non-trivial and skewed heteroplasmy dynamics

Our aim here is to show how a model without any explicit selection, meaning that mutant and wildtype mtDNAs are given equal replication and degradation rates, can still give rise to skew in heteroplasmy distribution. As shown in Chapter 4, and noted in previous studies [1, 2], changes in tissue homogenate heteroplasmy are expected. Here, however, we observe changes in cellular mean heteroplasmy. We use the linear feedback model introduced in Section 1.4.4 and mainly focus on a regime with $0 \leq \delta \leq 1$ as this seems to be the most relevant setting in the context of ageing (Section 5.2.2.1).

However, certain behaviours simply cannot be explained by our simple linear models. For example, it was observed that mtDNA copy numbers in leukocytes from patients with MELAS or MERRF syndromes were increased at a young age (< 30), but decreased at an older age [325, 336] (> 50) (i.e. non-monotonic changes in copy number). Such an effect is possible by using a quadratic feedback structure (Figure 5.2C), or possibly by using time-dependent parameters in our linear control.

5.2.1.1 A heteroplasmy-dependent diffusion coefficient leads to heteroplasmy skew

We first investigate a population of cells in which each cell is initialised with equal mutant and wildtype copy numbers. When $\delta = 1$ the system is entirely symmetric in w and m, and the cellular heteroplasmy distribution closely follows a normal distribution (as long as fixation is negligible) whose variance increases with time (Figure 5.1D, E). For long times, as expected,

chances of fixation on mutant or wildtype are 50:50. When $\delta \neq 1$, however, asymmetry is introduced and this is reflected in the heteroplasmy dynamics. Distributions become skewed and, if $\delta < 1$, the short-time probability of wildtype fixation ($h = 0$) is larger than mutant fixation ($h = 1$) (Figure 5.1D). This is consistent with findings that it takes longer to hit high than low heteroplasmy values (Figure 5.1A), and the probability flux into the absorbing boundary $h = 0$ is, for short times times, much larger that the flux into $h = 1$ (Figure 5.1C). For longer times, these asymmetries disappear and the probability of mutant fixation (i.e. $P(h = 1)$) is equal to the initial mutant fraction that was present, regardless of the value of δ.

These findings are interesting as it means that if an experiment is set up with cells initialised at $h = 0.5$, and single cell heteroplasmy values are measured some weeks later, then consistently finding more cells homoplasmic in wildtype than mutant does not necessarily imply a selection advantage of the former. In fact, mean cellular heteroplasmy values remain constant at $h = 0.5$, and most cells have heteroplasmy values exceeding 0.5 (Figure 5.1 F, B).

The observed skew can be explained by noting that mutant and wildtype species have different carrying capacities, which we define as the steady state copy number present in a cell homoplasmic in a particular species. Thus, mutants and wildtypes have carrying capacities of N_{ss}/δ and N_{ss}, respectively (Equation 1.3) (unless $\delta \leq 0$, in which case a mutant carrying capacity must be explicitly introduced, as shown in Figure 5.2C). This difference induces a drift along the steady state line towards the species with higher carrying capacity [328], though the dynamics in heteroplasmy space can be proven to be purely diffusive [328].

The intuition behind these dynamics is as follows. Due to the lack of selection, we expect an equal number of cells to fixate on mutant and wildtype species, but a large difference in carrying capacity means that, when $\delta < 1$, fewer events are required to reach $h = 0$ than $h = 1$ (Figure 5.2A). We then might expect a drift along the steady state line towards mutants to ensure equal fixation, as illustrated in Figure 5.2A. Due to the nonlinear mapping between (w, m)-space and heteroplasmy space (Figure 5.2B), a small distance in (w, m)-space does not necessarily correspond to a small distance in h-space. As illustrated in Figure 5.2B, though only few events are required to go from $h = 0.5$ to $h = 0$, the 'heteroplasmy distance' is still equally large as moving towards $h = 1$. The heteroplasmy dynamics can be described by diffusion with an h-dependent diffusion coefficient, being larger for low h values. Figures 5.2A,B are purely shown to gain intuition and do not provide a proof of these mechanisms. However, simulations of a 1-dimensional random walk with a position-dependent diffusion coefficient can qualitatively match the asymmetry in boundary fluxes shown in Figure 5.1C (Section C.1.1).

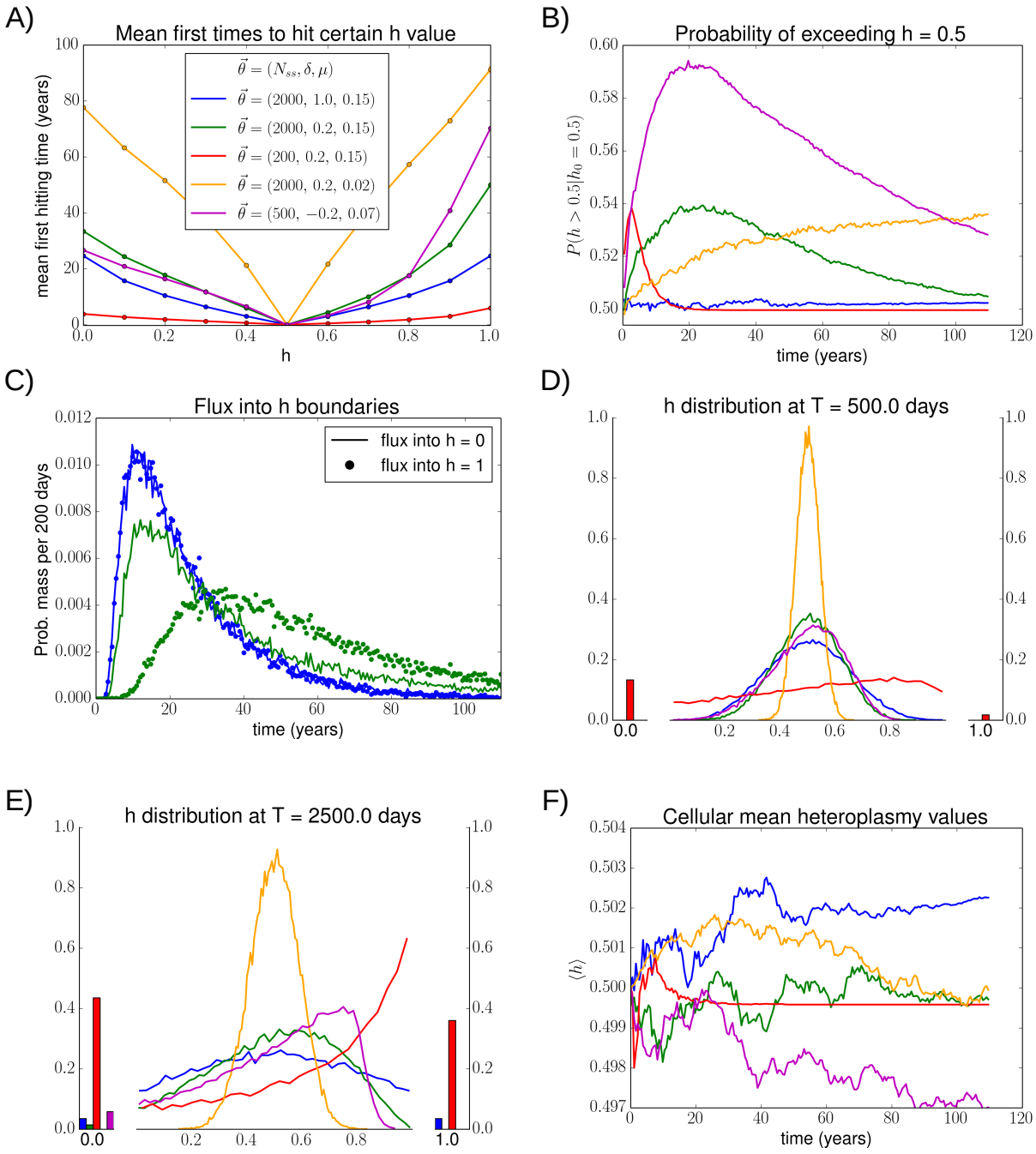


Figure 5.1: Difference in carrying capacity induces heteroplasmy assymetry. We performed Gillespie simulations (5×10^4 repeats) using the linear replication rate feedback control $\lambda(w, m) = \mu + c_1(N_{ss} - (w + \delta m))$ with constant death rate μ. The legend shown in (A) applies to all subfigures. **A)** Starting simulations at $h_0 = 0.5$, the mean first hitting times are shown for various h values (error bars are too small to be visualised). When $\delta \neq 1$ one of the boundaries tends to be hit sooner than the other. **B)** This shows the probability of passing the initial heteroplasmy of 0.5, which first increases and then decreases, unless $\delta = 1$ (blue). **C)** The flux (i.e. probability mass per time unit) into the absorbing boundaries $h = 0$ and $h = 1$ are shown. They are identical if $\delta = 1$, but when $\delta < 1$ the flux through $h = 0$ is largest for short times, but for longer times flux through $h = 1$ is larger. Only two parameter sets are shown for clarity, others show similar behaviour. **D) + E)** heteroplasmy distributions at 500 and 2500 days. The distribution is normal if $\delta = 1$ (in which case there is symmetry in w and m) but asymmetric otherwise. **F)** Cellular mean heteroplasmy values remain almost constant.

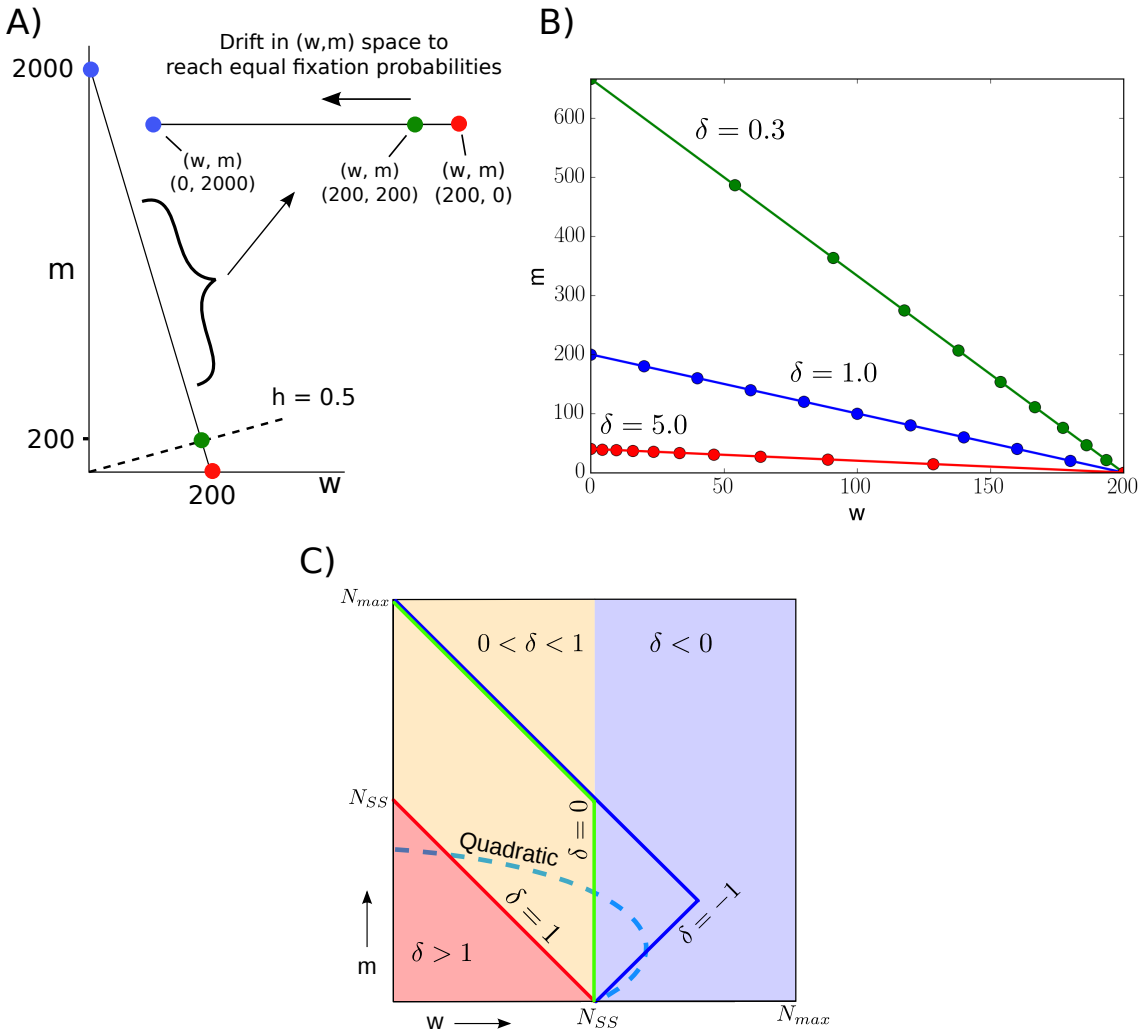


Figure 5.2: A nonlinear mapping between heteroplasmy and copy number space. A) This schematic illustrates a steady state line with $\delta = 0.1$ which, when starting at the green dot at $h = 0.5$, shows that the copy number distance to $h = 1$ is larger than to $h = 0$. A drift along the steady state line is required to obtain equal fixation probabilities at long times. **B)** Equally spaced heteroplasmy values $h = 0.1, 0.2, \cdots, 1.0$ are shown (dots) along the steady state lines of controls with different values of δ. When $\delta < 1$ copy number differences are higher between $h = 1.0$ and $h = 0.9$ than between $h = 0$ and $h = 0.1$. **C) Partitioning the regions in (w, m)-space according to the value of δ.** This cartoon is an extension of Figure 1.3 in the introduction. The parameters N_{ss} and N_{max} denote the steady state and maximum mtDNA copy numbers, respectively. An example steady state line of a quadratic control is shown (dashed line), which allows copy numbers to change non-monotonically with heteroplasmy.

When $\delta > 1$ all the observations above are reversed, e.g. the heteroplasmy distributions in Figure 5.1D, E are skewed in the opposite direction, and drift exists along the steady state line towards the wildtype species. A setting with negative or zero values of δ is more complicated, as the steady state line does not intersect with the $h = 1$ axis, and fluctuations along the line quickly lead to diverging populations. These problems can be overcome by introducing a maximum mtDNA copy number N_{max}, caused by e.g. volume constraints and resource limitations (Figure 5.2C). The results with $\delta < 0$ in Figure 5.1 assume $N_{max} = 10^4$. We have not investigated the effects of this extra parameter on heteroplasmy statistics, and therefore one needs to be careful comparing these simulations with ones using $\delta > 0$.

In conclusion, *a drift in copy number space can exist without explicit selection and is induced by a difference in carrying capacities between species. Despite this drift, mean cellular heteroplasmy values remain constant.* What are the biological consequences of these findings? Most mtDNA mutations that expand during ageing correspond to $\delta < 1$ (Section 5.2.2), a regime in which total mtDNA copy numbers increase with heteroplasmy. The skew in heteroplasmy distribution for these type of mutations results, in the short term, in a relatively large fraction of cells crossing a high heteroplasmy threshold. Though this 'bias' disappears at long times, the damage may have already been done as the severity of pathology depends on the amount of threshold crossing. It is the heteroplasmy *distribution* that determines the extent of dysfunctions, and a constant mean cellular h may be misleading. The effects we have observed are small and more care is required to determine their contribution to cellular dysfunction, an interesting future avenue of research.

5.2.1.2 Analytical methods can be used to probe small δ regimes

As seen in Chapter 4, mean mutant and wildtype copy numbers can change over time, even when trajectories are initialised in deterministic steady states. This is clear from the example shown in Figure 5.2A: at $t = 0$ we have $\langle m(0)\rangle = \langle w(0)\rangle = 200$, but for long times, when fixation of one species has occurred, $\langle m(t_{long})\rangle = 1000$ and $\langle w(t_{long})\rangle = 100$. A change in mean copy number is not predicted by deterministic analysis, nor by the linear noise approximation [101] (Chapter 4), but *is* predicted by considering higher order terms in the system size expansion (SSE) (Section C.1.5). The linear changes predicted by these higher order terms are accurate for short times, though cannot describe saturating behaviours which arise due to fixation (Section C.1.5).

When mutants are not sensed at all ($\delta = 0$), their numbers can in theory fluctuate off to infinity. The result is a constant wildtype but exponentially increasing mutant mean (Figure C.2) (with mean cellular heteroplasmy still constant). This exponential increase can be described by the higher order SSE if the linear term in $\langle m(t) \rangle$ is interpreted as the first term of a Taylor expansion; results agree well with stochastic simulations (Section C.1.5). Incorporating a maximum copy number leads to saturation of $\langle m(t) \rangle$, though an initial exponential increase is still present (Figure C.2D). Thus, *values of δ close to zero lead to very large increases in mean mutant copy numbers* which in turn increases tissue homogenate heteroplasmy values while cellular mean heteroplasmy remains constant (Section 4.2.1.1). Increases in homogenate heteroplasmy were found previously in a setting similar to our low-δ setting [1, 2].

In the case of $\delta = 0$, wildtype dynamics no longer depend on m and this partial decoupling allows for analytical treatments (Section C.1). Firstly, wildtype steady state distributions can be calculated numerically giving excellent agreement with stochastic simulations (Figure C.3). Secondly, time-varying solutions for mutant mean and variance can be approximated by describing wildtype dynamics by an Ornstein Uhlenbeck process (mean-reverting diffusion) and approximating wildtype mean and variance using a stochastic Lotka-Volterra (LV) model (Sections C.1.4 and C.1.2). Results agree well with simulations and predict that $\langle m(t) \rangle$ follows a log-normal distribution (Section C.1.2).

One interesting finding of these analytical treatments is that the stochastic and deterministic mean steady state wildtype values values do not agree, the former being slightly lower. A stochastic LV model predicts the following stochastic mean value:

$$\langle w \rangle_{ss} = \frac{3}{4} w_{ss} + \frac{1}{4} \sqrt{w_{ss}^2 - \frac{8\mu}{c_1}} \tag{5.1}$$

where w_{ss} denotes the deterministic steady state (Equation (C.27)). Because the replication and degradation rates are identical only at the deterministic steady state, the stochastic expected replication rate is slightly higher than the degradation rate: this is the main reason for the exponential increase in $\langle m(t) \rangle$. A very similar equation for $\langle w \rangle_{ss}$ is predicted by the higher order SSE (Section C.1.5.1).

Biologically, a setting with δ being exactly zero seems unrealistic (as it is unlikely mutant molecules are not sensed in any way), but it may be possible to Taylor expand the obtained solutions around $\delta = 0$ to obtain insight into a system with $\delta = \epsilon \ll 1$. This particular regime is very relevant as many mtDNA deletion mutations are experimentally observed at high copy numbers (Section 5.2.2.1), corresponding to low δ values.

5.2.1.3 MtDNA exchange: a deterministic setting predicts small changes in mean heteroplasmy

We here investigate the consequences of allowing cells, which have their own internal nuclear feedback control, to exchange mtDNA molecules with their neighbours. We mainly show results for 2-cell systems but also provide simulation results for 3- and 5-cell systems. This setting of sharing/exchange of components is relevant in various biological systems, and is a key element of the evolution of cooperation [337], examples of which are the production of 'public goods' in yeast [338] and bacteria [339].

In humans, mtDNA exchange likely occurs in skeletal muscle fibres. These fibres are long multinuclear cells, and it seems reasonable to assume that they contain local mtDNA control regions. This is supported by findings of isolated patches in which both heteroplasmy and copy numbers are high, while they are normal outside these patches; it is therefore not the entire fibre's mtDNA population that is affected by a local presence of mutant molecules. We argue that single muscle fibres can be partitioned into 'cells' and assume a feedback control acts on the level of these cells. Because fibres are continuous, mtDNAs are able to move from one cell to another. Expansion of mtDNAs along fibres was proposed previously [340] and is supported by findings that regions with high mutant levels tend to spread out along the fibre over time [85, 341], with the same mutant species being found in the entire region [21, 85, 341]. The mutant molecules must therefore have moved to neighbouring cells because it is unlikely that the same mutation event occurred multiple times in different sections of the same fibre region.

We assume a linear feedback control in each individual cell ($\lambda(w_i, m_i) = \mu + c_1(N_{ss} - (w_i + \delta m_i))$ where i denotes the ith cell), as well as a constant rate γ of mtDNA exchange between cells. The whole system is considered to have fixated on mutants or wildtypes if all cells reach $h = 1$ or $h = 0$; an illustration is provided in Figure 5.3.

Deterministically, the dynamics in a 2-cell system are governed by the following set of ODEs:

$$\begin{aligned}
\frac{dw_1}{dt} &= w_1 c_1 \Big(N_{ss} - (w_1 + \delta m_1) \Big) + \gamma(w_2 - w_1) \\
\frac{dm_1}{dt} &= m_1 c_1 \Big(N_{ss} - (w_1 + \delta m_1) \Big) + \gamma(m_2 - m_1) \\
\frac{dw_2}{dt} &= w_2 c_1 \Big(N_{ss} - (w_2 + \delta m_2) \Big) + \gamma(w_1 - w_2) \\
\frac{dm_2}{dt} &= m_2 c_1 \Big(N_{ss} - (w_2 + \delta m_2) \Big) + \gamma(m_1 - m_2)
\end{aligned} \tag{5.2}$$

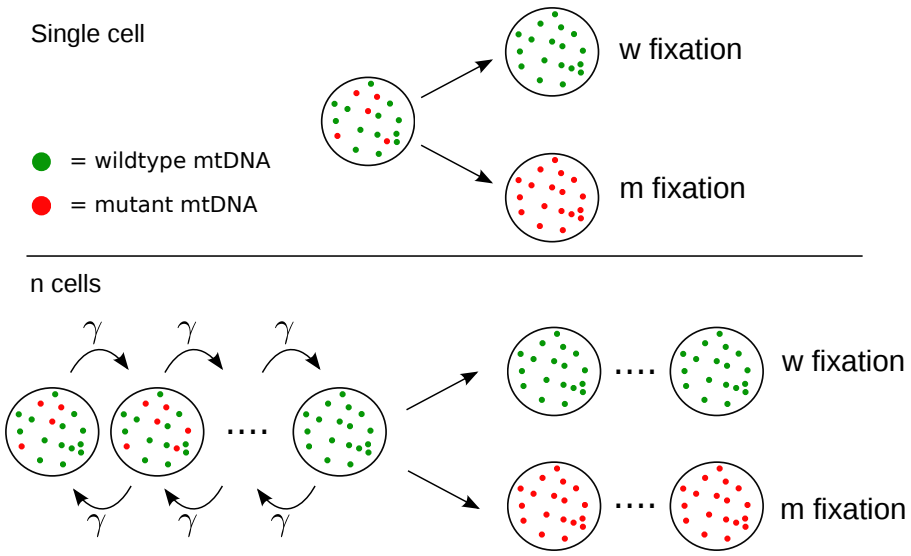


Figure 5.3: A model of interacting cells, allowing mtDNA exchange. We extend the single cell model to an n-cell model in which mtDNAs are exchanged at a fixed rate γ. Complete fixation has occurred when an mtDNA species has reached homoplasmy in all cells.

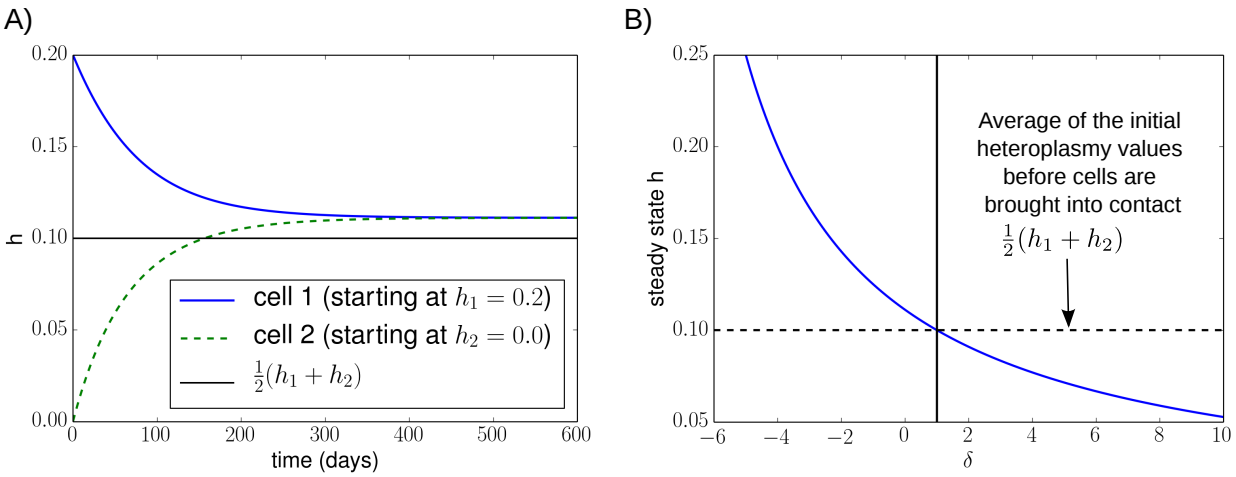


Figure 5.4: A deterministic setting predicts small changes in mean cellular heteroplasmy due to differences in carrying capacity. A) When two cells are initialised in a deterministic steady state with heteroplasmy values $h_1 = 0.2$, $h_2 = 0$, allowing intercellular mtDNA exchange leads to an increase (using $\delta = 0$) in mean heteroplasmy. Trajectories are obtained numerically by solving Equations (5.2). Other parameters used are $\gamma = 0.007, c_1 = 10^{-5}$ and $N_{ss} = 5000$. **B)** The final steady state heteroplasmy value is shown as a function of δ using Equation (5.3); parameters used are identical to Figure (A). Mean heteroplasmy is only conserved if $\delta = 1$ (vertical line).

Denoting $w_{i,ss}$ and $m_{i,ss}$ as the wildtype and mutant steady state copy numbers in cell i, the steady state of the system defined by equations (5.2) satisfies $w_{1,ss} = w_{2,ss}$, $m_{1,ss} = m_{2,ss}$ and $w_{i,ss} + \delta m_{i,ss} = N_{ss}$. Here we have assumed that the same mutant species is present in both cells; we later relax this condition and allow *de novo* mutations over time.

If two independent cells in steady state with heteroplasmies h_1 and h_2 are brought into contact with one another, the final deterministic steady state heteroplasmy value (present in both cells)

can be straightforwardly derived and is given by:

$$h_{ss} = \frac{h_1(\delta h_2 + 1 - h_2) + h_2(\delta h_1 + 1 - h_1)}{\delta h_2 + 1 - h_2 + \delta h_1 + 1 - h_1}$$
$$\equiv \frac{1}{\theta_1 + \theta_2}(\theta_1 h_2 + \theta_2 h_1) \tag{5.3}$$

where $\theta_i = 1 - h_i(1 - \delta)$. We thus find that the new heteroplasmy value forms a weighted average of h_1 and h_2. When $\delta = 1$, the weights are identical and $h_{ss} = \frac{1}{2}(h_1 + h_2)$. However, when $0 < \delta < 1$ a larger weight is given to the larger heteroplasmy value, meaning that average heteroplasmy has slightly increased (Figure 5.4A, B). When $\delta > 1$, the lower heteroplasmy value is weighted more heavily. The change in $\langle h \rangle$ is driven by the difference in carrying capacities. For example, if $\delta < 1$ the high-heteroplasmy cell has higher copy numbers, leading to a relatively large flux into the low-heteroplasmy cell. Equation (5.3) does not hold for all $\delta < 0$ as the weights may become negative. In conclusion, we make the straightforward observation that *during cell equilibration, mean heteroplasmy can increase, decrease or stay constant in a deterministic setting, depending on the difference in carrying capacity between the different species.*

5.2.1.4 MtDNA exchange: a stochastic setting introduces selection for low-δ mutants

Extreme regimes: a limited increase in mean heteroplasmy

In a stochastic description, mean cellular heteroplasmy also changes and the rate of change depends on the relative time-scales of mtDNA exchange between cells and mtDNA turnover within cells. In the limit of very small γ, it is assumed that both cells reach fixation on either species before an mtDNA molecule is exchanged. Note that there is no real interaction between the cells as they both fixate independently. A wildtype molecule entering a fully mutant cell has a probability of $\sim \delta/N_{ss}$ (its initial fraction) to fixate, whereas a mutant entering a wildtype cell has a fixation probability of $\sim 1/N_{ss}$. A series of coin flips now determines the overall fixation probabilities when starting with two cells at heteroplasmies h_1 and h_2, giving:

$$\langle h(t_{long}) \rangle = P(\text{mutant fixation at long times})$$
$$= \frac{(\delta + N_{ss})(h_1 + h_2 - h_1 h_2) + \delta^2 h_1 h_2 (1 + N_{ss})}{\delta^2(1 + N_{ss}) + \delta + N_{ss}} \tag{5.4}$$

where t_{long} refers to a long-time limit at which all pairs of cells have fixated (derivation given in Section C.2.1).

Equation (5.4) has a maximum at $\delta = 0$, namely $\langle h(t_{long})\rangle_{max} = h_1 + h_2 - h_1 h_2$ (Section C.2.1). Therefore, *in the limit of very slow mtDNA exchange, mean cellular heteroplasmy can never surpass the sum of the individual heteroplasmies before the two cells were brought into contact.* For example, when a cell with $h_1 = 0.2$ is connected to a cell homoplasmic in wildtype, the mean cellular heteroplasmy of the combined system cannot surpass 0.2. In the other extreme limit, when rates of mtDNA exchange are much larger than intracellular dynamics, the system behaves as a single cell with an effective population size twice that of the individual cells [328]; as expected, values of $\langle h(t)\rangle$ remain very close to $\frac{1}{2}(h_1 + h_2)$.

Intermediate regimes: stochastic fluctuations drive up heteroplasmy mean

In the intermediate regime, when rates of mtDNA exchange and turnover are more compatible, bringing two cells into contact initiates the following sequence of events: i) the high-heteroplasmy cell experiences a decrease in mean heteroplasmy, whereas the other cell experiences an increase, ii) once h_1 and h_2 have equilibrated, mean cellular heteroplasmy (which is now present in both cells) *continues* to change until saturation is reached due to complete fixation. We stress that this latter observation, which we refer to as a 'stochastic drive' in heteroplasmy, is in contrast both to the deterministic setting (in which, as soon as the two cells have equilibrated their heteroplasmy values, $\langle h\rangle$ remains constant) and a setting with independent cells (in which case $\langle h\rangle$ always remains constant), and may have implications for mutant accumulation rates during ageing (Section 5.2.3, Figure 5.8). We stress that though changes in $\langle h\rangle$ were observed in a similar system previously [328], we believe that no account of the stochastic drive we detect was provided.

When mutants have higher carrying capacity, $\langle h(t)\rangle$ increases after equilibration and we observe that, unlike in the small-exchange limit, *cellular mean heteroplasmy values can surpass the sum of the initial heteroplasmies when mtDNA exchange and turnover rates are comparable, and can increase even when negative mutant selection is present* (Figure 5.5A, C). The effects can be large, e.g. initializing 2 cells with $h_1 = 0.1$ and $h_2 = 0$ can lead to a four-fold increase in $\langle h(t)\rangle$ (from 0.05 to 0.2) (Figure 5.5A). Other parametrisations, however, show much smaller change in $\langle h(t)\rangle$ (Figure 5.5B), meaning care must be taken in interpreting the results. We discuss biologically relevant parameters in Section 5.2.2.3.

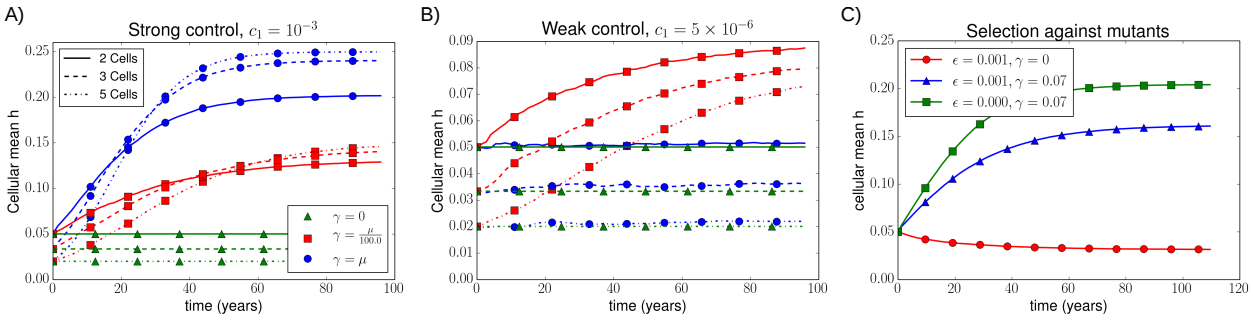


Figure 5.5: Stochastic dynamics can induce large increases in mean cellular heteroplasmy, even in the presence of negative mutant selection that otherwise acts to lower mean heteroplasmy. A) Stochastic simulations of a multicellular system (10^4 repeats) show mean cellular heteroplasmy increasing ($\delta = 0.1$) over time for various values of γ. When more exchanging cells are simulated, $\langle h(t) \rangle$ is higher at long times. One cell is initialised at $h = 0.1$, the rest at $h = 0$. $\mu = 0.07$ was used. Decreases in $\langle h(t) \rangle$ are expected when $\delta > 1$. **B)** Similar to Figure (A) except that a weaker control strength (smaller c_1) is used. Unlike the strong-control setting, a smaller exchange rate gives larger increases in $\langle h(t) \rangle$. **C)** Negative selection against mutants is introduced in a 2-cell simulation by letting wildtype and mutant death rates be μ and $\mu(1+\epsilon)$ with $\epsilon \geq 0$, respectively. Both without (green) and with a sufficiently small (blue) negative mutant selection, $\langle h(t) \rangle$ increases, whereas the negative selection would induce a decrease in heteroplasmy without mtDNA exchange (red). Other parameters are $\delta = 0.1$, $c_1 = 10^{-3}$ and $N_{ss} = 500$.

We compared 2-cell simulations with 3-cell and 5-cell simulations where each time all cells are initialised at $h = 0$ except for one cell at $h = 0.1$. As expected, when more cells are included $\langle h(t) \rangle$ is lower for short times (as e.g. fast equilibration leads to $\langle h \rangle = \frac{1}{3}\sum_{i=1}^{3} h_i = 0.033$ in 3 cells vs $\frac{1}{2}\sum_{i=1}^{2} h_i = 0.05$ in 2 cells). However, once appreciable heteroplasmy values are reached, the stochastic drive in $\langle h(t) \rangle$ is exaggerated and *final mean heteroplasmy values reach higher values when more cells are allowed to exchange mtDNAs (Figures 5.5A,B)*, as long as the rate of increase of $\langle h(t) \rangle$ is non-negligible.

An intuitive reason for the increase in $\langle h(t) \rangle$ when $\delta < 1$ is that whenever a fluctuation in h occurs in one cell, equilibration of heteroplasmies slightly increases the mean as it does deterministically (Figure 5.4A). An increasing $\langle h(t) \rangle$ is then the result of many stochastic up and down fluctuations. Perturbing the deterministic steady states by randomly introducing small (symmetric) increases and decreases in h indeed induces increases in $\langle h(t) \rangle$, where these increases are faster with larger perturbations (Figure 5.6A). This suggests a larger heteroplasmy variance might lead to faster changes in $\langle h(t) \rangle$, which is also seen in the stochastic system (Figure 5.6B). Because at long times h is either 0 or 1, the long-time variance can be written as $\mathrm{var}(h) = \langle h \rangle (1 - \langle h \rangle)$, meaning that we do indeed expect the curves in Figures and 5.6B and 5.5A to show the same ordering at saturation.

The extent to which $\langle h(t) \rangle$ increases or decreases depends on a subtle interplay between rates of mtDNA exchange, turnover, as well as the feedback control strength and δ. Some observations we made are: i) a tighter control (high c_1) leads to larger increases in $\langle h(t) \rangle$ (Figures 5.5A,

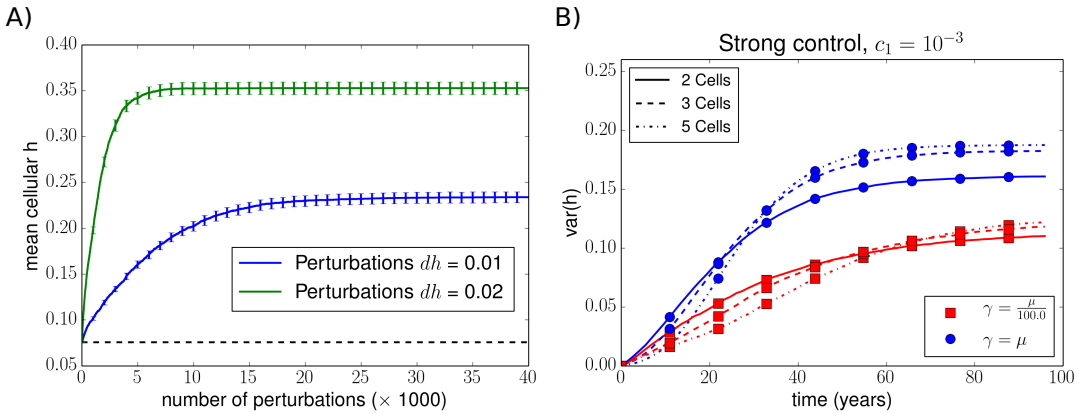


Figure 5.6: Stochastic heteroplasmy fluctuations induce changes in mean, which are larger when heteroplasmy variance is high. A) The deterministic system is perturbed as follows: i) two cells are initialised in steady state with heteroplasmies 0.1 and 0.05, ii) the final equilibrated h_{ss} is calculated using Equation (5.3), iii) a perturbation $+dh$ or $-dh$ (with equal probability) is applied to one cell, followed by equilibration, iv) if both cells reach $h < 0.001$ or $h > 0.999$ then we assume fixation at $h = 0$ or $h = 1$, respectively, after which the simulation is terminated. The last two step are repeated. Mean heteroplasmy increases over time and does so faster for larger dh (the observed saturation is caused by fixation). The dashed line indicates mean heteroplasmy without any perturbations. Error bars denote s.e.m. $(5000$ repeats$)$. **B)** Heteroplasmy variances are shown using the same simulations as presented in Figure 5.5. Note the similarity between these mean and variance simulations.

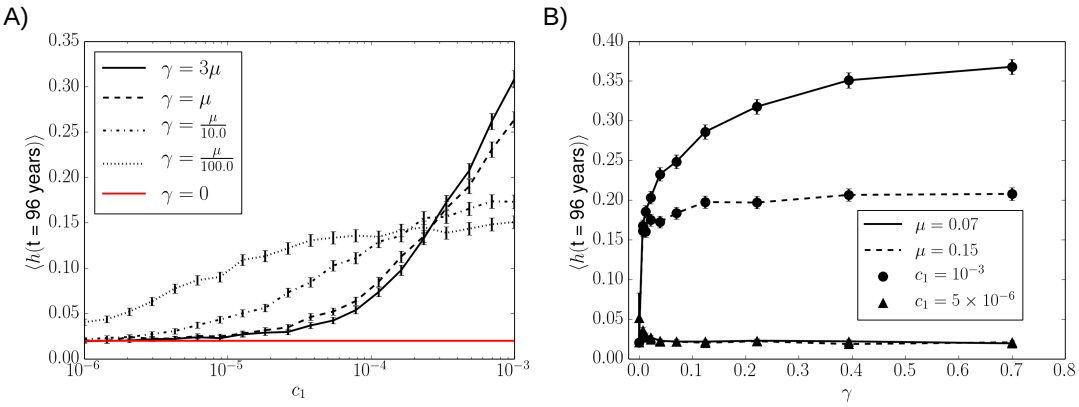


Figure 5.7: Investigating the dependence of heteroplasmy mean on model parameters A) The mean cellular heteroplasmy at long times ($t = 96$ years) is highest for a strong control (high c_1). Here we used 5 cells and show $\langle h\rangle = \frac{1}{5}\sum_i \langle h_i\rangle$ with $i = 1, \cdots, 5$ denoting the i-th cell. We note that not all simulations reached saturation at 96 years. We used $\mu = 0.07$, $\delta = 0.1$. **B)** Long-time steady state heteroplasmies (in a 5-cell simulation) can be an increasing or decreasing function of the ratio γ, depending on the control strength c_1. For a high degradation rate (i.e. higher turnover) μ, the increase in heteroplasmy is lower. $\delta = 0.1$ was used.

B and 5.7A), ii) the magnitude of c_1 can determine whether the change in $\langle h(t)\rangle$ is higher or lower for high or low γ; for example, the long-time mean heteroplasmy increases with γ for a strong control, but decreases for a weak control (Figures 5.5A,B and 5.7A, B), and iii) a larger degradation rate μ (i.e. larger turnover rate) tends to decrease $\langle h(t_{long})\rangle$ at fixed γ (Figure 5.7B). The absolute change in $\langle h(t)\rangle$ is likely some function of all parameters involved and though we currently do not know this function, some speculations on this topic are made in Section C.2.2.

Finally, we simulated an ageing tissue by initializing all cells at $h = 0$ and allowing mutants (with $\delta = 0.3$) to occur during replication. We observe that the more cells are connected, the faster the rate at which mean heteroplasmy (the mean taken over all cells) increases (Figure 5.8A). Though the initial rate at which mutants reach a high heteroplasmy threshold is lowest in the 3-cell simulation, it increases quickly and eventually surpasses that of the 1- and 2-cell systems (Figure 5.8B). Therefore *exchange of mtDNAs protects the population from mutant accumulation in the short term, but leads to more high-heteroplasmy cells in the long term when* $\delta < 1$. The delay in accumulation may be due to wildtype influx of neighbouring cells, and the eventual higher mutant levels are a combination of the stochastic drive observed earlier, as well as the effective higher mutation rate (as mutations in any one of the cells has a chance of expansion). Mutants with $\delta > 1$ will have less chances of expansion for all times.

In all previous simulations we used a single type of mutant with a single δ value. However, at any time during ageing a mixture of different mutant types may be present. We investigated this possibility in the simple setting of each mutation having two possible δ values with equal probability, namely $\delta = 1$ or $\delta = 0.1$. Without any selection or mtDNA exchange, we expect to observe $\langle\delta\rangle = 0.55$ in cells with non-zero heteroplasmy, as is indeed the case (Figure 5.8C). However, mtDNA exchange leads to lower values of $\langle\delta\rangle$ (Figure 5.8C), meaning that *mutant species with low values of* δ *preferentially expand during ageing without an explicit selection advantage, and do so to a larger extent when more interacting cells are present.*

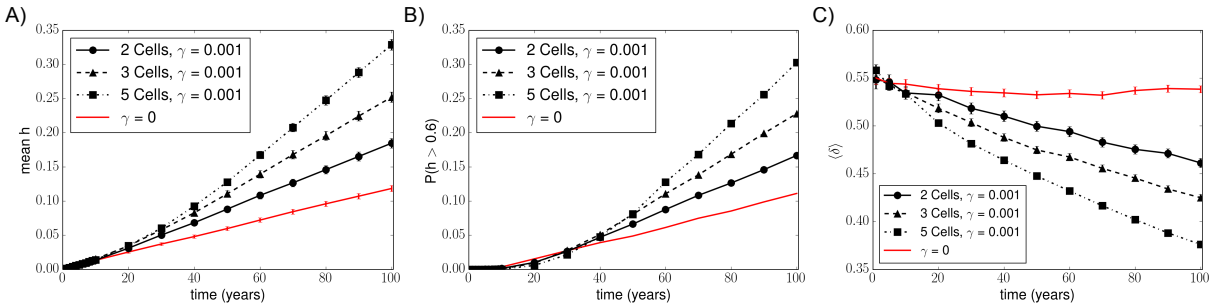


Figure 5.8: MtDNA exchange induces higher mean heteroplasmy and preferential mutant expansion during ageing. A) We compared mean heteroplasmy levels (here defined as $1/n \sum_i h_i$ with n the number of interacting cells) during ageing between i) single cells without interactions, and allowing mtDNA exchange between ii) 2 cell, iii) 3 cells, or iv) 5 cells. All cells are initialised at $(w, m) = (500, 0)$ and a mutation probability $P_{mut} = 5 \times 10^{-5}$ is used (denoting the probability that a wildtype replication event results in mutation). Other parameters used are $\mu = 0.07$ day^{-1}, $c_1 = 2.9 \times 10^{-5}, N_{ss} = 500$ and $\delta = 0.3$. Stochastic Gillespie simulations are performed with 5×10^4 repeats. **B)** The probability of crossing the heteroplasmy threshold $h = 0.6$ (for one individual cell) is shown for the system system in figure (A). The 5-cell exchange system starts off lowest but then quickly surpasses the others. **C)** Low-δ mutations preferentially expand during ageing as observed by a drop in $\langle\delta\rangle(t)$ (which denotes the mean over all cells). Every new mutation was assigned either $\delta = 0.1$ or $\delta = 1$ with equal probability. The value of $\langle\delta\rangle$ corresponds to the most abundant mutant.

To summarise, we found that allowing neighbouring cells to exchange their mtDNA molecules can qualitatively alter heteroplasmy dynamics. This finding, as well as being interesting in itself, may have biological implications for the rate of mutant accumulation in ageing tissues, as discussed further in Section 5.2.3. Our main findings of this section are: a 'neutral' model, with no explicit selective advantage for either species, can i) lead to systematic changes in mean cellular heteroplasmy, ii) induce heteroplasmy increases even in the presence of negative mutant selection, and iii) can lead to certain types of mutants preferentially expanding during ageing. These results all stem from a difference in carrying capacity between distinct types of mtDNA.

5.2.2 Connecting with reality: parameter estimations and biological interpretations

5.2.2.1 Mapping known mtDNA mutations onto values of δ

Here we investigate whether our linear model can account for experimentally observed mtDNA dynamics. First, we summarise the effect δ has on cellular mtDNA copy numbers (Table 5.1, Figure 5.9) by considering five ranges of δ: i) $\delta > 1$, ii) $\delta = 1$, iii) $0 < \delta < 1$, iv) $\delta \approx 0$, and v) $\delta < 0$. Possible physiological advantages and disadvantages corresponding to these ranges, and what kind of mutant characteristics could give rise to them, are also discussed in Table 5.1. The last column of Table 5.1 indicates changes in wildtype (w) and total (T) copy numbers that are expected to be observed when comparing a heteroplasmic cell with a cell homoplasmic in wildtype. For example, a high-heteroplasmy cell with $\delta = 1$ is expected to show no change in total copy number but a reduction in wildtype copy numbers.

Second, we aimed to link existing mtDNA mutations to the defined ranges of δ. We stress that we did not perform an exhaustive literature search to classify a large set of mutant species, but instead linked at least one mutation with each range (Table 5.2). We note that the majority of mtDNA mutations we investigated were associated with increases in copy number, consistent with $\delta < 1$ which would lead to their preferential expansion during ageing (Figure 5.8).

Of course a linear feedback model will not be the only model that is able to qualitatively account for the observed data. In fact, the experimental linkage provided holds for the relaxed replication model [1, 2] which also predicts straight steady state lines in (w, m)-space whose slope is influenced by a parameter denoting mutant contribution to replication rates. One advantage of our modelling approach is that we are able to decouple the feedback control strength (c_1) from the mutant feedback contribution (δ), whereas the relaxed replication model

[1, 2] cannot. We do not claim that our model represents the 'true' feedback control which, if one can even define such a mechanism, is likely to be highly complicated. However, we believe our model provides a good first order approximation of the underlying complex dynamics and, importantly, allows for predictions and intuitive reasoning.

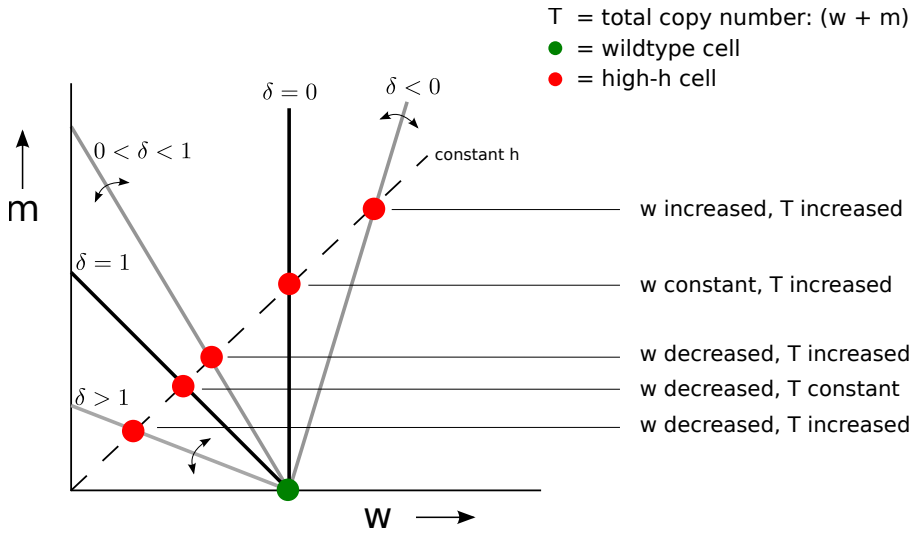


Figure 5.9: Mapping mtDNA mutations to values of δ. This figure complements Table 5.1 and explains the expected changes in wildtype copy number w and total mtDNA copy number $T = w + m$ as provided in the table. To find the value of δ of a particular mtDNA mutation, one can measure the values of w and T in a cell heteroplasmic in the mutation of interest (red) relative to a fully wildtype cell (green). For example, if $\delta = 0$ the mutant cell is expected to have, relative to the wildtype cell, a similar wildtype copy number (because w is constant along the deterministic steady state line) but a higher total copy number.

	Hypotheses on the advantages, disadvantages and mechanisms of having mutations within the indicated ranges of δ.	Changes w , T
$\delta > 1$	**Advantage:** Mean cellular heteroplasmy will tend to decrease when intercellular mtDNA exchange is possible. If $\delta \gg 1$ then cells with high heteroplasmy may not have sufficient numbers of total mtDNA to survive; selection on cellular level may occur, favouring cells with low heteroplasmy. **Disadvantage:** Might lead to higher apoptosis rates and relatively high mutant fixation for short times (Figure 5.1 with the roles of w and m reversed). **Mechanism:** Mutants producing excessive ROS may induce lowered mtDNA replication rates with increasing m.	Δ T $\downarrow$ Δ w $\downarrow$
$\delta = 1$	**Advantage:** Stable mtDNA copy numbers are ensured (Figure 5.3A). **Disadvantage:** If mutants are pathological, decreases in w as h increases may be undesirable. **Mechanism:** Mutants and wildtypes contribute identically to the quantity that is fed back on.	Δ T - Δ w $\downarrow$
$0 < \delta < 1$	**Advantage:** If mutants are deficient in their energy production, higher copy numbers are required to meet demands; $0 < \delta < 1$ ensures this is true. **Disadvantage:** Leads to high mutant copy numbers at high heteroplasmy values, and mean cellular h increases if intercellular mtDNA exchange is possible (Figures 5.5 and 5.8). **Mechanism:** Mutants contribute less to the quantity that is fed back on. For example, if ATP levels or the size of the mRNA pool are important in the cellular feedback, this δ range occurs if mutants produce less energy or generate less mRNA molecules.	Δ T $\uparrow$ Δ w $\downarrow$
$\delta \approx 0$	**Advantage:** A stable wildtype population is maintained (Figure 1.3). **Disadvantage:** This situation is unstable leading to very high mutant copy numbers ('runaway dynamics'), until some maximum is reached. Such high copy numbers may introduce extra dysfunctions. **Mechanism:** Mutants do not contribute to the quantity that is fed back on. For example, if ATP levels or the size of the mRNA pool are important in the cellular feedback, this δ range occurs if mutants produce no net ATP or do not generate mRNA molecules.	Δ T $\uparrow$ Δ w -
$\delta < 0$	**Advantage:** A negative value for δ ensures that wildtypes copy numbers increase with heteroplasmy (for low levels of heteroplasmy, Figure 1.3) which may be required to compensate for the presence of very deficient mutant species. **Disadvantage:** This situation is unstable, leading to very high total copy numbers ('runaway dynamics'), until some maximum is reached. Such high copy numbers may introduce extra dysfunctions. **Mechanism:** If mutants are energy sinks, consuming more energy than they produce, the cell may want to upregulate mtDNA replication to increase energy production. If mutants produce excessive ROS, the cell might interpret this as a dysfunction in its mitochondria and could respond by increasing total mtDNA replication rates.	Δ T $\uparrow$ Δ w $\uparrow$

Table 5.1: A breakdown of the different linear feedback regimes. This table summarises possible advantages and disadvantages of particular δ regimes, and speculates on how various mutant characteristics may have given rise to these regimes. We also show an overview of the changes in total copy number (ΔT) and wildtype copy number (Δ w) with increasing heteroplasmy: these quantities can increase ($\uparrow$), decrease ($\downarrow$) or remain constant (-). These changes are expected to be observed in heteroplasmic cells when compared to homoplasmic wildtype cells, allowing for the corresponding value of δ to be identified (as we did in Table 5.2).

Total copy number changes	Experimentally found mutations showing evidence for the indicated change in copy numbers (increased, decreased, or constant). Where possible, a more specific range of δ is given.
increased ($\delta < 1$)	$\delta < 0$
	C. elegans worms with high proportions of the large 3.1-kb deletion *uaDf5* were observed to have a slightly higher total mtDNA copy number than wildtype worms; wildtype copy number also slightly increased with increasing mutant copy numbers [278]. The worms harbouring the mutation generally had a larger spread in copy number values, indicating homeostatic control is stronger for wildtype mtDNAs [278]. A smaller 179-bp deletion *mptDf1* showed similar dynamics.
	Human skeletal muscle fibre sections with the m.3243A>G *MTTL1* point mutation showed stable wildtype copy numbers up until $\sim 80\%$ heteroplasmy, after which wildtype copy number increased $\sim$6-fold [104].
	$0 < \delta < 1$
	Human muscle fibres with the 4.9-kb common deletion, as well as a 2.3, 3.9, 4.5 and 7.1 kb deletion (associated with Kearns-Sayre syndrome or isolated ocular myopathy) showed very high mutant copy numbers almost always accompanied by a decrease of wildtype copy numbers [305].
	Human muscle fibres with the 4.9-kb common deletion showed an increase in total copy number as heteroplasmy increased, accompanied by a decrease of wildtype copy numbers [104].
	The point mutation m.10010T>C *MTTG* also led to larger total copy number and lower wildtype copy numbers in human muscle fibres with higher heteroplasmy levels [104].
	Human COX$^-$ muscle regions containing high levels of mtDNA deletion mutations were found to have higher total mtDNA copy numbers, and often lower wildtype copy numbers (compared to COX normal fibre regions) [85].
	$\delta < 1$ (either $\delta < 0$ or $0 < \delta < 1$)
	Increases in total copy number were seen in most tissues examined from MELAS patients harbouring the 3243A>G point mutation [304].
	A mutation interfering with the expression of complex I subunit ND6 caused excessive ROS production and led to a $\sim$3 fold increase in total copy number in mouse cybrid cells [324].
	qPCR performed on muscle samples of a patient with a large mtDNA deletion measured $\sim$ 9700 mtDNA molecules per diploid genome. In comparison, measurements in control samples were $\sim 1000-2000$. Another patient with the A8344G point mutation was found to have 4,245 mtDNA copies per diploid genome in muscle [342].
	The vast majority of human COX$^-$ fibres (most of which had a high percentage of mtDNA deletion mutations) showed increased mtDNA copy numbers as compared to COX normal fibres (up to 21-fold) [22].
decreased ($\delta > 1$)	In human leukocytes with the m.3243A>G *MTTL1* point mutation, a decrease in total mtDNA copy number was seen [343].
	Profound mtDNA depletion was found in muscle and kidney samples of patients with various deletion mutations. mtDNA copy numbers per diploid genome in muscle samples from three patients were 261 ± 45 (n = 3), 361 ± 18 (n = 2), and 26 ± 12 (n = 2) (compared to $\sim 1000 - 2000$ in controls) [342].
	$\sim 9\%$ of human COX$^-$ fibres (most of which had a high percentage of mtDNA deletion mutations) showed lower mtDNA copy numbers compared to adjacent normal COX fibres [22].
constant ($\delta \approx 1$)	Human osteosarcoma 143B cybrid cells with point mutation m.8993T>G were observed to have reduced heteroplasmy but constant total copy number [142].
	No consistent trend was found between heteroplasmy levels of the 3243A>G point mutation in human cybrid cells and mtDNA copy number [344].
	Total mtDNA copy number was observed to remain constant despite changes in heteroplasmy in cybrid HeLa cells [80].

Table 5.2: An overview of the effect of known mtDNA mutations on copy number levels. Here we map existing mutations onto our δ ranges (Table 5.1). Simultaneous measurements of wildtype and mutant copy numbers were not always performed, and therefore we split the different mutations in three main classes based on changes in total copy number, indicating more specific δ ranges when possible. We managed to link each of our five specified ranges to multiple mutations. Note that we can never be certain about the range of δ corresponding to a given mutant species, and our linear model is an approximation to more complicated behaviour; also, the changes in copy numbers may be due to other causes than a specific cellular feedback control.

5.2.2.2 Providing a target mutant load: skeletal muscle data predict low mutant accumulation rates

As mentioned in the thesis introduction (Section 1.4.2), the mutation probability used in mathematical modelling, P_{mut}, is chosen such that predicted mutant loads match the ones experimentally observed. Most models seem to use the following end-of-life targets for both humans and rodents: (5-10)% of cells must have reached a heteroplasmy level of $\geq 60\%$ [34, 36, 38]. We will refer to these two quantities as the threshold fraction and threshold value, respectively. We have various reasons to believe, as outlined in Box 5.1, that these target loads may be overestimating the actual load in post-mitotic tissues and therefore provide our own estimations based on skeletal muscle data.

We collected data from studies that simultaneously measure the threshold fraction and threshold value. We mainly focus on studies of skeletal muscle fibres of healthy mammals (which have been analysed in great detail in a variety of organisms) and we require that measurements were performed longitudinally along single fibres. Serial sections along fibres, rather than studying a single transverse section [19], give more information on the distribution of dysfunctional regions because of the mosaic structure of defective cells and because multiple mutated regions of varying lengths can exist along a fibre. Because we aim to study mtDNA dynamics in healthy subjects with age, we did not include studies involving patients with mtDNA diseases [340].

Summaries of the studies we included, which involve humans, rhesus monkeys and rodents, are provided in Table 5.3, Box 5.2 and its Figure 5.10. Briefly, hundreds of serial sections ($\sim$ 10µm) were cut along muscle fibres and stained for cytochrome *c* oxidase (COX) and succinate dehydrogenase (SDH) activities. COX negative regions identify mitochondrial dysfunction, and SDH activities indicate whether the original problem lies within the nucleus or represents an actual mtDNA dysfunction[†]. Abnormal fibre regions, i.e. regions containing mitochondrial dysfunctions, were shown to contain high levels ($> 90\%$) of deletion mutations, we therefore set our threshold value at 90%.

[†]Succinate dehydrogenase refers to complex II of the respiratory chain, the only complex fully encoded by the nucleus. Negative SDH activities indicate a nuclear defect, whereas normal or hyperactive activities (alongside negative COX activities) point towards mtDNA defects.

Box 5.1: Possible overestimations of mutant loads in aged subjects

Mathematical models of mtDNA dynamics during ageing often assume that in aged individuals, (5-10)% of cells have reached a heteroplasmy level of $\geq 60\%$ [34, 36, 38]. Where do these numbers come from? The threshold value of 60% is obtained from a study showing that a 5196 base pair mtDNA deletion mutation needs to accumulate to $> 60\%$ of the total mtDNA population before a reduction in COX activity is seen [80]. This result was obtained in cybrid HeLa cells and, as heteroplasmy threshold values are cell-type dependent [345], may not be representative of human or rodent post-mitotic tissues. For the threshold fraction of 5% [34, 36] (or even 10% [38]), three studies [19, 346, 347] are often cited. In the first study, the 5% threshold value represented the upper bound of a range of values, (0.1-5)% [19]. The second study found a maximum of 0.37% COX-negative fibres in human limb muscle over a large age range [346]. The last study did observe high percentages of COX^- muscle fibres ($\sim 40\%$) but, as explained later in this section, this does not mean that 40% of single cells show COX-deficiencies.
A sensitive mtDNA quantification method applied to mice revealed mutation loads two orders of magnitude lower than those obtained using polymerase chain reactions (PCR) [348], indicating that PCR artefacts may have played a role in earlier studies.

Box 5.2: Measuring heteroplasmy levels along skeletal muscle fibres

Taken together, the experimental studies summarised in Table 5.3 found that $\sim (0.1 - 1)\%$ of fibres contained abnormal regions (COX^- regions) at some point along their investigated length ($\sim$ 1000-2000µm). This percentage is very low compared to fibres of mtDNA disease patients, e.g. COX-negative regions in two patients carrying the 'common' deletion were present in 7% and 65% of sampled fibre sections [340]. In all studies in Table 5.3, deletion mutations were found in the abnormal regions but never in COX-normal sections of the same fibre. Abnormal regions were characterised by: i) very high mutant levels ($> 90\%$ and sometimes close to 100%), ii) high mtDNA copy numbers compared to normal fibre regions, iii) a single deletion mutation (rather than a mixture of different ones) being present in the entire region, iv) different deletion mutations being present in different abnormal regions, v) transition regions with relatively low mutant levels flanking both sides of the abnormal region (Figure 5.10, see also [305, 340]), and vi) a tendency to slowly increase in size with age, expanding longitudinally along the fibre (Figure 5.10). MtDNAs do not seem to spread between different fibres as COX negative fibres are randomly arranged rather than forming clusters [349] (though a recent study did find clusters of COX-negative skeletal muscle fibres in rats [350]).
Tissue homogenate measurements showed a mixture of deletions, some present at very low levels, with deletion breakpoints scattered randomly throughout the genome [21]. Clonally expanded mutations in the abnormal regions, however, showed less random breakpoint positions with the vast majority of deletions occurring in the major arc of the mitochondrial genome [21, 22, 85, 92, 351].

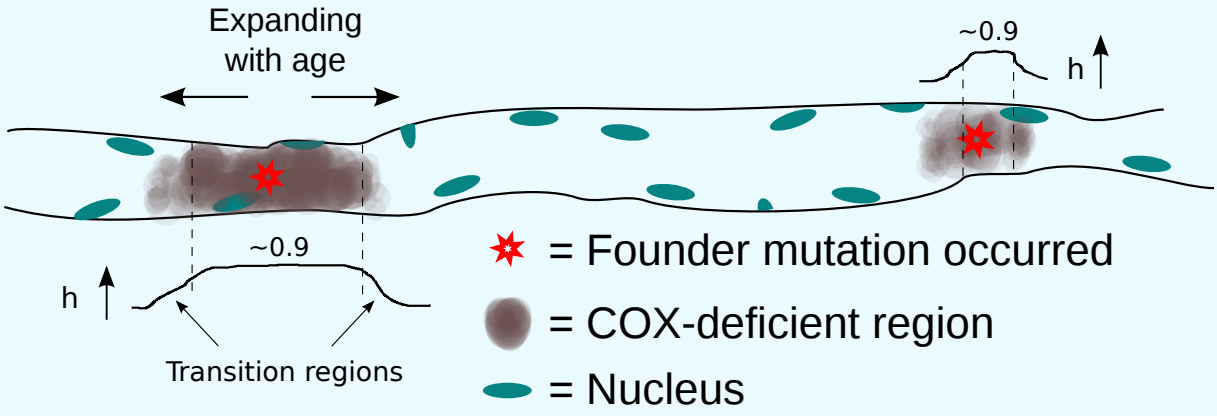


Figure 5.10: Visualisating of mutants spreading along muscle fibres with age. Heteroplasmy profiles in COX-deficient regions are shown. Transition regions can have an intermediate COX-phenotype.

	Ref. [85]	Ref. [92]	Ref. [341]	Ref. [21]
organism: muscle:	Human Vastus lateralis	Rat rectus femoris	Rhesus monkey Vastus lateralis	Rat Vastus lateralis and rectus femoris
Abnormality type	COX^{-}/SDH^{++}	COX^{-} and SDH^{++}, SDH^{normal} or SDH^{low}	COX^{-} and SDH^{++}, SDH^{normal} or SDH^{low}	COX^{-}/SDH^{++}
length fibre studied (% total)	2000μm ($\sim 3\%$)	1000 μm (~ 10 %)	1600 μm ($\sim 4\%$)	1000-2000μm (~ 10 %)
thickness single fibre section	10 μm	10 μm	8 μm	10 μm
% fibres with abnormal regions in length studied	0.2% (n = 18367) (49 years) 0.7% (n = 9285) (67 years) 0.92% (n = 10652) (92 years)	-	0.16% (n = 1848) (11 years) 0.55% (n = 3249) (23 years) 2.41% (n = 2115) (34 years) (more data in Ref. [341])	-
length of single abnormal region	170-800 μm (49 years) 100-800 μm (67 years) 660->2000 μm (92 years)	239 ± 17 μm (5 months) 266 ± 33 μm (18 months) 267 ± 14 μm (38 months)	104-224 μm (11 years) 68-544 μm (23 years) 32-1108 μm (34 years) (more data in Ref. [341])	440 μm 460 μm ~ 600 μm ~ 700 μm (all 36 months)
Estimated % fibres with abnormal regions	30% (92 years)	15% (38 months) (assuming 1 abnormal region per fibre)	60% (34 years)	-
h in abnormal region	>90%	-	-	>90%

Table 5.3: Summary of studies measuring frequencies of deletion mutations in ageing muscle. We provide various summary statistics of several extensive studies done in muscle fibres of human, rat and rhesus monkey, in which sections along individual muscle fibres were analysed. Errors denote mean ± se. SDH^{++} denotes hyperactive SDH activities, an indication of elevated mtDNA copy numbers. Another study not listed in the table found $\sim 0.4\%$ of fibres with abnormal regions in the 2000μm long sections that were studied from 7000 fibres in 38-month old rats (Wildtype mtDNA molecules could be detected in abnormal fibre regions) [351].

To estimate the fraction of cells with high heteroplasmy values in aged tissue, we make the following assumptions: i) a single muscle fibre can be partitioned into smaller 'cells' (as argued in the previous section) in which the feedback control acts, ii) an abnormal fibre region is the cause of a single mutation event which spreads along the fibre, and iii) each abnormal region contains a different mutation. Though it may be that nearby abnormal regions in a single fibre are the result of a single mutation event, this was not observed in the studies we investigated.

One way of estimating the rate at which a mutation accumulates and expands in a cell is to combine the rate of mutation per μm of fibre length (λ_{mut}) with an estimation of cellular length (L_c). In aged human Vastus Lateralis (VL) muscle, after analysing 10652 fibres along 2000 μm, 98 abnormal regions were found (Table 5.3). Therefore, the rate of the occurrence of expanded deletion mutations is $\lambda_{mut} = \frac{98}{10652 \cdot 2000} \approx 4.6 \times 10^{-6} \mu m^{-1}$. Note that λ_{mut} represents the rate per μm at which a mutation occurred *and* expanded to $\sim 90\%$ in its original cell as well as neighbouring cells. A natural way of defining cell size is to use inter-nuclear spacing. Measurements in mouse skeletal muscle found a nuclear density of ~ 30 nuclei per mm of fibre length, meaning $\sim$1 nucleus per 30 μm [352]; we thus assume $L_c = 30 \mu m$. The number of cells that were included in the measurements described above is now $N = \frac{10652 \cdot 2000}{30}$, meaning that the probability of observing a 'mutation generating cell', defined as a cell in which a mutation occurred and subsequently spread towards other cells, becomes $P_{obs} = 98/N \approx 1.42 \times 10^{-4}$. Other estimations of λ_{mut} and P_{obs} are provided in Table 5.4.

Additionally, we can estimate the expected number of fibres that show an abnormal region anywhere along their length; using a total fibre length of 6.5 cm in human VL muscle, the probability of observing at least one abnormal region in an entire fibre is given by $1 - e^{-\lambda_{mut} 6.5 \times 10^4} \approx 0.26$ for a 92-year old human subject [85]. Again, other such estimations are shown in Table 5.4.

Organism & age	$\lambda_{mut}(\mu m^{-1})$	P_{obs} ($\times 10^{-4}$)	Whole fibre mutation prob.	Ref.
Human 92 years	4.6×10^{-6}	1.42	26%	[85]
Rhesus monkey				
32 years	7.0×10^{-6}	2.1	24%	[341]
33 years	8.9×10^{-6}	2.7	30%	[341]
34 years	1.5×10^{-5}	4.5	45%	[341]

Table 5.4: Estimations of mutation rates in skeletal muscle fibres. λ_{mut}: the rate per μm at which a mutation occurred and expanded in its original cell as well as neighbouring cells. P_{obs}: the probability of observing a cell (with a length of 30μm) in which a deletion mutation occurred and subsequently spread towards other cells. Estimations of P_{obs} of a similar magnitude were made in Refs. [85, 341], though it is unclear how these estimations were obtained. All values are calculated in a similar manner as outlined in the main text.

In conclusion, we find a threshold value and fraction of $\sim 90\%$ and $\sim 0.01\%$ (P_{obs}), respectively, very different from the often-used combination of 60% and 5%. Several factors to keep in mind are i) more cells are expected to have passed the threshold $h = 0.6$ compared to $h = 0.9$, ii) when modelling single cells, it is possible that many more than $\sim 0.01\%$ reach the threshold as some mutants may not (yet) succeed in taking over neighbouring cells, iii) the threshold value and fraction may differ between cell types, and iv) measuring mutation levels is difficult and different measuring methods do not always agree [348]. Nonetheless, *our estimations suggest a much lower percentage of high-heteroplasmy cells in aged mammals than assumed in previous models.* Our lower estimate is due to our assumption that a single fibre consists of many individual cells – even if 100% of fibres are observed to contain an abnormal fibre region, the percentage of high-heteroplasmy 'cells' may still be low. Additionally, we assume that each abnormal fibre region is the result of an expansion of mutant mtDNA molecules in a single cell followed by a spread into neighbouring cells. Even if 5% of cells are experimentally observed to have $h = 0.9$, demanding that 5% of single cells in simulations without mtDNA exchange reach $h = 0.9$ is too strict of a condition because it is much easier for a cell to reach high mutant levels if its neighbouring cell contains high mutant levels.

5.2.2.3 Estimating mtDNA exchange rate and control strength

Movement of nucleoids, and therefore mtDNA molecules, through the mitochondrial network can be caused by intra-mitochondrial nucleoid diffusion and/or mitochondrial movements combined with frequent fusion and fission events. Various experimental studies suggest that the latter process is the largest component of mtDNA movement [190, 191, 353, 354]. Skeletal muscle fibres, however, are densely packed and mitochondrial longitudinal movement is not readily observed [260], meaning nucleoid movement in fibres is likely caused by slow diffusion through mitochondria. As mtDNA nucleoids are closely associated with (and likely attached to) the inner membrane [355], we used both diffusion coefficients of nucleoids and inner membrane proteins (which have been measured more abundantly) for our estimation of the mtDNA exchange rate γ. Additional estimations can be obtained using the rate at which abnormal fibre regions spread during ageing.

Our final estimates for γ lie in the range $\gamma \in [0.09, 6.0]$ day^{-1}, where we consider the lower part of this range more likely, as derived in Section C.2.4. Our large uncertainty reflects the complexities involved in mtDNA movement as well as experimental difficulties of measuring diffusion rates. How do these mtDNA exchange rates compare to intracellular mtDNA turnover

rates? The half-life of mtDNAs (indicative of turnover) was estimated to be $1-3$ weeks, corresponding to a death rate in the range $\mu \in [0.02, 0.1]$ day^{-1}. Though estimates for both μ and γ span orders of magnitude, *it is likely that the mtDNA dynamics do not lie in the extreme regimes $\gamma \ll \mu$ or $\gamma \gg \mu$, but rather in an intermediate regime which allows for the stochastic drive observed earlier (Section 5.2.1.4).*

Next, we estimate the feedback control strength c_1, which we deduce from the coefficient of variation (CV) of mtDNA copy number, a more robust quantity to consider. We explored different ways of estimating the CV, including using variations in mtDNA copy number along muscle fibres [21, 85] and intuition about biologically plausible copy number distributions (Section C.2.3). Our final estimate for the CV lies in the range CV $\sim [0.02, 0.25]$ where we consider the upper part of this range more likely (Section C.2.3). Using $N_{ss} = 500$ and $\mu = 0.07$ (as in Figures 5.7 and 5.5), this corresponds to $c_1 \sim [5.5 \times 10^{-6}, 7 \times 10^{-4}]$.

In Figure 5.11 we show a heatmap visualising the extent to which mtDNA exchange can induce changes in mean heteroplasmy dynamics. Our estimated parameter ranges for γ and the CV are indicated, showing that a non-negligible effect size is possible under biologically plausible parameterisations. We thus conclude that intercellular mtDNA exchange forms an interesting avenue for future research that needs further exploration.

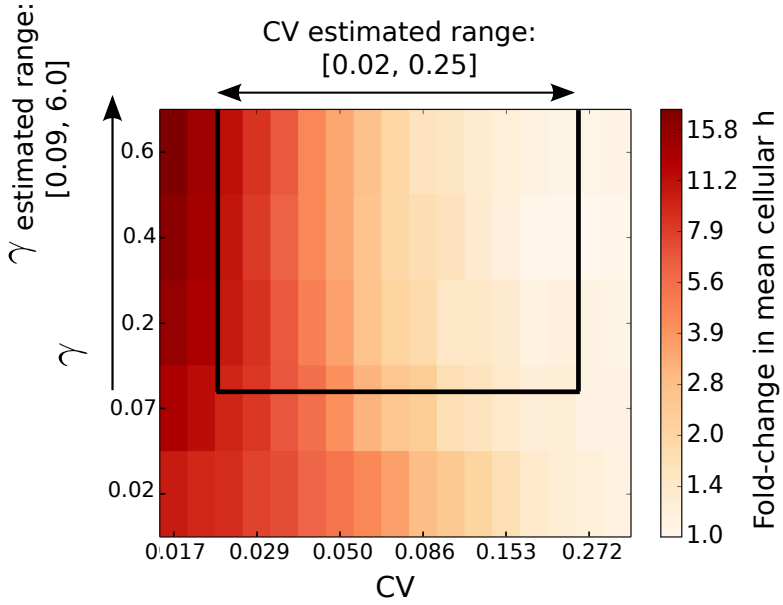


Figure 5.11: Significant effects of mtDNA exchange on heteroplasmy mean in physiological settings are plausible. Here we show an overview of the extent to which mtDNA exchange increases mean heteroplasmy values at long times, as a function of both γ and the CV. The black straight lines indicate the parameter regions we estimated to be biologically plausible. We use data obtained from simulations and show the fold-change in mean heteroplasmy when comparing i) heteroplasmy values without cellular exchange ($\gamma = 0$), and ii) mean cellular heteroplasmy values at 90 years in a 5-cell interaction system (i.e. $\frac{1}{5}\sum_i \langle h(\text{t} = 90 \text{ years})\rangle_i$). Four cells were initialised at $h = 0$, and one cell at $h = 0.1$ (i.e. without cellular interaction mean heteroplasmy is 0.02 and the colour map reflects the fold-change increase from this). Parameters used in simulations are $N_{ss} = 500, \mu = 0.07$ and $\delta = 0.1$.

5.2.3 Clonal expansion and random drift - Challenges and perspectives

The basic observation has been that to make random drift models accumulate the observed levels of mutated fibres in the lifespan of short-lived animals (e.g. rodents) the mutation rate has to be very high; this high mutation rate leads to a level of mutational diversity that is not observed experimentally [36, 38]. The neutral models thus dismissed, authors have moved to look at more exotic mechanisms. Here we present various arguments which mostly point towards reducing this problem, either through 1) lower values of P_{mut} or through 2) a lower number of distinct mutations (independent of P_{mut}). Though the influence of each of these arguments may be small, together they might make a difference and therefore more detailed analyses are required to exclude random drift as a possible driver of clonal expansion.

MtDNA exchange can lead to increased rates of expansion. Our work in the previous sections suggests a stochastic drive in heteroplasmy, generated without explicit selection (or even with negative selection on mutants), might serve to increase mutant load. If our model is relevant, lower values of P_{mut} can account for observed levels of mutation. However, mtDNA exchange can cause the fraction of cells crossing a certain heteroplasmy threshold to be lower at short times (Figure 5.8B), increasing the value of P_{mut} required in the short-term.

Mutant loads may be lower than expected. Our estimated mutant loads in aged tissues are orders of magnitude lower than the ones used often in modelling (Section 5.2.2.2), allowing for lower values of P_{mut}. Experimentally, it also appears previously assumed mutant levels are too high, as measurements of mutant fractions in aged tissues are lower when using methods supposedly less prone to artefacts [348].

Low heteroplasmy levels at birth increase accumulation rates. It is not clear to what extent mutations observed in older individuals are the result of *de novo* mutations throughout life, or of the expansion of low-heteroplasmy mutants that were present at birth [17]. Some evidence exists for the latter [20, 133, 356, 357]. Though, 95% of mutations that occurred during early development in human colonic and buccal epithelium were observed to be non-pathogenic [20], this does not necessarily imply all pathogenic mutations accumulate after birth. Initializing cells with low-h mutants will decrease the time required to reach the target value and threshold [357], allowing for a lower P_{mut}.

Different mutants have different mutation probabilities and cannot mutate indefinitely. Not all mutations are equally likely to occur and it is therefore incorrect to assume a constant P_{mut} for each mutation. Ideally, each mutant is considered unique with its own P_{mut} (its probability of occurring) and its own δ. Higher mutation probabilities or lower δ values for specific mutations increases their chance of expansion relative to others. Some of the models arguing against random drift allow for the possibility of an arbitrary number of sequential mutations [38] and, given that they aim to match deletion mutation levels, this implies the occurrence of deletion upon deletion upon deletion, etc. As certain parts of the genome nearly always remain intact (e.g. the origins of replication are often preserved [85]), a maximum number of sequential deletions should be imposed. All these factors may reduce the number of distinct mutations observed at the end of simulations.

The presence of many low-frequency mutants may not be detected experimentally. Even when many mutant types are present, some may exist at very low frequencies and may not be detected experimentally (i.e. predicting distinct mutants through simulation may not be at odds with observing ~ 1 mutation experimentally). This was partly accounted for by keeping track of the most dominant mutant fraction [34, 36, 38], arguing that if h is high but the dominant mutant frequency is low, other mutations present must be detectable. However, considering the average number of distinct mutations may be ~ 30 in simulations of short-lived animals [36, 38], it can still be that almost all of these are present below detection threshold. Ideally, one would keep track of copy numbers of all the different types of mtDNA present.

A mixture of different mutations is not necessarily pathological because the deficiencies of one can be complemented by another [358], meaning that cells with many low-frequency mutations need not be COX-negative. In many models, however, cells with $h > 0.6$ are considered COX-negative and heteroplasmy values are calculated by combining all mutants [34, 36, 38]. Alternatively, one could classify a cell as COX-negative once the most dominant mutant passed the threshold value, which would automatically reduce numbers of distinct mutants in cells passed threshold. However, different deletions may not complement each other as they often lack similar regions in the genome [21, 22, 85, 92, 351].

Reductions in copy number during ageing may increase the number of high-heteroplasmy cells. Mean mtDNA copy numbers have been reported to increase or decrease during ageing in various tissues [72, 359–364]. Other studies, however, do not find a change in mtDNA copy number with age (e.g. in human skeletal muscle and myocardium [69]). These discrepancies were suggested to be due to distinct measuring techniques as well as tissue-specific age-related dynamics [359].

It was shown that a sudden (temporary) drop in copy number can significantly increase the fraction of cells having crossed a high heteroplasmy threshold during ageing [22], and the same may be true for slow consistent decreases in copy number (as we expect stochastic effects to be more pronounced at low copy number). A lower P_{mut} would then be required to reach a given target load. It will be interesting to simulate a slowly decreasing steady state copy number value and discuss the effect on mutant accumulation rates.

Higher turnover rates in rodents increases rates of mutant expansion. Higher mtDNA turnovers – which may be expected in rodents due to their high metabolic rate – will accelerate mutant accumulation [37]. When simulations of clonal expansion in rodents are performed with higher turnover (currently, the turnover rate is often assumed constant for both human and rodent simulations), the required P_{mut} will be lowered.

5.3 Discussion

Stochastic systems can produce non-neutral dynamics when deterministic treatments do not, and we argued that this may apply to mtDNA dynamics, where stochastic selection is caused by differences in carrying capacities. The novel contributions of this work are: i) allowing intercellular mtDNA exchange, a setting relevant in skeletal muscle fibres due to their long multi-nuclear structure, can induce increases in cellular mean heteroplasmy even in the presence of selection against mutants (Section 5.2.1.4), ii) particular mutant mtDNA species can expand preferentially during ageing without explicit selection (Section 5.2.1.4), and iii) differences in carrying capacity induce heteroplasmy skew which can lead to temporary high fractions of cells passing some heteroplasmy threshold (Section 5.2.1.1). Additional results we obtained are: i) behaviours of many different mtDNA mutations can be explained by varying a single parameter (which is also true for the relaxed replication model [1, 2]) (Section 5.2.2.1), and ii) mutant loads in aged tissues may be lower than previously thought (Section 5.2.2.2). We further provide a critical overview of various model assumptions and suggest possible extensions. The overall conclusion is that random drift may be more influential than previously thought (though our model does not exclude any mutant selection advantages).

If relevant (see below) what would be the biological implications of our results? Our model may explain why only deletion mutations are seen to expand during ageing, and why they occur at high copy numbers. A recent study found no correlation between the length of COX^- regions and the deletion size within that region, arguing against faster replication of shorter genomes [365]. In our model, even with a constant exchange rate γ, low-δ mutations are expected to

expand faster, suggesting δ is not directly linked to deletion size. Because there *is* a direct link between δ and total copy numbers in high-heteroplasmy regions, it will be interesting to test the existence of a correlation between the size of COX^- region and copy number within.

One particular gene lacking in many deletion mutations is ND4, encoding for a subunit of complex I of the respiratory chain. ND4 transcription rates were suggested to reduce mtDNA replication, causing mutants which lack this negative feedback loop to obtain a replicative advantage [38]. This interpretation requires a (leaky) link between genotype and phenotype as the amount of transcripts and proteins produced by an mtDNA influences its own, but not others', replication rates. Frequent mitochondrial fusion and fission events, however, allow for mixing of proteins and blur the link, though there are indications that a leaky link nevertheless exists [188]. Our model allows for an identical interpretation but with the assumption that the link is sufficiently leaky such that local feedback is negligible. Instead of a local lack of transcripts failing to reduce replication of the nearest mutant, our model might, in this light, be interpreted as suggesting a global reduction in transcripts (due to mutant presence) fails to decrease replication, leading to a higher total population size as heteroplasmy increases. A complete absence of mutant transcript would be equivalent to using $\delta = 0$. Whether δ is related to ND4 can be tested by e.g. downregulating ND4 expression to various degrees and testing for a correlation with steady state copy numbers.

At the moment it is hard to speculate to what extent intercellular mtDNA exchange affects heteroplasmy dynamics in real biological systems, due to the large uncertainties in our parameter estimates (Section 5.2.2.1). To partially deal with this problem, we performed simulations with parameters varying over several orders of magnitude (Figures 5.7A, B) and commented on the different parameter regimes in which $\langle h(t) \rangle$ is likely to show significant changes (Figure 5.11). We note, however, that our results may be influenced by other factors such as i) changes in nuclear positions due to fibre damage [366], ii) inhomogeneous mitochondrial densities along fibres due to the banding pattern of myofibrils and across fibres due to steep oxygen gradients [367], and iii) changes in mitochondrial density induced by exercise [368, 369]. *Despite the effect-size of our results being uncertain, we would argue that the possibility of mtDNA exchange forms an interesting and worthwhile component of mathematical models of clonal expansion that needs further exploration.*

Our mutant load estimations predicted that at old age ($\sim$ 90 years in humans and $\sim$ 30 in rhesus monkeys) in $\sim 0.01\%$ of cells a mutation event occurred, clonally expanded within that cell, and spread along the fibre infecting other cells. When simulating an entire muscle fibre,

such affected regions can easily be counted. However, when only simulating one, three or five cells, if a mutation expanded to $> 90\%$ does that mean it would also have expanded in 50 cells? Would it have shown up as an affected region at the end of the simulation or not? We would argue that low-δ mutations are likely to continue expanding due to their much higher carrying capacity, but mutations with $\delta \approx 1$ may be more easily eliminated again by chance. Some care must be taken in interpreting few-cell simulations.

What evidence is there for faster mutant proliferation? It was initially found that cells homoplasmic in deletion mutations recover at a faster rate (after induced copy number depletion) than cells homoplasmic in wildtype [370]. However, this in principle does not imply a different birth rate for mutant and wildtype[‡], and does not straightforwardly extend to heteroplasmic cells. A later study by the same group on heteroplasmic cells found that h increases after depletion [283]. Heteroplasmy values were not measured directly after depletion and it may be that the treatment itself, instead of the recovery dynamics, changed heteroplasmy, though higher mutant replication rates still form the simplest explanation. We note that even if deletion mutants show a replicative advantage when replication rates are maximal, this does not necessarily imply such an advantage is significant in more physiological settings without severe depletion. Some mutations close to regulatory sites of replication do genuinely seem to show a replication advantage [371].

The work we presented here is a work in progress and can be extended in a variety of ways. The number of coupled cells can be increased, and cells can be assumed to lie on a lattice (making transverse motion possible, as has been observed experimentally [372]). It would also be interesting to investigate the consequences of allowing variation in steady state cellular copy numbers between cells, and copy number reductions over time. Analytically, an equation predicting (or approximating) the initial rate of increase of $\langle h(t) \rangle$ in the two cell setting seen in Figure 5.5, or even its final steady state value, is highly desirable. This will gain us a deeper understand of the process. For more analytical treatments one could take an approach similar to one in Ref. [328], namely deriving stochastic differential equations for motion along steady state lines. The authors results are valid in limits of slow or fast exchange of components, but may be extended to include intermediate regimes. Experimental tests suggested throughout this chapter are summarised in Table 5.5.

[‡]A heteroplasmic cell with $N_{ss} = 500$, $\delta = 0.1$ and $h = 0.7$ has steady state copy numbers $(w, m) \approx (400, 950)$. Depleting copy numbers (while preserving heteroplasmy) to e.g. $(w, m) = (30, 70)$, means that mutant and wildtype copy numbers need to increase by 880 and 370, respectively, to return to their original state; a faster mutant replication rate during recovery may therefore be expected.

To connect with previous studies [34, 36, 38] we need to simulate mutant expansion in short-lived animals (incorporating some of the extensions suggested in Section 5.2.3). We can find the value of P_{mut} required to match experimentally observed mutant loads through simulations, and determine the corresponding number of distinct mutant types in high-heteroplasmy cells. An analytical example route to pursue is to approximate P_{mut} analytically by predicting the number of abnormal fibre regions at a given age (given P_{mut}) and matching with experiments. For example, we could assume that a mutation is likely to spread along a fibre when it reaches a macroscopic fraction of $\sim 10\%$ in a single cell. The number of abnormal regions at a given time then roughly corresponds to the number of times we expect a mutation to have reached $h = 0.1$ (which may be estimated by using information on single cell copy numbers, turnover, and mutation rate). Such estimations allow us to quickly predict the value of P_{mut} and speculate on its plausibility. By performing these estimations and simulations we will able to make statements on whether random drift can account on for clonal expansion in short-lived animals in the context of cellular mtDNA exchange.

Suggested experiments to test model predictions or improve parameter estimations.
Non-destructive mtDNA copy number measurements (using e.g. fluorescent staining of nucleoids) in single cells over time will provide useful information on natural fluctuations in copy numbers. This method of estimating c_1 is arguably better than measuring copy numbers across a population of identical cells, as it eliminates the problem of heterogeneity caused by e.g. differences in cell volume.
We predicted a correlation between the length of a COX^- region and the total copy number within the region, this can easily be tested.
If the gene ND4 is related to our parameter δ, downregulating its expression in cells should increase steady state copy numbers in those cells.
Depleting mtDNA copy number to various degrees and measuring initial rates of repopulation will provide insight into the feedback control strength as a function of distance from steady state, and will therefore indicate the shape of the control function (i.e. whether it is nonlinear and at what point these nonlinearities become apparent).

Table 5.5: An overview of possible experiments to test model predictions and improve parameter estimates.

We conclude this thesis by highlighting a connection between mitochondrial dynamics (i.e. Chapters 2 and 3) and mtDNA dynamics (i.e. Chapters 4 and 5). Just like mitochondria reside inside cells and may be exchanged between cells – through e.g. diffusion or tunneling nanotubes [333, 373, 374] – mtDNA molecules reside inside mitochondria and can be exchanged through fusion events. The model of intercellular mtDNA exchange introduced in this chapter can be applied to any system in which particles undergo controlled dynamics in subcompartments and are exchanged between these subcompartments. This includes both mtDNA molecules being exchanged between mitochondrial fragments, and mitochondria and/or mtDNAs being exchanged between different mitochondrial subpopulations inside single cells. In these situ-

ations, it may be possible for mutant mtDNA molecules to preferentially expand (if $\delta < 1$) inside single cells without explicit selection. Such possibilities of local control in mitochondrial fragments or cellular subcompartments are not studied in this thesis but form an interesting extension of the work presented here.

A

Supplemental information complementing Chapter 2

This appendix is split into three sections:

1. The first section contains quantitative and mathematical details of various models presented in Chapter 2. Several of these models follow the philosophy of 'back-of-the-envelope' calculations, rough estimations of quantities which are increasingly recognised as powerful tools to gain insights and intuition about the behaviour of biological systems [375, 376]. The models we use are:

    - Ordinary differential equation model for selection bias through selective fusion;
    - Model for diffusion on a lattice with fluctuating bonds;
    - Fusion of charged spherical capacitors;
    - Calcium stimulation and energy output of fused mitochondria;
    - Mechanisms of calcium uptake;
    - Fusion buffers fluctuations in membrane potential.

2. The second section contains descriptions of additional hypotheses mentioned in Chapter 2:

- A genetic reservoir created through fusion;
- Fusion increases ATP synthesis through (i) inner membrane shape change; (ii) decreases in proton leak; (iii) decreases in mitochondrial degradation.
- Fusion creates distributional 'power cables'
- Meso- and hyperfusion have no function

3. The third section contains tables summarising quantitative and qualitative data on the following topics:

- Observations of hyperfusion;
- Mitochondrial morphology in different cell types;
- Diffusion constants of mitochondria proteins;
- Post-translational modifications of Drp1;
- Additional functions of mitochondrial fission and fusion proteins.

A.1 Quantitative and mathematical models

A.1.1 Model for increased selection bias through selective fusion

In Section 2.4.1 of Chapter 2 we introduced a simple ordinary differential equation (ODE) model to show that increased fusion strengthens the bias towards degrading dysfunctional mitochondria. The set of ODEs provided in Equation (2.1) can easily be derived by first writing the system in the intuitive form (for parameter definitions see Chapter 2)

$$\begin{aligned}
\dot{c}_{hs} &= (B - M - \gamma_{hf})c_{hs} + \gamma_f c_{hf} \\
\dot{c}_{us} &= (B - M - \gamma_{hf})c_{us} + \gamma_f c_{uf} \\
\dot{c}_{hf} &= c_{hf}(B - \gamma_f) + \gamma_{hf} c_{hs} \\
\dot{c}_{uf} &= c_{uf}(B - \gamma_f) + \gamma_{uf} c_{us}.
\end{aligned} \tag{A.1}$$

The first two equations state that the fragmented population can be increased through biogenesis (B) and fission of fused mitochondria, while it can be decreased through mitophagy (M) and through fusion. The latter two equations lack a term involving mitophagy due to our assumption that only fragmented mitochondria can be degraded. Constant total population size is obtained

by assuming $B\cdot(c_{hf}+c_{uf}+c_{hs}+c_{us}) = M\cdot(c_{hs}+c_{us})$, i.e. $M = B\cdot(c_{hf}+c_{uf}+c_{hs}+c_{us})/(c_{hs}+c_{us})$. Equations (2.1) in Chapter 2 are now simply obtained by eliminating M from Equation (A.1).

A cell can increase the connectedness of the mitochondrial network by either increasing fusion, decreasing fission, or both. When fusion rate is increased, while keeping the ratio γ_{hf}/γ_{uf} constant, we found that the population of dysfunctional mitochondria decreases faster (Figure 2.2B). Figure A.1A shows that the ratio $\frac{c_{us}}{c_{hs}+c_{us}}$, denoting the fraction of the fragmented population that is dysfunctional, is slightly lowered at high fusion rates, meaning a relative increase in the number of healthy mitochondria being targeted for mitophagy. Similarly, though decreasing fission (as well as increasing fission) leads to a slower decay of unhealthy mitochondria (Figure 2.2B), the number of degraded healthy mitochondria is relatively lower (Figure A.1A). Figure A.1B shows the total level of fusion (defined as $(c_{hf} + c_{uf})/(c_{hs} + c_{us} + c_{hf} + c_{uf})$) in the four different parameters settings we consider, showing a similar network connectedness for the settings of increased fusion and decreased fission (which we impose in order to properly compare these settings).

We note that, in reality, there will be a rate at which functional mitochondria become dysfunctional. This rate is very low if one only considers dysfunctionalities caused by rare events (like mtDNA mutations), in which case the model described above may be used as an approximation; e.g. mitochondria with a certain mtDNA mutation will be removed from the network before the next mtDNA mutation occurs. However, mitochondria can become dysfunctional in other ways (e.g. depolarization events or oxidative damage), in which case the described model is not sufficient. Extra terms can be added to Equations (2.1) to account for the possibility that a healthy mitochondrion becomes unhealthy. These extra terms allow for the possibility of steady states with a nonzero population size for all of the populations. In this scenario, increases in fusion rate (at constant γ_{hf}/γ_{uf}) induce increases in the steady state ratio $\frac{c_{hf}+c_{hs}}{c_{uf}+c_{us}}$ (i.e. the higher fusion rate, the higher the fraction of functional mitochondria in steady state).

A.1.2 Model for diffusion on lattice with fluctuating bonds

Diffusion on lattices with 'flickering' bonds (bonds that can appear and disappear over time) has been studied in Refs. [232, 233], using the theory described in Ref. [377]. An analytical approach, taking into account the state of all the bonds, is intractable and we therefore use an effective medium approximation [232, 233]. The fluctuating lattice is approximated by a static lattice in which the transition rate to a nearest neighbour is the same for all nearest neighbour

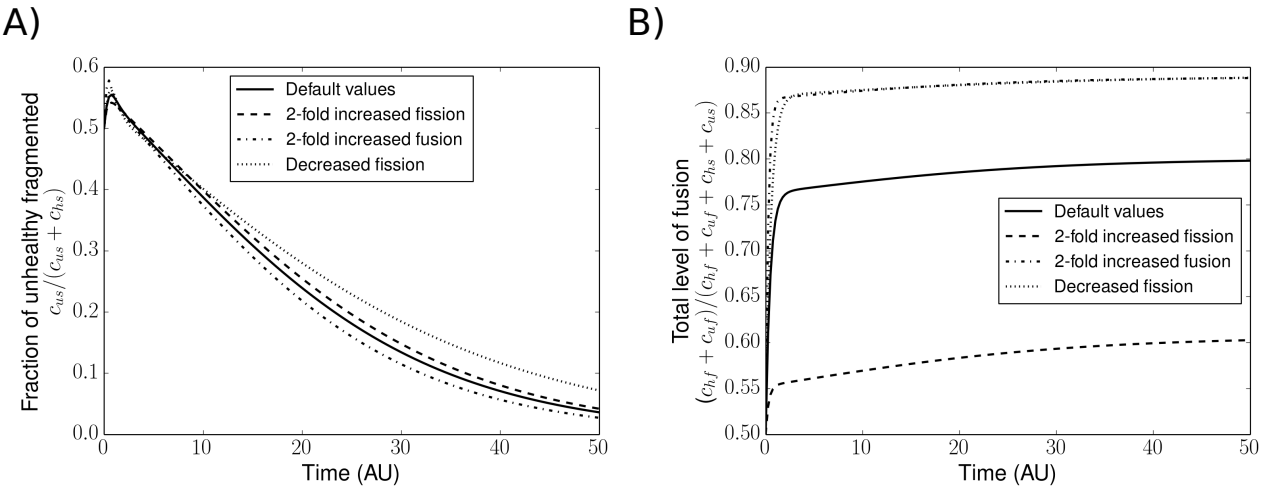


Figure A.1: Increased fusion leads to a relatively smaller unhealthy fragmented population. A) We consider the same four parameter regimes as defined in Figure 2.2 of Chapter 2. Increased fission rates (relative to the default setting) cause the fraction of unhealthy mitochondria in the fragmented population to be lower. This means that, relative to the default parameter setting, mitophagy events are more likely to degrade a healthy mitochondrion. Changes in fission rate have the opposite effect. **B)** Here we show the fraction of mitochondria that is fused for our four different parameter settings. In the setting of decreased fission (dotted line), we chose the value of γ_f such that the level of fusion was identical to that in the setting of increased fusion; this led to $\gamma_f = 0.55$.

pairs and is given by w_e (the effective transition rate), satisfying

$$\frac{p - w_e}{p_c(1 - w_e)} = 1 - \frac{1}{1 + n_c w_e \tau} G\left(0, 1 - \frac{1}{1 + n_c w_e \tau}\right) \tag{A.2}$$

where p is the fraction of bonds that are present, n_c is the number of nearest neighbours per site, $p_c = \frac{2}{n_c}$, τ is the characteristic relaxation time of the fluctuating bonds, and $G(0, z)$ is the appropriate lattice Green's function evaluated at the origin [232], which in the case of our 2D square lattice model is

$$G(0, z) = \frac{2}{\pi} K(z^2) \tag{A.3}$$

where K is the complete elliptical integral of the first kind.

This approximate model is equivalent to random diffusion on a lattice with a hopping rate given by w_e and therefore w_e can be interpreted as the diffusion coefficient D. Equation (A.2) is used to generate Figure 2.3A in Chapter 2.

A.1.3 Fusion of charged spherical capacitors

Here we explain how fusion of two charged objects can lead to a non-averaging of potentials, as claimed in Section 2.4.3 of Chapter 2. Suppose we have two charged shells, a small one with

radius r_{in} and a bigger one with radius r_{out}. The spheres are assumed to have opposite charges, i.e. one has charge Q and the other charge $-Q$. Applying Gauss' law, the potential difference between the shells is given by

$$V = \frac{Q}{4\pi\epsilon} \cdot \frac{r_{out} - r_{in}}{r_{in} r_{out}}. \tag{A.4}$$

where ϵ is the dielectric permittivity of the medium between the charged spheres. Because the capacitance C is given by $C = \frac{Q}{V}$, Equation (A.4) leads to

$$C = \frac{4\pi\epsilon r_{in}(r_{in} + d)}{d} \tag{A.5}$$

where we have denoted the distance between the inner and outer radius by d. In this model, r_{in} and r_{out} are meant to represent the inner and outer radii of the mitochondrial inner membrane (i.e. d denotes inner membrane thickness). We do not model the outer membrane because the electrochemical gradient only exists across the inner membrane.

We now consider a 'fusion' of two capacitors, while assuming that total volume and charge are conserved. We denote the inner radius and charge of capacitor i by r_i and Q_i, respectively, and label the initial two capacitors by '1' and '2', and the resultant fused capacitor by '3'. If we maintain a spherical structure in the resulting fused capacitor, conservation of volume translates into the constraint $r_3^3 = r_1^3 + r_2^3$. Conservation of charge gives $Q_3 = Q_1 + Q_2$. The capacitance of the fused capacitor is then given by

$$\begin{aligned} C_3 &= \frac{4\pi\epsilon r_3(r_3 + d)}{d} \\ &= \frac{4\pi\epsilon(r_1^3 + r_2^3)^{1/3}\left[(r_1^3 + r_2^3)^{1/3} + d\right]}{d}, \end{aligned} \tag{A.6}$$

and the potential V_3 can now be calculated as follows:

$$\begin{aligned} V_3 &= \frac{Q_1 + Q_2}{C_3} \\ &= \frac{V_1 C_1 + V_2 C_2}{C_3} \\ &= \frac{V_1 r_1(r_1 + d) + V_2 r_2(r_2 + d)}{(r_1^3 + r_2^3)^{1/3}\left[(r_1^3 + r_2^3)^{1/3} + d\right]}. \end{aligned} \tag{A.7}$$

For a mitochondrion, the thickness of the inner membrane is about 5 nm and is two orders of magnitude less than the value for r_{in} which can be around 0.5 µm. Using $d \ll r_i \, \forall i$, Equation

(A.7) becomes

$$\begin{aligned} V_3 &= \frac{V_1 r_1^2 + V_2 r_2^2}{(r_1^3 + r_2^3)^{2/3}} \\ &= \frac{V_1 A_1 + V_2 A_2}{(A_1^{3/2} + A_2^{3/2})^{2/3}}, \end{aligned} \tag{A.8}$$

where $A_i = 4\pi r_i^2$ is the surface area of capacitor i. When the two fusing capacitors have identical surface area (i.e. $A_1 = A_2$) the above equation reduces to

$$V_3 = (V_1 + V_2)2^{-2/3} \approx 0.63\ (V_1 + V_2) \tag{A.9}$$

This means that the voltage of the fused capacitor is higher than the average of the voltages of the identically-sized pre-fusion capacitors.

In this toy model, we have assumed that the inner and outer radii of the mitochondrial inner membrane are spheres, i.e. we have ignored cristae. Instead of assuming $A_i = 4\pi r_i^2$, we may assume $A_i \propto r_i^x$ with $x \in (2, 3)$; the higher x, the more the inner membrane fills up the volume of the mitochondrion. The final result given in Equation (A.9) stays the same. However, if we also assume that $V_i \propto r_i^y$ with $y \in (2, 3)$ then Equation (A.9) changes into

$$V_3 = (V_1 + V_2)2^{-2/y} < 0.63 \cdot (V_1 + V_2) \quad \text{for} \quad y \in (2, 3) \tag{A.10}$$

The amount by which the voltage V_3 exceeds the average of $V_1 + V_2$ decreases as y decreases from 3 to 2, with $V_3 = \frac{1}{2}(V_1 + V_2)$ if $y = 2$. This means that in mitochondria, because of the membrane invaginations, the fused potential will be closer to the average than predicted by this simple toy model (i.e. if $V_3 = x\ (V_1 + V_2)$ then x will be lower than 0.63, but still potentially higher than 0.5).

A.1.4 Energy output by calcium stimulation as function of the number of fused mitochondria

We will discuss a very simple model that describes how the total 'energy output' of a group of mitochondria depends on the number of fused mitochondria connected to a calcium source. This simple model explains the shape of the curve drawn in Figure 2.5B of Chapter 2.

We assume that all mitochondria that are not exposed to a calcium source have a basal $[Ca^{2+}]_{\text{matrix}}$, given by c_b. If calcium is emitted from a source (for example, a calcium channel

in the ER), a mitochondrion adjacent to the source will experience an increase in $[Ca^{2+}]_{\text{matrix}}$, denoted by c_{sig}, meaning its concentration becomes $c_b + c_{sig}$; mitochondria far from calcium channels keep their basal concentration.

We use a simple approximation where the energy output of a mitochondrion is sigmoidally dependent on $[Ca^{2+}]_{\text{matrix}}$ [244]. By using the generic term 'energy output' we are avoiding committing to a particular physiological variable and rather seek to demonstrate the principle at play. Specifically, we denote by $s(c)$ a sigmoidal function giving the energetic output of a mitochondrion with internal calcium concentration c. The total output of the mitochondrial system, E, is then defined as

$$E = \sum_i s(c_i) \tag{A.11}$$

where i indexes mitochondria, and c_i is the calcium concentration in the ith mitochondrion.

We can now model the effect of fusion on total mitochondrial energy output. If there are N mitochondria in total, with one mitochondrion near a calcium channel (this number can easily be generalised) and n mitochondria fused to this mitochondrion, then total output is given by

$$E = (N - n) \cdot s(c_b) + n \cdot s(c_b + c_{sig}/n) \tag{A.12}$$

where the first term describes the output generated by the $(N - n)$ isolated mitochondria, and the second term gives the output of the n fused mitochondria.

Figure 2.5B of Chapter 2 illustrates how E depends on n. To generate this figure, we chose c_{sig} to be two orders of magnitude larger than c_b (as has been observed in neurons [378]) and we chose an arbitrary sigmoid function. The details of the shape of the curve depend on the form of the sigmoid used, but the general behaviour shown in the figure (E increases first and then decreases) will be conserved. With this simple model we show that, inspired by the sigmoidal dependence of TCA cycle enzyme activity on calcium, there exists an 'optimal' number of fused mitochondria corresponding to maximal energy output. The quantitative details of this result will depend on the exact sigmoidal form of enzyme activity and on the value of the parameters c_b and c_{sig}.

A.1.5 Mechanisms of calcium uptake and amount of mitochondria-ER contact

Here we provide some additional information that serves as criticism of the calcium hypothesis discussed in Section 2.4.4 of Chapter 2. Controversy exists over kinetics of mitochondrial

calcium uptake and the mechanisms involved. Besides the uniporter, other mechanisms such as the Rapid Mode of uptake (RaM) and ryanodine sensitive transporters have been identified [203]. Ryanodine sensitive receptors located on the inner mitochondrial membrane become active around $[Ca^{2+}]_{cyt} \sim 100$ nM [379], whereas the mitochondrial uniporter is thought to have a low affinity for calcium with a dissociation constant around 10 μM [380]. We note that the activity of the uniporter is itself $[Ca^{2+}]$-dependent and the details of mitochondrial calcium influx (reviewed in Ref. [381]) are not fully understood. If uptake through ryanodine sensitive transporters is significant, then calcium uptake is not limited to mitochondria close to high $[Ca^{2+}]_{cyt}$ domains.

It is not certain what percentage of the total mitochondrial network has close contacts with the ER. There are studies suggesting this concerns ∼5-20% of the total mitochondrial surface [245], while others observe that 90% of fission events occur at sites of ER-mitochondria contact [253]. Mitochondria in the perinuclear region seem to have more ER-associations than those in the peripheral region [382]. It has been suggested that the amount of contact between mitochondria and the ER changes over time [383].

A.1.6 Increasing mitochondrial size buffers fluctuations in membrane potential

A.1.6.1 Changes in membrane potential upon changes in permeability of the inner mitochondrial membrane

Here we provide arguments for why fluctuations in membrane potential are of smaller magnitude in larger mitochondria (as stated in 2.4.5 of Chapter 2). We will use a physical model to consider how a perturbation that increases the flux of some charged chemical species into the mitochondrion (motivated by, for example, transient opening of the permeability transition pore, or proton leak), affects the membrane potential of mitochondria of different size.

The flux per unit area j_X of some chemical species X with charge z through a membrane (here the mitochondrial inner membrane) of width L is given by the Goldman equation

$$j_X = \frac{\beta \Delta\psi D_X z}{L} \left(\frac{[X]_{out} - [X]_{in} e^{\beta z \Delta\psi}}{1 - e^{\beta z \Delta\psi}} \right), \tag{A.13}$$

where $\beta = \frac{F}{RT}$, F is the Faraday constant, T the temperature, R the gas constant, $\Delta\psi$ the membrane potential, D_X the diffusion coefficient for chemical species X and $[X]_{in}$, $[X]_{out}$ are

the concentrations of species X on either side of the membrane. Written in this way, the flux j_X is the net flux into the mitochondrion through a piece of unit surface area. Assuming a spherical mitochondrion with area $A = 4\pi r^2$ the total flux of X through the membrane is given by

$$J_X = \oint_A j_X dA = 4\pi r^2 \alpha \Delta\psi z \left(\frac{[X]_{out} - [X]_{in} e^{\beta z \Delta\psi}}{1 - e^{\beta z \Delta\psi}} \right), \tag{A.14}$$

where $\alpha = D_X \beta / L$ is a measure of the permeability of the membrane.

We aim to explore how robust the membrane potential is with respect to perturbations including, for example, opening of the mitochondrial permeability transition pore or proton leak. In equilibrium, the net species' flux is zero. Setting equation (A.14) to zero we can solve for $\Delta\psi$ to obtain

$$(\Delta\psi)_{equilibrium} = \frac{1}{\beta z} \ln \frac{[X]_{out}}{[X]_{in}} \tag{A.15}$$

We consider small perturbations to this equilibrium state, resulting from changes in the internal concentration of a charged species $[X]_{in}$. For a small transient perturbation, we have:

$$\frac{d\Delta\psi}{dt} = \frac{-1}{\beta z [X]_{in}} \frac{d[X]_{in}}{dt}, \tag{A.16}$$

where we have assumed that $[X]_{out}$, the cytoplasmic concentration of X, stays constant due to its large volume compared to the mitochondrion.

Changes in $[X]_{in}$ are caused by net flux of X into the mitochondrion. Not all of these ions flowing in will increase $[X]_{in}$ as some of them may bind to proteins or ionic species inside the mitochondrion. This effect can be accounted for by a buffering factor, γ, which results in

$$\frac{d[X]_{in}}{dt} = \gamma \frac{J_X}{\frac{4}{3}\pi r^3}, \tag{A.17}$$

where we have related the absolute flux J_X to the change of concentration $[X]_{in}$ by normalizing by the volume of a (spherical) mitochondrion. The perturbation by which this influx is manifest is considered to cause an increase in permeability of the membrane, which we represent by scaling the permeability constant $\alpha \to \alpha' > \alpha$. Using equation (A.14) we obtain

$$\frac{d[X]_{in}}{dt} = \gamma \alpha' \Delta\psi z \left(\frac{[X]_{out} - [X]_{in} e^{\beta z \Delta\psi}}{1 - e^{\beta z \Delta\psi}} \right) \frac{3}{r} \tag{A.18}$$

meaning that

$$\frac{d\Delta\psi}{dt} = \frac{-\gamma \alpha' \Delta\psi}{\beta [X]_{in}} \left(\frac{[X]_{out} - [X]_{in} e^{\beta z \Delta\psi}}{1 - e^{\beta z \Delta\psi}} \right) \frac{3}{r} \tag{A.19}$$

This means that for large r (large mitochondria) fluctuations of $\Delta\psi$ will be of smaller magnitude, even if the perturbation in a larger mitochondrion happens over a larger surface area because the internal pool of ions is larger still ($r^3 > r^2$).

Treating mitochondria as spheres, we have neglected the invaginated structure of the inner membrane. Including these invaginations changes the r^{-1} dependence of $\Delta\psi$ to r^y with $y \in (-1, 0)$. Because, in spherical mitochondria (even when assuming membrane invaginations), volume will always scale with a larger power of r than surface area, fluctuations in $\Delta\psi$ will always be less in larger mitochondria. Fusing mitochondria into large networks thus protects them from perturbations.

A.1.6.2 Ising-type model for mitochondrial robustness

Alternative arguments independent of volume and surface area scaling can be given supporting the hypothesis discussed in Section 2.4.5. We will briefly discuss a picture based on the Ising model, an often-used class of physical models for collective dynamics. In the Ising model, a set of elements (originally spin domains) exists, with each entity i having a state s_i which may be -1 or 1. In a simple incarnation of the Ising model, the overall energy of the system is given by $E = \sum_i \sum_{j \geq i} J_{ij} s_i s_j$, summing over all individual elements and pairs of elements in the system, and J_{ij} is a matrix determining any energetic couplings (interactions) between elements i and j. The dynamics of the system can then be simulated by applying random perturbations to the states s_i and considering the change in energy that a given perturbation provokes.

If coupling is strong in a system (many off-diagonal elements of J_{ij} are of large magnitude), the effect of changing the state of one element depends strongly on the states of the elements with which it interacts. Consider an interaction matrix structured such that it is beneficial for interacting groups of elements to be in the same state (corresponding to a ferromagnetic regime, if elements represent spin domains). Strong coupling between elements will then disfavour events whereby one element changes to a state different to the state shared by its neighbours (for example, an element surrounded by elements of state 1 changing from 1 to -1). By contrast, if coupling between elements is weak, the energetic effect of such a change is localised, and the disfavouring of an isolated element changing state will be less pronounced.

We now draw an analogy to the mitochondrial system. Consider representing individual mitochondria as elements within the Ising model described above. Elements interact (with a non-zero J_{ij} term) if the corresponding mitochondria are fused; elements corresponding to isolated mitochondria do not interact with any others. We will consider the states 1 and -1 to

be heuristic markers of 'functionality' and 'dysfunctionality' respectively, but it is not difficult to picture more physical interpretations involving, for example, different states of matrix alkalinisation or membrane potential. Then, for an isolated mitochondrion to go from a functional to dysfunctional state, a change '$(1) \rightarrow (-1)$' has to occur. If several mitochondria are fused, the required change is now placed in a coupled context e.g. '$(1)(1)(1) \rightarrow (1)(-1)(1)$'. If interactions favour similar states in coupled elements (a ferromagnetic picture), the latter change will be less favoured and will occur with lower frequency. Such ferromagnet-like interaction are appropriate when we consider e.g. concentrations of chemical species within a contiguous fused matrix (or membrane potential across a continuous membrane), where perturbations are expected to equalise across the continuous domains involved. If, for example, a mitochondrion in a fused chain experiences a sudden change in membrane permeability, ions from neighbouring mitochondria will buffer the resulting change in $\Delta\psi$.

A chain of n fused mitochondria is then represented by a sequence of n digits and a mitochondrion chosen randomly from this chain is likely to have two neighbours that influence its state. Glauber dynamics [384] are useful for developing intuition about such a system. In short chains, randomly chosen elements have a higher probability of having fewer neighbours, and greater variability in their individual states is therefore supported. In longer chains, strings of identical digits are more likely to occur because of the tendency of elements to take the same value as their neighbours. This, combined with the observation that mitochondria with higher $\Delta\psi$ have a higher fusion probability (in our picture, elements that are fused to a chain are more likely to be in state 1 than -1) results in an all-1 state being more favoured in longer chains than shorter chains.

The system described above is only of use as a coarse-grained model for collective dynamics of fused mitochondria. Further progress could be made by considering continuous states (allowing elements to have states $s_i \in [-1, 1]$), which is more appropriate as e.g. chemical concentrations and membrane potential are continuous variables. With a more realistic representation of mitochondrial 'state', specific estimates of appropriate interaction terms J_{ij} could be explored.

A.2 Additional hypotheses on the function of mitochondrial meso- and hyperfusion

A.2.1 Fusion allows for the possibility of creating a genetic reservoir

Summary. If mitochondria are fused, they are protected from mitophagy [148, 158]. This means that mutant mtDNA molecules within a fused chain are safe from degradation, allowing the creation of a 'genetic reservoir' of mutations. Having a reservoir of a variety of mtDNA mutations in a population can be beneficial as it allows for adaptation to the environment, increasing the 'evolvability' of the population [385]. This idea is also briefly mentioned in Ref. [179].

Experimental support. Mitochondrial 'microheteroplasmy' [386], the universal presence of low levels of heteroplasmy, has been observed in human cells [88], supporting the idea that a pool of genetic variation is present in the mitochondrial population.

Limitations/Critique. (i) It is not immediately clear how important mitochondrial meso- or hyperfusion are in creating a genetic reservoir because the cell can fine-tune the level of quality control by changing the amount of mitochondrial biogenesis or the rate of mitophagy. (ii) We believe that even during hyperfusion, quality control is present in the background ($\gamma_{fis} \neq 0$) which may reduce the size of the reservoir created. A form of static hyperfusion, where mitochondria are permanently locked together, would likely be physiologically damaging (as suggested by studies on hFis1 or Drp1 knockouts [59, 64, 151, 173]). (iii) This hypothesis states that fusion prevents damaging mtDNA mutations from being lost because if the mitochondrion carrying the mutation had been fragmented, it would eventually have been degraded. However, if a mutation causes damage to a mitochondrion, then the mitochondrion may not even be able to fuse because only mitochondria with sufficiently high $\Delta\psi$ are capable of doing so [59]. Mutations that are not harmful may indeed survive longer if they reside inside a fused network, but they could have survived without a network too, especially if the mutation gives them a proliferative advantage. (iv) The link between genotype and phenotype in mitochondria is leaky [191], meaning that it may be hard for mitochondrial quality control mechanisms to select for mutated mtDNA and therefore even without increased fusion mtDNA mutations can survive.

Experimental tests. Start with a population of wildtype heteroplasmic cells (where one type of mtDNA is pathological) and then induce mitochondrial network forming in half of them (by either decreasing fission or increasing fusion). In both populations, the relative frequencies of the two types of mtDNA can be determined. One can measure these frequencies again at a

later time and observe whether the number of pathological mtDNAs that survived is higher in the cells with highly fused mitochondria.

A.2.2 Fusion increases ATP synthesis; hypotheses (i), (ii) and (iii)

Three hypotheses that complement Section 2.4.3 of Chapter 2 are briefly discussed here, though in less detail than the hypotheses discussed in the chapter.

A.2.2.1 Hypothesis (i): Higher [ATP] is caused by fusion-induced changes in inner membrane shape

Summary and Experimental support. Upon fusion, the activity of OPA1 can change cristae morphology [193–195] which may cause changes in respiratory capacity. Because ATP synthase dimers are mainly located at the crista membrane [45, 46], changes in cristae shape can alter the number of ATPase dimers embedded in the membrane [46].

Various experimental studies show support for the idea that fusion-induced reshaping of the crista membrane increases respiratory capacity [148, 149]. ATP synthase dimers may be able to curve the inner mitochondrial membrane, possibly leading to the formation of new cristae [387]. Indeed, not only the ratio of ATP synthase dimers to monomers was increased during starvation, also the number of cristae per unit mitochondrial surface area was increased [148]. Another way in which changes in shape of the inner membrane can modulate energy output is by inducing changes in proton densities. Membranes with high curvature can accommodate a higher proton density than membranes with low curvature [388].

Limitations/Critique. It is not clear why fusion should be required to allow for changes in inner membrane shape; presumably a fragmented mitochondrion can do this on its own. Indeed, it has recently been found that cristae regulation by OPA1 is independent of its role in fusion [196]. It is interesting, however, that the protein involved in inner membrane fusion is also responsible for reshaping the cristae structure. It could be that there is a reason these two processes are linked, perhaps fusion provides more space (and more lipids) to change cristae structure.

Experimental tests. Measure the number of cristae and ATP synthase dimers in fused filaments of mitochondria with different lengths, to search for a correlation between filament size and the number of cristae and ATP dimers. Similar experiments have been performed previously, in which both cristae- and dimer number were observed to increase upon starvation-

induced hyperfusion [148]. Starvation, however, will affect cell metabolism and it may be that the increases in cristae and dimer number are not a direct consequence of increased fusion.

A.2.2.2 Hypothesis (ii): Higher [ATP] is caused by fusion-induced decreases in proton leak

Summary. Proton leakage across the inner mitochondrial membrane leads to decreased efficiency of the electron transport chain machinery [389]. Fusion could lead to a decrease in the amount of proton leak, meaning that ATP production would become more efficient in a fused state (more ATP produced per substrate reduced).

Experimental support. This idea is supported by the observation that mitochondrial fragmentation in brown adipose tissue promotes a shift from using nutrient oxidation for ATP synthesis, to using it for heat generation (which is caused by increased proton leak) [197]. The authors find that fragmentation is required to induce this increased proton leak in hormonally stimulated brown adipocytes [197]. Mitochondrial dynamics might thus change the efficiency of ATP production, with efficiency being high if mitochondria are fused and low in fragmented states.

Limitations/Critique. This hypothesis is based on measurements of leak in brown adipose tissue; it is not clear whether the results hold for other tissues as well. Brown adipose tissue is specialised in heat generation and proton leak may play a less important role in other tissues. Moreover, the mechanism causing the changes in leak involved the protein Uncoupler Protein 1 (Ucp1) [197] which is specific to brown adipocytes and therefore this mechanism may not exist in other tissues (other tissues do contain isoforms of Ucp1, called Ucp2, Ucp3, Ucp4 and Ucp5).

Experimental tests. Measure whether there exists a correlation between the amount of proton leak and the length of a mitochondrial filament in cells other than brown adipocytes. To avoid side effects from overexpressing or downregulating specific proteins, one can use the natural heterogeneity of mitochondrial length in wildtype cells.

A.2.2.3 Hypothesis (iii): Higher [ATP] is caused by fusion-induced decreases in mitochondrial degradation

Summary. Mitochondria that are part of a large network are spared from mitophagy and it has been suggested that hyperfusion is a mechanism to protect mitochondria from degradation [148,

158]. The cause of less degradation during hyperfusion can simply be that only mitochondria under a certain threshold size can be captured by an autophagosomal membrane. Degradation of mitochondria, however, occurs for a reason and stopping this degradation can have negative consequences.

Experimental support. Inhibiting mitophagy causes both reductions in cellular ATP levels and increased ROS production, most likely because damaged mitochondria are unable to be removed [390]. Fragmentation of damaged mitochondria was observed to precede mitophagy [148]. Upon starvation, which causes mitochondrial elongation in wildtype cells, mitochondrial proteins were degraded faster in cells lacking OPA1 (i.e. cells unable to fuse their mitochondria) while they were retained in cells lacking Drp1 (i.e. cells unable to fission their mitochondria) [148]. Similar observations were made in Ref. [158].

Limitations/Critique. This hypothesis relies on an increase in mitochondrial mass as a result of a decrease in mitochondrial degradation. Whether this is true, however, is not clear. The cell may have control over total mitochondrial mass (energy production is crucial for the cell and one may expect it to be highly controlled) and reduce mitochondrial biogenesis in response to decreases in mitophagy. There could of course be other reasons for wanting to reduce rates of mitophagy that we are yet unaware of.

Experimental tests. Measure mitochondrial mass and the amount of mitophagy in a fragmented state and a hyperfused state, to see whether decreases in mitophagy levels (which occur in hyperfused states) lead to increases in mitochondrial mass. It would also be interesting to measure whether mitochondrial biogenesis is decreased as a response to a decrease in mitophagy. Such a homeostatic control is assumed in the models of mtDNA dynamics we discuss in Chapters 4 and 5.

A.2.3 Fusion creates distributional 'power cables'

Summary. Fused mitochondria facilitate the distribution of respiratory capacity through the cell. If mitochondria form long extended networks, then the electrochemical gradient (i.e. the proton motive force) may equilibrate across the whole network by movement of protons or other cations along mitochondria. This makes it possible for a mitochondrion at one end of a fused chain to use the electrochemical potential generated by a mitochondrion at another end of the chain to create ATP. Oxygen and nutrient levels will be higher at the cell's periphery and therefore mitochondria in central regions of the cell can take advantage of the electrochemical gradient produced by peripheral mitochondria. Mitochondrial networks may thus be used as

'power cables' to enable power transmission across the cell [180–186]. An illustration is given in Figure 2.6B of Chapter 2.

The cable mechanism suggests several cellular advantages of mitochondrial fusion. 3D diffusion of ATP or oxygen through the cytoplasm can be replaced by 1D movement of cations along mitochondrial filaments; the speed of energy transmission is therefore likely to increase due to the reduced dimensionality and increasingly directed nature of the motion. Another advantage is that cabling may reduce damage by reactive oxygen species (ROS) in the core of the cell where nuclear DNA is present. This is because ROS is generated at sites where the ETC is active and the power cabling hypothesis predicts that this is mainly at the cell periphery.

Experimental support. When ATP is used more in certain parts of the cell, mitochondria tend to cluster around these parts suggesting that ATP supply from distal mitochondria to these regions is not sufficient [391]. Several tissues have very limited mitochondrial movement (e.g. heart cells [261]); cabling could provide a way to ensure adequate ATP supply to these regions. A recent study found evidence for tight electrical coupling between peripherally and centrally located mitochondria in skeletal muscle [184], and similar observations were made in cardiomyocytes [185]. Moreover, the authors of Ref. [184] observed the density of complex IV (involved in creating the proton gradient) to be highest at the cell periphery, whereas complex V (which uses the gradient to synthesise ATP) was most abundant in intra-fibrillar regions, further away from oxygen-supplying blood vessels. A later study by the same authors suggested that proton movement along mitochondria is not sufficient to equilibrate the proton motive force between the peripheral and central regions in skeletal muscle cells at high respiration [186]. Instead, they suggest movement of K^+ and Na^+ (whose concentrations are much higher compared to protons) which can be exchanges for protons via K^+/H^+ and Na^+/H^+ antiporters at either end of the mitochondrial chain (Figure 2.6B).

Coarse-grained quantitative model. To make progress exploring the implications of the cable hypothesis for ATP production, we first estimate the speed gain obtained though cabling by comparing the diffusion time of oxygen through the cytoplasm with that of H^+ along mitochondrial membranes. Performing this calculation with values measured in biological experiments suggests that cables facilitate an order-of-magnitude increase in ATP production (see below), thus providing a quantitative suggestion that mitochondrial power cables can be beneficial to the cell. We note, however, that this estimation may be of limited use because of the recent finding that protons are unlikely to be the main contributors to equilibration of potential [186].

Further modelling. The flow of electricity in a leaky cable (a long cylindrical piece of mem-

brane) is described by the cable equation [392]. The cable equation is used to study electrical flow in neurons but may be applied to a chain of electrically continuous mitochondria as well, providing more fine-grained physical insight into the electrochemical dynamics of mitochondrial power cables.

Limitations/Critique. The speedup of ATP synthesis rate obtained by using cables is likely to be reduced because silent fission events, i.e. fission events without physical separation, will slow down the diffusing cations (these type of events were measured to occur with a probability around 50% over five minutes in a filament not longer than 4μm in COS7 cells [207]). The respiratory complex that uses oxygen (complex IV) has a reaction capacity which normally exceeds the maximal rate of the respiratory chain and can operate at low oxygen tension [393], which weakens the statement that oxygen supply is a rate limiting step in respiration. The cabling hypothesis may represent a reason for mitochondrial fusion in skeletal muscle cells because these are highly dependent on oxygen supply and have high ATP demands. It is less clear, however, how meso- and hyperfusion can be explained in other tissues less dependent on oxygen and with lower ATP demands. The hypothesis also has difficulties explaining the high frequency of fission and fusion rate. Finally, H_2O_2, a source for ROS damage, is able to diffuse freely across several cell lengths and can thus induce damage far from the site of ROS generation [394], questioning the ability of cabling to reduce ROS damage in the core of the cell where nuclear DNA is present.

Experimental tests. The power cabling hypothesis predicts that there exists an oxygen gradient between the periphery of the cell and the cell core, which can be tested experimentally. Measurements of pH differences and cationic fluxes between the peripheral and central regions will further elucidate the mechanisms by which the proton motive force is transported along the cables.

A.2.3.1 Order of magnitude increase in energy production using mitochondrial power cabling

We here provide an explanation of the claim made above that cabling facilitates an order-of-magnitude increase in ATP production. This quantitative argument proceeds by considering the ATP generation in a central region of the cell where oxygen concentration is low. We will compare two cases. Firstly, a 'null' case with no cabling, where oxygen must diffuse from a peripheral region of the cell to act as an electron acceptor for ETC complexes in this central region. Secondly, a 'cabling' case, where proton pumping is performed by ETC complexes in

the oxygen-rich peripheral region, then protons are 'cabled' to central, low-oxygen region to facilitate ATP production.

We will discuss diffusion of oxygen in skeletal muscle cells because the cable hypothesis was developed studying these cells. We will use a diffusion coefficient of $D_{O_2} = (2.7 \pm 0.3) \times 10^{-7}$ cm^2/s [395, 396] for oxygen diffusing through the cytoplasm. For protons we set $D_{H^+} = (5.7 \pm 0.7) \times 10^{-5}$ cm^2/s [397]. The proton diffusion coefficient was calculated assuming 2D diffusion so in our estimation we should treat it as such [397] (the calculated value of D_{H^+} would be different if 1D diffusion was assumed, so the diffusion constant obtained in Ref. [397] is specific for 2D diffusion). We argued before that proton diffusion along mitochondrial membranes can be described as a 1D diffusion process which increases the diffusion speed. We are merely providing an order of magnitude estimation here so for our purposes we can ignore dimensionality ambiguities. Assuming random diffusion (no bias) then the ratio of the time for oxygen to diffuse across a distance x, t_{O_2}, to that of protons, t_H^+, is given by

$$\frac{t_{O_2}}{t_H^+} \approx \frac{D_H^+}{D_{O_2}} \approx 214 \pm 36. \tag{A.20}$$

Suppose the number of protons necessary for the production of one ATP molecule is n ($n \approx 3$). The net reaction of complexes I, III and IV of the respiratory chain is

$$2NADH + 22H^+_{matrix} + O_2 \quad \rightarrow \quad 2NAD^+ + 20H^+_{IMS} + 2H_2O, \tag{A.21}$$

hence, for every oxygen molecule used, 20 protons are pumped into the intermembrane space.

We now compare ATP production in the case that oxygen concentration is limiting. We assume that the flux of n protons down the electrochemical gradient and through complex V is required to create one ATP molecule. The presence of one oxygen molecule thus facilitates the production of about $20/n$ ATP molecules, or 20 times more than are produced through the presence of one proton. The rate at which oxygen is supplied to a mitochondrion can thus be 20 times less than the rate at which protons are supplied while still resulting in the same rate of ATP synthesis. Combining this with Equation (A.20), we estimate that using proton diffusion along mitochondrial membranes to generate ATP where oxygen diffusion is limited, the rate of ATP production will be about an order of magnitude larger.

A.2.4 Meso- and hyperfusion have no function

Summary. It is possible that mitochondrial meso- and hyperfusion do not provide any additional advantage to the cell. Changes in the balance between fusion and fission events can arise naturally as a consequence of changes in activities of mitochondrial fission and fusion proteins; large-scale fusion may thus represent an epiphenomenon. Mesofusion may also be a side effect of mitochondrial clustering in regions of high ATP demand.

Experimental support. Mammalian mitochondria are connected to microtubules via motor proteins that mediate their (ATP-dependent) transport, which can cause long strings of mitochondria to form [398]. These 'long bundles' of mitochondria have been observed in cardiomyocytes [261]. When changes occur in the activities of mitochondrial fusion/fission proteins, this manner of alignment can facilitate connected filaments to arise because the mitochondria are already lying end-to-end, ready to form a continuous filament. Changes in the microtubule network may also alter mitochondrial morphology.

The main fusion and fission proteins, OPA1, MFN1,2 and Drp1, all have other functions in the cell and Drp1 can undergo numerous post-translational modifications. Overviews of these additional functions and post-translational modifications are given in Tables A.4 and A.5. OPA1 also undergoes modifications and can be cleaved to shorter isoforms by various proteins [236, 399–403]. We stress that the fact that many different proteins and post-translational modifications have effects on mitochondrial morphology can lead to two entirely different conclusions: i) mitochondrial dynamics has a highly important function and needs to be controlled by various pathways, and ii) mitochondrial dynamics is an epiphenomenon and changes in morphology occur because of natural fluctuations in the activities of the mitochondrial shaping proteins.

Experimental tests. We do not propose approaches to model or experimentally test this case, but instead suggest that it is regarded as the 'null hypothesis' against which other alternative hypotheses for mitochondrial network formation may be compared.

A.3 Tables

Condition under which extended fusion is observed	Cell type	Cause of extended fusion.	Ref.
G1-S or G1 phase of the cell cycle	Normal rat kidney cells (G1-S) and human osteosarcoma cells (G1)	Not reported	[151, 404]
Various kinds of stress including starvation, oxidative stress, UV irradiation and cycloheximide	Various cell types including MEFs, mouse primary fibroblasts, hepatocytes, human HeLa and Cos-7 cells and HEK293T cells	In the case of starvation, decreased Drp1 Ser-616 and increased Drp1 Ser-637 phosphorylation was observed [148, 158]. The stress induced hyperfusion studied by [149] was suggested to be caused by increased fusion rather than decreased fission	[148, 149, 158, 167, 405]
In long-living individuals (100.67 ± 2.88 years) mitochondria formed more fused, elongated structures than in young (27.83 ± 3.97 years) or old (75.67 ± 10.86 years) individuals	Dermal fibroblasts	The cause was suggested to be mainly decreased fission rather than increased fusion	[154]
Mitochondrial length increased during aging, senescent cells shows long and interconnected mitochondria	HUVEC cells	A reduced expression of hFis1 and Drp1 was observed	[254]
Prolonged incubation with 20 nM MitoQ, an antioxidant	HeLa cells and normal human fibroblasts	Suggested to be decreased fission	[406]
Cells grown in glucose rather than galactose media	HeLa cells	Not reported	[407]

Table A.1: Occurrences and causes of hyperfusion in wildtype cells. Here we list conditions under which wildtype cells show highly fused mitochondrial structures. The cause of the fused morphology (increased fusion, decreased fission or both) is reported if known.

Normal morphological state	Cell type	Ref.
- 1 day old cells show mainly tubular or intermediate (both fragmented and elongated) morphologies - 5 days old cells show an intermediate morphology - 11 days old cells show intermediate or very fragmented mitochondria - 16 days old cells show mostly very fragmented mitochondria	*C. elegans* body wall muscle	[408]
Typical cells show mitochondria dispersed throughout the cytosol and their shape seems to be round, ellipsoid-, or sausage-like	human Cos-7 cells	[409]
Wildtype cells typically show a tubular network structure	MEFs	[62]
Under standard culturing conditions, 40% of the cells had mostly tubular mitochondria, 50% mostly fragmented mitochondria and 10% of the cells had an intermediate state (in which both fragmented and branched mitochondria coexisted in roughly equal amounts).	human osteosarcoma cells	[404]
Mitochondria in wildtype cells grown in media containing galactose appear interconnected. Shifting cells from aerobic to anaerobic growth did not affect mitochondrial structure (at least not within 7 hours)	yeast *S. cerevisiae*	[410]
Both glucose and glycerol-grown cells show a single large mitochondrial component with few fragmented smaller ones. The large mitochondrial component was about four times more branched in glycerol grown cells, and mitochondrial volume was three times larger in glycerol grown cells	yeast *S. cerevisiae*	[411]
- Cells grown in media with 2% glucose showed an elongated mitochondrial structure - in media with 0.5% glucose mitochondria appeared shorter - in media with 4% glucose mitochondria had few connections and branches	yeast *S. cerevisiae*	[412]
- Cells grown in glucose cultures show elongated and branched mitochondria - Cells grown in ethanol have smaller/shorter mitochondria compared to those grown in glucose cultures (total mitochondrial volume was the same) - Cells in aerobic glucose-limited chemostat cultures have many short mitochondria - Cells in anaerobic fermentative chemostat cultures have elongated mitochondria	yeast *S. cerevisiae*	[413]

Table A.2: Typical mitochondrial morphology in a variety of cells. To obtain a better idea of the 'normal' morphological state of mitochondria, we provide an overview of observed 'typical' mitochondrial distributions. One has to keep in mind that the morphological state depends on cell function and cell cycle. Many studies investigate mitochondrial morphology by staining with TMRE, JC-1 (both of which are dyes for mitochondrial membrane potential) or matrix targeted GFP (Green Fluorescent Protein). However, as was stated in Ref. [207]: 'the non-fragmented shape of the web as revealed by TMRE alone does not reliably predict the boundaries of a network'. It is therefore hard to know exactly how fused mitochondria actually were in studies that do not check for continuity with photoactivatable GFP.

Species of interest	Diffusion coefficient ($\mu m^2/s$)	Ref.
Complex V:		
(mobile fraction)	0.082 ± 0.002 (s.e.m.)	[190]
(less mobile fraction)	0.019 ± 0.001 (s.e.m.)	[190]
(immobile fraction)	0.006 ± 0.001 (s.d.)	[190]
Complex II:		
(mobile fraction)	0.140 ± 0.005 (s.e.m.)	[190]
(less mobile fraction)	0.039 ± 0.002 (s.e.m.)	[190]
(immobile fraction)	0.004	[190]
(mobile fraction)	0.161	[353]
(less mobile fraction)	0.003	[353]
Matrix targeted GFP	20-30	[234]
Matrix targeted EYFP: In stationary mitochondria In moving mitochondria	 22 ± 2.1 (s.d., N = 12) 18 ± 4.7 (s.d., N = 46)	[414]
Mobile fraction of TFAM labelled mtDNA	0.05 ± 0.01	[191]
mtDNA stained with ethidium	10^{-3}	[354]
Mobile fraction (93 ± 6%) of outer membrane protein TOM7	0.7-1	[415]
Mobile fraction (93 ± 5%) of outer membrane protein hFis1	0.4-1	[415]
Outer membrane protein Tom40	0.5	[416]

Table A.3: Diffusion constants of several mitochondrial proteins. GFP and EYFP stand for Green Fluorescent Protein and Enhanced Yellow Fluorescen Protein, respectively.

Modifier	Modification effect on Drp1	Ref.
Protein Kinase A (PKA)	Phosphorylation of Drp1 at Ser-637 which prevents Drp1 from tethering to mitochondria. Drp1 remains retained in the cytosol instead	[417]
CaM kinase Iα, ROCK1	Phosphorylation of Drp1 at Ser-637 which caused increased mitochondrial fission	[418, 419]
Cdk1, Cdk5, PKCδ, Erk1/2	Phosphorylation of Drp1 at Ser-616 which activates Drp1	[420–423]
Calcineurin	Dephosphorylation of Drp1 at Ser-637 making Drp1 capable of translocating to mitochondria	[424]
MAPL, SUMO1,2,3	Sumoylation of Drp1 which affects it GTPase cycle	[425, 426]
O-GlcNAc-transferase and N-acetyl-glucosaminidase	O-linked-N-acetyl-glucosamine glycosylation of Drp1 at threonine 585 or 586. This decreases phosphorylation at Ser-637 and results in increased translocation of Drp1 to mitochondria	[427]
Bax and Bak	Promotion of sumoylation of Drp1 during apoptosis	[428]
MITOL/MARCH5	Ubiquitination of both hFis1 and Drp1	[429, 430]

Table A.4: Overview of various post-translational modifications of the GTPase Drp1 which mediates mitochondrial fission.

Protein name	Processes other than fusion and fission in which the protein is involved	Role of the protein	Ref.
OPA1	Regulation of cristae morphology	OPA1 oligomers may wrap around crista junctions to keep them tight	[193, 194]
	Apoptosis	By tightening crista junctions, cytochrome c is kept inside the cristae instead of diffusing into the cytosol and inducing apoptosis	[58, 193, 194]
	Depolarization events	OPA1 causes reversible depolarization events after matrix contractions	[431, 432]
MFN2	Mitochondria-ER interactions and calcium homeostasis	MFN2 tethers mitochondria to the ER	[433]
	Oxidative phosphorylation gene expression	Independently of its role in fusion, MFN2 regulates expression of OXPHOS genes	[434]
	Apoptosis	A MFN2 mutant has been observed to increase cytochrome c release following DNA damage and ROS damage, suggesting that MFN2, just like OPA1, works to keep cytochrome c inside the cristae	[161]
MFN1	Apoptosis	MFN1 may regulate activation of the pro-apoptotic protein Bax	[435]
Drp1	Apoptosis	Drp1 is transported to mitochondria upon apoptosis induction. Inhibition of Drp1 can prevent apoptosis	[436]

Table A.5: Functions of the mitochondrial fusion and fission proteins other than inducing mitochondrial fusion or fission.

B

Supplemental information complementing Chapter 4

This appendix complements Chapter 4, and is split into five sections:

1. In the first section we provide details on our choice of parameters in comparing different control strategies
2. In the second section we define and motivate our linear and saturating output models
3. In the third section we estimate, derive and/or motivate all parameter values used in our cost function
4. In the fourth section we show various cost function outputs and illustrate the cause and robustness of expensive intermediate heteroplasmy states
5. In the last section we show predictions based on our nuclease treatment model

B.1 Feedback control of a heteroplasmic mtDNA population

Figure 4.1 in Chapter 4 shows the near equivalence of mean wildtype, mutant, and heteroplasmy dynamics between three different forms of control, all of the form $\lambda(w, m) = \lambda(w + \delta m)$: i)

$c_0 - c_1(w + \delta m)$, ii) $d_0 + d_1/(w + \delta m)$ and iii) $s_0 - s_1(w + \delta m)^2$ with $c_0, c_1, d_0, d_1, s_0, s_1 > 0$. Here we complement this figure by showing that the variance dynamics are also nearly identical (Figure B.1A, B, C).

We merely show that these different controls *can* give rise to similar dynamics by parameterising them such that they do. First, we set the variances of each control to be equal in the absence of mutants. From Table 4.1E it can be seen that the wildtype variance is now completely specified by the mtDNA degradation rate μ, the steady state copy number w_{ss} and the control derivative $\partial_w \lambda(w)$ evaluated at steady state. The latter quantity is given by i) $-c_1$, ii) $-d_1/w_{ss}^2$ and iii) $-2s_1 w_{ss}$ for the three controls defined above. These expressions were all set to be -7.21×10^{-6}, a value that was chosen such that the wildtype steady state distribution has a coefficient of variation of $CV = 0.1$. This value is arbitrary, other choices of give similar results. We use a deterministic wildtype steady state of 1000 (in the absence of mutants), which fixes the other control parameters. Note that it is not surprising that these different controls yield similar dynamics after we have parameterised them to do so; we want to illustrate these similarities to stress that *which quantity is being controlled can be more important than how it is controlled.* This is particularly true when dynamics are close to steady state, in which case a linear control forms a good approximation to many non-linear controls.

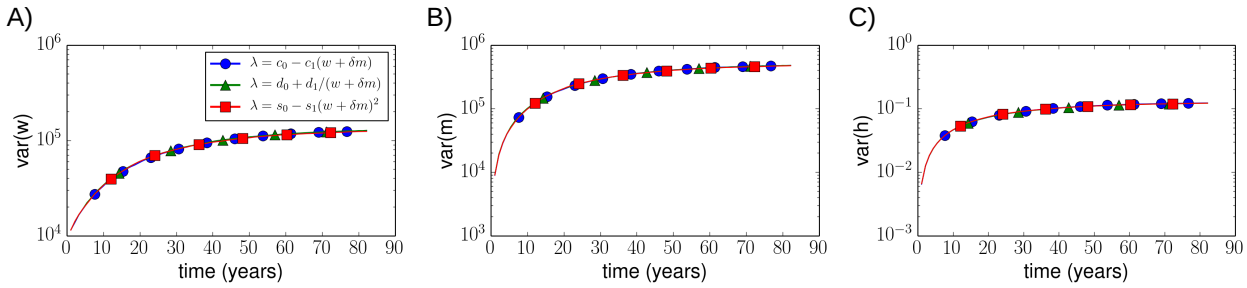


Figure B.1: Equal variances for different feedback control mechanisms. Related to Figure 4.1A-C; Three different controls (see legend), all of the form $\lambda(w + \delta m)$ with $\delta = 0.5$, show nearly identical wildtype, mutant and heteroplasmy variances. Other parameters used are $N_{ss} = 1000$ (referring to the steady state copy number present in the absence of mutants), $\mu = 0.07$ (corresponding to a half-life of 10 days), and initial copy numbers $(w_0, m_0) = (920, 160)$ (corresponding to an initial heteroplasmy of ~ 0.15).

B.2 The relationship between resource consumption and energy production: $s_i(r_i)$

B.2.1 A linear output model

In our cost function we need to specify how s_i, the power supply measured in ATP/s (including leak) of a mitochondrion of type i, depends on r_i, a quantity resembling the resource consumption rate of the mitochondrion. For robustness, we use two different equations for $s_i(r_i)$.

The first model is based on measurements in isolated mitochondria which found a linear relationship between r_i and s_i (e.g. [295–297]). Specifically, we use the following equation:

$$s_w(r_w) = \phi(r_w - \beta) \tag{B.1}$$

where ϕ can be mapped to the effective P/O ratio (explained in Section B.3.1) and β indicates the respiration rate at zero energy production and therefore specifies the amount of leak. We used the data from Ref. [295] to fit the parameters of this linear model (Table 4.3, Section B.3.1), the result of which is shown in Figure B.2A in Section B.4.

It is not clear, however, whether the observations made in isolated mitochondria, without any interactions between the mitochondria and the nucleus or the endoplasmic reticulum, still hold *in vivo*. This is one of the reasons to also consider another type of model, as described below.

B.2.2 A saturating output model

Our cost function contains a term which penalises the consumption of resources, meaning that the cheapest state is the one that satisfies demand with the smallest net resource consumption rate. A linear function $s_i(r_i)$ then implies that, for a given demand, the optimal number of mitochondria is the minimum number required to satisfy the demand with these mitochondria respiring as fast as they can (as can be seen in Figure B.2E). However, containing a minimally required number of mitochondria will make a cell less robust to stochastic fluctuations in both mitochondrial copy numbers and demand. Moreover, mitochondria are known to have large spare capacities [298, 299] indicating that in resting state they do not operate near their limits. We therefore expect that there is some extra cellular cost associated with this 'maximally respiring' state, causing it to be non-optimal in resting conditions.

This is why we have chosen to use a second model which describes a saturating relationship between r_i and s_i (visualised in Figure B.2A). Note that we do not claim that mitochondria become less efficient as they respire faster, we impose the saturating shape merely to effectively assign a higher cost to high respiring states. By imposing this saturation, the variable on the y-axis of Figure B.2A can be interpreted an 'effective energy production'. We will refer to the two models as 'the linear output model' and 'the saturating output model'.

A changing energy production efficiency is not entirely unreasonable, though, because in experiments with isolated mitochondria one usually uses a particular substrate (or a particular combination of substrates) whereas a larger mixture of substrates will be available in the cell, and the relative presence of each substrate may fluctuate over time. The efficiency of respiration depends on the kind of substrate that is used, so it may be possible that at high demand (and high respiration) the substrate of first choice has become limited and another less efficient substrate is used instead. Also, it was suggested that spare capacity can be caused by an increase in substrate entrance in the TCA cycle* [437]. This would mean that a state of high respiration is caused by an increase in electron transport chain substrates (e.g. NADH and $FADH_2$). A 'push' to the proton pumping complexes instead of a 'pull' at the ATP synthase would lead to an increase in the electrochemical gradient across the membrane and therefore an increase in leak. These arguments are speculative but show that the saturation model may not be unreasonable.

The saturating model is defined by the equation:

$$\begin{aligned} s_w(r_w) &= 2\frac{s_{max}}{1+e^{-kr_w}} - (1+\Delta)s_{max} \\ s_w(r_w) &= 2\frac{s_{max}}{1+e^{-kr_w}} - 1.1s_{max} \end{aligned} \tag{B.2}$$

where k is the rate at which the model saturates, s_{max} is an indication of the maximum energy production rate, and $\Delta > 0$ is introduced to ensure that, like in the linear model, a nonzero amount of resource is required to maintain a zero energy output (due to proton leak). As proton leak accounts for $\sim 10\%$ of the total energy production in the linear model, we chose $\Delta = 0.1$. We will set the parameter values k and s_{max} such that the saturating and linear model show similar behaviour for low values of r_w (Section B.3.5), as shown in Figure B.2A of Section B.4.

*The tricarboxylic acid (TCA) cycle represents a series of reactions and provides, amongst others, the reducing agent NADH which is used as an input to the electron transport chain.

B.3 Parameter values for the cost function

Some of our results will be a consequence of the exact structure of our cost function, and might have been different if another type of cost function was used. We would argue, however, that the main elements in our cost function are quite general: terms involving supply, demand, and resource. We aimed at making our cost function simple, and using biologically interpretable parameters. We do not aim to give a detailed kinetic description of the energetic costs involved, but present a simpler description that allows us to compare distinct strategies relative to each other rather than providing absolute costs. We use our cost function as a tool to characterise cost landscapes and begin to explore optimal control strategies.

In the spirit of 'back-of-the-envelope' reasoning in biology [116] we seek plausible and interpretable parameter estimates, using both order-of-magnitude estimations and values found in the literature. Default parameter values are summarised in Table 4.3.

The final goal is to obtain a cost for a state with a certain number of mtDNA molecules; we therefore need to express our cost as a cost 'per mtDNA molecule'. Because the density of mtDNA molecules within the mitochondrial network seems to be roughly constant [280], we assume every mtDNA molecule is associated to a particular amount of mitochondrial volume which we here define as a 'mitochondrial unit'. All our parameters refer to these mitochondrial units.

B.3.1 Mitochondrial energy production and leak: ϕ and β

Mitochondrial respiration is a process by which energy from nutrients is converted into (amongst others) ATP. Part of this process involves the pumping of protons across the inner mitochondrial membrane to create an electrochemical potential across the membrane. Energy is released when protons flow back into the matrix and this energy can be used to create ATP. However, the coupling between proton pumping and ATP synthesis is not perfect and protons can leak through the membrane, reducing the efficiency of respiration. An often measured quantity in experimental studies is the mechanistic P/O ratio [438, 439] which refers to the theoretical maximum amount of ATP (P) produced per oxygen (O) reduced by the respiratory chain. The effective P/O ratio is more physiologically relevant and takes into account leak [297].

In our linear model we assume a linear relationship between mitochondrial ATP production rate and mitochondrial oxygen consumption rate, based on experimental data [295–297]. In Refs. [295, 296] measurements show an almost perfect linear relationship between these two

quantities, which is consistent with data from Ref. [297].The parameters ϕ and β correspond to the slope and intercept of the linear function, respectively. In Ref. [295] this slope was measured to be 2.03 ± 0.13 for isolated pectoralis muscle cell mitochondria in the presence of pyruvate and malate; we have decided to use $\phi = 2$, mainly based on these experiments.

The value of β is an indication of the 'leakiness' of the mitochondrion: it represents the rate of oxygen consumption that is required to balance the leakage of protons across the membrane in order to maintain the mitochondrial membrane potential. To obtain a consistent value for β we also use the data presented in Ref. [295]. Their measurements find that β is about a tenth of the maximum respiration rate. This maximum respiration rate is obtained by adding high (unlimited) concentrations of ADP; the state of the cell in these conditions is known as state 3_{ADP}. Because state 3_{ADP} does not necessarily correspond to *in vivo* conditions, we define the respiration rate in this state as $r_{max,t}$: the maximum 'theoretical' respiration rate. We will fix $r_{max,t} = 1$ and use this to scale our other parameters. This means that our parameter value for β is $\beta = 0.1$.

We stress that though we have based our parameter values here on a specific study, changes in their values will not affect the qualitative structure of our cost function but merely changes the slope and intercept of the linear output function defined in equation (B.1).

B.3.2 Resource and supply and maintenance cost: r_{max}, r_n and s_n

A cell *in vivo* is unlikely to experience the high concentrations of ADP present in state 3_{ADP} (defined above). We therefore set our parameter r_{max}, the physiological maximum respiration rate, to be slightly below $r_{max,t}$, i.e. $r_{max} = 0.95 \cdot r_{max,t} = 0.95$.

We introduce r_n and s_n as the 'normal' respiration rate and ATP production rate which are present in resting conditions, respectively. Their values are not used directly in our model equations, but only to connect our parameter estimates to actual physiological values (Section B.3.8). Mitochondria have spare capacity, i.e. in normal unstressed conditions they use only part of their maximal oxygen consumption rate (OCR). The amount of spare capacity is usually measured as the fold-change in OCR that occurs after adding FCCP to cells, a mitochondrial uncoupler. Several measurements of the fold-change in OCR are: in the range (2-4)-fold [440], 1.4- to 2.5-fold [437], about 2-fold [298] and about 2.5-fold [299]. The maximum respiration rate when adding FCCP is known as State 3_{FCCP}, and is higher than State 3_{ADP} (see e.g. [441]). We interpret the spare capacity as the ratio State $3_{\text{FCCP}}/r_n$, meaning that the ratio r_{max}/r_n is lower than this. We have decided to take $r_{max}/r_n = 1.5$, meaning that $r_n = r_{max}/1.5 \approx 0.63$.

For the linear output model, the value of s_n is now simply $s_n = s_w(r_n) \approx 1.1$ (this abstract value is related to actual values in ATP/s in Section B.3.8).

B.3.3 Maintaining, building and degrading: ρ_1, ρ_2 and ρ_3

The model organism with the most quantitative data on mitochondrial energy budgets is budding yeast, *Saccharomyces cerevisiae*. Reasoning that the scales of biophysical costs of mitochondria are likely comparable across eukaryotes, we first draw from this literature to motivate order-of-magnitude estimates for a range of essential mitochondrial processes. We will later construct parallel estimates using other organisms.

We first focus on estimating the mitochondrial building cost ρ_2 (in ATP). We provide three distinct estimations and combine them to obtain our final estimate.

For the first estimation we use a list of mitochondrial proteins in yeast [442], and obtain information on turnover rates, abundance (per yeast cell), and lengths (amino acid length) of these proteins by using the Saccharomyces Genome Database [443]. We end up with a list of $\sim$ 200 mitochondrial proteins in yeast *S. cerevisiae*. We incorporate the observation that it takes about 5.2 ATP molecules to elongate a growing peptide chain by adding an amino acid [444], which means that the total synthesis cost of the mitochondrial proteins included in our list is given by $5.2 \sum_i \text{length}_i \text{abundance}_i \approx 2 \times 10^{10}$ ATP per yeast cell. The known number of mitochondrial proteins in *S. cerevisiae* is on the order of 1000 [445]; we will therefore assume that the protein synthesis cost obtained from our protein list corresponds to roughly a fifth of the total mitochondrial protein synthesis cost. We might expect that the proteins best known [442] are the more abundant ones, meaning that our final cost is likely to be an overestimate. We also assume that all of the mitochondrially associated proteins are used exclusively for mitochondrial function. In *E. coli*, the mitochondrial protein synthesis cost represents $\sim$50% of the total mitochondrial synthesis cost (two other major contributors are phospholipid synthesis and RNA synthesis)[444]; we will make the assumption that this observation in *E. coli* holds in mitochondria as well. This brings the total mitochondrial building cost in a single yeast cell to be $\sim 1.9 \times 10^{11}$ ATP. Assuming 50-100 mtDNA molecules per yeast *S. cerevisiae* cell [446], the building cost associated with a single mtDNA molecule (and therefore the building cost of a mitochondrial unit) is given by $(2 - 4) \times 10^9$ ATP.

For our second estimation we use the total protein weight of a single mitochondrion which was measured to be about 3×10^{-10} mg in rat liver [447], as well as the typical weight of a single protein which is about 5×10^{-17} mg [444]. This means that a mitochondrion contains about

6×10^6 proteins. Using that the typical length of a protein is 300 amino acids [444, 448, 449] together with the 5.2 ATP cost of adding amino acids and the estimation that protein costs represent 50% of the entire building cost, the mitochondrial building cost is estimated to be 2×10^{10} ATP. Note that this cost does not necessarily represent our mitochondrial unit because it is unknown how many mtDNAs a 'mitochondrion' corresponded to when measuring its weight in Ref. [447].

The third estimation is based on the building cost of an *E. coli*, which is about 10^{10} ATP [444]. Keeping in mind that we want the building cost of a fraction of mitochondrial volume corresponding to a single mtDNA molecule, we need to convert the building cost of an *E. coli* (which has a volume of about 1 μm^3) to represent our mitochondrial unit. It was estimated that the total mitochondrial network length in yeast *S. cerevisiae* is about 25 μm with a total mtDNA copy number of 50-100 [446]. Assuming that the mitochondria form tubules with a constant diameter of 300 nm [178] gives a total mitochondrial volume of about 1.8 μm^3; another total mitochondrial volume estimate in yeast *S. cerevisiae* is 1.5 μm^3 [178]. Uniform distributions for the mitochondrial volume (1.5-1.8 μm^3) and mtDNA copy numbers (50-100) leads to a volume of $(2.3 \pm 0.5) \times 10^{-2} \mu m^3$ per mitochondrial unit. This means that rescaling the *E. coli* building cost gives us an estimate of $(2.3 \pm 0.5) \times 10^{-2} \cdot 10^{10} = (2.3 \pm 0.5) \times 10^8$ ATP to build a single mitochondrial unit. Note that this may represent an overestimation because *E. coli* is a unicellular organism, whereas the mitochondrion is an organelle which cannot survive in isolation [450].

While there are differences in these estimates, arising both from uncertainty and different quantitative lines of reasoning, they together give an overall scale for mitochondrial building cost of around 10^9 ATP. Because in our model we only need a rough estimate of the mitochondrial building cost, we use $\rho_2 = 10^9$ ATP.

We interpret the maintenance cost, denoted by ρ_1, as the cost in molecules ATP/s corresponding to, for example, maintaining the mitochondrial lipid membranes, importing/exporting proteins, and synthesizing new proteins. To obtain an estimation of ρ_1, we again use the Saccharomyces Genome Database [443]. We can calculate the cost of continuously turning over the ~ 200 proteins in our list (obtained from [442]), leading to $5.2 \sum_i \text{length}_i \text{abundance}_i (\text{degradation rate})_i \approx 6 \times 10^5$ ATP/s per yeast cell. In other words, the maintenance cost per second of our set of mitochondrial proteins is about five orders of magnitude less than their synthesis cost. We therefore assume $\rho_1 = 10^{-5} \rho_2$.

The mitochondrial degradation cost ρ_3 is the most challenging parameter to estimate, as the

process of mitochondrial degradation remains poorly characterised. Protein production and biosynthesis costs form the bulk of mitochondrial production requirements, and from cell-wide studies on energy budgets are among the most considerable demands in cell biology. We therefore assume that degradation has lower energy requirements than production, and set its upper limit at $\rho_3 = 0.1 \cdot \rho_2$. Lowering ρ_3 further has little impact on the outcomes of our model.

B.3.4 Demand and resource availability: D and R

We want to model two kinds of cells: low copy number cells (1000 wildtype mtDNAs in resting state) and high copy number cells (5000 wildtype mtDNAs in resting state). Denoting this desired number of 'normal' mitochondria by w_n (which are assumed to operate at the 'normal' production rate s_n (Section B.3.2)), we obtain

$$D = w_n(s_n - \rho_1 - \mu\rho_3 - \lambda\rho_2) \tag{B.3}$$

where μ and λ are the degradation and replication rates per second. This equation states that the overall net output of w_n mitochondria exactly satisfies demand. Using $w_n = 1000$ and $w_n = 5000$ leads to $D \approx 1055$ and $D \approx 5275$ ATP/s. These abstract values for demand are mapped to actual cellular ATP demands in Section B.3.8.

The parameter R denotes the maximum rate at which resource can be consumed by all of the mitochondria together and represents a cellular resource availability. In normal resting state the total resource that is consumed is $w_n r_n$, and the resource consumed when these mitochondria respire as fast as they can is $w_n r_{max}$. We then assume this maximal respiration rate is achieved by using all of the available resources, i.e. $R \approx w_n r_{max}$. It may be, however, that a state of maximum respiration can only be maintained for a short time, and in our cost function we want to describe the 'steady state cost' for different states. We therefore use $R < w_n r_{max}$ (R now denotes the maximal respiration rate that can be maintained for longer periods of time). We chose to use $R = 0.8 w_n r_{max}$ leading to $R = 760$ and $R = 3800$ for $w_n = 1000$ and $w_n = 5000$, respectively.

B.3.5 Saturating model parameters: s_{max} and k

We set the parameters of the saturating model described in equation (B.2) such that it matches the linear model for low respiration. This lead to $k = 3.0$ and $s_{max} = 1.54$.

B.3.6 The cost of resource consumption α

The value of α, i.e. the scaling parameter that appears in the cost function given by

$$C(w, m) = |D - S(w, m)| + \alpha(wr_w + mr_m) \tag{B.4}$$

is hard to determine. Its value describes the cost of a unit of resource consumption relative to the cost of a unit of 'energy deficiency' (the cost of $S(w, m)$ being one energy-unit below D). We estimated that a penalty for resource consumption usage should be about an order-of-magnitude less than the penalty for not-satisfying demand, and have therefore decided to assume $\alpha = 0.1$. We note that the value of α has no influence on the shape of the demand-satisfying region, it only changes the relative costs within (and outside of) the region.

B.3.7 Mutant parameters: ϵ_1, ϵ_2

In Chapter 4 we vary the parameter ϵ_1, describing the resource uptake rate of mutants relative to wildtypes. Additionaly, mutants can be less efficient than wildtypes, producing less energy per resource consumed; we denote this lower mutant efficiency by $\epsilon_2 \in [0, 1]$. Because the number of protons that are pumped across the mitochondrial inner membrane by the electron transport chain complexes for every unit of resource (NADH) that is consumed is fixed, a lower ϵ_2 would have to mean that either i) the mutation has increased proton leak (or other ways of depolarising the membrane), or ii) the mutation has made the ATP synthase dysfunctional. The value of ϵ_2 can be related to the P/O ratio of the mutants relative to that of the wildtypes. Most mtDNA mutations, however, affect the electron transport chain complexes themselves and are therefore likely to reduce the flow of resources through the chain (which would mean a low value for ϵ_1). This is why we assume $\epsilon_2 = 1$ in our main model and only vary the parameter $0 < \epsilon_1 < 1$. For completion, here in the SI we provide a heatmap showing the cost in (w, m) space for various values of ϵ_2 (Figure B.3).

B.3.8 Parameter units

We can relate our parameter values to actual values, e.g. expressing our demand D in ATP/s. As an example of an ATP demand we use the ATP production rate in unstressed human skin fibroblasts. Assuming that these healthy cells satisfy their demand, their net ATP production rate should equal their ATP demand. The rate of ATP production in skin fibroblasts was

estimated to be about 10^9 ATP/s, the large majority of which is supplied by mitochondria [451]. The number of mtDNAs in healthy human skin fibroblasts was measured to be roughly in the range 2400-5200 [452] (the variation in copy number was partly due to variation in ages of the individuals), and we will use the value 4000 as an estimation. Using $w_n = 4000$ we obtain

$$\begin{aligned} 10^9 &= 4000(s_n - \rho_1 - \lambda\rho_2 - \mu\rho_3) \\ &\approx 4000(s_n - \rho_2(10^{-5} + \lambda + 0.1\mu) \\ &\approx 4000\Big(s_n - 10^9\Big[10^{-5} + 0.07/(24 \cdot 3600) + 0.1 \cdot 0.07/(24 \cdot 3600)\Big]\Big) \end{aligned} \tag{B.5}$$

Here we used an mtDNA half-life ($T_{1/2}$) of 10 days, giving a degradation rate $\ln(2)/10 \approx 0.07$ day^{-1}, and assumed that the cells are in steady state with $\lambda = \mu$. This leads to $s_n \approx 2.6 \times 10^5$ ATP/s meaning that, considering we used $s_n \approx 1.1$, our parameters s_n, D are expressed in units of about 2.6×10^5 ATP/s. This means that, in our units, the parameter values we use for ρ_1, ρ_2 and ρ_3 are $\rho_1 \approx 0.04$, $\rho_2 \approx 3828$, and $\rho_3 \approx 383$.

B.4 Cost function outputs

B.4.1 Output visualisations

Figure B.2A shows the behaviour of equations (B.1) - (B.2) for various parameter values. Note that none of the lines in the figure crosses the origin, because even when no ATP is created, respiration is required to maintain the gradient which would otherwise be lost due to proton leak. Figure B.2B-E shows how resource consumption rate and cost change as the number of mtDNAs changes. Three regimes can be distinguished: 1) there are too few mitochondria present to satisfy demand and they use their maximum possible resource uptake to get their energy production rate as close to D as possible; 2) demand can be satisfied and the cost now only depends on the amount of resource that is used; 3) resource has become limiting and demand cannot be satisfied any more. The main difference between the two models is that in the linear model, when demand is satisfied, the cheapest state is the one with the smallest mtDNA copy number possible whereas the saturating model is cheapest at a higher copy number. This is because mitochondria in the saturating model becomes more efficient as less resources are being consumed.

Figures B.3A,B show the cost function as a heatmap in (w, m) space. This figure is similar to Figure 4.2 in Chapter 4 but here we have fixed $\epsilon_1 = 1$ and varied ϵ_2. Mutants are now

less tolerated because they consume just as many resources as wildtypes, but still produce less output. It is now not the case that intermediate heteroplasmies are less efficient; *intermediate heteroplasmies are only less efficient when* $\epsilon_1 < 1$ *(mutants consume less resource) and when a saturating output model (Figure B.2) is used.* When $\epsilon_1, \epsilon_2 < 1$, it is possible for intermediate heteroplasmies to be less efficient but the smaller the value of ϵ_2, the smaller the range of values of ϵ_1 for which this is true; therefore, the effect of intermediate heteroplasmies being less efficient will be most easily observed when the mutant efficiency is close to that of the wildtypes.

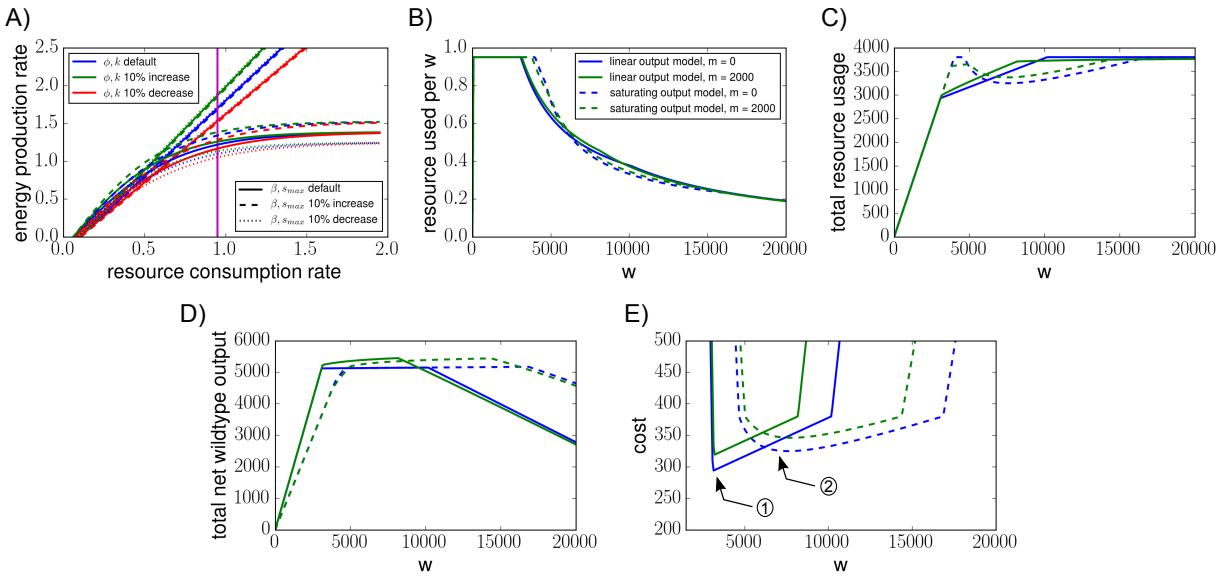


Figure B.2: Relationship between resource consumption and energy output. A) The energy production rate of a single wildtype mitochondrion as a function of its resource consumption rate is shown, as given by equations (B.1) and (B.2). For the linear model (corresponding to the straight lines) the parameters ϕ and β are changed by 10%, for the saturating model we vary s_{max} and k. The magenta line indicates r_{max}. **B)** As w increases, demand is shared between more mitochondria and each individual one can afford to consume resources at a lower rate (the same figure legend applies for figures C, D and E). **C)** The total resource consumption increases with w because the mitochondria need to consume a non-zero amount of resources to produce a net energy output and each mitochondrion comes with a maintenance cost. **D)** The total energy produced by wildtypes increases when mutants are present. **E)** When demand is satisfied, the cost increases with w in the linear model, resulting in minimal costs when copy numbers attain the minimum number required to satisfy demand (1). In contrast, for the saturating model the cost decreases at first because as individual resource consumption drops, the energy production efficiency increases. Minimum cost now occurs when mitochondria are working most efficiently (2). Parameters $\epsilon_1 = 0.1$ and $\epsilon_2 = 1.0$ were used.

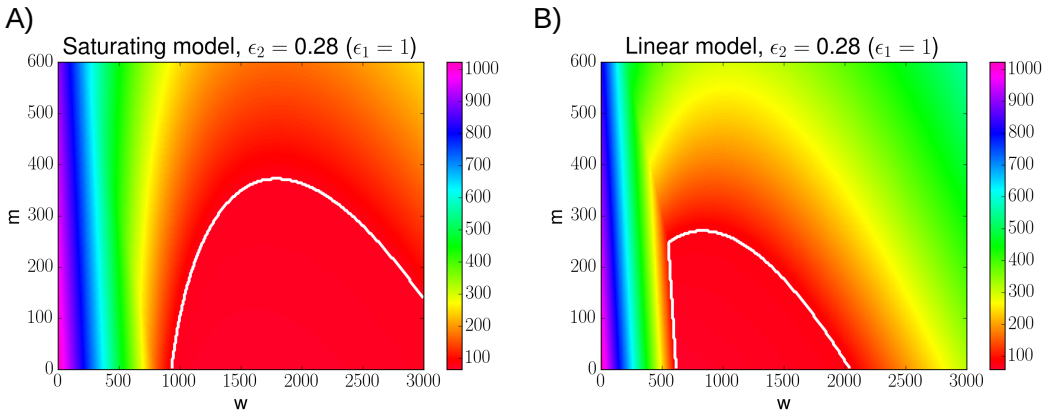


Figure B.3: Changing mutant efficiency (ϵ_2) does not lead to expensive intermediate heteroplasmies. **A) + B)** Similar to Figure 4.2 in Chapter 4, these figures show the cost values in (w, m) space, but now as a function of ϵ_2 (mutant efficiency) instead of ϵ_1. This time we show the cost in the entire space. The white lines show the region in which demand is satisfied for our default parameter values. Because mutants consume the same amount of resource as wildtypes ($\epsilon_1 = 1$), resource becomes limiting at relatively low values of m compared to when $\epsilon_1 < 1$. Note that intermediate heteroplasmies are not less efficient here.

B.4.2 Expensive intermediate heteroplasmies - explanation and robustness

Here we attempt to provide an explanation for why, in certain cases, intermediate heteroplasmy values are more expensive than high or low values. In these cases, in high heteroplasmy regions it is more efficient to increase heteroplasmy even more, whereas in low h conditions it is more efficient to decrease h; this automatically implies there exists some intermediate heteroplasmy value that is least efficient. Figures B.4A, B show the amount of resource consumed by individual wildtype and mutant mitochondria in four different example states. All states have identical total copy numbers ($w + m = 10^4$) and total outputs (equal to demand), but different heteroplasmy values ($h = 0.1, 0.3, 0.7$ and 0.9). When heteroplasmy increases, the individual resource consumption rates r_w and r_m both increase to compensate for the higher mutant copy number; this is true both in a low-h region (h increases from 0.1 to 0.3, Figure B.4A) and a high-h region (h increases from 0.7 to 0.9, Figure B.4B). However, the total resource consumption rate does not necessarily increase because the increase in h has caused a number of wildtype mitochondria to become mutants, thereby decreasing the combined wildtype resource usage. Computing the values of the resource consumption rates for the states with $h = 0.1$ and

0.3, while referring to Figure B.4A, gives:

$$\begin{aligned} w_1 r_{w_1} &= 9000 \cdot r_{w_1} \approx 3227 \\ m_1 r_{m_1} &= 1000 \cdot r_{m_1} \approx 125 \\ w_2 r_{w_2} &= 7000 \cdot r_{w_2} \approx 2981 \\ m_2 r_{m_2} &= 3000 \cdot r_{m_2} \approx 447, \end{aligned} \tag{B.6}$$

while the states $h = 0.7$ and 0.9 (referring to Figure B.4B) give

$$\begin{aligned} w_1 r_{w_1} &= 3000 \cdot r_{w_1} \approx 1982 \\ m_1 r_{m_1} &= 7000 \cdot r_{m_1} \approx 1618 \\ w_2 r_{w_2} &= 1000 \cdot r_{w_2} \approx 846 \\ m_2 r_{m_2} &= 9000 \cdot r_{m_2} \approx 2665. \end{aligned} \tag{B.7}$$

Comparing the states with $h = 0.1$ and $h = 0.3$, the *total* rates of resource usage are 3352 and 3428 respectively; the lower heteroplasmy state is more efficient. However, when heteroplasmies are higher, the high heteroplasmy state (0.9 rather than 0.7, with total resource usage 3511 vs 3600) is most efficient. This effect is due to the nonlinearity of Equation B.2.

Next, we investigate how robust the existence of an expensive intermediate heteroplasmy value is. Let h_{max} denote the value of h with maximum cost at fixed total copy number $(w + m)$. Figure B.5A shows h_{max} as a function of both total copy number and ϵ_1, setting all other parameters to their default values. The range of total copy numbers was chosen to correspond roughly to the range for which demand can be satisfied in a fully wildtype cell (with the objective of considering 'plausible' copy number regions). We see that an intermediate value of h_{max} exists for a wide range of parameter values, but only for large enough ϵ_1. This means we only expect to see expensive intermediate h values when neither of the two mtDNA species are severely dysfunctional. We further varied the parameters ρ_1 and s_{max} which play important roles in the cost function overall (ρ_1) and the specifics of the saturating output model (s_{max}), examples of which are shown in Figure B.5B,C,D which illustrates their values have little influence on h_{max}. Similar results were obtained by varying the parameters ρ_2 and ρ_3 by an order of magnitude.

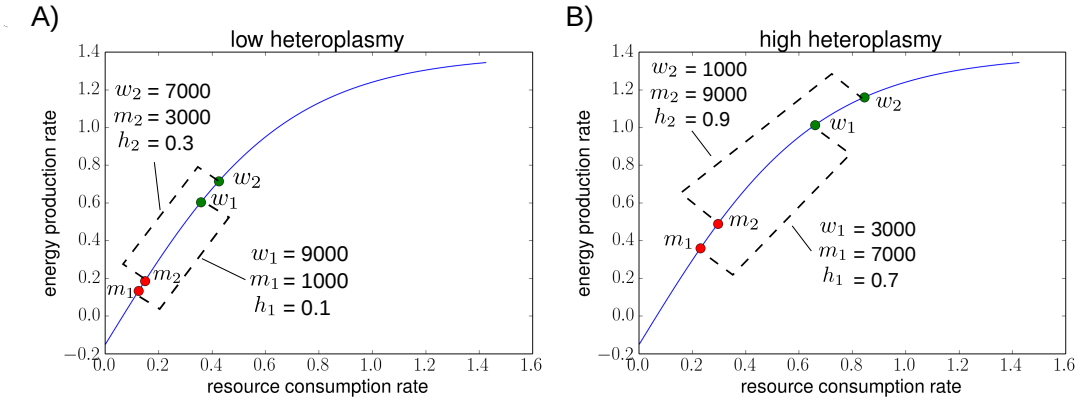


Figure B.4: Intermediate h values require more resources to satisfy demand, but only if mutants consume less resources. A) The resource consumption rates and energy production rates of wildtypes and mutants are shown for two states: $(w_1, m_1, h_1) = (9000, 1000, 0.1)$ and $(w_2, m_2, h_2) = (7000, 3000, 0.3)$. In both cases, the total energy output is equal to the demand. When heteroplasmy is higher ($h = 0.3$), the individual resource consumption rates are higher in order to maintain a constant total energy output. Overall, the state with $h = 0.1$ uses the least resources (Equations B.6). $\epsilon_1 = 0.35$ was used. **B)** This figure is similar to Figure (D) but now the two states $(w_1, m_1, h_1) = (3000, 7000, 0.7)$ and $(w_2, m_2, h_2) = (1000, 9000, 0.9)$ are compared. The state with $h = 0.9$ uses the least resources (Equations (B.7)).

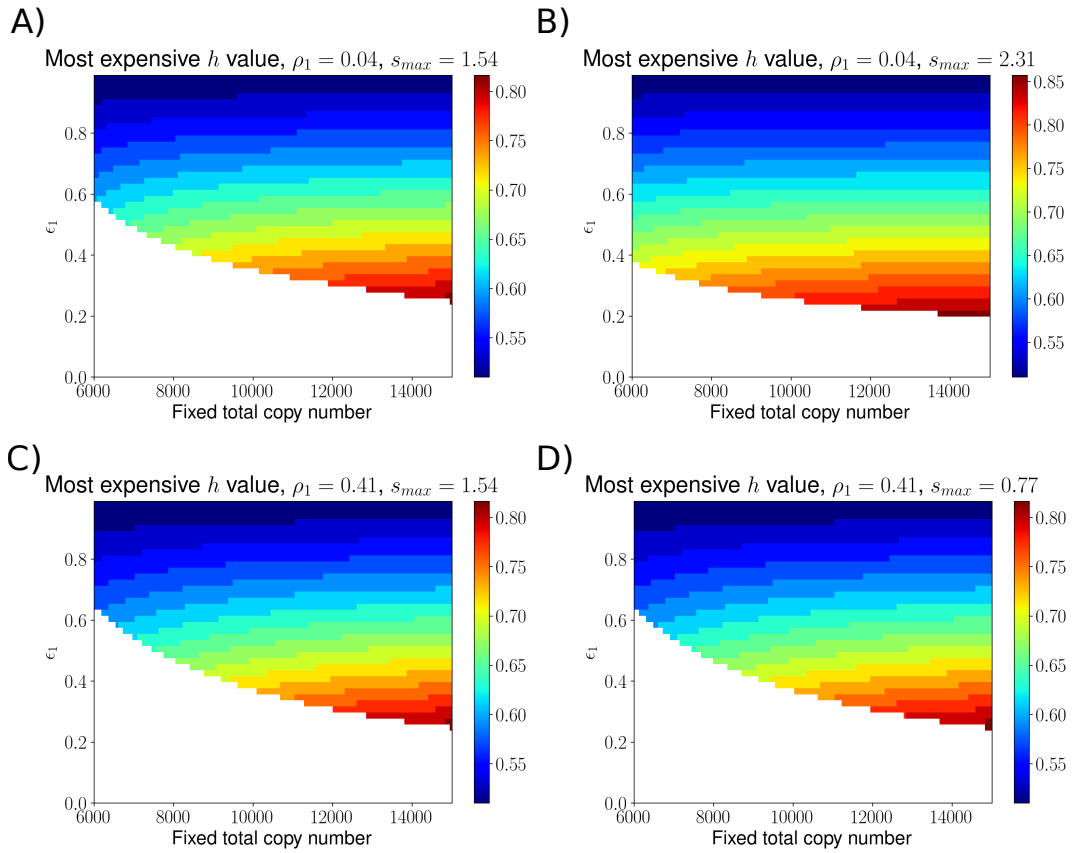


Figure B.5: The existence of intermediate heteroplasmy values is a robust feature of the saturating output model. We show the value of h_{max}, the most expensive heteroplasmy value at constant copy number, as a function of total copy number and ϵ_1 (describing mutant pathology). White regions correspond to $h_{max} = 1$. **A)** Using our default parameter values, an intermediate h_{max} exists for large enough mutant functionality ϵ_1. **B)** The parameter s_{max} is increased by 50% with minimal effect on the output. We kept the parameter k fixed as it defines the amount of proton leak (the resource consumption rate at zero energy output) which agrees with the amount of proton leak in the linear output model whose parameters are based on experimental data. **C)** The parameter ρ_1 is increased by an order of magnitude with minimal effect on the output. **D)** The parameter ρ_1 is increased by an order of magnitude and s_{max} is decreased by 50%. Again, change in h_{max} are small.

Label	Control	optimal parameters satisfying our two constraints
I	$\lambda(w) = \mu + c_1(w_{opt} - w)$	$c_1 = \alpha_R \mu / w_{opt}$
II	$\lambda(w+m) = \mu + c_1(w_{opt} - (w+m))$	$c_1 = \alpha_R \mu / w_{opt}$
III	$\lambda(w+\delta m) = \mu + c_1(w_{opt} - (w+\delta m))$	$c_1 = \alpha_R \mu / w_{opt}$ δ is optimised
IV	$\lambda(w,m) = \frac{\mu(\alpha_R(w_{opt} - w - \eta m) + w + \eta m)}{(w+m)}$	$\alpha_R = 10.0$ η is optimised

Table B.1: Parameter values for the four different control mechanisms we employ. Two parameters of each control are set by the two constraints we impose. The parameter α_R was proposed to lie in the range 5-17 [1] and here we used $\alpha_R = 10$. The values for δ and η are found by optimizing our cost function over the steady states corresponding to our initial conditions. We used 50 initial conditions equally spread over the range $h_0 \in [0, 0.2]$. The two values used for w_{opt} are 1524 and 7616 (Table 4.3). We further use $\mu = 0.07$ day^{-1}.

B.4.3 Comparison of the cost of different control mechanisms

In Section 4.2.3 of Chapter 4 we introduced four different feedback controls and compared their mean costs. Here, we additionally show the means and variances of the wildtypes, mutants and cost up to ~ 82 years resulting from stochastic simulations. The parameter values we used to compare the four controls are summarised in Table B.1 for clarity. We observe that the increase in cost for the linear control with $\delta = 0$ is mainly caused by an increase in mean mutant copy number, the cause of which is discussed in more detail in the next chapter.

Figure B.7 shows the optimal values for δ in the linear feedback control $\lambda(w,m) = \mu + c_1(N_{ss} - (w + \delta m))$ as a function of ϵ_1. Stochastic simulations starting in steady state at either $h_0 = 0.1$ or $h_0 = 0.8$ were performed for $T = 10^4$ days. The mean integrated cost over these 10^4 days was evaluated for different values of δ, and the optimal δ values are shown. This was done for both the linear and the saturating model. The general trend is, as was shown for $T = 100$ in Chapter 4, that the lower ϵ_1 the lower the optimal δ.

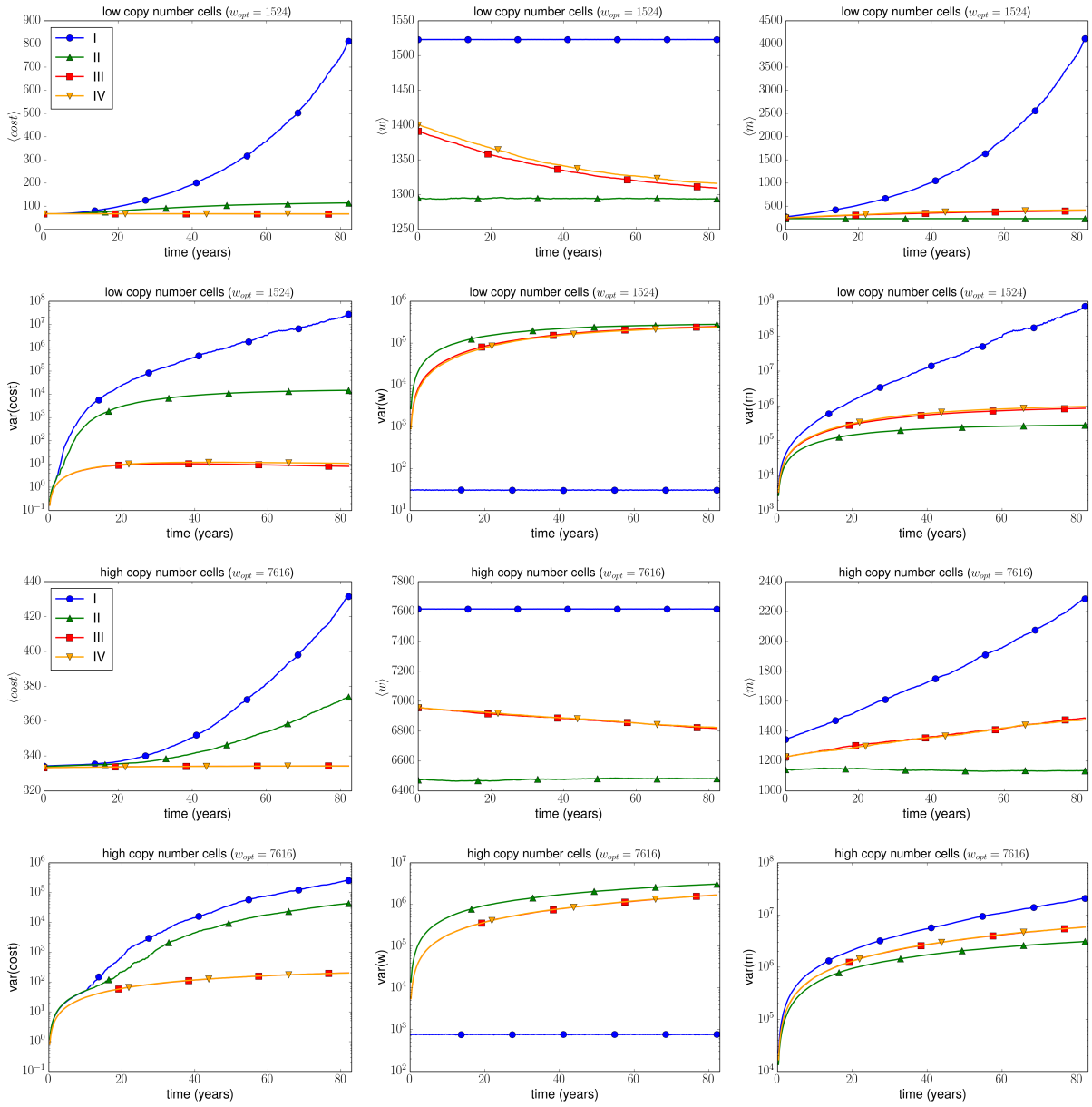


Figure B.6: Wildtype, mutant and cost dynamics for four different control strategies. Dynamics are shown for the four controls I, II, III, and IV defined in Table B.1. Again, we see that the effects of the control are more noticeable in low copy number cells. Parameter are set as given in Table B.1. Values for w_{opt} are those for the saturating output model at low and high copy number. The free parameters in control III and IV (δ and η) were optimised over initial conditions in the range $h \in [0, 0.2]$. For the optimization the default cost function parameters were used as well as $\epsilon_1 = 0.3$.

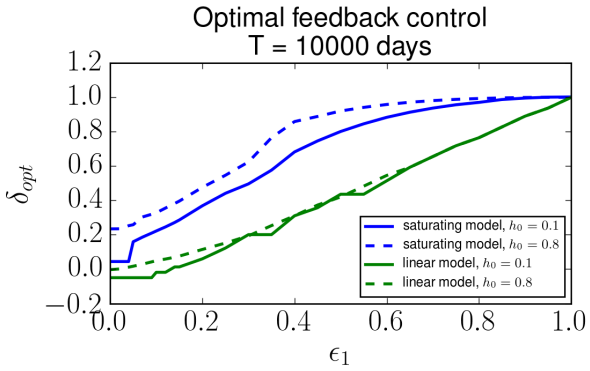


Figure B.7: At long times and high heteroplasmies, energy sensing control becomes suboptimal. Related to Figure 4.3C; The optimal value of δ in a linear feedback control is shown as a function of ϵ_1. Here we used $T = 10^4$ days (optimization time) and low copy numbers for both the linear and saturating model. The solid and dashed lines correspond to trajectories starting at $h_0 = 0.1$ and $h_0 = 0.8$, respectively. The less resources the mutants consume (and the less output they therefore produce) the lower their optimal contribution to the control.

B.5 Zinc Finger nuclease treatment model

B.5.1 Visualisation of Zinc Finger concentrations during treatment

As explained in the 'Methods' section of Chapter 4, we simulate the treatment of cells by mitochondrially targeted Zinc Finger Nucleases (mtZFNs). The concentration of the mtZFNs is modelled by the following equation:

$$[ZFN](t) = \frac{I_0}{\mu_z - b}\left(e^{-bt} - e^{-\mu_z t}\right) \tag{B.8}$$

where I_0 is the treatment strength (e.g. the initially added mtZFN concentration), b indicates the treatment duration and μ_z is the mtZFN degradation rate. Figure B.8A shows this equation for different treatment durations. As we found in Chapter 4, the weaker and longer treatment option leads to larger heteroplasmy shifts.

B.5.2 Heteroplasmy values can increase after nuclease treatments

As mentioned in Section 4.2.3.2 of Chapter 4, there is a possibility for cellular heteroplasmy to increase after a treatment has been applied. This is true especially if the selectivity of the treatment is low (i.e. ξ is close to 1) and the initial heteroplasmy of a cell is high; in this case treating a cell may even eliminate all wildtype mitochondria, increasing heteroplasmy to 1. To model the extent of this effect we initialise a cell with a given heteroplasmy h_0, and let

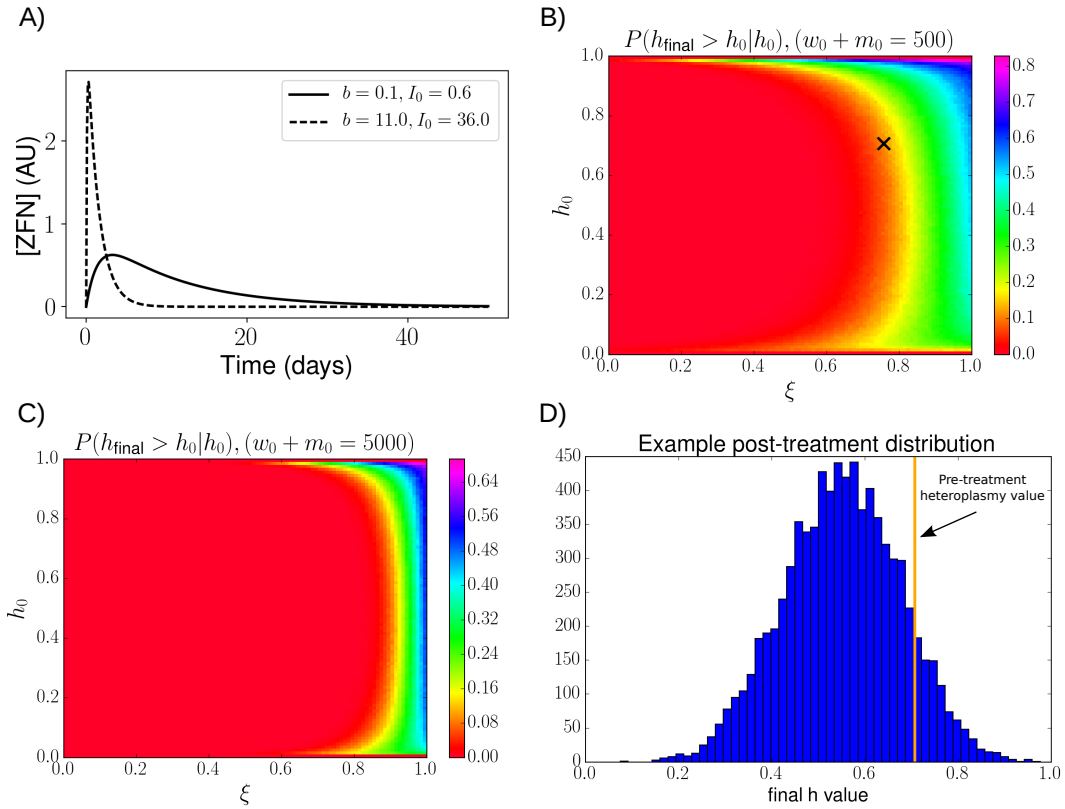


Figure B.8: Zinc Finger Nuclease concentrations for short and long treatments. A) Here we show the concentration of mitochondrially targeted Zinc Fingers as modelled by Equation (B.8). The parameter values for the short and strong treatment ($I_0 = 36, b = 11$) are similar to those found in fitting the model to the data. For the mtZFN degradation rate we used $\mu_Z = \log(2)$ day^{-1} (corresponding to a mtZFN half-life of 1 day). **There exists a possibility of increasing heteroplasmy levels through treatment. B)** The probability of increasing heteroplasmy above its initial pre-treatment value h_0, after one round of treatment and recovery, is shown as a function of h_0 and ξ. Cells are initialised with a total copy number of 500. The cross indicates the parameters used in Figure (D). The parameter values for I_0, b and c_1 are set to their fitted values: $(I_0, b, c_1) \approx (39, 20, 3 \times 10^{-4})$. We used $\delta = 1$. **C)** Similar to figure (B), but now cells are initialised with a total copy number of 5000; in these large copy number cells stochastic fluctuations in copy number have less effect and the probabilities of exceeding initial heteroplasmy values are smaller compared to Figure (B). **D)** An example of a distribution of post-treatment heteroplasmy values is shown using parameters h_0 and ξ as indicated by the cross in Figure (B). The orange line indicates the value of h_0 (the heteroplasmy that was present before the treatment started).

it undergo one round of treatment and recovery after which the final heteroplasmy is recorded. This process is repeated to obtain the probability that, given an initial heteroplasmy h_0, the final heteroplasmy after treatment exceeds h_0 ($P(h_{\text{final}} > h_0|h_0)$). Figures B.8B,C show these probabilities as a function of h_0 and selectivity parameter ξ, for initial mtDNA copy numbers 500 and 5000; the effect-size is larger for low copy number cells. Figure B.8D shows an example of the distribution of post-treatment heteroplasmies. The recovery time used in the simulations is 30 days which is long enough for the cells to recover their initial copy numbers and short enough for the change in h to be almost completely due to treatment, rather than due to naturally occurring random drifts in heteroplasmy values. Chances of increasing heteroplasmy are highest when h_0 is very high or very low (if h_0 is low the low mutant copy numbers increase

the effect of stochastic fluctuations). In the examples shown, when $\xi <= 0.6$ (i.e. for every mutant that is cleaved, 0.6 wildtypes are cleaved) increases in heteroplasmy are very unlikely to occur.

B.5.3 Bayesian inference model outputs

As explained in Section 4.2.3.2 of Chapter 4, we expect a high correlation between the nuclease treatment strength parameters $I_0^{(\mathrm{N})}$, $I_0^{(\mathrm{H})}$ and $I_0^{(\mathrm{L})}$ (referring to normal, high and low mtZFN concentrations) and the treatment duration parameter b; this is confirmed in Figure B.9A. The ratio I_0/b is expected to be higher at high mtZFN concentration since the parameter I_0 represents mtZFN concentrations directly after treatment (Section 4.4). We observe that this is indeed the case (Figure B.9B).

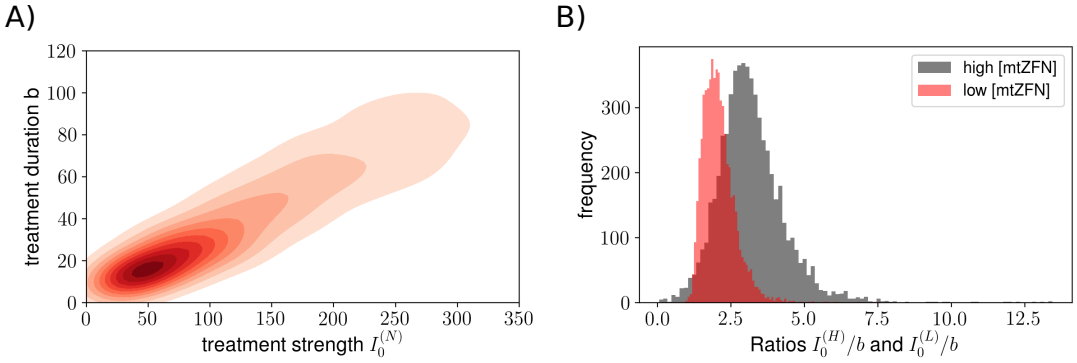


Figure B.9: High correlation between nuclease treatment strength and duration. A) We show the correlation between posterior samples of the mtZFN nuclease treatment strength $I_0^{(\mathrm{N})}$ and the treatment duration parameter b, using kernel density estimation (with Gaussian kernels whose bandwidth is set by Scott's rule [453]). Similar results are obtained for $I_0^{(\mathrm{H})}$ and $I_0^{(\mathrm{L})}$. **B)** Distributions of the ratios $I_0^{(\mathrm{H})}/b$ and $I_0^{(\mathrm{L})}/b$ are shown (using posterior samples). As expected, the high mtZFN concentration setting appears to show higher ratio values. Ratio distributions using normal mtZFN concentrations very closely resemble the high concentration ratios.

C

Supplemental information complementing Chapter 5

This appendix complements Chapter 5, and is split into two sections:

1. The first section contains various analytical descriptions of mtDNA dynamics:
   - We show that the asymmetry in fluxes into the absorbing boundaries $h = 0$ and $h = 1$ can be qualitatively reproduced by considering a model of diffusion in heteroplasmy space with a heteroplasmy-dependent diffusion coefficient.
   - We analytically approximate the exponential increase in mutant mean observed when $\delta = 0$ in our linear feedback model.
   - The birth-death model we employ in Chapter 5 is an example of a stochastic Lotka Volterra (LV) model, which can be solved and leads to set of ordinary differential equations describing the evolution of the moments of wildtype and mutant copy numbers.
   - We use the van Kampen system size expansion [294] to approximate the master equation describing our mtDNA dynamics.
2. The last section contains explanations and estimations concerning the system of intercellular mtDNA exchange introduced in Sections 5.2.1.3 and 5.2.1.4.

- We illustrate the derivation of an equation for the long-time mean cellular heteroplasmy value in a 2-cell mtDNA exchange system in the limit of slow mtDNA exchange (Equation 5.4).
- We provide suggestions as to why the stochastic drive observed in Section 5.2.1.4 occurs, and how the various control parameters influence the effect-size of this drive.
- We provide intuition about the mechanisms involved in creating a drift in (w, m)-space along the steady state line.
- We estimate the feedback control strength.
- We estimate the mtDNA exchange rate γ.

C.1 Analytical descriptions of mutant and wildtype dynamics under various simplifying conditions

C.1.1 Heteroplasmy-dependent diffusion produces results qualitatively similar to heteroplasmy dynamics in our birth-death dynamics

Here we show that the results given in Figure 5.1 can be qualitatively reproduced by a random walk in heteroplasmy space with an h-dependent diffusion coefficient. The work in this particular section was in collaboration with Juvid Aryaman. Consider a diffusion equation

$$\frac{dx}{dt} = \sqrt{2D(x)}\xi(t) \tag{C.1}$$

where $D(x)$ denotes a position-dependent diffusion coefficient and $\xi(t)$ represents white noise. The Fokker-Planck equation for the probability density $p(x,t)$ of $x(t)$ is given by (see e.g. [454])

$$\frac{\partial p(x,t)}{\partial t} = \frac{\partial^2}{\partial x}\Big(D(x)p(x,t)\Big) \tag{C.2}$$

As an example, we take $D(x) = x^2/2$ (i.e. $dx/dt = x(t)\xi(t)$) and introduce absorbing boundaries at $x = 1$ and $x = 2$ by setting $p(1,t) = p(2,t) = 0$. The reason for considering diffusion in the range $x \in [1,2]$ rather than $x \in [0,1]$ (which may seem a more natural choice in relation to heteroplasmy) is that in the latter case diffusion near the left boundary becomes vanishingly small and consequently no flux is seen into the boundary (alternatively, we could have assumed $D(x) = x^2/2 + c$ for some constant c). We assumed $x(t=0) = 1.5$, i.e. the starting position is equidistant to either absorbing boundary, as is the case in our simulations of heteroplasmy dynamics discussed in Section 5.2.1.1. Due to conservation of probability, the probability flux

$J(x)$ satisfies

$$\frac{\partial p(x,t)}{\partial t} = -\frac{\partial}{\partial x} J(x,t) \tag{C.3}$$

and the flux into the absorbing boundaries $x = 1$ and $x = 2$ is then given by

$$\begin{aligned} J(1,t) &= \frac{\partial}{\partial x} \left(D(x) p(x,t) \right) |_{x=1} \\ J(2,t) &= \frac{\partial}{\partial x} \left(D(x) p(x,t) \right) |_{x=2} \end{aligned} \tag{C.4}$$

Numerical evaluations of these fluxes are shown in Figure C.1, yielding qualitatively similar results to the ones provided in Figure 5.1C. Flux into the boundary at the high-diffusion end of the range is initially larger, but is later surpassed by flux into the low-diffusion boundary. This is consistent with the interpretation illustrated in Figure 5.2 which suggests that, for low values of δ, diffusion in heteroplasmy space is faster at low h compared to high h values which leads to the initial dominant flux into $h = 0$ (Figure 5.1C). When integrating the boundary fluxes over time, we find equal total flux into both boundaries, consistent with a constant $\langle h \rangle$. Hence, heteroplasmy dynamics in our birth-death system with distinct mutant and wildtype carrying capacities is qualitatively similar to the dynamics obtained from random diffusion with a heteroplasmy-dependent diffusion coefficient.

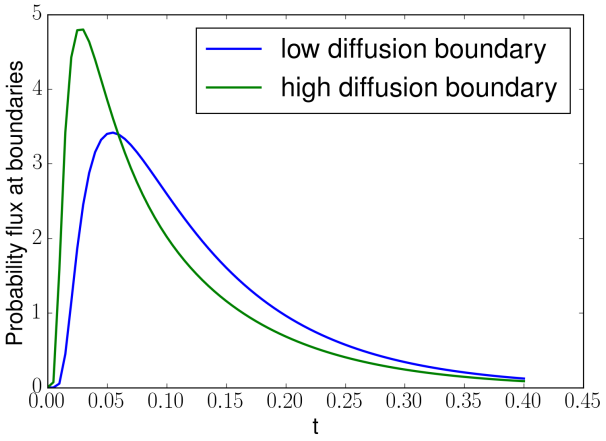


Figure C.1: Position-dependent diffusion yields asymmetric boundary fluxes. We show the probability fluxes into the absorbing boundaries as defined in equations (C.4). Like in Figure 5.1C, the flux into the boundary at high diffusion is initially dominant.

C.1.2 Exponential increase in mutant mean can be described analytically

We here consider $\delta = 0$, in which case wildtype dynamics are completely independent of mutant dynamics. However, the mutant replication rate still depends on wildtype copy numbers

through the relation $\lambda(w) = \mu + c_1(w_{ss} - w)$. The wildtype population will fluctuate over time, which is experienced by the mutant population as a fluctuating replication rate $\lambda(t)$. Using this time-varying rate, the mutant probability density function $P_m(t)$ can be described by the master equation

$$\frac{\partial P_m}{\partial t} = \lambda(t)(m-1)P_{m-1} + \mu(m+1)P_{m+1} - mP_m\left[\lambda(t) + \mu\right] \tag{C.5}$$

which can be solved analytically to give the following expression for the expected value of m:

$$\langle m(t)\rangle = m_0 e^{\int_0^t (\lambda(\tau)-\mu)d\tau}. \tag{C.6}$$

An analytical expression for $\int_0^t \lambda(\tau)d\tau$ cannot be obtained using the wildtype birth-death dynamics, but it *can* be obtained if the wildtype dynamics are approximated by an Ornstein-Uhlenbeck (OU) process. An OU process is a continuous time random walk which is steered towards a central location, just like the wildtype population is steered towards its steady state value. We will therefore approximate the wildtype dynamics $w(t)$ by an OU process $X(t)$, which means that $\lambda(t) - \mu$ is also an OU process. Both the OU process $X(t)$ as well as its time integral $Y(t) = \int_0^t X(\tau)d\tau$ are Gaussian random variables (see e.g. [455]). The mutant dynamics can then be described by

$$\langle m(t)\rangle = m_0 e^{N(\tilde{\mu}(t),\tilde{\sigma}^2(t))} \tag{C.7}$$

where $\tilde{\mu}(t)$ and $\tilde{\sigma}(t)$ are the mean and variance of the integrated OU process $\int_0^t(\lambda(\tau)-\mu)d\tau = \int_0^t(c_1(w_{ss} - X(t)))d\tau$, respectively. In this approximation, $\langle m(t)\rangle$ is described by a log-normal distribution.

We will now proceed as follows: 1) we present equations for the means and variances of a general OU process $X(t)$ and its time integral $Y(t)$, 2) we express these equations in terms of our control parameters μ, c_1 and w_{ss}, and 3) we evaluate Equation (C.7) and comment on the results.

Analytical expressions can be obtained for the means and variances of $X(t)$ and $Y(t)$, by writing the OU process in the form of a Stochastic Differential Equation: $dX(t) = \theta(\mu_X - X(t))dt + \sigma dW(t)$ where $W(t)$ is a Wiener process. The following equations can then be derived using

standard methods [455]:

$$\langle X(t)\rangle = (x_0 - \mu_X)e^{-\theta(t-t_0)} + \mu_X \tag{C.8}$$

$$\mathrm{var}(X(t)) = \frac{\sigma^2}{2\theta}\Big(1 - e^{-2\theta(t-t_0)}\Big) \tag{C.9}$$

$$\langle Y(t)\rangle = \frac{x_0 - \mu_X}{\theta}\Big(1 - e^{-\theta(t-t_0)}\Big) + \mu_X(t - t_0) + y_0 \tag{C.10}$$

$$\mathrm{var}(Y(t)) = \frac{\sigma^2}{\theta^2}\left((t - t_0) - \frac{2}{\theta}\Big[1 - e^{-\theta(t-t_0)}\Big] + \frac{1}{2\theta}\Big[1 - e^{-2\theta(t-t_0)}\Big]\right) \tag{C.11}$$

where $X(t_0) = x_0$ and $Y(t_0) = y_0$ denote initial conditions. For long times, the mean and variance of the OU process $X(t)$ can be written as $\langle X(t)\rangle_{t\to\infty} = \mu_X$ and $\mathrm{var}(X(t))_{t\to\infty} = \sigma^2/(2\theta)$, meaning the process converges to the normal distribution $N(\mu_X, \frac{\sigma^2}{2\theta})$.

Because $X(t)$ represents our wildtype dynamics, Equations (C.8) and (C.9) correspond to the wildtype mean and variance, respectively. Expressions for wildtype mean and variance under our linear control can be obtained (derived in Section C.1.4.1, Equations (C.27) and (C.28)), meaning that we can write the parameter μ_X, θ and σ in terms of our control parameters μ, c_1 and N_{ss}*. However, equalizing the mean and variance of the OU process and our controlled wildtype dynamics only provides us with two constraints. As a third constraint, we set $\frac{1}{\theta} = c_1 N_{ss}$ which approximately equalises the relaxation times of the OU process and the wildtype birth-death process.These three constraints are now sufficient to express the parameters μ_X, θ, σ in terms of the control parameters μ, c_1 and N_{ss}; results match well with stochastic simulations (Figure C.2A, B).

To evaluate Equation (C.7) we write

$$\begin{aligned} d(\lambda(t) - \mu) &= d\lambda(t) \\ &= -c_1 dX(t) \\ &= \theta c_1(w_{ss} - \mu_X)dt - \theta\eta(t)dt - c_1\sigma dW(t) \end{aligned} \tag{C.12}$$

and then use Equation (C.10), to derive†

$$\left\langle \int (\lambda(\tau) - \mu)d\tau \right\rangle = \frac{c_1(\mu_X - x_0)}{\theta}(1 - e^{-\theta(t-t_0)}) + c_1(w_{ss} - \mu_X)(t - t_0). \tag{C.13}$$

*We set $\mu_X = \frac{3}{4}w_{ss} + \frac{1}{4}\sqrt{w_{ss}^2 - \frac{8\mu}{c_1}}$ (using Equation (C.27)) and $\frac{\sigma^2}{2\theta} = \frac{w_{ss}}{8}\Big(w_{ss} \mp \sqrt{w_{ss}^2 - \frac{8\mu}{c_1}}\Big) + \frac{\mu}{2c_1}$ (using Equation (C.28)).

†Assuming $y_0 = 0$.

This last equation represents the mean of the normal distribution in Equation (C.7).

If we simulate our wildtype and mutant dynamics with $\delta = 0$ and start the wildtype population in steady state, then $x_0 = w_{ss}$ and μ_X represents the stochastic expected value of w. If $\mu_X = w_{ss}$, then Equation (C.13) is equal to zero and Equation (C.7) can be written as $\langle m(t) \rangle = m_0 e^{N(0,\tilde{\sigma}^2(t))}$. However, we will find in Section (C.1.4.1) that the deterministic wildtype mean is slightly higher than the stochastic wildtype mean. This means that the mean of the normal distribution describing $\langle m(t) \rangle$ is increasing with time, leading to the exponential increase of $\langle m(t) \rangle$. We note that even if this normal distribution would have zero mean, there would still be an exponential increase in $\langle m(t) \rangle$ but at a much slower rate (Figure C.2).

In conclusion, by approximating wildtype dynamics by an OU process, we were able to derive the exponential increase in mean mutant dynamics observed under our linear feedback function with $\delta = 0$. We found that the main cause of this exponential increase is the disagreement between the deterministic and stochastic mean values for the wildtype dynamics, as derived in Section (C.1.4.1).

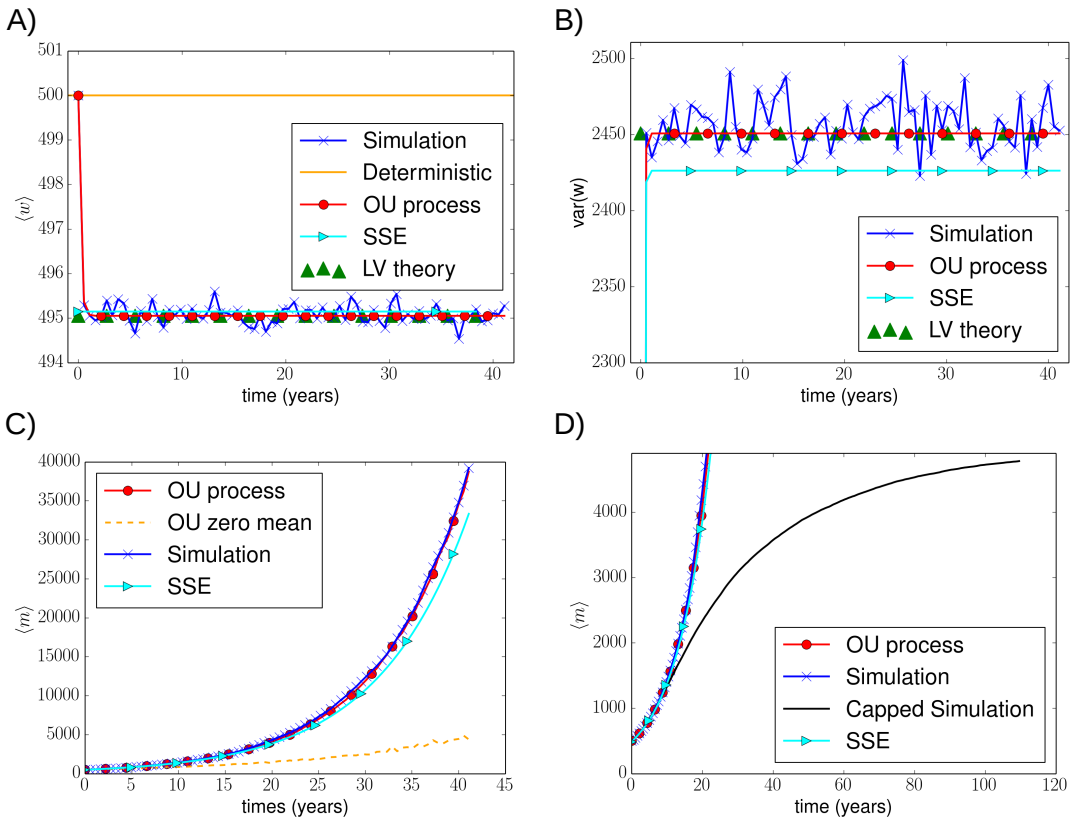


Figure C.2: Exponential increases in mean mutant copy numbers can be approximated analytically. A) Mean wildtype copy numbers are shown for our linear feedback function with $\delta = 0$ and $N_{ss} = w_{ss} = 500$). Stochastic simulations (5×10^4 repeats) are compared with i) deterministic values, and approximations based on ii) a Lotka-Volterra model (Section (C.1.4.1)), iii) an OU-process, and iv) a system size expansion (SSE) (Section C.1.5.1). The mean and variance of the OU-process were set to be identical to those predicted by the Lotka-Volterra model; their equivalence is therefore trivial. **B)** The wildtype variance is shown for the same models as shown in figure (A). **C)** The exponential-like increase in mean mutant copy number $\langle m(t) \rangle$ is shown using stochastic simulations and various approximations as indicated. We also show predictions based on the OU-process approximation, but using $\tilde{\mu}(t) = 0$ in Equation (C.7). **D)** Here we have added a simulation in which total copy numbers were capped at 10^4, providing a more biologically realistic situation.

C.1.3 Approximating the wildtype steady state distribution

If wildtypes are uncoupled from mutants ($\delta = 0$), their dynamics are less complicated and though closed form solutions for the general dynamics do not exist, solutions for the equilibrium state can be obtained. We first outline the derivation of this equilibrium solution for a more general system and then apply this result to our specific model. Let π_N denote the equilibrium probability distribution of observing copy number N, with $\sum_{N=0}^{\infty} \pi_N = 1$. The master equation reduces to the simpler form

$$0 = \mu_{N+1}\pi_{N+1} - (\lambda_N + \mu_N)\pi_N + \lambda_{N-1}\pi_{N-1} \tag{C.14}$$

for all N, due to the equality $d\pi_N/dt = 0$. Following the approach outlined in Ref. [100], the equation can be rewritten as

$$\mu_{N+1}\pi_{N+1} - \lambda_N\pi_N = \mu_N\pi_N - \lambda_{N-1}\pi_{N-1} \tag{C.15}$$

Because the left and right hand side of this equation are equal except for N (left) being replaced by $N-1$ (right), both sides can be considered constant. Using $\mu_0 = 0$ and $\pi_{-1} = 0$, the constant is found to be 0 and one obtains the balance equation

$$\mu_N\pi_N = \lambda_{N-1}\pi_{N-1} \tag{C.16}$$

This equation shows that the probability flow from state N to $N-1$ is equal to the flow from state $N-1$ to N, and can be applied repeatedly to find an expression for π_N [100].

In the particular system we study, $\mu_w = \mu w$ and $\lambda_w = w(\mu + c_1(N_{ss} - w)$ (we denoted N by w to specifically refer to wildtype copy numbers). Inserting $w = 1$ in equation (C.16) yields $\mu_1\pi_1 = \lambda_0\pi_0 = 0$ (because $\lambda_0 = 0$). In order to satisfy $\mu_1\pi_1 = 0$, we impose the condition $\mu_1 = 0$. This condition is not true in our system and it will alter the underlying process, but it forms an accurate approximation provided that π_1 is small compared to the mode of the distribution. Repeated application of equation (C.16) yields

$$\pi_N = \frac{\lambda_1\lambda_2\cdots\lambda_{N-1}}{\mu_2\mu_3\cdots\mu_N}\pi_1 \tag{C.17}$$

with π_1 chosen such that $\sum_{i=1}^{\infty} \pi_i = 1$. Application of equation (C.17) yields accurate approximation to the true equilibrium probability distribution, as shown in Figure C.3.

The approximation we derived in this section is only valid when a single mtDNA species is present and can therefore be applied to homoplasmic cells. Its usefulness stems from the fact that it can be applied for any form of λ_N and μ_N provided that the fraction in Equation (C.17) can be evaluated. This approach provides a way of quickly examining the long-time equilibrium mtDNA distribution without the need of time-consuming stochastic simulations. We will use these results in Section C.2.3 to estimate the control strength parameter c_1.

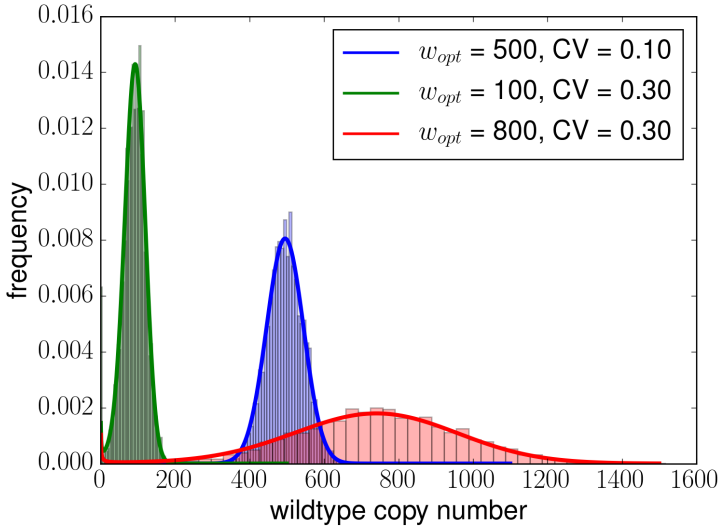


Figure C.3: Wildtype steady state distributions are accurately approximated numerically. Here we show the wildtype steady state distributions as obtained through stochastic simulations (histograms) and numerical approximations (Equation C.17).

C.1.4 Lotka Volterra model

The Lotka-Volterra model has been used to describe the dynamics of interacting species since 1910 and is part of a wider class of multivariate birth-death processes [456]. Because we only consider systems with two species (wildtype and mutant mtDNA molecules) we will present equations for a stochastic two-species generalised Lotka Volterra system. We use the notation $\lambda_i(N,t)$, $\mu_i(N,t)$ to describe the birth and death rates of species i, where $i = 1, 2$ refers to wildtype and mutant, respectively. The vector $N = \binom{n_1}{n_2}$ contains the species' copy numbers. The Lotka-Volterra interaction model involves a particular form of $\lambda_i(N,t)$ and $\mu_i(N,t)$, namely

$$\lambda_i(N,t) = \lambda_i(t)n_i + \sum_{j=1}^{2} \lambda_{ij}(t)n_i n_j \tag{C.18}$$

$$\mu_i(N,t) = \mu_i(t)n_i + \sum_{j=1}^{2} \mu_{ij}(t)n_i n_j \tag{C.19}$$

where the first terms describe the characteristics of each individual species and the last terms specify inter-species interactions.

A master equation describing the trajectory of the probability density function $P(N;t)$ can be

derived and is given by

$$\begin{aligned}\frac{\partial P(N,t)}{\partial t} = \sum_{i=1}^{2} \Big(& \lambda_i(N-e_i,t)P(N-e_i;t) \\ & + \mu_i(N+e_i,t)P(N+e_i;t) \\ & - \Big[\lambda_i(N,t)+\mu_i(N,t)\Big]P(N;t)\Big),\end{aligned} \tag{C.20}$$

where $e_1 = \binom{1}{0}$ and $e_2 = \binom{0}{1}$ denote unit vectors.

An exact solution to Equation (C.20) cannot be found for general forms of $\lambda_i(N,t)$ and $\mu_i(N,t)$, but useful statistics (e.g. means and variances) can be derived from the generating function $G(Z,t)$, defined as

$$G(Z,t) = \sum_{n_1=0}^{\infty}\sum_{n_2=0}^{\infty} P(N;t) z_1^{n_1} z_2^{n_2} \tag{C.21}$$

with $Z = (z_1, z_2)$. Derivatives of $G(Z,t)$ correspond to species' means, variances and higher order moments. Combining equations (C.20) and (C.21) leads to a set of ordinary differential equations describing the time evolutions of these moments. This is a standard procedure (see, for example, [457]) and we here only provide the final result for the Lotka-Volterra system defined in Equations (C.18) and (C.19):

$$\begin{aligned}\frac{d\langle n_i\rangle}{dt} = & \Big(\lambda_i(t)-\mu_i(t)\Big)\langle n_i\rangle \\ & + \sum_{j=1}^{2}\Big(\lambda_{ij}(t)-\mu_{ij}(t)\Big)(\langle n_i\rangle\langle n_j\rangle + \sigma_{ij})\end{aligned} \tag{C.22}$$

$$\begin{aligned}\frac{d\langle \sigma_{ii}\rangle}{dt} = & \Big(\lambda_i(t)+\mu_i(t)\Big)\langle n_i\rangle + 2\Big(\lambda_i(t)-\mu_i(t)\Big)\sigma_{ii} \\ & + \sum_{j=1}^{2}\Bigg(2\Big[\lambda_{ij}(t)-\mu_{ij}(t)\Big]\Big[\langle n_i\rangle\sigma_{ij} + \langle n_j\rangle\sigma_{ii} + \sigma_{iij}\Big] \\ & + \Big[\lambda_{ij}(t)+\mu_{ij}(t)\Big]\Big[\langle n_i\rangle\langle n_j\rangle + \sigma_{ij}\Big]\Bigg)\end{aligned} \tag{C.23}$$

$$\begin{aligned}\frac{d\langle \sigma_{ik}\rangle}{dt} = & \Big(\lambda_i(t)-\mu_i(t)+\lambda_k(t)-\mu_k(t)\Big)\sigma_{ik} \\ & + \sum_{j=1}^{2}\Bigg(\Big[\lambda_{ij}(t)-\mu_{ij}(t)\Big]\Big[\langle n_i\rangle\sigma_{kj} + \langle n_j\rangle\sigma_{ik} + \sigma_{ikj}\Big] \\ & + \Big[\lambda_{kj}(t)-\mu_{kj}(t)\Big]\Big[\langle n_k\rangle\sigma_{ij} + \langle n_j\rangle\sigma_{ik} + \sigma_{ikj}\Big]\Bigg)\end{aligned} \tag{C.24}$$

where $\langle n_i\rangle$, $\langle \sigma_{ii}\rangle$ and $\langle \sigma_{ik}\rangle$ describe the mean, variance and covariance of the different species.

The equation describing the evolution of the first moment depends on the second moment, whose own evolution depends on the third moment, etc. Moment closure schemes need to be applied to make progress.

C.1.4.1 Solution for the mean and variance of a single species

Here we apply the results derived above to our linear feedback model in the setting of only a single species being present (here assumed to be wildtype). In this situation, the stationary copy number distribution closely follows a normal distribution which means we can set the third order moments σ_{ijk} to zero without much loss of accuracy. Using $\lambda_w = w(\mu + c_1(w_{ss} - w))$ and $\mu_w = w\mu$, we find

$$\frac{d\langle w\rangle}{dt} = c_1 w_{ss}\langle w\rangle + c_1\Big(\langle w\rangle^2 + \sigma^2\Big) \tag{C.25}$$

$$\frac{d\sigma^2}{dt} = (2\mu + c_1 w_{ss})\langle w\rangle + 2c_1 w_{ss}\sigma^2 - 4c_1\langle w\rangle\sigma^2 - c_1\Big(\langle w\rangle^2 + \sigma^2\Big) \tag{C.26}$$

with $\langle w\rangle, \sigma^2$ and w_{ss} denoting wildtype expected value, variance and deterministic mean, respectively. The above equations can be solved for steady state, giving $w \sim N(\langle w\rangle_{ss}, \sigma^2_{ss})$ with

$$\langle w\rangle_{ss} = \frac{3}{4}w_{ss} \pm \frac{1}{4}\sqrt{w_{ss}^2 - \frac{8\mu}{c_1}} \tag{C.27}$$

$$\sigma^2_{ss} = \frac{w_{ss}}{8}\Big(w_{ss} \mp \sqrt{w_{ss}^2 - \frac{8\mu}{c_1}}\Big) + \frac{\mu}{2c_1}. \tag{C.28}$$

The upper sign solution agrees well with simulations. This equation breaks down for very small c_1 (in which case copy number extinction becomes significant). We note that the expected value of the stochastic process does not coincide with the deterministic mean; this deviation is larger when turnover is large (large μ) or when the negative feedback term is small (small c_1). Equations (C.27) and (C.28) are used in Section C.1.2 to represent the mean and variance of the OU-process approximating wildtype dynamics.

We can use Equations (C.27) and (C.28) to calculate the Coefficient of Variation (CV) of the wildtype population, giving

$$\mathrm{CV} = \frac{\sqrt{\frac{8\mu}{c_1} + 2w_{ss}(w_{ss} - \sqrt{w_{ss}^2 - \frac{8\mu}{c_1}})}}{3w_{ss} + \sqrt{w_{ss}^2 - \frac{8\mu}{c_1}}} \tag{C.29}$$

Finally, we can rewrite this equation to give

$$c_1 = -\frac{(1+\mathrm{CV}^2)^2\mu}{\mathrm{CV}^2(\mathrm{CV}^2-1)w_{ss}^2} \tag{C.30}$$

These two relations are useful as they allow us to relate the control parameter c_1 to the more robust CV.

C.1.5 System Size Expansion

Stochastic birth-death processes can be described analytically by a master equation. For our model, with birth rate $\lambda(w,m)$ and constant death rate μ, we obtain:

$$\begin{aligned}\frac{\partial P_{i,j}}{\partial t} &= \lambda(i-1,j)(i-1)P_{i-1,j} + \mu(i+1)P_{i+1,j} \\ &+ \lambda(i,j-1)(j-1)P_{i,j-1} + \mu(j+1)P_{i,j+1} \\ &- (i+j)\Big(\lambda(i,j)+\mu\Big)P_{i,j}\end{aligned} \tag{C.31}$$

where $P_{i,j}(t)$ gives the probability of being in state $(i,j) = (w,m)$ (the time dependence is dropped for convenience). In general, this equation will not be analytically solvable and suitable approximation methods are required.

In this section, we use van Kampen's system size expansion (SSE) [294] to approximate the above equation. First, we derive the leading order solution of the expansion, known as the linear noise approximation (LNA). As we will see, the LNA provides useful insights and can accurately describe the dynamics of our system for short time-scales. However, for longer time-scales higher order terms are required to maintain accuracy. We provide a solution to the expansion one order higher than the LNA in Section C.1.5.1, following the method developed in Ref. [458]. Other approximation techniques, such as the Kramers-Moyal expansion [459, 460], are not considered in this thesis. It was previously noted that the Kramers-Moyal expansion fails to accurately describe birth-death master equations [454].

Generally, a master equation can be written in the form

$$\dot{p}_{\vec{n}}(t) = \Omega \sum_{j=1}^{R} \left(\prod_{i=1}^{N} \mathbb{E}^{-S_{ij}} - 1 \right) f_j(\vec{n}, \Omega) p_{\vec{n}}(t) \tag{C.32}$$

where Ω is the system volume, R is the number of reactions involved, N is the number of species, $(S)_{ij}$ is the stoichiometry matrix, $\vec{n} = (n_1, n_2, \cdots, n_N)$ gives the number of particles

of each species, $\mathbb{E}$ is a raising and lowering operator[‡], and $p_{\vec{n}}(t)$ is the probability distribution of states $\vec{n}$ at time t. The equations $f_j(\vec{n}, \Omega)$ specify the reaction rates. The SSE provides an expansion of this master equation in powers of the inverse square root of the system volume Ω.

The expansion starts by expressing the state of the system in terms of a deterministic and stochastic component. Consider a single species whose concentration and copy number are denoted by $\phi(t)$ and n, respectively. One expects the distribution of n to be centered around $\Omega\phi(t)$ and to have a width of order $\sqrt{n} \propto \sqrt{\Omega}$. This motivates the following equation

$$n_i = \Omega\phi_i(t) + \Omega^{1/2}\xi_i \tag{C.33}$$

where ξ_i describe the fluctuations around the deterministic solution $\phi_i(t)$. All terms in the master equation can now be expressed in the new fluctuation variables ξ_i according to the following transformations[§]

$$\begin{aligned}
p_{\vec{n}}(t) &= \Pi(\vec{\xi}, t) \\
\mathbb{E}_i &\to 1 + \Omega^{-1/2}\frac{\partial}{\partial\xi_i} + \frac{1}{2}\Omega^{-1}\frac{\partial^2}{\partial\xi_i^2} + \cdots \\
\dot{p}_{\vec{n}} &= \frac{\partial\Pi(\vec{\xi}, t)}{\partial t} - \Omega^{1/2}\sum_{i=1}^{N}\frac{\partial\phi_i}{\partial t}\frac{\partial\Pi(\vec{\xi}, t)}{\partial\xi_i} \quad \text{(chain rule)} \\
f(\frac{n_i}{\Omega}) &= f(\phi_i + \Omega^{-1/2}\xi_i).
\end{aligned} \tag{C.34}$$

Substituting Equations (C.34) into Equation (C.32) gives

$$\begin{aligned}
\frac{\partial\Pi(\vec{\xi}, t)}{\partial t} - \Omega^{1/2}\sum_{i=1}^{N}\frac{d\phi_i}{dt}\frac{\partial\Pi(\vec{\xi}, t)}{\partial\xi_i} = \Omega\sum_{j=1}^{R}\Bigg[&- \Omega^{-1/2}\sum_{i=1}^{N}S_{ij}\frac{\partial}{\partial\xi_i} + \frac{1}{2}\Omega^{-1}\sum_{i,k}S_{ij}S_{kj}\frac{\partial^2}{\partial\xi_i\partial\xi_k} \\
&+ O(\Omega^{-3/2})\Bigg] \\
&\times \left[f_j(\vec{\phi}) + \Omega^{-1/2}\sum_i\frac{\partial f_j(\vec{\phi})}{\partial\phi_i}\xi_i + O(\Omega^{-1})\right]\Pi(\vec{\xi}, t)
\end{aligned} \tag{C.35}$$

which can be solved by collecting powers of $\Omega^{-1/2}$. Terms proportional to $\Omega^{1/2}$ form the macroscopic rate equations. The terms of order Ω^0 form a Fokker-Planck equation, the solution of

[‡]Its effect on an arbitrary function $f(\vec{n})$ is given by e.g. $\mathbb{E}_i f(\vec{n}) = f(\vec{n} + e_i)$ and $\mathbb{E}_i^{-1} f(\vec{n}) = f(\vec{n} - e_i)$ (where e_i is a column vector with all zeros and a 1 at entry i). Using a Taylor expansion, the operator can be written as $\mathbb{E}_i = 1 + \frac{\partial}{\partial n_i} + \frac{1}{2!}\frac{\partial^2}{\partial n_i^2} + \cdots$.

[§]$\mathbb{E}_i$ changes n_i into $n_i + 1$, which is equivalent to changing ξ_i into $\xi_i + \Omega^{-1/2}$.

which is the LNA:

$$\frac{\partial \Pi(\vec{\xi},t)}{\partial t} = -\sum_{i,j=1}^{2} A_{ij}\frac{\partial(\xi_j \Pi(\vec{\xi},t))}{\partial \xi_i} + \frac{1}{2}\sum_{i,j=1}^{2} B_{ij}\frac{\partial^2 \Pi(\vec{\xi},t)}{\partial \xi_i \partial \xi_j} \tag{C.36}$$

The coefficients A_{ij} and B_{ij} can be found by expanding equation (C.35) and are defined as

$$\begin{aligned} A_{ij} &= \sum_{k=1}^{R} S_{ik}\frac{\partial f_k}{\partial \phi_j} \\ B_{ij} &= \sum_{k=1}^{R} S_{ik}S_{jk}f_k \end{aligned} \tag{C.37}$$

The system we consider has two species ($N = 2$), four rate equations ($R = 4$) given by

$$\begin{aligned} f_1 &= w\lambda(w,m) \\ f_2 &= m\lambda(w,m) \\ f_3 &= w\mu \\ f_4 &= m\mu, \end{aligned} \tag{C.38}$$

and a stoichiometry matrix by

$$S = \begin{pmatrix} 1 & 0 & -1 & 0 \\ 0 & 1 & 0 & -1 \end{pmatrix} \tag{C.39}$$

where the two rows refer to the wildtype and mutant species, respectively, and the columns represent the reactions f_i.

In order to continue, it is useful to rewrite Equation (C.35) as an expansion in derivatives with respect to $\vec{\xi}$, namely $\partial_t \Pi = \sum_i \left(-\frac{\partial}{\partial \xi_i} A_i + \frac{1}{2!}\frac{\partial^2}{\partial \xi_i^2} B_i - \frac{1}{3!}\frac{\partial^3}{\partial \xi_i^3} C_i + \cdots \right)$ where $A_i, B_i, \ldots$ are functions of $\vec{\xi}$, Ω and $\vec{f}$. Evolution equations for the moments $\langle \xi_i \xi_j \ldots \rangle$ can be obtained by multiplying this equation by $\xi_i \xi_j \ldots$ and integrating over all $\vec{\xi}$. Using integration by parts, the following set of coupled ODEs can be obtained for our $N = 2$ system:

$$\begin{aligned} d_t\langle \xi_1^2 \rangle &= 2A_{11}\langle \xi_1^2 \rangle + 2A_{12}\langle \xi_1 \xi_2 \rangle + B_{11} \\ d_t\langle \xi_2^2 \rangle &= 2A_{22}\langle \xi_2^2 \rangle + 2A_{21}\langle \xi_1 \xi_2 \rangle + B_{22} \\ d_t\langle \xi_1 \xi_2 \rangle &= (A_{11} + A_{22})\langle \xi_1 \xi_2 \rangle + A_{12}\langle \xi_2^2 \rangle + A_{21}\langle \xi_1^2 \rangle + B_{12} \end{aligned} \tag{C.40}$$

which can be solved to give

$$\begin{aligned}\langle\xi_1^2\rangle = \frac{\mu w_{ss}^2}{(\partial_m\lambda m_{ss}+\partial_w\lambda w_{ss})^3}\Big(&2m_{ss}(1+\frac{m_{ss}}{w_{ss}})(\partial_m\lambda)^2(\partial_m\lambda m_{ss}+\partial_w\lambda w_{ss})t\\&-4(\partial_m\lambda)(\partial_w\lambda)m_{ss}-(\partial_w\lambda)^2w_{ss}+3(\partial_m\lambda)^2m_{ss}\\&+4e^{(\partial_m\lambda m_{ss}+\partial_w\lambda w_{ss})t}\left\{\partial_m\lambda\partial_w\lambda m_{ss}-(\partial_m\lambda)^2m_{ss}\right\}\\&+e^{2(\partial_m\lambda m_{ss}+\partial_w\lambda w_{ss})t}\left\{(\partial_w\lambda)^2w_{ss}+(\partial_m\lambda)^2m_{ss}\right\}\Big)\end{aligned} \tag{C.41}$$

$$\begin{aligned}\langle\xi_2^2\rangle = \frac{\mu m_{ss}^2}{(\partial_m\lambda m_{ss}+\partial_w\lambda w_{ss})^3}\Big(&2w_{ss}(1+\frac{w_{ss}}{m_{ss}})(\partial_w\lambda)^2(\partial_m\lambda m_{ss}+\partial_w\lambda w_{ss})t\\&-4(\partial_m\lambda)(\partial_w\lambda)w_{ss}-(\partial_m\lambda)^2m_{ss}+3(\partial_w\lambda)^2w_{ss}\\&+4e^{(\partial_m\lambda m_{ss}+\partial_w\lambda w_{ss})t}\left\{\partial_m\lambda\partial_w\lambda w_{ss}-(\partial_w\lambda)^2w_{ss}\right\}\\&+e^{2(\partial_m\lambda m_{ss}+\partial_w\lambda w_{ss})t}\left\{(\partial_w\lambda)^2w_{ss}+(\partial_m\lambda)^2m_{ss}\right\}\Big)\end{aligned} \tag{C.42}$$

$$\begin{aligned}\langle\xi_1\xi_2\rangle = \frac{\mu w_{ss}m_{ss}}{(\partial_m\lambda m_{ss}+\partial_w\lambda w_{ss})^3}\Big(&-2(w_{ss}+m_{ss})(\partial_m\lambda)(\partial_w\lambda)(\partial_m\lambda m_{ss}+\partial_w\lambda w_{ss})t\\&+(\partial_w\lambda)^2w_{ss}+(\partial_m\lambda)^2m_{ss}-2(\partial_w\lambda)(\partial_m\lambda)(w_{ss}+m_{ss})\\&+2e^{(\partial_m\lambda m_{ss}+\partial_w\lambda w_{ss})t}\left\{(\partial_m\lambda)(\partial_w\lambda)(w_{ss}+m_{ss})-(\partial_w\lambda)^2w_{ss}-(\partial_m\lambda)^2m_{ss}\right\}\\&+e^{2(\partial_m\lambda m_{ss}+\partial_w\lambda w_{ss})t}\left\{(\partial_w\lambda)^2w_{ss}+(\partial_m\lambda)^2m_{ss}\right\}\Big)\end{aligned} \tag{C.43}$$

where $\langle\xi_1^2\rangle$, $\langle\xi_2^2\rangle$ and $\langle\xi_1\xi_2\rangle$ denote the wildtype and mutant variance and covariance, respectively. This solution assumes trajectories starting in the deterministic steady state (w_{ss}, m_{ss}); all partial derivatives are evaluated at this steady state. The means of w and m are calculated from the macroscopic rate equations at order $\Omega^{1/2}$ and are identical to the deterministic means. The intermediate-time forms of these expressions (when the exponentially decaying terms have died out) are given in Table 4.2 of Chapter 4.

Heteroplasmy variance can be derived using a Taylor expansion which, keeping only the leading order, gives: $\mathrm{var}(h) \approx (\frac{\partial h}{\partial w})^2\sigma_w^2 + (\frac{\partial h}{\partial m})^2\sigma_m^2 + 2(\frac{\partial h}{\partial w})(\frac{\partial h}{\partial m})\mathrm{cov}(w,m) = \frac{1}{(w+m)^4}(m^2\sigma_w^2 + w^2\sigma_m^2 - 2w\,m\,\mathrm{cov}(w,m))$.

C.1.5.1 Higher order terms

In order to obtain expressions up to order Ω^{-1}, we use the approach outlined in Ref. [458]. First, the probability distribution $\Pi(\vec{\xi}, t)$ is written in powers of the inverse square root of the

system volume, i.e. $\Pi(\vec{\xi},t)=\sum_{j=0}^{\infty}\Pi_j(\vec{\xi},t)\Omega^{-j/2}$. The moments follow a similar expansion:

$$\langle\xi_k\xi_m\dots\xi_r\rangle=\sum_{j=0}^{\infty}[\xi_k\xi_m\dots\xi_r]_j\Omega^{-j/2} \tag{C.44}$$

with

$$[\xi_k\xi_m\dots\xi_r]_j=\int\xi_k\xi_m\dots\xi_r\Pi_j(\vec{\xi},t)d\vec{\xi}. \tag{C.45}$$

The final equation describing the evolution of the means of mutant and wildtype molecules to order Ω^{-1} for our birth-death process, is given by [458]

$$\partial_t\langle\phi_i\rangle=J_i^w\left(\langle\phi_w\rangle-\phi_w\right)+\frac{1}{2}\Omega^{-1}J_i^{wp}[\xi_w\xi_p]_0 \tag{C.46}$$

where ϕ_i refers to the concentration of species i, and

$$J_{i,j,\dots,r}^{s,t,\dots,z}=\frac{\partial}{\partial\phi_s}\frac{\partial}{\partial\phi_t}\cdots\frac{\partial}{\partial\phi_z}D_{i,j,\dots,r} \tag{C.47}$$

$$D_{i,j,\dots,r}=\sum_{k=1}^{R}S_{ik}S_{jk}\dots S_{rk}f_k(\vec{\phi}) \tag{C.48}$$

are introduced for more convenient notation (summation over repeated indices is used). Evolution equations for the moments $\langle\xi_k\xi_m\dots\xi_r\rangle$ can be obtained in a similar way as before, giving [458]

$$\frac{\partial}{\partial t}[\xi_w\xi_p]_0=J_w^r[\xi_r\xi_p]_0+J_p^r[\xi_r\xi_w]_0+D_{wp}. \tag{C.49}$$

Inserting Equations (C.47) and (C.48) into the above equation, and using our linear feedback model, gives

$$
\begin{aligned}
[\xi_1\xi_1]_0(t) = \frac{(\lambda+\mu)w_{ss}^2}{2(m_{ss}\partial_m\lambda + w_{ss}\partial_w\lambda)^3}\Big[&2(\partial_m\lambda)^2(w_{ss}+m_{ss})m_{ss}\left((\partial_m\lambda)\frac{m_{ss}}{w_{ss}} + (\partial_w\lambda)\right)t \\
&+ 3(\partial_m\lambda)^2 m_{ss} - (\partial_w\lambda)^2 w_{ss} - 4(\partial_m\lambda)(\partial_w\lambda)m_{ss} \\
&+ 4e^{(\partial_m\lambda m_{ss}+\partial_w\lambda w_{ss})t}\left((\partial_w\lambda)(\partial_m\lambda)m_{ss} - (\partial_m\lambda)^2 m_{ss}\right) \\
&+ e^{2(\partial_m\lambda m_{ss}+\partial_w\lambda w_{ss})t}\left((\partial_w\lambda)^2 w_{ss} + (\partial_m\lambda)^2 m_{ss}\right)\Big] \qquad \text{(C.50)} \\
[\xi_2\xi_2]_0(t) = \frac{(\lambda+\mu)m_{ss}^2}{2(m_{ss}\partial_m\lambda + w_{ss}\partial_w\lambda)^3}\Big[&2(\partial_w\lambda)^2(w_{ss}+m_{ss})w_{ss}\left((\partial_m\lambda) + (\partial_w\lambda)\frac{w_{ss}}{m_{ss}}\right)t \\
&+ 3(\partial_w\lambda)^2 w_{ss} - (\partial_m\lambda)^2 m_{ss} - 4(\partial_m\lambda)(\partial_w\lambda)w_{ss} \\
&+ 4e^{(\partial_m\lambda m_{ss}+\partial_w\lambda w_{ss})t}\left((\partial_w\lambda)(\partial_m\lambda)w_{ss} - (\partial_w\lambda)^2 w_{ss}\right) \\
&+ e^{2(\partial_m\lambda m_{ss}+\partial_w\lambda w_{ss})t}\left((\partial_w\lambda)^2 w_{ss} + (\partial_m\lambda)^2 m_{ss}\right)\Big] \qquad \text{(C.51)} \\
[\xi_1\xi_2]_0(t) = \frac{-(\lambda+\mu)w_{ss}m_{ss}}{2(m_{ss}\partial_m\lambda + w_{ss}\partial_w\lambda)^3}\Big[&2(\partial_w\lambda)(\partial_m\lambda)(w_{ss}+m_{ss})\Big((\partial_m\lambda)m_{ss} + (\partial_w\lambda)w_{ss}\Big)t \\
&- w_{ss}(\partial_w\lambda)^2 - m_{ss}(\partial_m\lambda)^2 + 2(\partial_m\lambda)(\partial_w\lambda)(w_{ss}+m_{ss}) \\
&+ 2e^{(\partial_m\lambda m_{ss}+\partial_w\lambda w_{ss})t}\Big((\partial_w\lambda)^2 w_{ss} + (\partial_m\lambda)^2 m_{ss} - 2(\partial_w\lambda)(\partial_m\lambda)(w_{ss}+m_{ss})\Big) \\
&+ e^{2(\partial_m\lambda m_{ss}+\partial_w\lambda w_{ss})t}\left((\partial_w\lambda)^2 w_{ss} + (\partial_m\lambda)^2 m_{ss}\right)\Big] \qquad \text{(C.52)}
\end{aligned}
$$

where w_{ss} and m_{ss} denote the deterministic steady states, and all partial derivatives (as well as λ itself) are evaluated at steady state. Finally, we can solve Equation (C.46) which gives

$$\begin{aligned}\langle w(t)\rangle = w_{ss} + \Omega^{-1}\frac{w_{ss}(\lambda+\mu)}{2(m_{ss}\partial_m\lambda + w_{ss}\partial_w\lambda)^3}\Bigg[&2(\partial_m\lambda)m_{ss}\Big\{(\partial_m\lambda)^2 m_{ss} - (\partial_w\lambda)^2 w_{ss} \\ &+ (\partial_w\lambda)(\partial_m\lambda)(w_{ss}-m_{ss})\Big\}t \\ &+ 3(\partial_m\lambda)^2 m_{ss} + (\partial_w\lambda)^2 w_{ss} - 2(\partial_m\lambda)(\partial_w\lambda)m_{ss} \\ &+ 2e^{(\partial_m\lambda m_{ss}+\partial_w\lambda w_{ss})t}\Big((\partial_w\lambda)(\partial_m\lambda)m_{ss} - (\partial_w\lambda)^2 w_{ss} - 2(\partial_m\lambda)^2 m_{ss}\Big) \\ &+ e^{2(\partial_m\lambda m_{ss}+\partial_w\lambda w_{ss})t}((\partial_m\lambda)^2 m_{ss} + (\partial_w\lambda)^2 w_{ss})\Bigg]\end{aligned} \tag{C.53}$$

$$\begin{aligned}\langle m\rangle(t) = m_{ss} + \Omega^{-1}\frac{m_{ss}(\lambda+\mu)}{2(m_{ss}\partial_m\lambda + w_{ss}\partial_w\lambda)^3}\Bigg[&2(\partial_w\lambda)w_{ss}\Big\{(\partial_w\lambda)^2 w_{ss} - (\partial_m\lambda)^2 m_{ss} \\ &+ (\partial_w\lambda)(\partial_m\lambda)(m_{ss}-w_{ss})\Big\}t \\ &+ 3(\partial_w\lambda)^2 w_{ss} + (\partial_m\lambda)^2 m_{ss} - 2(\partial_m\lambda)(\partial_w\lambda)w_{ss} \\ &+ 2e^{(\partial_m\lambda m_{ss}+\partial_w\lambda w_{ss})t}\Big((\partial_w\lambda)(\partial_m\lambda)w_{ss} - (\partial_m\lambda)^2 m_{ss} - 2(\partial_w\lambda)^2 w_{ss}\Big) \\ &+ e^{2(\partial_m\lambda m_{ss}+\partial_w\lambda w_{ss})t}((\partial_m\lambda)^2 m_{ss} + (\partial_w\lambda)^2 w_{ss})\Bigg]\end{aligned} \tag{C.54}$$

Unlike the LNA, these higher order solutions predict time-varying means. In reality $\langle w(t)\rangle$ and $\langle m(t)\rangle$ will always saturate due to one species inevitably reaching extinction after long times, meaning the above equations are not valid for all times.

When $\partial_m\lambda = 0$, we know that $\langle m(t)\rangle$ increase in an exponential-like fashion and we can therefore make the ansatz that the linear term given above represents the first term of a Taylor expansion. This leads to $\langle m(t)\rangle = e^{2\mu/w_{ss}t}$, which agrees well with simulations for short times (Figure C.2C). We can also derive the long-time value for $\langle w(t)\rangle$ in the case that $\partial_m\lambda = 0$, giving

$$\begin{aligned}\langle w\rangle_{t\to\infty} &= w_{ss} - \frac{\mu}{c_1 w_{ss}} \\ &= \frac{3}{4}w_{ss} + \frac{1}{4}\sqrt{w_{ss}^2 - \frac{8\mu}{c_1} + \frac{16\mu^2}{c_1^2 w_{ss}^2}}\end{aligned} \tag{C.55}$$

This result is very similar to the prediction made by the Lotka-Volterra model (Equation (C.27)), the only difference being an extra term $(16\mu^2)/(c_1^2 w_{ss}^2)$ appearing under the square root. Because an 'average' cell has ~ 1000 mtDNA molecules, this additional term is likely

to be small. Equation (C.55) shows that the larger the deterministic steady state w_{ss}, the smaller the difference between this steady state and the stochastic expected value; this is why the exponential increase in $\langle m(t) \rangle$ is relatively large in low copy number cells. We note that the solutions provided above can be extended to more general settings involving e.g. quadratic controls or controls on both replication and degradation rates. In the latter case, all occurrences of $\partial_m \lambda$ and $\partial_w \lambda$ are simply replaced by $\partial_m(\lambda - \mu)$ and $\partial_w(\lambda - \mu)$, respectively.

C.2 Intercellular mtDNA exchange

C.2.1 Fixation probabilities in the limit of slow mtDNA exchange

Here we calculate long-time cellular heteroplasmy values in the limit of slow mtDNA exchange, i.e. $\gamma \ll \mu$. In this limit, each cell is expected to fixate on mutant or wildtype before a new intercellular mtDNA exchange event occurs. This extreme setting allows us to calculate the fixation probabilities of each species analytically. The two-cell system we described here is an example of a Moran process and fixation probabilities follow from standard results [461]. We illustrate the derivation of these probabilities for our particular system, and use the result to derive other quantities of interest.

We initialise two cells at heteroplasmy values h_1 and h_2, and denote the wildtype and mutant steady state copy numbers in homoplasmic cells by w_{ss} and m_{ss}, respectively. Before any mtDNA exchange event occurs, both cells fixate on either $h = 0$ or $h = 1$. Three possible scenarios exist after this initial fixation: i) both cells fixated on w (with probability $(1 - h_1)(1 - h_2) \equiv \zeta$), ii) both cells fixated on m (with probability $h_1 h_2 \equiv \zeta'$) , or iii) one cell fixated on w and the other on m (with probability $1 - \zeta - \zeta'$); an illustration of the system is provided in Figure C.4A. In the first two scenarios, the cells will remain in their fixated state forever (assuming no mutations can occur). In the latter scenario, however, a new exchange event will eventually occur, again giving rise to three possible scenarios (Figure C.4A).

Consider the situation in which the two cells have heteroplasmy values $h = 0$ and $h = 1$; we will refer to these cells as c_0 and c_1, respectively. Full wildtype fixation occurs when a wildtype mtDNA hops from c_0 to c_1 (before a mutant mtDNA hops from c_1 to c_0) and subsequently takes over the existing mutant population. The rate at which a wildtype mtDNA hops out of c_0 is given by $\gamma\, w_{ss}$. The probability that a wildtype molecule hops before a mutant does, is simply given by $w_{ss}/(w_{ss} + m_{ss})$. Finally, the probability of subsequent wildtype fixation is equal to the fraction of w in c_1, i.e. $1/(1 + m_{ss})$. Similar arguments hold for the probability of

complete mutant fixation. We can now write down the following equations:

$$\begin{aligned}
\mathrm{P}(w \text{ hops before } m \text{ and } w \text{ fixates}) &= \mathrm{P}(w \text{ hops before } m)\ \mathrm{P}(w \text{ fixates}) \\
&= \frac{w_{ss}}{w_{ss}+m_{ss}}\frac{1}{1+m_{ss}} \\
&\equiv \alpha \qquad \text{(C.56)} \\
\mathrm{P}(m \text{ hops before } w \text{ and } m \text{ fixates}) &= \mathrm{P}(m \text{ hops before } w)\ \mathrm{P}(m \text{ fixates}) \\
&= \frac{m_{ss}}{w_{ss}+m_{ss}}\frac{1}{1+w_{ss}} \\
&\equiv \beta \qquad \text{(C.57)}
\end{aligned}$$

If the mtDNA (mutant or wildtype) that hopped is unsuccessful at invading the host cell, then the two cells will remain in their original configuration (i.e. one having $h = 0$ and the other having $h = 1$); this occurs with probability $1 - \alpha - \beta$ (Figure C.4A).

The process described above will repeat itself until full mutant or wildtype fixation has been reached. We can now straightforwardly derive the following equation:

$$\begin{aligned}
\mathrm{P}\big(\text{w fixation} \,\big|\, h_1, h_2, w_{ss}, m_{ss}\big) &= \zeta + (1-\zeta-\zeta')\alpha + (1-\zeta-\zeta')(1-\alpha-\beta)\alpha + \cdots \\
&= \zeta + (1-\zeta-\zeta')\alpha \sum_{i=0}^{\infty}(1-\alpha-\beta)^i \\
&= \zeta + (1-\zeta-\zeta')\frac{\alpha}{\alpha+\beta} \\
&\equiv P_w \qquad \text{(C.58)}
\end{aligned}$$

where α, β, ζ and ζ' are defined above. When the first step in the diagram shown in Figure C.4 is omitted and cells are initialised at $h_1 = 0$ and $h_2 = 1$ (or vice versa), the above expression reduces to $P_w = \frac{\alpha}{\alpha+\beta}$. This simplified system is part of a more general result of N interacting cells, in which case $P_w = \frac{1-1/r}{1-1/r^N}$ with $r = \alpha/\beta$ [328, 461]. We can now evaluate mean cellular heteroplasmy at long times, which is given by

$$\begin{aligned}
\langle h \rangle_{t\to\infty} &= \mathrm{P}(\text{w fixation}) \cdot 0 + \mathrm{P}(\text{m fixation}) \cdot 1 \\
&= 1 - P_w \qquad \text{(C.59)}
\end{aligned}$$

where we have assumed that the mtDNA population does not reach extinction in either cell.

If the mutant species has a higher carrying capacity, i.e. $m_{ss} > w_{ss}$, then both fractions appearing in the definition of β (Equation (C.57)) are larger than those appearing in the

definition of α (Equation (C.56)). This means that every time the system is in a state with $h_1 = 0$ and $h_2 = 1$, chances of mutant fixation are slightly higher than those of wildtype fixation. This eventually leads to an increase in mean heteroplasmy and it can be shown that the inequality $\langle h \rangle_{t\to\infty} > \frac{1}{2}(h_1 + h_2)$ holds when $m_{ss} > w_{ss}$. Similarly, if $w_{ss} > m_{ss}$ we obtain $\langle h \rangle_{t\to\infty} < \frac{1}{2}(h_1 + h_2)$.

Implementing our linear control strategy gives $m_{ss} = w_{ss}/\delta$, which means Equation (C.59) can be rewritten as

$$\langle h \rangle_{t\to\infty} = \frac{(\delta + w_{ss})(h_1 + h_2 - h_1 h_2) + \delta^2 h_1 h_2 (1 + w_{ss})}{\delta^2(1 + w_{ss}) + \delta + w_{ss}}. \tag{C.60}$$

This equation is shown in Figure C.4B as a function of δ, for $h_1 = h_2 = 0.1$ (the qualitative shape of the graph is identical for any non-trivial values h_1 and h_2). Solving $\partial_\delta \langle h \rangle_{t\to\infty} = 0$ gives $\delta = 0$ or $\delta = -2w_{ss}$, the latter solution (which forms a minimum) being unphysiological as it corresponds to a highly unstable system. The maximum mean heteroplasmy value at $\delta = 0$ is given by $\langle h \rangle_{t\to\infty,\max} = h_1 + h_2 - h_1 h_2$.

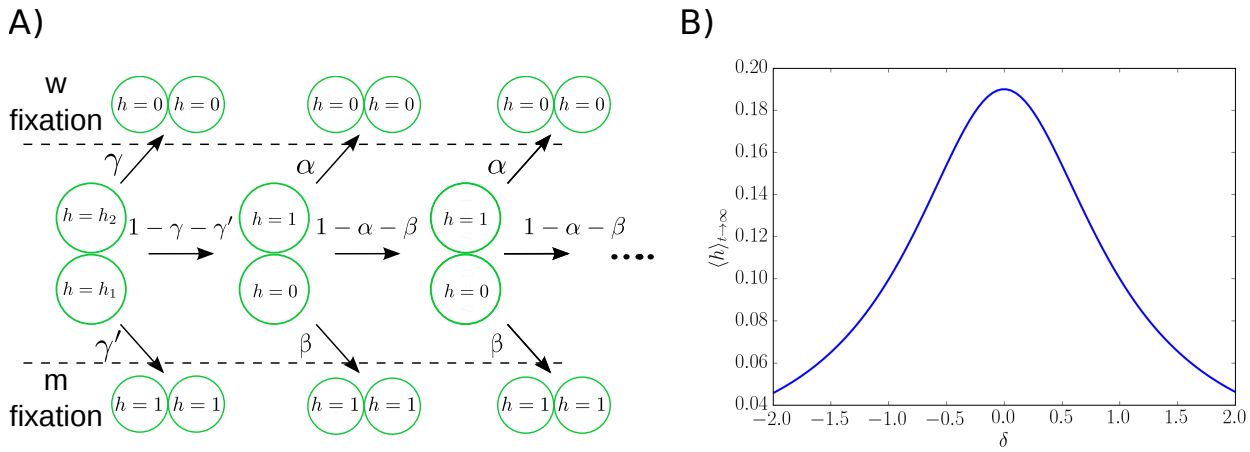


Figure C.4: Fixation probabilities in the limit of slow hopping. A) This cartoon illustrates all possible scenarios that can take place in the limit $\gamma \ll \mu$, meaning that both cells reach fixation before an exchange of mtDNA molecules takes place. The parameters ζ, ζ', α and β, denoting the probabilities of the indicated events, are defined in the text. We have neglected the probability that both cells reach extinction. An infinite chain arises in which two cells at $h = 0$ and $h = 1$ can either fully fixate on wildtype (both cells reaching $h = 0$), fully fixate on mutant (both cells reaching $h = 1$) or remain in their original state. **B)** We show $\langle h \rangle_{t\to\infty}$ as a function of δ for $h_1 = h_2 = 0.1$ and $w_{ss} = 200$. The maximum value of $\langle h \rangle_{t\to\infty}$ occurs at $\delta = 0$ and is given by $(1 - h_1)(1 - h_2)$.

C.2.2 Intuitions behind stochastic drive and copy number drift

How does the interplay between mtDNA exchange rate, turnover rate, and control strength determine heteroplasmy dynamics? Though we do not provide an analytical formula predicting changes in mean h (an interesting future challenge), we can provide some intuition as to how the relative strengths of inter- and intracellular mtDNA dynamics determine copy number dynamics that exists.

When stochastic fluctuations move wildtype and mutant copy numbers away from steady state, both the feedback control as well as intercellular interactions force copy numbers towards a new steady state. The type of fluctuations that are seen depends on the relative strength of these two forces. Figure C.5 shows an example of a system which, for fixed turnover μ, has either a strong control and a slow exchange rate or a weak control and a fast exchange rate. In the former case copy number dynamics mostly occurs along the steady state line, whereas in the latter case cells are highly coupled and together fluctuate through (w, m)-space.

In Figure 5.4 we observed that deterministically, copy number equilibration between different cells results in a slight increase (when $\delta < 1$) in mean heteroplasmy due to a higher copy number in a high-heteroplasmy cell. This, combined with many stochastic fluctuations in h, can lead to increases in $\langle h(t) \rangle$ (Figure 5.6). Intuitively, we may expect a faster change in $\langle h(t) \rangle$ if a new fluctuation in heteroplasmy (due to intracellular mtDNA dynamics) occurs

after full equilibration of heteroplasmies between cells (as a response to previous heteroplasmy fluctuations) has taken place. In this way, maximum advantage is being taken of the small increases in mean heteroplasmy after each cellular equilibration. Therefore, the higher the mtDNA exchange rate relative to the intracellular mtDNA dynamics, the faster the increase in $\langle h(t) \rangle$. Because we based part of this argument on deterministic dynamics, the conclusion only holds in the strong control setting (deterministically, the dynamics only ever approach the steady state line, which can be considered a strong control). In conclusion, we have provided an intuitive explanation of why $\langle h(t) \rangle$ increases faster at higher mtDNA exchange rates in the strong control setting, as observed through stochastic simulations in Figure 5.5A.

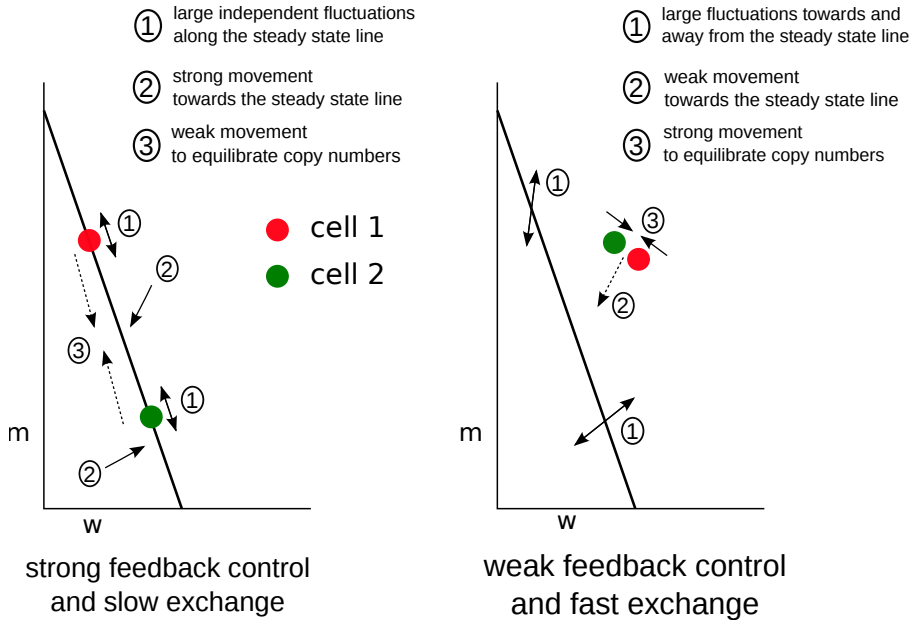


Figure C.5: The interplay between mtDNA turnover, feedback control and intercellular exchange determine the type of copy number dynamics seen. This cartoon shows two settings which are assumed to have identical mtDNA turnover rates: i) a strong feedback control (large b) and slow mtDNA exchange (left), and iii) a weak feedback control and fast mtDNA exchange (right). In the former setting, states of both cells remain close to the slow manifold whereas in the latter setting the two states remain close together and fluctuate further away from the manifold.

What is the cause of a drift in (w, m)-space along the steady state line? Imagine a cell in a deterministic steady state (w_{ss}, m_{ss}). As birth and death rates are balanced, fluctuations increasing or decreasing w, to reach states $(w_{ss} + \Delta w, m_{ss})$ or $(w_{ss} - \Delta w, m_{ss})$, are equally likely (similarly for m). When the new state, after a fluctuation occurred, is mapped back towards the steady state line along a line of constant heteroplasmy[¶], the position on the steady state line has changed (Figure C.6). When $\delta < 1$, a downwards wildtype fluctuation leads to a shift up the line towards mutant fixation (after having mapped back towards the steady state line) whereas an upwards fluctuation leads to a net shift down the line towards wildtype

[¶]This is the case for deterministic dynamics, and is also true on average in a stochastic setting.

fixation. However, the size of these shifts is not symmetric, the upwards shift being larger than the downwards shift (Figure C.6). This argument was made previously in Ref. [328] to explain the existence of drift towards the species of higher carrying capacity. However, the situation is more subtle because fluctuations in mutant species lead to exactly the opposite behaviour (i.e. the downwards shift is larger than the upwards shift along the steady state line, Figure C.6). To add to the complexity, wildtype fluctuations are more likely to occur than mutant ones if $h < 0.5$ whereas mutant fluctuations are more frequent when $h > 0.5$ (Figure C.6). We thus stress that the explanation for the drift provided by the authors in Ref. [328] is incomplete.

How can we make progress in providing an analytical approximation to the rate of increase of cellular mean heteroplasmy $\langle h(t) \rangle$? As observed in Section 5.2.1.4, heteroplasmy variance is indicative of this rate of increase, and thus providing an equation for e.g. the initial rate of increase of $\mathrm{var}(h)$ may give some new insights.

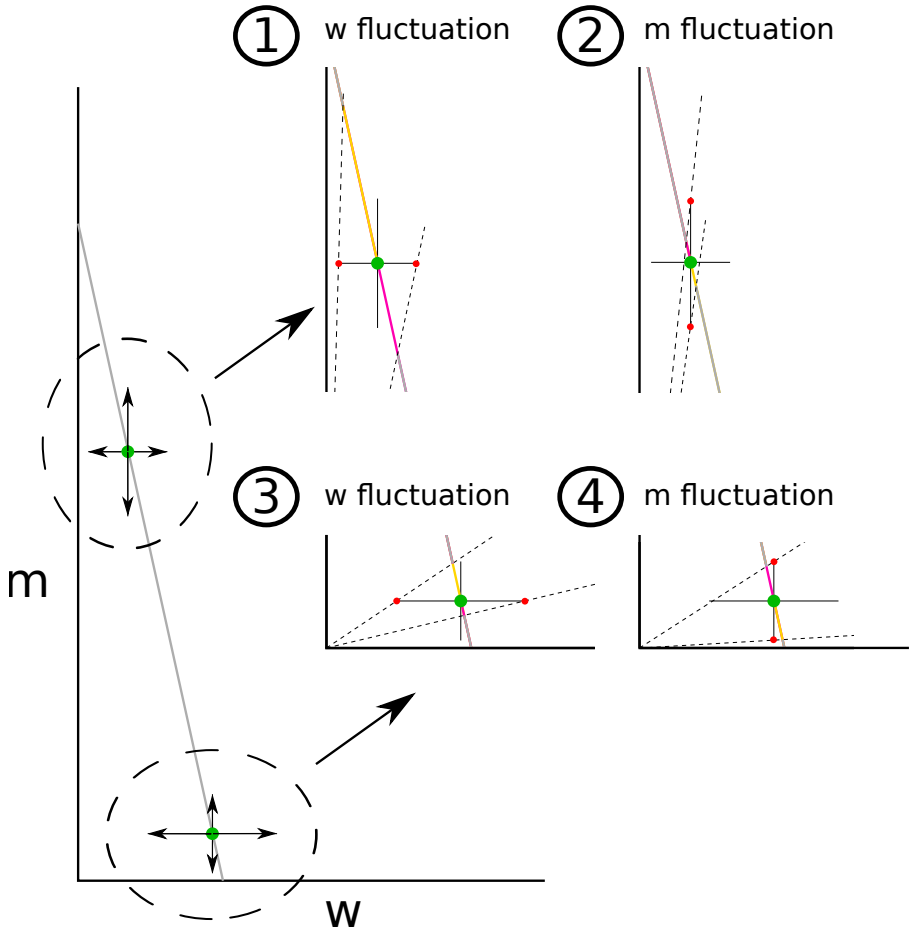


Figure C.6: The emergence of drift along the steady state line. Here we show a cartoon (not drawn to scale) of the effect mutant and wildtype fluctuations around their steady states have on movement along the deterministic steady state line. The yellow and pink lines highlight shifts that are produced by fluctuations in mutant and wildtype species, the yellow line indicating the larger shift. After a fluctuation, states are mapped back towards the steady state line along lines of constant heteroplasmy (dashed lines). The green dots represent the initial state from which up or down fluctuations in w or m (illustrated by the red dots) can occur with equal probability. The shift towards mutant fixation caused by downward fluctuations of w is larger than the shift towards wildtype fixation caused by upwards fluctuations of w (observed in (1) and (3)). The opposite is true for mutants, in which case a net shift towards wildtype fixation is seen. When $h < 0.5$ ((3) and (4)) wildtype copy numbers are higher than mutant numbers and therefore fluctuations in w are more likely to occur, which is illustrated through asymmetric fluctuation sizes. The relatively frequency of all the fluctuations occurring, as well as the size and direction of the shifts they induce along the steady state line, together give rise to the existence of a drift term.

C.2.3 Estimation of control strength parameter c_1

In order to estimate the control strength parameter c_1, we focus on estimating the coefficient of variation (CV) of wildtype copy numbers across cells homoplasmic in wildtype; we can then obtain c_1 using Equation (C.30). The CV is a measure of the width of the copy number distribution across cells (or over time in a single cell), and therefore an indication of control strength, and has the advantage of not depending on mean copy numbers.

We explored different methods of estimating the CV, one of which involves determining the variation in wildtype copy number along skeletal muscle fibres. Because we assume a single fibre consists of many 'cells', a copy number distribution along a fibre can be interpreted as a distribution across cells. We collected data from two studies (Refs. [21, 85]), and only use data from fibre regions homoplasmic in wildtype or from fibre regions in which w show little correlation with heteroplasmy (in which case $\delta \approx 0$ and the control strength is not affected by the presence of mutants). The resulting copy number distributions from three fibres are shown in Figure C.7A,B, and lead to the following estimations for the CV: 0.69, 0.55 and 0.49. Such high values for the CV, however, would lead to high chances of mtDNA extinction in single cells (see below) which seems unrealistic. We thus conclude that it is likely these CV's do not solely reflect the actual control feedback strength, but mostly reflect changes in in fibre volume or mitochondrial density (mitochondria are more concentrated near neuromuscular junctions, nuclei and capillaries [462]). Therefore, despite the high copy number variance observed along the fibres, it may still be that copy numbers within local fibre regions are strongly controlled.

To obtain a better intuition about how the CV affects mtDNA distributions, we plotted example wildtype distributions for several CV values (Figure C.7A). These distributions are obtained by i) using Equation (C.17) to obtain the steady state wildtype distribution for a given value of c_1 (assuming a linear control $\lambda(w) = \mu + c_1(N_{ss} - w)$) and ii) using Equation (C.29) to obtain a value for the CV. We observe that when CV $\gtrsim 0.3$, an appreciable rate of fixation occurs. This means that in a population of cells, each containing a linear feedback control steering copy number towards some fixed value[‖], some mtDNA-less cells exist which experience a large stochastic fluctuation driving their copy numbers towards extinction. Figure C.7B shows the probability of mtDNA extinction as a function of CV, obtained through stochastic simulations. Because it seems unlikely that a feedback control is so loose as to allow for copy number extinction, we use CV = 0.25 as an upper bound (Figure C.7B); at this value extinction probability is very low. As a lower bound we pick the value CV = 0.02 because it seems unlikely

[‖]The probability of a cell reaching copy number extinction does not depend on the value of N_{ss}.

mtDNA populations are controlled more tightly than as indicated by the magenta distribution in Figure C.7C.

We appreciate the our upper and low bound choices for the CV are somewhat arbitrary, but we would argue they provide a plausible biological parameter range. We do not use this range to make quantitative statements, we only use it to speculate about whether cellular mtDNA exchange could plausibly lead to significant changes in mean cellular heteroplasmy (Section 5.2.2.3).

To conclude, we estimate that the CV of a (wildtype) mtDNA population across identical cells lies in the range CV $\sim [0.02, 0.25]$. Using $N_{ss} = 500$ and $\mu = 0.07$, as assumed in Figures 5.5 - 5.8, this corresponds to $c_1 \sim [5.5 \times 10^{-6}, 7 \times 10^{-4}]$. We note that the unrealistically high values for the CV obtained by using skeletal muscle data suggest that most of this variation is due to external factors (e.g. volume changes along the fibres). As such, measuring wildtype copy number distributions across a population of cells (which will always show heterogeneity in volume) may not provide a good estimate of the CV. Instead, non-destructive copy number measurements in single quiescent cells over time can be used (as suggested in Table 5.5 of Chapter 5).

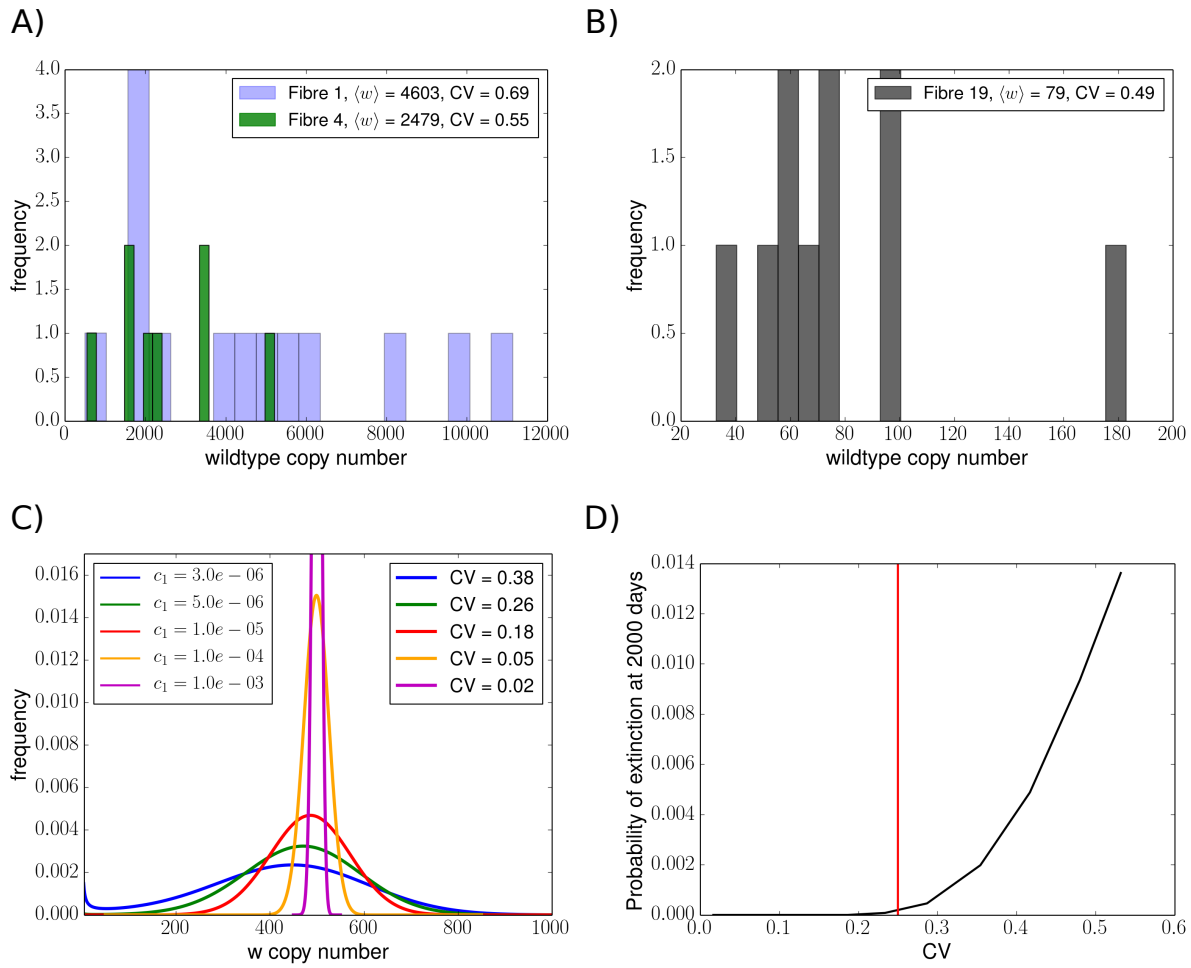


Figure C.7: Estimating the feedback control strength. A) Wildtype copy number values measured along single fibres are shown for two fibres defined as 'fibre 1' and 'fibre 4' in Figure 7 of Ref. [21]. Copy numbers were measured in 10μm thick slices of 36-month old rat quadriceps. **B)** Data from 'fibre 19' was taken from Figure 3 of Ref. [85]. These copy numbers were measured in 10μm thick vastus lateralis muscle slices from a 76-year old male human subject. **C)** Steady state wildtype copy number distributions, with their corresponding coefficient of variations, are shown at $h = 0$ for different control strengths using $N_{ss} = 500$ and $\mu = 0.07$. Distributions were obtained by using the analytical approximation derived in Section C.1.3. These approximations show good agreement with stochastic simulations. **D)** Here we show the probability of copy number extinction, when using a linear feedback function $\lambda(w) = \mu + c_1(N_{ss} - w)$, as a function of the CV. We used $\mu = 0.07$ and $N_{ss} = 500$, which then fixes c_1 given a value for the CV (Equation (C.29)). The fixation probability is defined at 2000 days and obtained through stochastic Gillespie simulations (5×10^4 repeats). The vertical line denotes the upper bound of our CV estimations, namely CV $= 0.25$; at this value, extinction is still very low. We note that any nonzero fixation probabilities shown here will continue to increase over time until all trajectories have gone extinct.

C.2.4 Estimation of mtDNA exchange rate

Here we estimate the intercellular mtDNA exchange rate γ in two different ways: 1) using experimentally measured diffusion coefficients of mtDNA and mitochondrial proteins, and 2) using the rate at which high-heteroplasmy regions spread out over time along muscle fibres.

C.2.4.1 Estimating γ using mtDNA and protein diffusion coefficients

For our first estimation, we use diffusion coefficients of both mtDNA nucleoids as well as mitochondrial inner membrane proteins (as nucleoids are closely associated with the inner membrane [355]). Assuming 1D random diffusion of an mtDNA molecule along the length of a fibre, the position of the molecule is described by a Gaussian centered at the initial position of the mtDNA. The variance of the Gaussian increases with time. As discussed in Section 5.2.2.2, we assume a single fibre can partitioned into 'cells' whose length we denote by L_c. To estimate the rate of mtDNA exchange between cells, we want to know the average time it takes for the mtDNA to diffuse along the length of a cell. We use two different ways to estimate this time, as outlined below.

First, we use the first passage time, i.e. the first time at which the mtDNA molecule reaches a neighbouring cell (given that it just entered the current cell). Though the expected first passage time for 1D random diffusion diverges, the most likely first passage time, i.e. the 'typical' first passage time t_{typ}, can be calculated analytically using standard methods (Equation (C.61)). Due to the diverging expected value, however, the first passage time distribution is heavy-tailed and t_{typ} may therefore not be representative of first hitting times in general; hence the reason for considering an alternative estimation.

Second, we use the root-mean-square displacement L_{RMS}, which represents the standard deviation of the probability distribution centered at the initial point and is a measure of the spatial extent of random diffusion. The time it takes for L_{RMS} to be equal to L_c, t_{RMS}, is provided in Equation (C.62). We see that these two estimates estimates we provided only differ by a factor of 3.

$$t_{typ} = \frac{L_c^2}{6D} \tag{C.61}$$

$$t_{RMS} = \frac{L_c^2}{2D} \tag{C.62}$$

We can now estimate the mtDNA exchange rate between cells γ, which is modelled as a Poisson process. The waiting times in between hopping events (t_w) are exponentially distributed: $t_w \sim \text{Exp}(\gamma)$, meaning that $\langle t_w \rangle = 1/\gamma$. We want this waiting time to be equal to the time it takes to diffuse across a cell. Using the estimates derived above, we obtain

$$\gamma = \frac{2D}{L_c^2} \quad (\text{using } t_{RMS}) \tag{C.63}$$

$$\gamma = \frac{6D}{L_c^2} \quad (\text{using } t_{typ}) \tag{C.64}$$

Table A.3 in Section A.3 shows experimentally measured diffusion coefficients of various mitochondrial components. From this table, we find that the values for D corresponding to mtDNA nucleoids and complex II and V of the respiratory chain (which are large inner membrane complexes and may be indicative of nucleoid diffusion) lie in the range $D \sim [0.001, 0.1]\,\mu\text{m}^2/\text{s}$. We can now calculate the corresponding range of γ by assuming $L_c = 30\mu\text{m}$ (as discussed in Section 5.2.2.2) and using Equations (C.63), giving $\gamma \sim [0.2, 60]\ \text{day}^{-1}$. We note that the diffusion coefficients of order $0.1\mu\text{m}^2/\text{s}$ correspond to mobile subpopulations of complex II and V; less mobile populations and mtDNA nucleoids mostly fall into the range $\sim [0.001, 0.01]\,\mu\text{m}^2/\text{s}$; we therefore argue that γ is most likely to lie in the range $\gamma \sim [0.2, 6.0]\ \text{day}^{-1}$.

C.2.4.2 Estimating γ using the spread of abnormal fibre regions

For our second method we use the rate of spreading of high-heteroplasmy regions along muscle fibres. Measurements of the length of these COX-negative regions (L) in humans, rhesus monkeys and rats are summarised in Table 5.3 of Chapter 5. We only use the upper bound of these measurements because shorter regions are likely to have originated from a mutation event later in life**. Though even the longest regions may have started to form years after birth, we believe the data will be sufficient to provide us with another order-of-magnitude estimation. Figure C.8 shows the measured values of L plotted against the age of the organism in which they were measured.

Given a value for D, the predicted length of an abnormal region at time T_i is given by $\sqrt{2DT_i}$††. We denote the experimentally measured values of L corresponding to time T_i by y_i ($\vec{y}$ consists

**We assume that if a COX-negative region of length L was measured in e.g. a 40-year old subject, the mutant took 40 years to spread over the distance L. As it is likely that the mutation expanded in less time, the actual mtDNA diffusion coefficient is likely to be higher than our estimate.

††Here we use the root-mean-square distance travelled. We take it as a given that the mutation has successfully expanded.

of N different experimental measurements). Assuming a Gaussian error model, we can write

$$y_i = \sqrt{2DT_i} + N(0, \sigma^2) \tag{C.65}$$

Because it is easier to work with a linear model, we write $y_i^2 = 2DT_i + N(0, \tilde{\sigma}^2)$ where $\tilde{\sigma}$ is a re-scaled noise variance. The log-likelihood of the model is given by

$$\mathcal{L} = -\frac{N}{2}\log(2\pi\tilde{\sigma}^2) - \frac{1}{2\tilde{\sigma}^2}\sum_{i=1}^{N}(y_i^2 - 2DT_i)^2 \tag{C.66}$$

The maximum likelihood estimate of D, D_{MLE}, is the value of D that minimises the quantity $\sum_{i=1}^{N}(y_i^2 - 2DT_i)^2$. Using the experimental data we find $D_{MLE} \approx 4.6 \times 10^{-4}\mu\text{m}^2/\text{s}$, which leads to $\gamma \approx 0.09$ day^{-1} (using Equation (C.63)). The predicted values of L using this MLE are shown in Figure C.8. Additionally, we show predictions based $D = 0.001$ and $D = 0.01$.

As noted before, experimentally observed COX-negative regions can be the result of a mutation that occurred years after birth; our maximum likelihood estimator can therefore be considered a lower bound. The predicted values for L when using $D = 10^{-2}\mu\text{m}^2/\text{s}$ are much higher than the observed data (Figure C.8), though we do expect most data to lie below our predictions and it could be that mtDNA molecules reach a neighbouring cell relatively quickly but other factors (e.g. extinction of the mutant in some cells, or fission of mitochondria which blocks further diffusion) slow down its rate of spreading along the fibre. We therefore consider $D = 10^{-2}\mu\text{m}^2/\text{s}$ an upper bound on the mtDNA diffusion coefficient (using $D = 0.1\mu\text{m}^2/\text{s}$ leads to unrealistically high predictions of L, confirming speculations in the previous section that such high coefficients (observed for mobile subpopulations of complex II and V) are not applicable to mtDNA).

In conclusion, based on both our estimation methods we estimate the mtDNA (i.e. nucleoid) diffusion coefficient to lie in the range $D \in [4.6 \times 10^{-4}, 0.01]\,\mu\text{m}^2/\text{s}$, giving $\gamma \in [0.09, 6]$ day^{-1}. We believe γ is most likely to lie in the lower region of this range. We note that it is difficult to provide accurate estimates for γ as e.g. the rate of mtDNA diffusion may not be constant along fibres and may also change with age.

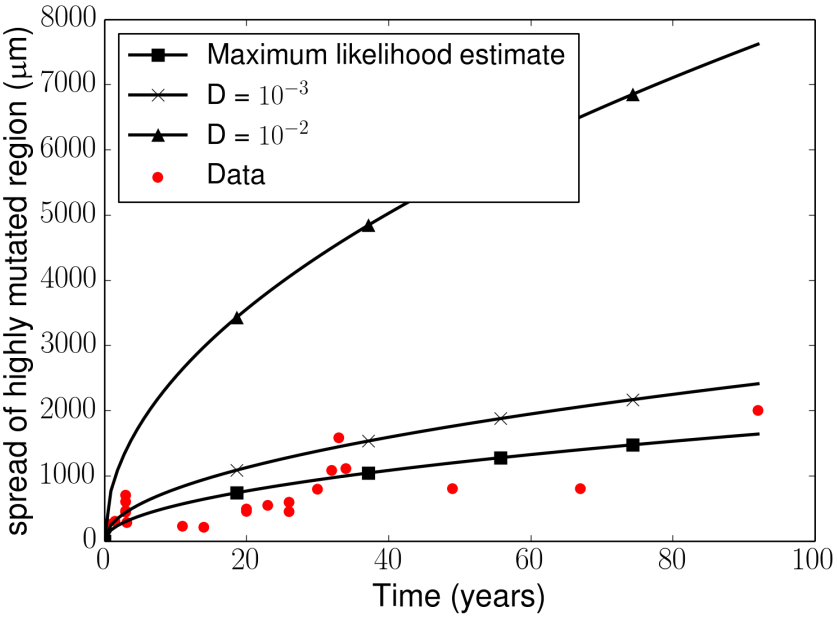


Figure C.8: Estimating mtDNA diffusion coefficients using the spread of abnormal fibre regions. We plot the relation between age and the length of a COX-negative region (L) along a muscle fibre. The data we used is summarised in Table 5.3 (only upper bounds were used), extra data was taken from Ref. [341] (not shown in the table). Predictions arising from our maximum-likelihood estimate D_{MLE}, as well as $D = 10^{-3}\mu m^2/s$ and $D = 10^{-2}\mu m^2/s$ are shown (using $L = \sqrt{2DT}$ with T denoting time in seconds).

References

[1] Chinnery, P. F. and Samuels, D. C. Relaxed replication of mtDNA: a model with implications for the expression of disease. *The American Journal of Human Genetics* **64**(4), 1158–1165 (1999).

[2] Capps, G. J., Samuels, D. C., and Chinnery, P. F. A model of the nuclear control of mitochondrial DNA replication. *Journal of theoretical biology* **221**(4), 565–583 (2003).

[3] Martin, W. and Mentel, M. The origin of mitochondria. *Nature Education* **3**(9), 58 (2010).

[4] Lill, R., Hoffmann, B., Molik, S., Pierik, A. J., Rietzschel, N., Stehling, O., Uzarska, M. A., Webert, H., Wilbrecht, C., and Mühlenhoff, U. The role of mitochondria in cellular iron–sulfur protein biogenesis and iron metabolism. *Biochimica et Biophysica Acta (BBA)-Molecular Cell Research* **1823**(9), 1491–1508 (2012).

[5] Wang, C. and Youle, R. J. The role of mitochondria in apoptosis. *Annual review of genetics* **43**, 95 (2009).

[6] Rizzuto, R., De Stefani, D., Raffaello, A., and Mammucari, C. Mitochondria as sensors and regulators of calcium signalling. *Nature reviews Molecular cell biology* **13**(9), 566–578 (2012).

[7] Laar, V. S. V. and Berman, S. B. Mitochondrial dynamics in parkinson's disease. *Exp Neurol* **218**(2), 247 – 256 (2009).

[8] Liesa, M., Palacín, M., and Zorzano, A. Mitochondrial dynamics in mammalian health and disease. *Physiol Rev* **89**(3), 799–845 (2009).

[9] Grandemange, S., Herzig, S., and Martinou, J.-C. Mitochondrial dynamics and cancer. *Semin Cancer Biol* **19**(1), 50–56 (2009).

[10] Zhu, X., Perry, G., Smith, M. A., and Wang, X. Abnormal mitochondrial dynamics in the pathogenesis of alzheimer's disease. *J Alzheimers Dis* **33**, S253–S262 (2013).

[11] Chan, D. C. Fusion and fission: Interlinked processes critical for mitochondrial health. *Annu Rev Genet* **46**(1), 265–287 (2012).

[12] Chen, H. and Chan, D. C. Mitochondrial dynamics - fusion, fission, movement, and mitophagy - in neurodegenerative diseases. *Hum Mol Genet* **18**(R2), R169–R176 (2009).

[13] Shokolenko, I. N., Wilson, L. G., and Alexeyev, F. M. Aging: A mitochondrial DNA perspective, critical analysis and an update. *World J Exp Med* **4**(4), 46–57 (2014).

[14] Bratic, A. and Larsson, N.-G. The role of mitochondria in aging. *The Journal of clinical investigation* **123**(3), 951–957 (2013).

[15] Krishnan, K. J., Greaves, L. C., Reeve, A. K., and Turnbull, D. The ageing mitochondrial genome. *Nucleic acids research* **35**(22), 7399–7405 (2007).

[16] Larsson, N.-G. Somatic mitochondrial DNA mutations in mammalian aging. *Annual review of biochemistry* **79**, 683–706 (2010).

[17] Khrapko, K. The timing of mitochondrial DNA mutations in aging. *Nature genetics* **43**(8), 726 (2011).

[18] Khrapko, K. and Vijg, J. Mitochondrial DNA mutations and aging: a case closed? *Nature genetics* **39**(4), 445–446 (2007).

[19] Brierley, E. J., Johnson, M. A., Lightowlers, R. N., James, O. F., and Turnbull, D. M. Role of mitochondrial DNA mutations in human aging: implications for the central nervous system and muscle. *Annals of neurology* **43**(2), 217–223 (1998).

[20] Greaves, L. C., Nooteboom, M., Elson, J. L., Tuppen, H. A., Taylor, G. A., Commane, D. M., Arasaradnam, R. P., Khrapko, K., Taylor, R. W., Kirkwood, T. B., et al. Clonal expansion of early to mid-life mitochondrial dna point mutations drives mitochondrial dysfunction during human ageing. *PLoS Genet* **10**(9), e1004620 (2014).

[21] Herbst, A., Pak, J. W., McKenzie, D., Bua, E., Bassiouni, M., and Aiken, J. M. Accumulation of mitochondrial DNA deletion mutations in aged muscle fibers: evidence for a causal role in muscle fiber loss. *The Journals of Gerontology Series A: Biological Sciences and Medical Sciences* **62**(3), 235–245 (2007).

[22] Payne, B. A., Wilson, I. J., Hateley, C. A., Horvath, R., Santibanez-Koref, M., Samuels, D. C., Price, D. A., and Chinnery, P. F. Mitochondrial aging is accelerated by anti-retroviral therapy through the clonal expansion of mtDNA mutations. *Nature genetics* **43**(8), 806–810 (2011).

[23] Payne, B. A. and Chinnery, P. F. Mitochondrial dysfunction in aging: much progress but many unresolved questions. *Biochimica et Biophysica Acta (BBA)-Bioenergetics* **1847**(11), 1347–1353 (2015).

[24] Trifunovic, A., Wredenberg, A., Falkenberg, M., Spelbrink, J. N., Rovio, A. T., Bruder, C. E., Bohlooly-y, M., Gidlöf, S., Oldfors, A., Wibom, R., et al. Premature ageing in mice expressing defective mitochondrial DNA polymerase. *Nature* **429**(6990), 417–423 (2004).

[25] Boengler, K., Kosiol, M., Mayr, M., Schulz, R., and Rohrbach, S. Mitochondria and ageing: role in heart, skeletal muscle and adipose tissue. *Journal of Cachexia, Sarcopenia and Muscle* (2017).

[26] Szczepanowska, K. and Trifunovic, A. Origins of mtDNA mutations in ageing. *Essays In Biochemistry* **61**(3), 325–337 (2017).

[27] Kauppila, T. E., Kauppila, J. H., and Larsson, N.-G. Mammalian mitochondria and aging: an update. *Cell metabolism* (2016).

[28] Sun, N., Youle, R. J., and Finkel, T. The mitochondrial basis of aging. *Molecular cell* **61**(5), 654–666 (2016).

[29] Kimura, M. Solution of a process of random genetic drift with a continuous model. *Proceedings of the National Academy of Sciences* **41**(3), 144–150 (1955).

[30] Wright, S. Evolution and the genetics of population. *The theory of gene frequencies* **2** (1987).

[31] Johnston, I. G. and Jones, N. S. Closed-form stochastic solutions for non-equilibrium dynamics and inheritance of cellular components over many cell divisions. In *Proc. R. Soc. A*, volume 471, 20150050. The Royal Society, (2015).

[32] Johnston, I. G., Burgstaller, J. P., Havlicek, V., Kolbe, T., Rülicke, T., Brem, G., Poulton, J., and Jones, N. S. Stochastic modelling, bayesian inference, and new in vivo measurements elucidate the debated mtDNA bottleneck mechanism. *eLife* **4**, e07464 (2015).

[33] Wonnapinij, P., Chinnery, P. F., and Samuels, D. C. Previous estimates of mitochondrial DNA mutation level variance did not account for sampling error: comparing the mtDNA genetic bottleneck in mice and humans. *The American Journal of Human Genetics* **86**(4), 540–550 (2010).

[34] Elson, J., Samuels, D., Turnbull, D., and Chinnery, P. Random intracellular drift explains the clonal expansion of mitochondrial DNA mutations with age. *The American Journal of Human Genetics* **68**(3), 802–806 (2001).

[35] Khrapko, K. and Turnbull, D. Mitochondrial DNA mutations in aging. *Prog Mol Biol Transl Sci* **127**, 29–62 (2014).

[36] Kowald, A. and Kirkwood, T. B. Mitochondrial mutations and aging: random drift is insufficient to explain the accumulation of mitochondrial deletion mutants in short-lived animals. *Aging cell* **12**(4), 728–731 (2013).

[37] Kowald, A., Dawson, M., and Kirkwood, T. B. Mitochondrial mutations and ageing: can mitochondrial deletion mutants accumulate via a size based replication advantage? *Journal of theoretical biology* **340**, 111–118 (2014).

[38] Kowald, A. and Kirkwood, T. B. Transcription could be the key to the selection advantage of mitochondrial deletion mutants in aging. *Proceedings of the National Academy of Sciences* **111**(8), 2972–2977 (2014).

[39] Coller, H. A., Khrapko, K., Bodyak, N. D., Nekhaeva, E., Herrero-Jimenez, P., and Thilly, W. G. High frequency of homoplasmic mitochondrial DNA mutations in human tumors can be explained without selection. *Nature genetics* **28**(2), 147–150 (2001).

[40] Mouli, P. K., Twig, G., and Shirihai, O. S. Frequency and selectivity of mitochondrial fusion are key to its quality maintenance function. *Biophys J* **96**(9), 3509 – 3518 (2009).

[41] Patel, P., Shirihai, O., and Huang, K. Optimal dynamics for quality control in spatially distributed mitochondrial networks. *PLoS Comput Biol* **9**, e1003108 (2013).

[42] Figge, M. T., Reichert, A. S., Meyer-Hermann, M., and Osiewacz, H. D. Deceleration of fusion–fission cycles improves mitochondrial quality control during aging. *PLoS Comput Biol* **8**(6), e1002576 (2012).

[43] Tam, Z. Y., Gruber, J., Halliwell, B., and Gunawan, R. Mathematical modeling of the role of mitochondrial fusion and fission in mitochondrial DNA maintenance. *PLoS ONE* **8** (2013).

[44] Tam, Z. Y., Gruber, J., Halliwell, B., and Gunawan, R. Context-dependent role of mitochondrial fusion-fission in clonal expansion of mtDNA mutations. *PLoS Comput Biol* **11**(5), e1004183 (2015).

[45] Gilkerson, R. W., Selker, J. M., and Capaldi, R. A. The cristal membrane of mitochondria is the principal site of oxidative phosphorylation. *FEBS Lett* **546**(23), 355 – 358 (2003).

[46] Jimenez, L., Laporte, D., Duvezin-Caubet, S., Courtout, F., and Sagot, I. Mitochondrial atp synthases cluster as discrete domains that reorganize with the cellular demand for oxidative phosphorylation. *J Cell Sci* **127**, 719–26 (2013).

[47] Cogliati, S., Enriquez, J. A., and Scorrano, L. Mitochondrial cristae: where beauty meets functionality. *Trends in biochemical sciences* **41**(3), 261–273 (2016).

[48] Letts, J. A., Fiedorczuk, K., and Sazanov, L. A. The architecture of respiratory supercomplexes. *Nature* **537**(7622), 644–648 (2016).

[49] Laursen, W. J., Mastrotto, M., Pesta, D., Funk, O. H., Goodman, J. B., Merriman, D. K., Ingolia, N., Shulman, G. I., Bagriantsev, S. N., and Gracheva, E. O. Neuronal ucp1 expression suggests a mechanism for local thermogenesis during hibernation. *Proceedings of the National Academy of Sciences* **112**(5), 1607–1612 (2015).

[50] Lemasters, J. J. Selective mitochondrial autophagy, or mitophagy, as a targeted defense against oxidative stress, mitochondrial dysfunction, and aging. *Rejuvenation Res* **8**, 3–5 (2005).

[51] Saito, T. and Sadoshima, J. Molecular mechanisms of mitochondrial autophagy/mitophagy in the heart. *Circulation research* **116**(8), 1477–1490 (2015).

[52] Suen, D.-F., Narendra, D. P., Tanaka, A., Manfredi, G., and Youle, R. J. Parkin overexpression selects against a deleterious mtDNA mutation in heteroplasmic cybrid cells. *Proceedings of the National Academy of Sciences* **107**(26), 11835–11840 (2010).

[53] Valenci, I., Yonai, L., Bar-Yaacov, D., Mishmar, D., and Ben-Zvi, A. Parkin modulates heteroplasmy of truncated mtDNA in caenorhabditis elegans. *Mitochondrion* **20**, 64–70 (2015).

[54] Martinez-Vicente, M. Neuronal mitophagy in neurodegenerative diseases. *Frontiers in Molecular Neuroscience* **10** (2017).

[55] Sterky, F. H., Lee, S., Wibom, R., Olson, L., and Larsson, N.-G. Impaired mitochondrial transport and parkin-independent degeneration of respiratory chain-deficient dopamine neurons in vivo. *Proceedings of the National Academy of Sciences* **108**(31), 12937–12942 (2011).

[56] Greaves, L. C., Elson, J. L., Nooteboom, M., Grady, J. P., Taylor, G. A., Taylor, R. W., Mathers, J. C., Kirkwood, T. B., and Turnbull, D. M. Comparison of mitochondrial mutation spectra in ageing human colonic epithelium and disease: absence of evidence for purifying selection in somatic mitochondrial DNA point mutations. *PLoS Genetics* (2012).

[57] Kandul, N. P., Zhang, T., Hay, B. A., and Guo, M. Selective removal of deletion-bearing mitochondrial DNA in heteroplasmic drosophila. *Nature communications* **7**, 13100 (2016).

[58] Gottlieb, E. OPA1 and PARL keep a lid on apoptosis. *Cell* **126**, 27–29 (2006).

[59] Twig, G., Elorza, A., Molina, A. J., Mohamed, H., Wikstrom, J. D., Walzer, G., Stiles, L., Haigh, S. E., Katz, S., Las, G., et al. Fission and selective fusion govern mitochondrial segregation and elimination by autophagy. *EMBO J* **27**(2), 433–446 (2008).

[60] Mannella, C. A., Pfeiffer, D. R., Bradshaw, P. C., Moraru, I. I., Slepchenko, B., Loew, L. M., Hsieh, C.-e., Buttle, K., and Marko, M. Topology of the mitochondrial inner membrane: dynamics and bioenergetic implications. *IUBMB life* **52**(3-5), 93–100 (2001).

[61] Braschi, E. and McBride, H. M. Mitochondria and the culture of the borg. *BioEssays* **32**(11), 958–966 (2010).

[62] Chen, H., Chomyn, A., and Chan, D. C. Disruption of fusion results in mitochondrial heterogeneity and dysfunction. *J Biol Chem* **280**(28), 26185–26192 (2005).

[63] Jheng, H.-F., Tsai, P.-J., Guo, S.-M., Kuo, L.-H., Chang, C.-S., Su, I.-J., Chang, C.-R., and Tsai, Y.-S. Mitochondrial fission contributes to mitochondrial dysfunction and insulin resistance in skeletal muscle. *Molecular and Cellular Biology* **32**(2), 309–319 (2012).

[64] Parone, P. A., Da Cruz, S., Tondera, D., Mattenberger, Y., James, D. I., Maechler, P., Barja, F., and Martinou, J.-C. Preventing mitochondrial fission impairs mitochondrial function and leads to loss of mitochondrial dna. *PLos ONE* **3**(9), e3257 (2008).

[65] Scheckhuber, C., Erjavec, N., Tinazli, A., Hamann, A., Nyström, T., and Osiewacz, H. Reducing mitochondrial fission results in increased life span and fitness of two fungal ageing models. *Nature cell biology* **9**(1), 99 (2007).

[66] Scheckhuber, C. Q., Wanger, R. A., Mignat, C. A., and Osiewacz, H. D. Unopposed mitochondrial fission leads to severe lifespan shortening. *Cell Cycle* **10**(18), 3105–3110 (2011).

[67] Yang, C. C., Chen, D., Lee, S. S., and Walter, L. The dynamin-related protein drp-1 and the insulin signaling pathway cooperate to modulate caenorhabditis elegans longevity. *Aging cell* **10**(4), 724–728 (2011).

[68] Rana, A., Oliveira, M. P., Khamoui, A. V., Aparicio, R., Rera, M., Rossiter, H. B., and Walker, D. W. Promoting drp1-mediated mitochondrial fission in midlife prolongs healthy lifespan of drosophila melanogaster. *Nature communications* **8**(1), 448 (2017).

[69] Miller, F. J., Rosenfeldt, F. L., Zhang, C., Linnane, A. W., and Nagley, P. Precise determination of mitochondrial DNA copy number in human skeletal and cardiac muscle by a pcr-based assay: lack of change of copy number with age. *Nucleic acids research* **31**(11), e61–e61 (2003).

[70] Power, G. A., Dalton, B. H., and Rice, C. L. Human neuromuscular structure and function in old age: a brief review. *Journal of sport and health science* **2**(4), 215–226 (2013).

[71] Short, K. R., Bigelow, M. L., Kahl, J., Singh, R., Coenen-Schimke, J., Raghavakaimal, S., and Nair, K. S. Decline in skeletal muscle mitochondrial function with aging in humans. *Proceedings of the National Academy of Sciences of the United States of America* **102**(15), 5618–5623 (2005).

[72] Barazzoni, R., Short, K. R., and Nair, K. S. Effects of aging on mitochondrial DNA copy number and cytochromec oxidase gene expression in rat skeletal muscle, liver, and heart. *Journal of Biological Chemistry* **275**(5), 3343–3347 (2000).

[73] Van Blerkom, J. Mitochondria in human oogenesis and preimplantation embryogenesis: engines of metabolism, ionic regulation and developmental competence. *Reproduction* **128**(3), 269–280 (2004).

[74] Kukat, C., Wurm, C. A., Spåhr, H., Falkenberg, M., Larsson, N.-G., and Jakobs, S. Super-resolution microscopy reveals that mammalian mitochondrial nucleoids have a uniform size and frequently contain a single copy of mtdna. *Proceedings of the National Academy of Sciences* **108**(33), 13534–13539 (2011).

[75] Chatre, L. and Ricchetti, M. Prevalent coordination of mitochondrial DNA transcription and initiation of replication with the cell cycle. *Nucleic acids research* **41**(5), 3068–3078 (2013).

[76] Bogenhagen, D. and Clayton, D. A. Mouse L cell mitochondrial DNA molecules are selected randomly for replication throughout the cell cycle. *Cell* **11**(4), 719–727 (1977).

[77] Kennedy, S. R., Salk, J. J., Schmitt, M. W., and Loeb, L. A. Ultra-sensitive sequencing reveals an age-related increase in somatic mitochondrial mutations that are inconsistent with oxidative damage. *PLoS genetics* **9**(9), e1003794 (2013).

[78] Alexeyev, M., Shokolenko, I., Wilson, G., and LeDoux, S. The maintenance of mitochondrial DNA integritycritical analysis and update. *Cold Spring Harbor perspectives in biology* **5**(5), a012641 (2013).

[79] Holt, I. J. and Reyes, A. Human mitochondrial DNA replication. *Cold Spring Harbor perspectives in biology* **4**(12), a012971 (2012).

[80] Hayashi, J.-L., Ohta, S., Kikuchi, A., Takemitsu, M., Goto, Y.-i., and Nonaka, I. Introduction of disease-related mitochondrial DNA deletions into HeLa cells lacking mitochondrial DNA results in mitochondrial dysfunction. *Proceedings of the National Academy of Sciences* **88**(23), 10614–10618 (1991).

[81] Attardi, G., Yoneda, M., and Chomyn, A. Complementation and segregation behavior of disease-causing mitochondrial DNA mutations in cellular model systems. *Biochimica et Biophysica Acta (BBA)-Molecular Basis of Disease* **1271**(1), 241–248 (1995).

[82] Boulet, L., Karpati, G., and Shoubridge, E. Distribution and threshold expression of the tRNA (Lys) mutation in skeletal muscle of patients with myoclonic epilepsy and ragged-red fibers (MERRF). *American journal of human genetics* **51**(6), 1187 (1992).

[83] Nakada, K., Inoue, K., Ono, T., Isobe, K., Ogura, A., Goto, Y.-i., Nonaka, I., and Hayashi, J.-I. Inter-mitochondrial complementation: mitochondria-specific system preventing mice from expression of disease phenotypes by mutant mtDNA. *Nature medicine* **7**(8), 934–940 (2001).

[84] Moraes, C. T. and Schon, E. A. Detection and analysis of mitochondrial DNA and RNA in muscle by in situ hybridization and single-fiber pcr. *Methods in enzymology* **264**, 522–540 (1996).

[85] Bua, E., Johnson, J., Herbst, A., Delong, B., McKenzie, D., Salamat, S., and Aiken, J. M. Mitochondrial DNA–deletion mutations accumulate intracellularly to detrimental levels in aged human skeletal muscle fibers. *The American Journal of Human Genetics* **79**(3), 469–480 (2006).

[86] Gorman, G. S., Schaefer, A. M., Ng, Y., Gomez, N., Blakely, E. L., Alston, C. L., Feeney, C., Horvath, R., Yu-Wai-Man, P., Chinnery, P. F., et al. Prevalence of nuclear and mitochondrial DNA mutations related to adult mitochondrial disease. *Annals of Neurology* **77**(5), 753–759 (2015).

[87] Elliott, H. R., Samuels, D. C., Eden, J. A., Relton, C. L., and Chinnery, P. F. Pathogenic mitochondrial DNA mutations are common in the general population. *The American journal of human genetics* **83**(2), 254–260 (2008).

[88] Payne, B. A., Wilson, I. J., Yu-Wai-Man, P., Coxhead, J., Deehan, D., Horvath, R., Taylor, R. W., Samuels, D. C., Santibanez-Koref, M., and Chinnery, P. F. Universal heteroplasmy of human mitochondrial dna. *Hum Mol Genet* **22**(2), 384–390 (2013).

[89] Schon, E. A., Bonilla, E., and DiMauro, S. Mitochondrial DNA mutations and pathogenesis. *Journal of bioenergetics and biomembranes* **29**(2), 131–149 (1997).

[90] Durham, S., Samuels, D., and Chinnery, P. Is selection required for the accumulation of somatic mitochondrial DNA mutations in post-mitotic cells? *Neuromuscular Disorders* **16**(6), 381–386 (2006).

[91] Fayet, G., Jansson, M., Sternberg, D., Moslemi, A.-R., Blondy, P., Lombès, A., Fardeau, M., and Oldfors, A. Ageing muscle: clonal expansions of mitochondrial dna point mutations and deletions cause focal impairment of mitochondrial function. *Neuromuscular Disorders* **12**(5), 484–493 (2002).

[92] Wanagat, J., Cao, Z., Pathare, P., and Aiken, J. M. Mitochondrial DNA deletion mutations colocalize with segmental electron transport system abnormalities, muscle fiber atrophy, fiber splitting, and oxidative damage in sarcopenia. *The FASEB Journal* **15**(2), 322–332 (2001).

[93] Michikawa, Y., Mazzucchelli, F., Bresolin, N., Scarlato, G., and Attardi, G. Aging-dependent large accumulation of point mutations in the human mtDNA control region for replication. *Science* **286**(5440), 774–779 (1999).

[94] Wallace, D. C. Mitochondrial genetics: a paradigm for aging and degenerative diseases? *Science* **256**(5057), 628 (1992).

[95] De Grey, A. D. A proposed refinement of the mitochondrial free radical theory of aging. *Bioessays* **19**(2), 161–166 (1997).

[96] Yoneda, M., Chomyn, A., Martinuzzi, A., Hurko, O., and Attardi, G. Marked replicative advantage of human mtDNA carrying a point mutation that causes the MELAS encephalomyopathy. *Proceedings of the National Academy of Sciences* **89**(23), 11164–11168 (1992).

[97] Shoubridge, E. A., Karpati, G., and Hastings, K. E. Deletion mutants are functionally dominant over wild-type mitochondrial genomes in skeletal muscle fiber segments in mitochondrial disease. *Cell* **62**(1), 43–49 (1990).

[98] Holt, I. J., Speijer, D., and Kirkwood, T. B. The road to rack and ruin: selecting deleterious mitochondrial DNA variants. *Phil. Trans. R. Soc. B* **369**(1646), 20130451 (2014).

[99] Kowald, A. and Kirkwood, T. B. Accumulation of defective mitochondria through delayed degradation of damaged organelles and its possible role in the ageing of post-mitotic and dividing cells. *Journal of theoretical biology* **202**(2), 145–160 (2000).

[100] Renshaw, E. *Stochastic population processes: analysis, approximations, simulations*. Oxford University Press, (2015).

[101] Johnston, I. G. and Jones, N. S. Evolution of cell-to-cell variability in stochastic, controlled, heteroplasmic mtDNA populations. *The American Journal of Human Genetics* **99**(5), 1150–1162 (2016).

[102] Hoitzing, H., Gammage, P. A., Minczuk, M., Johnston, I. G., and Jones, N. S. Energetic costs of cellular and therapeutic control of stochastic mtDNA populations. *bioRxiv* , 145292 (2017).

[103] Brodland, G. W. How computational models can help unlock biological systems. In *Seminars in cell & developmental biology*, volume 47, 62–73. Elsevier, (2015).

[104] Durham, S. E., Samuels, D. C., Cree, L. M., and Chinnery, P. F. Normal levels of wild-type mitochondrial DNA maintain cytochrome c oxidase activity for two pathogenic mitochondrial DNA mutations but not for m. 3243a g. *The American Journal of Human Genetics* **81**(1), 189–195 (2007).

[105] Wallace, D. C. and Chalkia, D. Mitochondrial DNA genetics and the heteroplasmy conundrum in evolution and disease. *Cold Spring Harbor Perspectives in Biology* **5**(11), a021220 (2013).

[106] Wilson, I. J., Carling, P. J., Alston, C. L., Floros, V. I., Pyle, A., Hudson, G., Sallevelt, S. C., Lamperti, C., Carelli, V., Bindoff, L. A., et al. Mitochondrial DNA sequence characteristics modulate the size of the genetic bottleneck. *Human molecular genetics* **25**(5), 1031–1041 (2016).

[107] Cree, L. M., Samuels, D. C., de Sousa Lopes, S. C., Rajasimha, H. K., Wonnapinij, P., Mann, J. R., Dahl, H.-H. M., and Chinnery, P. F. A reduction of mitochondrial DNA molecules during

embryogenesis explains the rapid segregation of genotypes. *Nature genetics* **40**(2), 249–254 (2008).

[108] Poovathingal, S. K., Gruber, J., Halliwell, B., and Gunawan, R. Stochastic drift in mitochondrial DNA point mutations: a novel perspective ex silico. *PLoS computational biology* **5**(11), e1000572 (2009).

[109] Cenettlsr, H. and McGill, P. Random genetic drift in the female germline explains the rapid segregation of mammalian mitochondrial dna. *Nature genetics* **14** (1996).

[110] Brown, D., Samuels, D., Michael, E., Turnbull, D., and Chinnery, P. Random genetic drift determines the level of mutant mtdna in human primary oocytes. *The American Journal of Human Genetics* **68**(2), 533–536 (2001).

[111] Wolff, J. N., White, D. J., Woodhams, M., White, H. E., and Gemmell, N. J. The strength and timing of the mitochondrial bottleneck in salmon suggests a conserved mechanism in vertebrates. *PLoS One* **6**(5), e20522 (2011).

[112] Howell, N., Halvorson, S., Kubacka, I., McCullough, D., Bindoff, L., and Turnbull, D. Mitochondrial gene segregation in mammals: is the bottleneck always narrow? *Human genetics* **90**(1-2), 117–120 (1992).

[113] Wai, T., Teoli, D., and Shoubridge, E. A. The mitochondrial DNA genetic bottleneck results from replication of a subpopulation of genomes. *Nature genetics* **40**(12), 1484–1488 (2008).

[114] Cao, L., Shitara, H., Horii, T., Nagao, Y., Imai, H., Abe, K., Hara, T., Hayashi, J.-I., and Yonekawa, H. The mitochondrial bottleneck occurs without reduction of mtDNA content in female mouse germ cells. *Nature genetics* **39**(3), 386–390 (2007).

[115] Csilléry, K., Blum, M. G., Gaggiotti, O. E., and François, O. Approximate bayesian computation (abc) in practice. *Trends in ecology & evolution* **25**(7), 410–418 (2010).

[116] Johnston, I. G., Rickett, B. C., and Jones, N. S. Explicit tracking of uncertainty increases the power of quantitative rule-of-thumb reasoning in cell biology. *Biophysical journal* **107**(11), 2612–2617 (2014).

[117] Shoffner, J. M., Lott, M. T., Voljavec, A. S., Soueidan, S. A., Costigan, D. A., and Wallace, D. C. Spontaneous kearns-sayre/chronic external ophthalmoplegia plus syndrome associated with a mitochondrial DNA deletion: a slip-replication model and metabolic therapy. *Proceedings of the National Academy of Sciences* **86**(20), 7952–7956 (1989).

[118] Kowald, A., Jendrach, M., Pohl, S., Bereiter-Hahn, J., and Hammerstein, P. On the relevance of mitochondrial fusions for the accumulation of mitochondrial deletion mutants: a modelling study. *Aging cell* **4**(5), 273–283 (2005).

[119] Gross, N. J., Getz, G. S., and Rabinowitz, M. Apparent turnover of mitochondrial deoxyribonucleic acid and mitochondrial phospholipids in the tissues of the rat. *Journal of Biological Chemistry* **244**(6), 1552–1562 (1969).

[120] Korr, H., Kurz, C., Seidler, T., Sommer, D., and Schmitz, C. Mitochondrial DNA synthesis studied autoradiographically in various cell types in vivo. *Brazilian journal of medical and biological research* **31**(2), 289–298 (1998).

[121] Huemer, R., Lee, K.-D., Reeves, A., and Bickert, C. Mitochondrial studies in senescent miceii. specific activity, buoyant density, and turnover of mitochondrial dna. *Experimental gerontology* **6**(5), 327–334 (1971).

[122] Kim, I. and Lemasters, J. J. Mitophagy selectively degrades individual damaged mitochondria after photoirradiation. *Antioxidants & redox signaling* **14**(10), 1919–1928 (2011).

[123] Harman, D. Free radical theory of aging: dietary implications. *The American journal of clinical nutrition* **25**(8), 839–843 (1972).

[124] Kowald, A. and Kirkwood, T. Mitochondrial mutations, cellular instability and ageing: modelling the population dynamics of mitochondria. *Mutation Research/DNAging* **295**(3), 93–103 (1993).

[125] Kowald, A. and Kirkwood, T. A network theory of ageing: the interactions of defective mitochondria, aberrant proteins, free radicals and scavengers in the ageing process. *Mutation Research/DNAging* **316**(5), 209–236 (1996).

[126] Sukhorukov, V. M., Dikov, D., Reichert, A. S., and Meyer-Hermann, M. Emergence of the mitochondrial reticulum from fission and fusion dynamics. *PLoS Comput Biol* **8**(10), e1002745 (2012).

[127] Gillespie, D. T. Exact stochastic simulation of coupled chemical reactions. *The journal of physical chemistry* **81**(25), 2340–2361 (1977).

[128] Quiros, P. M., Mottis, A., and Auwerx, J. Mitonuclear communication in homeostasis and stress. *Nature reviews Molecular cell biology* **17**(4), 213–227 (2016).

[129] Jenuth, J. P., Peterson, A. C., and Shoubridge, E. A. Tissue-specific selection for different mtDNA genotypes in heteroplasmic mice. *Nature genetics* **16**(1), 93–95 (1997).

[130] Vermulst, M., Bielas, J. H., Kujoth, G. C., Ladiges, W. C., Rabinovitch, P. S., Prolla, T. A., and Loeb, L. A. Mitochondrial point mutations do not limit the natural lifespan of mice. *Nature genetics* **39**(4), 540 (2007).

[131] Kujoth, G., Hiona, A., Pugh, T., Someya, S., Panzer, K., Wohlgemuth, S., Hofer, T., Seo, A., Sullivan, R., Jobling, W., et al. Mitochondrial DNA mutations, oxidative stress, and apoptosis in mammalian aging. *Science* **309**(5733), 481–484 (2005).

[132] Tyynismaa, H., Mjosund, K. P., Wanrooij, S., Lappalainen, I., Ylikallio, E., Jalanko, A., Spelbrink, J. N., Paetau, A., and Suomalainen, A. Mutant mitochondrial helicase twinkle causes multiple mtDNA deletions and a late-onset mitochondrial disease in mice. *Proceedings of the National Academy of Sciences of the United States of America* **102**(49), 17687–17692 (2005).

[133] Payne, B. A., Wilson, I. J., Yu-Wai-Man, P., Coxhead, J., Deehan, D., Horvath, R., Taylor, R. W., Samuels, D. C., Santibanez-Koref, M., and Chinnery, P. F. Universal heteroplasmy of human mitochondrial dna. *Human molecular genetics* **22**(2), 384–390 (2012).

[134] Lightowlers, R. N., Taylor, R. W., and Turnbull, D. M. Mutations causing mitochondrial disease: What is new and what challenges remain? *Science* **349**(6255), 1494–1499 (2015).

[135] Bonnen, P. E., Yarham, J. W., Besse, A., Wu, P., Faqeih, E. A., Al-Asmari, A. M., Saleh, M. A., Eyaid, W., Hadeel, A., He, L., et al. Mutations in fbxl4 cause mitochondrial encephalopathy and a disorder of mitochondrial DNA maintenance. *The American Journal of Human Genetics* **93**(3), 471–481 (2013).

[136] Craven, L., Tuppen, H. A., Greggains, G. D., Harbottle, S. J., Murphy, J. L., Cree, L. M., Murdoch, A. P., Chinnery, P. F., Taylor, R. W., Lightowlers, R. N., et al. Pronuclear transfer in human embryos to prevent transmission of mitochondrial DNA disease. *Nature* **465**(7294), 82–85 (2010).

[137] Sato, A., Kono, T., Nakada, K., Ishikawa, K., Inoue, S.-I., Yonekawa, H., and Hayashi, J.-I. Gene therapy for progeny of mito-mice carrying pathogenic mtDNA by nuclear transplantation. *Proceedings of the National Academy of Sciences of the United States of America* **102**(46), 16765–16770 (2005).

[138] Burgstaller, J. P., Johnston, I. G., Jones, N. S., Albrechtova, J., Kolbe, T., Vogl, C., Futschik, A., Mayrhofer, C., Klein, D., Sabitzer, S., et al. Mtdna segregation in heteroplasmic tissues is common in vivo and modulated by haplotype differences and developmental stage. *Cell reports* **7**(6), 2031–2041 (2014).

[139] St. John, J. C. Ooplasm donation in humans: the need to investigate the transmission of mitochondrial DNA following cytoplasmic transfer. *Human Reproduction* **17**(8), 1954–1958 (2002).

[140] Sharpley, M. S., Marciniak, C., Eckel-Mahan, K., McManus, M., Crimi, M., Waymire, K., Lin, C. S., Masubuchi, S., Friend, N., Koike, M., et al. Heteroplasmy of mouse mtDNA is genetically unstable and results in altered behavior and cognition. *Cell* **151**(2), 333–343 (2012).

[141] Burgstaller, J. P., Johnston, I. G., and Poulton, J. Mitochondrial DNA disease and developmental implications for reproductive strategies. *Molecular human reproduction* **21**(1), 11–22 (2015).

[142] Gammage, P. A., Gaude, E., Van Haute, L., Rebelo-Guiomar, P., Jackson, C. B., Rorbach, J., Pekalski, M. L., Robinson, A. J., Charpentier, M., Concordet, J.-P., et al. Near-complete elimination of mutant mtDNA by iterative or dynamic dose-controlled treatment with mtZFNs. *Nucleic Acids Research* , 7804–7816 (2016).

[143] Minczuk, M., Papworth, M. A., Miller, J. C., Murphy, M. P., and Klug, A. Development of a single-chain, quasi-dimeric zinc-finger nuclease for the selective degradation of mutated human mitochondrial DNA. *Nucleic acids research* **36**(12), 3926–3938 (2008).

[144] Bacman, S. R., Williams, S. L., Pinto, M., Peralta, S., and Moraes, C. T. Specific elimination of mutant mitochondrial genomes in patient-derived cells by mitoTALENs. *Nature Medicine* **19**(9), 1111–1113 (2013).

[145] Reddy, P., Ocampo, A., Suzuki, K., Luo, J., Bacman, S. R., Williams, S. L., Sugawara, A., Okamura, D., Tsunekawa, Y., Wu, J., Lam, D., Xiong, X., Montserrat, N., Esteban, C. R., Liu, G.-H., Sancho-Martinez, I., Manau, D., Civico, S., Cardellach, F., del Mar OCallaghan, M., Campistol, J., Zhao, H., Campistol, J. M., Moraes, C. T., and Belmonte, J. C. I. Selective elimination of mitochondrial mutations in the germline by genome editing. *Cell* **161**(3), 459 – 469 (2015).

[146] Tanaka, D. M., Borgeld, H.-J., Zhang, J., Muramatsu, S.-i., Gong, J.-S., Yoneda, M., Maruyama, W., Naoi, M., Ibi, T., Sahashi, K., et al. Gene therapy for mitochondrial disease by delivering restriction endonucleasesmai into mitochondria. *Journal of biomedical science* **9**(6), 534–541 (2002).

[147] Hashimoto, M., Bacman, S. R., Peralta, S., Falk, M. J., Chomyn, A., Chan, D. C., Williams, L. S., and Moraes, C. T. Mitotalen: A general approach to reduce mutant mtDNA loads and restore oxidative phosphorylation function in mitochondrial diseases. *Molecular Therapy* (2015).

[148] Gomes, L. C., Benedetto, G. D., and Scorrano, L. During autophagy mitochondria elongate, are spared from degradation and sustain cell viability. *Nat Cell Biol* **13**, 589 (2011).

[149] Tondera, D., Grandemange, S., Jourdain, A., Karbowski, M., Mattenberger, Y., Herzig, S., Cruz, S. D., Clerc, P., Raschke, I., Merkwirth, C., Ehses, S., Krause, F., Chan, D. C., Alexander, C., Bauer, C., Youle, R., Langer, T., and Martinou, J.-C. Slp-2 is required for stress-induced mitochondrial hyperfusion. *EMBO J* **28**(11), 1589–1600 (2009).

[150] Westrate, L. M., Sayfie, A. D., Burgenske, D. M., and MacKeigan, J. P. Persistent mitochondrial hyperfusion promotes g2/m accumulation and caspase-dependent cell death. *PLos ONE* **9**(3), e91911 03 (2014).

[151] Mitra, K., Wunder, C., Roysam, B., Lin, G., and Lippincott-Schwartz, J. A hyperfused mitochondrial state achieved at g1s regulates cyclin e buildup and entry into s phase. *Proc Natl Acad Sci USA* **106**(29), 11960–11965 (2009).

[152] Ono, T., Isobe, K., Nakada, K., and Hayashi, J.-I. Human cells are protected from mitochondrial dysfunction by complementation of DNA products in fused mitochondria. *Nat Genet* **28**(3), 272–275 (2001).

[153] Jiang, H.-C., Hsu, J.-M., Yen, C.-P., Chao, C.-C., Chen, R.-H., and Pan, C.-L. Neural activity and camkii protect mitochondria from fragmentation in aging caenorhabditis elegans neurons. *Proceedings of the National Academy of Sciences* **112**(28), 8768–8773 (2015).

[154] Sgarbi, G., Matarrese, P., Pinti, M., Lanzarini, C., Ascione, B., Gibellini, L., Dika, E., Patrizi, A., Tommasino, C., Capri, M., et al. Mitochondria hyperfusion and elevated autophagic activity are key mechanisms for cellular bioenergetic preservation in centenarians. *Aging (Albany NY)* **6**(4), 296 (2014).

[155] Hoitzing, H., Johnston, I. G., and Jones, N. S. What is the function of mitochondrial networks? A theoretical assessment of hypotheses and proposal for future research. *Bioessays* **37**(6), 687–700 (2015).

[156] Hoitzing, H., Gammage, P. A., Minczuk, M., Johnston, I. G., and Jones, N. S. Energetic costs of cellular and therapeutic control of stochastic mtDNA populations. *bioRxiv* (2017).

[157] Rolland, S. G., Motori, E., Memar, N., Hench, J., Frank, S., Winklhofer, K. F., and Conradt, B. Impaired complex iv activity in response to loss of LRPPRC function can be compensated by mitochondrial hyperfusion. *Proc Natl Acad Sci USA* **110**(32), E2967–E2976 (2013).

[158] Rambold, A. S., Kostelecky, B., Elia, N., and Lippincott-Schwartz, J. Tubular network formation protects mitochondria from autophagosomal degradation during nutrient starvation. *Proc Natl Acad Sci USA* **25**, 10190 – 5 (2011).

[159] Lee, Y.-j., Jeong, S.-Y., Karbowski, M., Smith, C. L., and Youle, R. J. Roles of the mammalian mitochondrial fission and fusion mediators fis1, drp1, and opa1 in apoptosis. *Mol Biol Cell* **15**(11), 5001–5011 (2004).

[160] Ong, S.-B., Subrayan, S., Lim, S. Y., Yellon, D. M., Davidson, S. M., and Hausenloy, D. J. Inhibiting mitochondrial fission protects the heart against ischemia/reperfusion injury. *Circulation* **121**(18), 2012–2022 (2010).

[161] Jahani-Asl, A., Cheung, E. C. C., Neuspiel, M., MacLaurin, J. G., Fortin, A., Park, D. S., McBride, H. M., and Slack, R. S. Mitofusin 2 protects cerebellar granule neurons against injury-induced cell death. *J Biol Chem* **282**(33), 23788–23798 (2007).

[162] Jahani-Asl, A., Pilon-Larose, K., Xu, W., MacLaurin, J. G., Park, D. S., McBride, H. M., and Slack, R. S. The mitochondrial inner membrane gtpase, optic atrophy 1 (opa1), restores mitochondrial morphology and promotes neuronal survival following excitotoxicity. *J Biol Chem* **286**(6), 4772–4782 (2011).

[163] Mitra, K. Mitochondrial fission-fusion as an emerging key regulator of cell proliferation and differentiation. *BioEssays* **35**(11), 955–964 (2013).

[164] McBride, H. M., Neuspiel, M., and Wasiak, S. Mitochondria: More than just a powerhouse. *Curr Biol* **16**(14), R551 – R560 (2006).

[165] Castanier, C., Garcin, D., Vazquez, A., and Arnoult, D. Mitochondrial dynamics regulate the rig-i-like receptor antiviral pathway. *EMBO Rep* **11**(2), 133–138 (2010).

[166] Picard, M., Shirihai, O. S., Gentil, B. J., and Burelle, Y. Mitochondrial morphology transitions and functions: implications for retrograde signaling? *Am J Physiol-Reg I* **304**(6), R393–R406 (2013).

[167] Zemirli, N., Pourcelot, M., Ambroise, G., Hatchi, E., Vazquez, A., and Arnoult, D. Mitochondrial hyperfusion promotes nf-b activation via the mitochondrial e3 ligase mulan. *FEBS J* **14**, 3095–112 (2014).

[168] Song, Z., Ghochani, M., McCaffery, J. M., Frey, T. G., and Chan, D. C. Mitofusins and OPA1 mediate sequential steps in mitochondrial membrane fusion. *Mol Biol Cell* **20**(15), 3525–3532 (2009).

[169] van der Bliek, A. M., Shen, Q., and Kawajiri, S. Mechanisms of mitochondrial fission and fusion. *Cold Spring Harb Pers Biol* **5**(6), a011072 (2013).

[170] Senft, D. and Zeev, A. R. Regulators of mitochondrial dynamics in cancer. *Current opinion in cell biology* **39**, 43–52 (2016).

[171] Bertholet, A., Delerue, T., Millet, A., Moulis, M., David, C., Daloyau, M., Arnaune-Pelloquin, L., Davezac, N., Mils, V., Miquel, M., et al. Mitochondrial fusion/fission dynamics in neurodegeneration and neuronal plasticity. *Neurobiology of disease* **90**, 3–19 (2016).

[172] Stauffer, D. and Aharony, A. *Introduction to Percolation Theory*. CRC Press, London, (1994).

[173] Qian, W., Choi, S., Gibson, G. A., Watkins, S. C., Bakkenist, C. J., and Van Houten, B. Mitochondrial hyperfusion induced by loss of the fission protein drp1 causes atm-dependent g2/m arrest and aneuploidy through DNA replication stress. *J Cell Sci* **125**(23), 5745–5757 (2012).

[174] Legros, F., Lombs, A., Frachon, P., and Rojo, M. Mitochondrial fusion in human cells is efficient, requires the inner membrane potential, and is mediated by mitofusins. *Mol Biol Cell* **13**(12), 4343–4354 (2002).

[175] Meeusen, S., McCaffery, J. M., and Nunnari, J. Mitochondrial fusion intermediates revealed in vitro. *Science* **305**(5691), 1747–1752 (2004).

[176] Cagalinec, M., Safiulina, D., Liiv, M., Liiv, J., Choubey, V., Wareski, P., Veksler, V., and Kaasik, A. Principles of the mitochondrial fusion and fission cycle in neurons. *J Cell Sci* **126**(10), 2187–2197 (2013).

[177] Rafelski, S. M. Mitochondrial network morphology: building an integrative, geometrical view. *BMC Biol* **11**(1), 71 (2013).

[178] Rafelski, S. M., Viana, M. P., Zhang, Y., Chan, Y.-H. M., Thorn, K. S., Yam, P., Fung, J. C., Li, H., Costa, L. d. F., and Marshall, W. F. Mitochondrial network size scaling in budding yeast. *Science* **338**(6108), 822–824 (2012).

[179] Rodell, A. B., Rasmussen, L. J., Bergersen, L. H., Singh, K. K., and Gjedde, A. Natural selection of mitochondria during somatic lifetime promotes healthy aging. *Front Neuroenergetics* **5**(7) (2013).

[180] Bakeeva, L., Chentsov, Y., and Skulachev, V. Mitochondrial framework (reticulum mitochondriale) in rat diaphragm muscle. *Biochim Biophys Acta* **501**, 349–369 (1978).

[181] Skulachev, V. P. Power transmission along biological membranes. *J. Membrane Biol* **114**, 97 (1990).

[182] Amchenkova, A. A., Bakeeva, L. E., Chentsov, Y. S., Skulachev, V. P., and Zorov, D. B. Coupling membranes as energy-transmitting cables. i. filamentous mitochondria in fibroblasts and mitochondrial clusters in cardiomyocytes. *J Cell Biol* **107**(2), 481–495 (1988).

[183] Skulachev, V. P. Mitochondrial filaments and clusters as intracellular power-transmitting cables. *Trends Biochem Sci* **26**(1), 23 – 29 (2001).

[184] Glancy, B., Hartnell, L. M., Malide, D., Yu, Z.-X., Combs, C. A., Connelly, P. S., Subramaniam, S., and Balaban, R. S. Mitochondrial reticulum for cellular energy distribution in muscle. *Nature* **523**(7562), 617 (2015).

[185] Glancy, B., Hartnell, L. M., Combs, C. A., Fenmou, A., Sun, J., Murphy, E., Subramaniam, S., and Balaban, R. S. Power grid protection of the muscle mitochondrial reticulum. *Cell Reports* **19**(3), 487–496 (2017).

[186] Patel, K. D., Glancy, B., and Balaban, R. S. The electrochemical transmission in i-band segments of the mitochondrial reticulum. *Biochimica et Biophysica Acta (BBA)-Bioenergetics* **1857**(8), 1284–1289 (2016).

[187] Wikstrom, J. D., Twig, G., and Shirihai, O. S. What can mitochondrial heterogeneity tell us about mitochondrial dynamics and autophagy? *Int J Biochem Cell Biol* **41**(10), 1914 – 1927 (2009).

[188] Kowald, A. and Kirkwood, T. B. Evolution of the mitochondrial fusion–fission cycle and its role in aging. *Proc Natl Acad Sci USA* **108**(25), 10237–10242 (2011).

[189] Chen, H., Vermulst, M., Wang, Y. E., Chomyn, A., Prolla, T. A., McCaffery, J. M., and Chan, D. C. Mitochondrial fusion is required for mtDNA stability in skeletal muscle and tolerance of mtDNA mutations. *Cell* **141**(2), 280 – 289 (2010).

[190] Wilkens, V., Kohl, W., and Busch, K. Restricted diffusion of oxphos complexes in dynamic mitochondria delays their exchange between cristae and engenders a transitory mosaic distribution. *J Cell Sci* **126**(1), 103–116 (2013).

[191] Busch, K. B., Kowald, A., and Spelbrink, J. N. Quality matters: how does mitochondrial network dynamics and quality control impact on mtDNA integrity? *Philos Trans R Soc Lond B Biol Sci* **369**(1646), 1–12 (2014).

[192] Liu, X., Weaver, D., Shirihai, O., and Hajnóczky, G. Mitochondrial kiss-and-run: interplay between mitochondrial motility and fusion–fission dynamics. *EMBO J* **28**(20), 3074–3089 (2009).

[193] Cipolat, S., Rudka, T., Hartmann, D., Costa, V., Serneels, L., Craessaerts, K., Metzger, K., Frezza, C., Annaert, W., D'Adamio, L., Derks, C., Dejaegere, T., Pellegrini, L., D'Hooge, R., Scorrano, L., and Strooper, B. D. Mitochondrial rhomboid {PARL} regulates cytochrome c release during apoptosis via OPA1-dependent cristae remodeling. *Cell* **126**(1), 163 – 175 (2006).

[194] Frezza, C., Cipolat, S., de Brito, O. M., Micaroni, M., Beznoussenko, G. V., Rudka, T., Bartoli, D., Polishuck, R. S., Danial, N. N., Strooper, B. D., and Scorrano, L. {OPA1} controls apoptotic cristae remodeling independently from mitochondrial fusion. *Cell* **126**(1), 177 – 189 (2006).

[195] Olichon, A., Baricault, L., Gas, N., Guillou, E., Valette, A., Belenguer, P., and Lenaers, G. Loss of OPA1 perturbates the mitochondrial inner membrane structure and integrity, leading to cytochrome c release and apoptosis. *J Biol Chem* **278**(10), 7743–7746 (2003).

[196] Patten, D. A., Wong, J., Khacho, M., Soubannier, V., Mailloux, R. J., Pilon-Larose, K., MacLaurin, J. G., Park, D. S., McBride, H. M., Trinkle-Mulcahy, L., et al. Opa1-dependent cristae modulation is essential for cellular adaptation to metabolic demand. *EMBO J* **33**(22), 2676–2691 (2014).

[197] Wikstrom, J. D., Mahdaviani, K., Liesa, M., Sereda, S. B., Si, Y., Las, G., Twig, G., Petrovic, N., Zingaretti, C., Graham, A., Cinti, S., Corkey, B. E., Cannon, B., Nedergaard, J., and Shirihai, O. S. Hormone-induced mitochondrial fission is utilized by brown adipocytes as an amplification pathway for energy expenditure. *EMBO J* (2014).

[198] Bernardi, P. Mitochondrial transport of cations: Channels, exchangers, and permeability transition. *Physiol Rev* **79**(4), 1127–1155 (1999).

[199] Malli, R., Frieden, M., Osibow, K., Zoratti, C., Mayer, M., Demaurex, N., and Graier, W. F. Sustained ca2+ transfer across mitochondria is essential for mitochondrial ca2+ buffering, store-operated ca2+ entry, and ca2+ store refilling. *J Biol Chem* **278**(45), 44769–44779 (2003).

[200] Szabadkai, G., Simoni, A., Chami, M., Wieckowski, M., and Youle, R. Drp-1-dependent division of the mitochondrial network blocks intraorganellar ca2+ waves and protects against ca2+-mediated apoptosis. *Mol Cell* **16**, 59–68 (2004).

[201] Patergnani, S., Suski, J. M., Agnoletto, C., Bononi, A., Bonora, M., De Marchi, E., Giorgi, C., Marchi, S., Missiroli, S., Poletti, F., et al. Calcium signaling around mitochondria associated membranes (mams). *Cell Commun Signal* **9**(1), 19 (2011).

[202] Vinnakota, K. C., Dash, R. K., and Beard, D. A. Stimulatory effects of calcium on respiration and nad(p)h synthesis in intact rat heart mitochondria utilizing physiological substrates cannot explain respiratory control in vivo. *J Biol Chem* **286**(35), 30816–30822 (2011).

[203] Dedkova, E. N. and Blatter, L. A. Calcium signaling in cardiac mitochondria. *J Mol Cell Cardiol* **58**(0), 125 – 133 (2013).

[204] Beard, D. A. A biophysical model of the mitochondrial respiratory system and oxidative phosphorylation. *PLoS Comput Biol* **1**, e36 (2006).

[205] Saa, A. and Siqueira, K. M. Modelling the atp production in mitochondria. *B Math Biol* **75**, 1636 (2013).

[206] Wu, F., Yang, F., Vinnakota, K. C., and Beard, D. A. Computer modeling of mitochondrial tricarboxylic acid cycle, oxidative phosphorylation, metabolite transport, and electrophysiology. *J Biol Chem* **282**(34), 24525–24537 (2007).

[207] Twig, G., Graf, S. A., Wikstrom, J. D., Mohamed, H., Haigh, S. E., Elorza, A., Deutsch, M., Zurgil, N., Reynolds, N., and Shirihai, O. S. Tagging and tracking individual networks within a complex mitochondrial web with photoactivatable GFP. *Am J Physiol Cell Physiol* **291**(1), C176–C184 (2006).

[208] Groen, A. K., Wanders, R. J., Westerhoff, H. V., van der Meer, R., and Tager, J. M. Quantification of the contribution of various steps to the control of mitochondrial respiration. *J Biol Chem* **257**(6), 2754–2757 (1982).

[209] Murphy, M. P. How understanding the control of energy metabolism can help investigation of mitochondrial dysfunction, regulation and pharmacology. *Biochim Biophys Acta* **1504**(1), 1 – 11 (2001).

[210] Soboll, S., Oh, M.-H., and Brown, G. C. Control of oxidative phosphorylation, gluconeogenesis, ureagenesis and atp turnover in isolated perfused rat liver analyzed by top-down metabolic control analysis. *Eur J Biochem* **254**(1), 194–201 (1998).

[211] Brand, M. Top-down elasticity analysis and its application to energy metabolism in isolated mitochondria and intact cells. *Mol Cell Biochem* **184**(1-2), 13–20 (1998).

[212] Ainscow, E. K. and Brand, M. D. Top-down control analysis of atp turnover, glycolysis and oxidative phosphorylation in rat hepatocytes. *Eur J Biochem* **263**(3), 671–685 (1999).

[213] Cortassa, S., Aon, M. A., Marbn, E., Winslow, R. L., and ORourke, B. An integrated model of cardiac mitochondrial energy metabolism and calcium dynamics. *Biophys J* **84**(4), 2734 – 2755 (2003).

[214] Song, D. H., Park, J., Maurer, L. L., Lu, W., Philbert, M. A., and Sastry, A. M. Biophysical significance of the inner mitochondrial membrane structure on the electrochemical potential of mitochondria. *Phys Rev E* **88**(6), 062723 (2013).

[215] Magnus, G. and Keizer, J. Minimal model of b-cell mitochondrial ca2+ handling. *Am J Physiol* **42**(2), C717 (1997).

[216] Bazil, J. N., Buzzard, G. T., and Rundell, A. E. Modeling mitochondrial bioenergetics with integrated volume dynamics. *PLoS Comput Biol* **6**(1), e1000632 (2010).

[217] Fischer, F., Hamann, A., and Osiewacz, H. D. Mitochondrial quality control: an integrated network of pathways. *Trends Biochem Sci* **37**(7), 284 – 292 (2012).

[218] Hemion, C., Flammer, J., and Neutzner, A. Quality control of oxidatively damaged mitochondrial proteins is mediated by p97 and the proteasome. *Free Radic Biol Med* **75**, 121–128 (2014).

[219] Neuspiel, M., Schauss, A. C., Braschi, E., Zunino, R., Rippstein, P., Rachubinski, R. A., Andrade-Navarro, M. A., and McBride, H. M. Cargo-selected transport from the mitochondria to peroxisomes is mediated by vesicular carriers. *Curr Biol* **18**(2), 102–108 (2008).

[220] Soubannier, V., Rippstein, P., Kaufman, B. A., Shoubridge, E. A., and McBride, H. M. Reconstitution of mitochondria derived vesicle formation demonstrates selective enrichment of oxidized cargo. *PLos ONE* **7**(12), e52830 (2012).

[221] Ehses, S., Raschke, I., Mancuso, G., Bernacchia, A., Geimer, S., Tondera, D., Martinou, J.-C., Westermann, B., Rugarli, E. I., and Langer, T. Regulation of OPA1 processing and mitochondrial fusion by m-aaa protease isoenzymes and oma1. *J Cell Biol* **187**(7), 1023–1036 (2009).

[222] Head, B., Griparic, L., Amiri, M., Gandre-Babbe, S., and van der Bliek, A. M. Inducible proteolytic inactivation of OPA1 mediated by the OMA1 protease in mammalian cells. *J Cell Biol* **187**(7), 959–966 (2009).

[223] Glauser, L., Sonnay, S., Stafa, K., and Moore, D. J. Parkin promotes the ubiquitination and degradation of the mitochondrial fusion factor mitofusin 1. *Journal of neurochemistry* **118**(4), 636–645 (2011).

[224] Chen, Y. and Dorn, G. W. Pink1-phosphorylated mitofusin 2 is a parkin receptor for culling damaged mitochondria. *Science* **340**(6131), 471–475 (2013).

[225] Narendra, D., Tanaka, A., Suen, D.-F., and Youle, R. J. Parkin is recruited selectively to impaired mitochondria and promotes their autophagy. *J Cell Biol* **183**(5), 795–803 (2008).

[226] Liu, L., Feng, D., Chen, G., Chen, M., Zheng, Q., Song, P., Ma, Q., Zhu, C., Wang, R., Qi, W., et al. Mitochondrial outer-membrane protein fundc1 mediates hypoxia-induced mitophagy in mammalian cells. *Nat Cell Biol* **14**(2), 177–185 (2012).

[227] Youle, R. J. and Narendra, D. P. Mechanisms of mitophagy. *Nat Rev Mol Cell Biol* **12**, 9–14 (2011).

[228] Kim, I., Rodriguez-Enriquez, S., and Lemasters, J. J. Selective degradation of mitochondria by mitophagy. *Arch Biochem Biophys* **462**(2), 245 – 253 (2007).

[229] Imai, Y. Mitochondrial regulation by pink1-parkin signaling. *ISRN Cell Biol* **2012** (2012).

[230] Gilkerson, R. W., De Vries, R. L., Lebot, P., Wikstrom, J. D., Torgyekes, E., Shirihai, O. S., Przedborski, S., and Schon, E. A. Mitochondrial autophagy in cells with mtDNA mutations results from synergistic loss of transmembrane potential and mtorc1 inhibition. *Hum Mol Genet* **21**(5), 978–990 (2012).

[231] Picard, M. and Burelle, Y. Mitochondria: Starving to reach quorum? *Bioessays* **34**(4), 272–274 (2012).

[232] Harrison, A. K. and Zwanzig, R. Transport on a dynamically disordered lattice. *Phys Rev A* **32**(2), 1072 (1985).

[233] Sahimi, M. Dynamic percolation and diffusion in disordered systems. *J Phys C: Solid State Phys* **19**(9), 1311 (1986).

[234] Partikian, A., lveczky, B., Swaminathan, R., Li, Y., and Verkman, A. Rapid diffusion of green fluorescent protein in the mitochondrial matrix. *J Cell Biol* **140**(4), 821–829 (1998).

[235] Verkman, A. S. Solute and macromolecule diffusion in cellular aqueous compartments. *Trends Biochem Sci* **27**(1), 27 – 33 (2002).

[236] Mishra, P., Carelli, V., Manfredi, G., and Chan, D. C. Proteolytic cleavage of opa1 stimulates mitochondrial inner membrane fusion and couples fusion to oxidative phosphorylation. *Cell Metab* **19**(4), 630 – 641 (2014).

[237] das Neves, R. P., Jones, N. S., Andreu, L., Gupta, R., Enver, T., and Iborra, F. J. Connecting variability in global transcription rate to mitochondrial variability. *PLoS Biol* **8**(12), e1000560 12 (2010).

[238] Johnston, J. M., Wang, H., Provasi, D., and Filizola, M. Assessing the relative stability of dimer interfaces in g protein-coupled receptors. *PLoS Comput Biol* **8**(8), e1002649 08 (2012).

[239] Junesch, U. and Graber, P. The rate of atp-synthase as a function of dph and dpsi catalyzed by the active, reduced h+-atpase from chloroplasts. *FEBS* **294**, 275–278 (1991).

[240] Soga, N., Kinosita, K., Yoshida, M., and Suzuki, T. Kinetic equivalence of transmembrane ph and electrical potential differences in atp synthesis. *J Biol Chem* **287**(12), 9633–9639 (2012).

[241] Denton, R. M., Randle, P. J., and Martin, B. R. Stimulation by calcium ions of pyruvate dehydrogenase phosphate phosphatase. *Biochem. J.* **128**, 161–163 (1972).

[242] Denton, R. M., Richards, D., and Chin, J. Calcium ions and the regulation of nad+-linked isocitrate dehydrogenase from the mitochondria of rat heart and other tissues. *Biochem. J.* **176**, 899–906 (1978).

[243] McCormack, J. and Denton, R. The effects of calcium ions and adenine nucleotides on the activity of pig heart 2-oxoglutarate dehydrogenase complex. *Biochem. J.* **180**, 533–544 (1979).

[244] Wan, B., LaNoue, K. F., Cheung, J. Y., and Scaduto, R. C. Regulation of citric acid cycle by calcium. *J Biol Chem* **264**(23), 13430–9 (1989).

[245] Rizzuto, R., Pinton, P., Carrington, W., Fay, F. S., Fogarty, K. E., Lifshitz, L. M., Tuft, R. A., and Pozzan, T. Close contacts with the endoplasmic reticulum as determinants of mitochondrial ca2+ responses. *Science* **280**(5370), 1763–1766 (1998).

[246] Rizzuto, R., Brini, M., Murgia, M., and Pozzan, T. Microdomains with high ca2+ close to ip3-sensitive channels that are sensed by neighboring mitochondria. *Science* **262**(5134), 744–747 (1993).

[247] Maltecca, F., De Stefani, D., Cassina, L., Consolato, F., Wasilewski, M., Scorrano, L., Rizzuto, R., and Casari, G. Respiratory dysfunction by afg3l2 deficiency causes decreased mitochondrial calcium uptake via organellar network fragmentation. *Hum Mol Genet* **21**(17), 3858–3870 (2012).

[248] Lawrie, A. M., Rizzuto, R., Pozzan, T., and Simpson, A. W. A role for calcium influx in the regulation of mitochondrial calcium in endothelial cells. *Journal of Biological Chemistry* **271**(18), 10753–10759 (1996).

[249] Chouhan, A. K., Ivannikov, M. V., Lu, Z., Sugimori, M., Llinas, R. R., and Macleod, G. T. Cytosolic calcium coordinates mitochondrial energy metabolism with presynaptic activity. *J Neurosci* **32**(4), 1233–1243 (2012).

[250] Viola, H. M. and Hool, L. C. How does calcium regulate mitochondrial energetics in the heart? new insights. *Heart Lung Circ* **7**(0), 602–9 (2014).

[251] Logan, C. V., Szabadkai, G., Sharpe, J. A., Parry, D. A., Torelli, S., Childs, A.-M., Kriek, M., Phadke, R., Johnson, C. A., Roberts, N. Y., et al. Loss-of-function mutations in micu1 cause a brain and muscle disorder linked to primary alterations in mitochondrial calcium signaling. *Nat Genet* **46**(2), 188–193 (2014).

[252] De Marchi, U., Thevenet, J., Hermant, A., Dioum, E., and Wiederkehr, A. Calcium co-regulates oxidative metabolism and atp synthase-dependent respiration in pancreatic beta cells. *J Biol Chem* **289**(13), 9182–9194 (2014).

[253] Friedman, J. R., Lackner, L. L., West, M., DiBenedetto, J. R., Nunnari, J., and Voeltz, G. K. Er tubules mark sites of mitochondrial division. *Science* **334**(6054), 358–362 (2011).

[254] Mai, S., Klinkenberg, M., Auburger, G., Bereiter-Hahn, J., and Jendrach, M. Decreased expression of drp1 and fis1 mediates mitochondrial elongation in senescent cells and enhances resistance to oxidative stress through pink1. *J Cell Sci* **123**(6), 917–926 (2010).

[255] Estaquier, J. and Arnoult, D. Inhibiting drp1-mediated mitochondrial fission selectively prevents the release of cytochrome c during apoptosis. *Cell Death Differ* **14**, 1086–1094 (2007).

[256] Gottlieb, E., Armour, S., Harris, M., and Thompson, C. Mitochondrial membrane potential regulates matrix configuration and cytochrome c release during apoptosis. *Cell Death Differ* **10**(6), 709–717 (2003).

[257] Krapivsky, P. L., Redner, S., and Ben-Naim, E. *A kinetic view of statistical physics*. Cambridge University Press, Cambridge, (2010).

[258] Wu, S., Zhou, F., Zhang, Z., and Xing, D. Mitochondrial oxidative stress causes mitochondrial fragmentation via differential modulation of mitochondrial fission–fusion proteins. *FEBS J* **278**(6), 941–954 (2011).

[259] Zhang, B., Davidson, M. M., Zhou, H., Wang, C., Walker, W. F., and Hei, T. K. Cytoplasmic irradiation results in mitochondrial dysfunction and drp1-dependent mitochondrial fission. *Cancer Res* **73**(22), 6700–6710 (2013).

[260] Mishra, P., Varuzhanyan, G., Pham, A. H., and Chan, D. C. Mitochondrial dynamics is a distinguishing feature of skeletal muscle fiber types and regulates organellar compartmentalization. *Cell metabolism* **22**(6), 1033–1044 (2015).

[261] Huang, X., Sun, L., Ji, S., Zhao, T., Zhang, W., Xu, J., Zhang, J., Wang, Y., Wang, X., Franzini-Armstrong, C., Zheng, M., and Cheng, H. Kissing and nanotunneling mediate intermitochondrial communication in the heart. *Proc Natl Acad Sci USA* **110**(8), 2846–2851 (2013).

[262] Twig, G., Liu, X., Liesa, M., Wikstrom, J. D., Molina, A. J., Las, G., Yaniv, G., Hajnóczky, G., and Shirihai, O. S. Biophysical properties of mitochondrial fusion events in pancreatic β-cells and cardiac cells unravel potential control mechanisms of its selectivity. *American Journal of Physiology-Cell Physiology* **299**(2), C477–C487 (2010).

[263] Tandler, B. and Hoppel, C. L. Possible division of cardiac mitochondria. *The Anatomical Record* **173**(3), 309–323 (1972).

[264] OReilly, C. M., Fogarty, K. E., Drummond, R. M., Tuft, R. A., and Walsh, J. V. Quantitative analysis of spontaneous mitochondrial depolarizations. *Biophysical journal* **85**(5), 3350–3357 (2003).

[265] Duchen, M. R., Leyssens, A., and Crompton, M. Transient mitochondrial depolarizations reflect focal sarcoplasmic reticular calcium release in single rat cardiomyocytes. *The Journal of cell biology* **142**(4), 975–988 (1998).

[266] Buckman, J. F. and Reynolds, I. J. Spontaneous changes in mitochondrial membrane potential in cultured neurons. *Journal of Neuroscience* **21**(14), 5054–5065 (2001).

[267] Vergun, O., Votyakova, T. V., and Reynolds, I. J. Spontaneous changes in mitochondrial membrane potential in single isolated brain mitochondria. *Biophysical journal* **85**(5), 3358–3366 (2003).

[268] Hüser, J. and Blatter, L. A. Fluctuations in mitochondrial membrane potential caused by repetitive gating of the permeability transition pore. *Biochemical Journal* **343**(2), 311–317 (1999).

[269] Hüser, J., Rechenmacher, C. E., and Blatter, L. A. Imaging the permeability pore transition in single mitochondria. *Biophysical Journal* **74**(4), 2129–2137 (1998).

[270] Nivala, M. M., Korge, P., Weiss, J. N., and Qu, Z. Relating mitochondrial flickering to whole-cell oscillations in cardiac mitochondrial networks. *Biophysical Journal* **100**(3), 46a (2011).

[271] Ichas, F., Jouaville, L. S., and Mazat, J.-P. Mitochondria are excitable organelles capable of generating and conveying electrical and calcium signals. *Cell* **89**(7), 1145–1153 (1997).

[272] De Giorgi, F., Lartigue, L., and Ichas, F. Electrical coupling and plasticity of the mitochondrial network. *Cell calcium* **28**(5-6), 365–370 (2000).

[273] Nicholls, D. G. and Ward, M. W. Mitochondrial membrane potential and neuronal glutamate excitotoxicity: mortality and millivolts. *Trends in neurosciences* **23**(4), 166–174 (2000).

[274] Nicholls, D. G. Simultaneous monitoring of ionophore-and inhibitor-mediated plasma and mitochondrial membrane potential changes in cultured neurons. *Journal of Biological Chemistry* **281**(21), 14864–14874 (2006).

[275] Gerencser, A. A., Chinopoulos, C., Birket, M. J., Jastroch, M., Vitelli, C., Nicholls, D. G., and Brand, M. D. Quantitative measurement of mitochondrial membrane potential in cultured cells: calcium-induced de-and hyperpolarization of neuronal mitochondria. *The Journal of physiology* **590**(12), 2845–2871 (2012).

[276] Chretien, D., Benit, P., Ha, H.-H., Keipert, S., El-Khoury, R., Chang, Y.-T., Jastroch, M., Jacobs, H., Rustin, P., and Rak, M. Mitochondria are physiologically maintained at close to 50 c. *bioRxiv* , 133223 (2017).

[277] Niblack, W. *An Introduction to Digital Image Processing*. Strandberg Publishing Company, Birkeroed, Denmark, Denmark, (1985).

[278] Gitschlag, B. L., Kirby, C. S., Samuels, D. C., Gangula, R. D., Mallal, S. A., and Patel, M. R. Homeostatic responses regulate selfish mitochondrial genome dynamics in c. elegans. *Cell Metabolism* **24**(1), 91–103 (2016).

[279] Posakony, J. W., England, J. M., and Attardi, G. Mitochondrial growth and division during the cell cycle in hela cells. *The Journal of cell biology* **74**(2), 468–491 (1977).

[280] Jajoo, R., Jung, Y., Huh, D., Viana, M. P., Rafelski, S. M., Springer, M., and Paulsson, J. Accurate concentration control of mitochondria and nucleoids. *Science* **351**(6269), 169–172 (2016).

[281] Otten, A. B., Theunissen, T. E., Derhaag, J. G., Lambrichs, E. H., Boesten, I. B., Winandy, M., van Montfoort, A. P., Tarbashevich, K., Raz, E., Gerards, M., et al. Differences in strength and timing of the mtDNA bottleneck between zebrafish germline and non-germline cells. *Cell Reports* **16**(3), 622–630 (2016).

[282] Tang, Y., Schon, E. A., Wilichowski, E., Vazquez-Memije, M. E., Davidson, E., and King, M. P. Rearrangements of human mitochondrial DNA (mtDNA): new insights into the regulation of mtDNA copy number and gene expression. *Molecular biology of the cell* **11**(4), 1471–1485 (2000).

[283] Diaz, F., Bayona-Bafaluy, M. P., Rana, M., Mora, M., Hao, H., and Moraes, C. T. Human mitochondrial DNA with large deletions repopulates organelles faster than full-length genomes under relaxed copy number control. *Nucleic acids research* **30**(21), 4626–4633 (2002).

[284] Røyrvik, E., Burgstaller, J. P., and Johnston, I. G. mtDNA diversity in human populations highlights the merit of haplotype matching in gene therapies. *Molecular Human Reproduction* **22**(11), 809–817 (2016).

[285] Kim, Y.-G., Cha, J., and Chandrasegaran, S. Hybrid restriction enzymes: zinc finger fusions to Fok i cleavage domain. *Proceedings of the National Academy of Sciences* **93**(3), 1156–1160 (1996).

[286] Urnov, F. D., Miller, J. C., Lee, Y.-L., Beausejour, C. M., Rock, J. M., Augustus, S., Jamieson, A. C., Porteus, M. H., Gregory, P. D., and Holmes, M. C. Highly efficient endogenous human gene correction using designed zinc-finger nucleases. *Nature* **435**(7042), 646–651 (2005).

[287] Bibikova, M., Golic, M., Golic, K. G., and Carroll, D. Targeted chromosomal cleavage and mutagenesis in drosophila using zinc-finger nucleases. *Genetics* **161**(3), 1169–1175 (2002).

[288] Christian, M., Cermak, T., Doyle, E. L., Schmidt, C., Zhang, F., Hummel, A., Bogdanove, A. J., and Voytas, D. F. Targeting DNA double-strand breaks with tal effector nucleases. *Genetics* **186**(2), 757–761 (2010).

[289] Li, T., Huang, S., Zhao, X., Wright, D. A., Carpenter, S., Spalding, M. H., Weeks, D. P., and Yang, B. Modularly assembled designer tal effector nucleases for targeted gene knockout and gene replacement in eukaryotes. *Nucleic acids research* , gkr188 (2011).

[290] Miller, J. C., Tan, S., Qiao, G., Barlow, K. A., Wang, J., Xia, D. F., Meng, X., Paschon, D. E., Leung, E., Hinkley, S. J., et al. A TALE nuclease architecture for efficient genome editing. *Nature biotechnology* **29**(2), 143–148 (2011).

[291] Joung, J. K. and Sander, J. D. TALENs: a widely applicable technology for targeted genome editing. *Nature reviews Molecular cell biology* **14**(1), 49–55 (2013).

[292] Bacman, S. R., Williams, S. L., Pinto, M., and Moraes, C. T. The use of mitochondria-targeted endonucleases to manipulate mtDNA. *Methods in enzymology* **547**, 373 (2014).

[293] Gammage, P. A., Van Haute, L., and Minczuk, M. Engineered mtZFNs for manipulation of human mitochondrial DNA heteroplasmy. *Mitochondrial DNA: Methods and Protocols* , 145–162 (2016).

[294] Van Kampen, N. G. *Stochastic processes in physics and chemistry*, volume 1. Elsevier, (1992).

[295] Monternier, P.-A., Marmillot, V., Rouanet, J.-L., and Roussel, D. Mitochondrial phenotypic flexibility enhances energy savings during winter fast in king penguin chicks. *Journal of Experimental Biology* **217**(15), 2691–2697 (2014).

[296] Salin, K., Roussel, D., Rey, B., and Voituron, Y. David and Goliath: a mitochondrial coupling problem? *Journal of Experimental Zoology Part A: Ecological Genetics and Physiology* **317**(5), 283–293 (2012).

[297] Brand, M. D., Harper, M.-E., and Taylor, H. C. Control of the effective P/O ratio of oxidative phosphorylation in liver mitochondria and hepatocytes. *Biochemical Journal* **291**(3), 739–748 (1993).

[298] Yadava, N. and Nicholls, D. G. Spare respiratory capacity rather than oxidative stress regulates glutamate excitotoxicity after partial respiratory inhibition of mitochondrial complex i with rotenone. *The Journal of neuroscience* **27**(27), 7310–7317 (2007).

[299] Hill, B. G., Dranka, B. P., Zou, L., Chatham, J. C., and Darley-Usmar, V. M. Importance of the bioenergetic reserve capacity in response to cardiomyocyte stress induced by 4-hydroxynonenal. *Biochemical Journal* **424**(1), 99–107 (2009).

[300] Minczuk, M., Papworth, M. A., Kolasinska, P., Murphy, M. P., and Klug, A. Sequence-specific modification of mitochondrial DNA using a chimeric zinc finger methylase. *Proceedings of the National Academy of Sciences* **103**(52), 19689–19694 (2006).

[301] Gammage, P. A., Rorbach, J., Vincent, A. I., Rebar, E. J., and Minczuk, M. Mitochondrially targeted ZFNs for selective degradation of pathogenic mitochondrial genomes bearing large-scale deletions or point mutations. *EMBO molecular medicine* **6**(4), 458–466 (2014).

[302] Freyer, C., Cree, L. M., Mourier, A., Stewart, J. B., Koolmeister, C., Milenkovic, D., Wai, T., Floros, V. I., Hagström, E., Chatzidaki, E. E., et al. Variation in germline mtDNA heteroplasmy is determined prenatally but modified during subsequent transmission. *Nature genetics* **44**(11), 1282–1285 (2012).

[303] Stewart, J. B. and Chinnery, P. F. The dynamics of mitochondrial DNA heteroplasmy: implications for human health and disease. *Nature Reviews Genetics* **16**(9), 530–542 (2015).

[304] Kaufmann, P., Shanske, S., Hirano, M., DiMauro, S., King, M. P., Koga, Y., and Schon, E. A. Mitochondrial DNA and RNA processing in MELAS. *Annals of neurology* **40**(2), 172–180 (1996).

[305] Moraes, C. T., Ricci, E., Petruzzella, V., Shanske, S., DiMauro, S., Schon, E. A., and Bonilla, E. Molecular analysis of the muscle pathology associated with mitochondrial DNA deletions. *Nature genetics* **1**(5), 359–367 (1992).

[306] Tokunaga, M., Mita, S., Murakami, T., Kumamoto, T., Uchino, M., Nonaka, I., and Ando, M. Single muscle fiber analysis of mitochondrial myopathy, encephalopathy, lactic acidosis, and stroke-like episodes (melas). *Annals of neurology* **35**(4), 413–419 (1994).

[307] Nicholas, A., Kraytsberg, Y., Guo, X., and Khrapko, K. On the timing and the extent of clonal expansion of mtDNA deletions: evidence from single-molecule pcr. *Experimental neurology* **218**(2), 316–319 (2009).

[308] Schwarze, S. R., Lee, C. M., Chung, S. S., Roecker, E. B., Weindruch, R., and Aiken, J. M. High levels of mitochondrial DNA deletions in skeletal muscle of old rhesus monkeys. *Mechanisms of ageing and development* **83**(2), 91–101 (1995).

[309] Reznik, E., Miller, M. L., Şenbabaoğlu, Y., Riaz, N., Sarungbam, J., Tickoo, S. K., Al-Ahmadie, H. A., Lee, W., Seshan, V. E., Hakimi, A. A., et al. Mitochondrial DNA copy number variation across human cancers. *eLife* **5**, e10769 (2016).

[310] Majamaa-Voltti, K., Peuhkurinen, K., Kortelainen, M.-L., Hassinen, I. E., and Majamaa, K. Cardiac abnormalities in patients with mitochondrial DNA mutation 3243A>G. *BMC cardiovascular disorders* **2**(1), 12 (2002).

[311] Ciafaloni, E., Ricci, E., Servidei, S., Shanske, S., Silvestri, G., Manfredi, G., Schon, E., and DiMauro, S. Widespread tissue distribution of a trnaleu (uur) mutation in the mitochondrial DNA of a patient with melas syndrome. *Neurology* **41**(10), 1663–1663 (1991).

[312] Anan, R., Nakagawa, M., Miyata, M., Higuchi, I., Nakao, S., Suehara, M., Osame, M., and Tanaka, H. Cardiac involvement in mitochondrial diseases a study on 17 patients with documented mitochondrial DNA defects. *Circulation* **91**(4), 955–961 (1995).

[313] Jeppesen, T. D., Schwartz, M., Olsen, D. B., and Vissing, J. Oxidative capacity correlates with muscle mutation load in mitochondrial myopathy. *Annals of Neurology* **54**(1), 86–92 (2003).

[314] Stein, L. R. and Imai, S.-i. The dynamic regulation of nad metabolism in mitochondria. *Trends in Endocrinology & Metabolism* **23**(9), 420–428 (2012).

[315] Alano, C. C., Ying, W., and Swanson, R. A. Poly (adp-ribose) polymerase-1-mediated cell death in astrocytes requires NAD+ depletion and mitochondrial permeability transition. *Journal of Biological Chemistry* **279**(18), 18895–18902 (2004).

[316] Bai, P., Cantó, C., Oudart, H., Brunyánszki, A., Cen, Y., Thomas, C., Yamamoto, H., Huber, A., Kiss, B., Houtkooper, R. H., et al. PARP-1 inhibition increases mitochondrial metabolism through SIRT1 activation. *Cell Metabolism* **13**(4), 461–468 (2011).

[317] Pittelli, M., Felici, R., Pitozzi, V., Giovannelli, L., Bigagli, E., Cialdai, F., Romano, G., Moroni, F., and Chiarugi, A. Pharmacological effects of exogenous nad on mitochondrial bioenergetics, DNA repair, and apoptosis. *Molecular pharmacology* **80**(6), 1136–1146 (2011).

[318] Korzeniewski, B., Harper, M.-E., and Brand, M. D. Proportional activation coefficients during stimulation of oxidative phosphorylation by lactate and pyruvate or by vasopressin. *Biochimica et Biophysica Acta (BBA)-Bioenergetics* **1229**(3), 315–322 (1995).

[319] Nobes, C., Hay, W., and Brand, M. The mechanism of stimulation of respiration by fatty acids in isolated hepatocytes. *Journal of Biological Chemistry* **265**(22), 12910–12915 (1990).

[320] Affourtit, C. and Brand, M. D. Uncoupling protein-2 contributes significantly to high mitochondrial proton leak in INS-1E insulinoma cells and attenuates glucose-stimulated insulin secretion. *Biochemical Journal* **409**(1), 199–204 (2008).

[321] Kowald, A. and Klipp, E. Mathematical models of mitochondrial aging and dynamics. *Prog Mol Biol Transl Sci* **127**, 63–92 (2014).

[322] Korzeniewski, B. and Mazat, J.-P. Theoretical studies on the control of oxidative phosphorylation in muscle mitochondria: application to mitochondrial deficiencies. *Biochemical Journal* **319**(1), 143–148 (1996).

[323] Chinnery, P. F. Mitochondrial disorders overview. *GeneReviews* (2014).

[324] Moreno-Loshuertos, R., Acín-Pérez, R., Fernández-Silva, P., Movilla, N., Pérez-Martos, A., de Cordoba, S. R., Gallardo, M. E., and Enríquez, J. A. Differences in reactive oxygen species production explain the phenotypes associated with common mouse mitochondrial DNA variants. *Nature Genetics* **38**(11), 1261–1268 (2006).

[325] Liu, C.-S., Cheng, W.-L., Lee, C.-F., Ma, Y.-S., Lin, C.-Y., Huang, C.-C., and Wei, Y.-H. Alteration in the copy number of mitochondrial DNA in leukocytes of patients with mitochondrial encephalomyopathies. *Acta neurologica Scandinavica* **113**(5), 334–341 (2006).

[326] Parsons, T. L., Quince, C., and Plotkin, J. B. Absorption and fixation times for neutral and quasi-neutral populations with density dependence. *Theoretical population biology* **74**(4), 302–310 (2008).

[327] Lin, Y. T., Kim, H., and Doering, C. R. Features of fast living: on the weak selection for longevity in degenerate birth-death processes. *Journal of Statistical Physics* **148**(4), 647–663 (2012).

[328] Constable, G. W., Rogers, T., McKane, A. J., and Tarnita, C. E. Demographic noise can reverse the direction of deterministic selection. *Proceedings of the National Academy of Sciences* , 201603693 (2016).

[329] Parsons, T. L. and Quince, C. Fixation in haploid populations exhibiting density dependence i: the non-neutral case. *Theoretical population biology* **72**(1), 121–135 (2007).

[330] Parsons, T. L. and Quince, C. Fixation in haploid populations exhibiting density dependence ii: The quasi-neutral case. *Theoretical population biology* **72**(4), 468–479 (2007).

[331] Constable, G. W. and McKane, A. J. Models of genetic drift as limiting forms of the lotka-volterra competition model. *Physical review letters* **114**(3), 038101 (2015).

[332] Kogan, O., Khasin, M., Meerson, B., Schneider, D., and Myers, C. R. Two-strain competition in quasineutral stochastic disease dynamics. *Physical Review E* **90**(4), 042149 (2014).

[333] Rustom, A., Saffrich, R., Markovic, I., Walther, P., and Gerdes, H.-H. Nanotubular highways for intercellular organelle transport. *Science* **303**(5660), 1007–1010 (2004).

[334] Gerdes, H.-H., Bukoreshtliev, N. V., and Barroso, J. F. Tunneling nanotubes: a new route for the exchange of components between animal cells. *FEBS letters* **581**(11), 2194–2201 (2007).

[335] Jackson, M. V., Morrison, T. J., Doherty, D. F., McAuley, D. F., Matthay, M. A., Kissenpfennig, A., O'Kane, C. M., and Krasnodembskaya, A. D. Mitochondrial transfer via tunneling nanotubes is an important mechanism by which mesenchymal stem cells enhance macrophage phagocytosis in the in vitro and in vivo models of ards. *Stem cells* **34**(8), 2210–2223 (2016).

[336] Liu, C.-S., Tsai, C.-S., Kuo, C.-L., Chen, H.-W., Lii, C.-K., Ma, Y.-S., and Wei, Y.-H. Oxidative stress-related alteration of the copy number of mitochondrial DNA in human leukocytes. *Free radical research* **37**(12), 1307–1317 (2003).

[337] Axelrod, R. M. *The evolution of cooperation: revised edition*. Basic books, (2006).

[338] Koschwanez, J. H., Foster, K. R., and Murray, A. W. Sucrose utilization in budding yeast as a model for the origin of undifferentiated multicellularity. *PLoS biology* **9**(8), e1001122 (2011).

[339] Kümmerli, R. and Brown, S. P. Molecular and regulatory properties of a public good shape the evolution of cooperation. *Proceedings of the National Academy of Sciences* **107**(44), 18921–18926 (2010).

[340] Elson, J. L., Samuels, D. C., Johnson, M. A., Turnbull, D. M., and Chinnery, P. F. The length of cytochrome c oxidase-negative segments in muscle fibres in patients with mtDNA myopathy. *Neuromuscular Disorders* **12**(9), 858–864 (2002).

[341] Lopez, M. E., Van Zeeland, N. L., Dahl, D. B., Weindruch, R., and Aiken, J. M. Cellular phenotypes of age-associated skeletal muscle mitochondrial abnormalities in rhesus monkeys. *Mutation Research/Fundamental and Molecular Mechanisms of Mutagenesis* **452**(1), 123–138 (2000).

[342] Barthélémy, C., Ogier De Baulny, H., Diaz, J., Armelle Cheval, M., Frachon, P., Romero, N., Goutieres, F., Fardeau, M., and Lombès, A. Late-onset mitochondrial DNA depletion: DNA copy number, multiple deletions, and compensation. *Annals of neurology* **49**(5), 607–617 (2001).

[343] Pyle, A., Taylor, R. W., Durham, S. E., Deschauer, M., Schaefer, A. M., Samuels, D. C., and Chinnery, P. F. Depletion of mitochondrial DNA in leucocytes harbouring the 3243a g mtDNA mutation. *Journal of medical genetics* **44**(1), 69–74 (2007).

[344] Picard, M., Zhang, J., Hancock, S., Derbeneva, O., Golhar, R., Golik, P., OHearn, S., Levy, S., Potluri, P., Lvova, M., et al. Progressive increase in mtDNA 3243A>G heteroplasmy causes abrupt transcriptional reprogramming. *Proceedings of the National Academy of Sciences* **111**(38), E4033–E4042 (2014).

[345] Hämäläinen, R. H., Manninen, T., Koivumäki, H., Kislin, M., Otonkoski, T., and Suomalainen, A. Tissue-and cell-type–specific manifestations of heteroplasmic mtDNA 3243A>G mutation in human induced pluripotent stem cell-derived disease model. *Proceedings of the National Academy of Sciences* **110**(38), E3622–E3630 (2013).

[346] Müller-Höcker, J. Cytochrome c oxidase deficient fibres in the limb muscle and diaphragm of man without muscular disease: an age-related alteration. *Journal of the neurological sciences* **100**(1), 14–21 (1990).

[347] Cottrell, D., Ince, P., Blakely, E., Johnson, M., Chinnery, P., Hanna, M., and Turnbull, D. Neuropathological and histochemical changes in a multiple mitochondrial DNA deletion disorder. *Journal of Neuropathology & Experimental Neurology* **59**(7), 621–627 (2000).

[348] Khrapko, K. and Vijg, J. Mitochondrial DNA mutations and aging: devils in the details? *Trends in Genetics* **25**(2), 91–98 (2009).

[349] Chinnery, P., Howel, D., Turnbull, D., and Johnson, M. Clinical progression of mitochondrial myopathy is associated with the random accumulation of cytochrome c oxidase negative skeletal muscle fibres. *Journal of the neurological sciences* **211**(1), 63–66 (2003).

[350] Herbst, A., Wanagat, J., Cheema, N., Widjaja, K., McKenzie, D., and Aiken, J. M. Latent mitochondrial DNA deletion mutations drive muscle fiber loss at old age. *Aging cell* **15**(6), 1132–1139 (2016).

[351] Cao, Z., Wanagat, J., McKiernan, S. H., and Aiken, J. M. Mitochondrial DNA deletion mutations are concomitant with ragged red regions of individual, aged muscle fibers: analysis by laser-capture microdissection. *Nucleic acids research* **29**(21), 4502–4508 (2001).

[352] Bruusgaard, J., Liestøl, K., Ekmark, M., Kollstad, K., and Gundersen, K. Number and spatial distribution of nuclei in the muscle fibres of normal mice studied in vivo. *The Journal of physiology* **551**(2), 467–478 (2003).

[353] Appelhans, T., Richter, C. P., Wilkens, V., Hess, S. T., Piehler, J., and Busch, K. B. Nanoscale organization of mitochondrial microcompartments revealed by combining tracking and localization microscopy. *Nano Letters* **12**(2), 610–616 (2012).

[354] Iborra, F. J., Kimura, H., and Cook, P. R. The functional organization of mitochondrial genomes in human cells. *BMC biology* **2**(1), 9 (2004).

[355] Brown, T. A., Tkachuk, A. N., Shtengel, G., Kopek, B. G., Bogenhagen, D. F., Hess, H. F., and Clayton, D. A. Superresolution fluorescence imaging of mitochondrial nucleoids reveals their spatial range, limits, and membrane interaction. *Molecular and cellular biology* **31**(24), 4994–5010 (2011).

[356] He, Y., Wu, J., Dressman, D. C., Iacobuzio-Donahue, C., Markowitz, S. D., Velculescu, V. E., Diaz Jr, L. A., Kinzler, K. W., Vogelstein, B., and Papadopoulos, N. Heteroplasmic mitochondrial DNA mutations in normal and tumour cells. *Nature* **464**(7288), 610–614 (2010).

[357] Ross, J. M., Stewart, J. B., Hagström, E., Brené, S., Mourier, A., Coppotelli, G., Freyer, C., Lagouge, M., Hoffer, B. J., Olson, L., et al. Germline mtDNA mutations aggravate ageing and can impair brain development. *Nature* **501**(7467), 412 (2013).

[358] Sato, A., Nakada, K., and Hayashi, J.-I. Mitochondrial complementation preventing respiratory dysfunction caused by mutant mtdna. *Biofactors* **35**(2), 130–137 (2009).

[359] Santoro, A., Salvioli, S., Raule, N., Capri, M., Sevini, F., Valensin, S., Monti, D., Bellizzi, D., Passarino, G., Rose, G., et al. Mitochondrial DNA involvement in human longevity. *Biochimica et Biophysica Acta (BBA)-Bioenergetics* **1757**(9), 1388–1399 (2006).

[360] Masuyama, M., Iida, R., Takatsuka, H., Yasuda, T., and Matsuki, T. Quantitative change in mitochondrial DNA content in various mouse tissues during aging. *Biochimica et Biophysica Acta (BBA)-General Subjects* **1723**(1), 302–308 (2005).

[361] Welle, S., Bhatt, K., Shah, B., Needler, N., Delehanty, J. M., and Thornton, C. A. Reduced amount of mitochondrial DNA in aged human muscle. *Journal of applied physiology* **94**(4), 1479–1484 (2003).

[362] Pesce, V., Cormio, A., Fracasso, F., Lezza, A. M., Cantatore, P., and Gadaleta, M. N. Age-related changes of mitochondrial DNA content and mitochondrial genotypic and phenotypic alterations in rat hind-limb skeletal muscles. *The Journals of Gerontology Series A: Biological Sciences and Medical Sciences* **60**(6), 715–723 (2005).

[363] Pesce, V., Cormio, A., Fracasso, F., Vecchiet, J., Felzani, G., Lezza, A. M., Cantatore, P., and Gadaleta, M. N. Age-related mitochondrial genotypic and phenotypic alterations in human skeletal muscle. *Free Radical Biology and Medicine* **30**(11), 1223–1233 (2001).

[364] Wachsmuth, M., Huebner, A., Li, M., Madea, B., and Stoneking, M. Age-related and heteroplasmy-related variation in human mtDNA copy number. *PLoS Genet* **12**(3), e1005939 (2016).

[365] Campbell, G., Krishnan, K. J., Deschauer, M., Taylor, R. W., and Turnbull, D. M. Dissecting the mechanisms underlying the accumulation of mitochondrial DNA deletions in human skeletal muscle. *Human molecular genetics* **23**(17), 4612–4620 (2014).

[366] Folker, E. S. and Baylies, M. K. Nuclear positioning in muscle development and disease. *Frontiers in physiology* **4** (2013).

[367] Pathi, B., Kinsey, S. T., Howdeshell, M., Priester, C., McNeill, R., and Locke, B. The formation and functional consequences of heterogeneous mitochondrial distributions in skeletal muscle. *Journal of Experimental Biology* **215**(11), 1871–1883 (2012).

[368] Hood, D. A., Irrcher, I., Ljubicic, V., and Joseph, A.-M. Coordination of metabolic plasticity in skeletal muscle. *Journal of experimental biology* **209**(12), 2265–2275 (2006).

[369] Holloszy, J. Regulation by exercise of skeletal muscle content of mitochondria and glut4. *J Physiol Pharmacol* **59**(Suppl 7), 5–18 (2008).

[370] Moraes, C. T., Kenyon, L., and Hao, H. Mechanisms of human mitochondrial DNA maintenance: the determining role of primary sequence and length over function. *Molecular biology of the cell* **10**(10), 3345–3356 (1999).

[371] Samuels, D. C., Li, C., Li, B., Song, Z., Torstenson, E., Clay, H. B., Rokas, A., Thornton-Wells, T. A., Moore, J. H., Hughes, T. M., et al. Recurrent tissue-specific mtDNA mutations are common in humans. *PLoS Genetics* (2013).

[372] Eisner, V., Lenaers, G., and Hajnóczky, G. Mitochondrial fusion is frequent in skeletal muscle and supports excitation–contraction coupling. *J Cell Biol* , jcb–201312066 (2014).

[373] Önfelt, B., Nedvetzki, S., Yanagi, K., and Davis, D. M. Cutting edge: Membrane nanotubes connect immune cells. *The Journal of Immunology* **173**(3), 1511–1513 (2004).

[374] Vignais, M.-L., Caicedo, A., Brondello, J.-M., and Jorgensen, C. Cell connections by tunneling nanotubes: Effects of mitochondrial trafficking on target cell metabolism, homeostasis, and response to therapy. *Stem Cells International* **2017** (2017).

[375] Phillips, R. and Milo, R. A feeling for the numbers in biology. *Proc Natl Acad Sci USA* **106**(51), 21465–21471 (2009).

[376] Moran, U., Phillips, R., and Milo, R. Snapshot: key numbers in biology. *Cell* **141**(7), 1262–1262 (2010).

[377] Kirkpatrick, S. Percolation and conduction. *Rev Mod Phys* **45**(4), 574 (1973).

[378] Ivannikov, M. V. and Macleod, G. T. Mitochondrial free ca levels and their effects on energy metabolism in drosophila motor nerve terminals. *Biophys J* **104**(11), 23532361 June (2013).

[379] Altschafl, B. A., Beutner, G., Sharma, V. K., Sheu, S.-S., and Valdivia, H. H. The mitochondrial ryanodine receptor in rat heart: A pharmaco-kinetic profile. *Biochim Biophys Acta* **1768**(7), 1784 – 1795 (2007).

[380] Duszyski, J., Kozie, R., Brutkowski, W., Szczepanowska, J., and Zabocki, K. The regulatory role of mitochondria in capacitative calcium entry. *Biochim Biophys Acta* **1757**(56), 380 – 387 (2006).

[381] Ahuja, M. and Muallem, S. The gatekeepers of mitochondrial calcium influx: Micu1 and micu2. *EMBO Rep* **15**(3), 205–206 (2014).

[382] Collins, T. J. and Bootman, M. D. Mitochondria are morphologically heterogeneous within cells. *J Exp Biol* **206**(12), 1993–2000 (2003).

[383] Pacher, P., Sharma, K., Csordás, G., Zhu, Y., and Hajnóczky, G. Uncoupling of er-mitochondrial calcium communication by transforming growth factor-. *Am J Physiol Renal Physiol* **295**(5), F1303–F1312 (2008).

[384] Martinelli, F. Lectures on glauber dynamics for discrete spin models. In *Lectures on probability theory and statistics*, 93–191. Springer (1999).

[385] Pigliucci, M. Is evolvability evolvable? *Nat Rev Genet* **9**(1), 75–82 (2008).

[386] Smigrodzki, R. M. and Khan, S. M. Mitochondrial microheteroplasmy and a theory of aging and age-related disease. *Rejuvenation Res* **8**(3), 172–198 (2005).

[387] Davies, K. M., Anselmi, C., Wittig, I., Faraldo-Gmez, J. D., and Khlbrandt, W. Structure of the yeast f1fo-atp synthase dimer and its role in shaping the mitochondrial cristae. *Proc Natl Acad Sci USA* **109**(34), 13602–13607 (2012).

[388] Strauss, M., Hofhaus, G., Schröder, R. R., and Kühlbrandt, W. Dimer ribbons of atp synthase shape the inner mitochondrial membrane. *EMBO J* **27**(7), 1154–1160 (2008).

[389] Divakaruni, A. S. and Brand, M. D. The regulation and physiology of mitochondrial proton leak. *Physiology* **26**(3), 192–205 (2011).

[390] Melser, S., Chatelain, E. H., Lavie, J., Mahfouf, W., Jose, C., Obre, E., Goorden, S., Priault, M., Elgersma, Y., Rezvani, H. R., Rossignol, R., and Bnard, G. Rheb regulates mitophagy induced by mitochondrial energetic status. *Cell Metab* **17**(5), 719 – 730 (2013).

[391] Jones, D. t. Intracellular diffusion gradients of o2 and atp. *Am J Physiol* **250**(5), C663–C675 (1986).

[392] Keener, J. P. and Sneyd, J. *Mathematical physiology*, volume 8. Springer, (1998).

[393] Gnaiger, E. and Kuznetsov, A. Mitochondrial respiration at low levels of oxygen and cytochrome c. *Biochem Soc Trans* **30**(2), 252–257 (2002).

[394] Kirkinezos, I. G. and Moraes, C. T. Reactive oxygen species and mitochondrial diseases. *Seminars in Cell and Developmental Biology* **12**(6), 449 – 457 (2001).

[395] Moll, W. The diffusion coefficient of myoglobin in muscle homogenate. *Pflger's Archiv fr die gesamte Physiologie des Menschen und der Tiere* **299**(3), 247–251 (1968).

[396] Stroeve, P. Myoglobin-facilitated oxygen transport in heterogeneous red muscle tissue. *Annals of Biomedical Engineering* **10**(2), 49–70 (1982).

[397] Zhang, C., Knyazev, D. G., Vereshaga, Y. A., Ippoliti, E., Nguyen, T. H., Carloni, P., and Pohl, P. Water at hydrophobic interfaces delays proton surface-to-bulk transfer and provides a pathway for lateral proton diffusion. *Proc Natl Acad Sci USA* **109**(25), 9744–9749 (2012).

[398] Heggeness, M. H., Simon, M., and Singer, S. J. Association of mitochondria with microtubules in cultured cells. *Proc Natl Acad Sci USA* **75**(8), 3863–3866 (1978).

[399] Song, Z., Chen, H., Fiket, M., Alexander, C., and Chan, D. C. OPA1 processing controls mitochondrial fusion and is regulated by mrna splicing, membrane potential, and yme1l. *J Cell Biol* **178**(5), 749–755 (2007).

[400] Guillery, O., Malka, F., Landes, T., Guillou, E., Blackstone, C., Lombs, A., Belenguer, P., Arnoult, D., and Rojo, M. Metalloprotease-mediated OPA1 processing is modulated by the mitochondrial membrane potential. *Biol Cell* **100**(5), 315–325 (2008).

[401] Baricault, L., Sgui, B., Gugand, L., Olichon, A., Valette, A., Larminat, F., and Lenaers, G. {OPA1} cleavage depends on decreased mitochondrial {ATP} level and bivalent metals. *Experimental Cell Research* **313**(17), 3800 – 3808 (2007).

[402] Duvezin-Caubet, S., Jagasia, R., Wagener, J., Hofmann, S., Trifunovic, A., Hansson, A., Chomyn, A., Bauer, M. F., Attardi, G., Larsson, N.-G., Neupert, W., and Reichert, A. S. Proteolytic processing of OPA1 links mitochondrial dysfunction to alterations in mitochondrial morphology. *J Biol Chem* **281**(49), 37972–37979 (2006).

[403] Ishihara, N., Fujita, Y., Oka, T., and Mihara, K. Regulation of mitochondrial morphology through proteolytic cleavage of OPA1. *EMBO J* **25**(13), 2966–2977 (2006).

[404] Margineantu, D. H., Cox, W. G., Sundell, L., Sherwood, S. W., Beechem, J. M., and Capaldi, R. A. Cell cycle dependent morphology changes and associated mitochondrial {DNA} redistribution in mitochondria of human cell lines. *Mitochondrion* **1**(5), 425 – 435 (2002).

[405] Redpath, C. J., Khalil, M. B., Drozdal, G., Radisic, M., and MacBride, H. M. Mitochondrial hyperfusion during oxidative stress is coupled to a dysregulation in calcium handling within a c2c12 cell model. *PLos ONE* **7**, e69165 (2013).

[406] Pletjushkina, O., Lyamzaev, K., Popova, E., Nepryakhina, O., Ivanova, O., Domnina, L., Chernyak, B., and Skulachev, V. Effect of oxidative stress on dynamics of mitochondrial reticulum. *Biochim Biophys Acta* **1757**(56), 518 – 524 (2006). 14th European Bioenergetics Conference.

[407] Rossignol, R., Gilkerson, R., Aggeler, R., Yamagata, K., Remington, S. J., and Capaldi, R. A. Energy substrate modulates mitochondrial structure and oxidative capacity in cancer cells. *Cancer Res* **64**(3), 985–993 (2004).

[408] Regmi, S. G., Rolland, S. G., and Conradt, B. Age-dependent changes in mitochondrial morphology and volume are not predictors of lifespan. *Aging (Albany NY)* **6**(2), 118 (2014).

[409] Smirnova, E., Shurland, D.-L., Ryazantsev, S. N., and van der Bliek, A. M. A human dynamin-related protein controls the distribution of mitochondria. *J Cell Biol* **143**(2), 351–358 (1998).

[410] Nunnari, J., Marshall, W. F., Straight, A., Murray, A., Sedat, J., and Walter, P. Mitochondrial transmission during mating in saccharomyces cerevisiae is determined by mitochondrial fusion and fission and the intramitochondrial segregation of mitochondrial dna. *Mol Biol Cell* **7**, 1233–42 (1997).

[411] Egner, A., Jakobs, S., and Hell, S. W. Fast 100-nm resolution three-dimensional microscope reveals structural plasticity of mitochondria in live yeast. *Proc Natl Acad Sci USA* **99**(6), 3370–3375 (2002).

[412] Aung-Htut, M. T., Lam, Y. T., Lim, Y.-L., Rinnerthaler, M., Gelling, C. L., Yang, H., Breitenbach, M., and Dawes, I. W. Maintenance of mitochondrial morphology by autophagy and its role in high glucose effects on chronological lifespan of saccharomyces cerevisiae. *Oxid Med Cell Longev* **2013** (2013).

[413] Visser, W., van Spronsen, E., Nanninga, N., Pronk, J., Kuenen, J., and van Dijken, J. Effects of growth conditions on mitochondrial morphology insaccharomyces cerevisiae. *Antonie van Leeuwenhoek* **67**(3), 243–253 (1995).

[414] Koopman, W. J., Hink, M. A., Verkaart, S., Visch, H.-J., Smeitink, J. A., and Willems, P. H. Partial complex i inhibition decreases mitochondrial motility and increases matrix protein diffusion as revealed by fluorescence correlation spectroscopy. *Biochim Biophys Acta* **1767**(7), 940 – 947 (2007).

[415] Sukhorukov, V. M., Dikov, D., Busch, K., Strecker, V., Wittig, I., and Bereiter-Hahn, J. Determination of protein mobility in mitochondrial membranes of living cells. *Biochim Biophys Acta* **1798**(11), 2022 – 2032 (2010).

[416] Kuzmenko, A., Tankov, S., English, B. P., Tarassov, I., Tenson, T., Kamenski, P., Elf, J., and Hauryliuk, V. Single molecule tracking fluorescence microscopy in mitochondria reveals highly dynamic but confined movement of tom40. *Scientific reports* **1** (2011).

[417] Chang, C.-R. and Blackstone, C. Cyclic AMP-dependent protein kinase phosphorylation of drp1 regulates its gtpase activity and mitochondrial morphology. *J Biol Chem* **282**(30), 21583–21587 (2007).

[418] Han, X.-J., Lu, Y.-F., Li, S.-A., Kaitsuka, T., Sato, Y., Tomizawa, K., Nairn, A. C., Takei, K., Matsui, H., and Matsushita, M. Cam kinase iα–induced phosphorylation of drp1 regulates mitochondrial morphology. *J Cell Biol* **182**(3), 573–585 (2008).

[419] Wang, W., Wang, Y., Long, J., Wang, J., Haudek, S. B., Overbeek, P., Chang, B. H., Schumacker, P. T., and Danesh, F. R. Mitochondrial fission triggered by hyperglycemia is mediated by rock1 activation in podocytes and endothelial cells. *Cell Metab* **15**(2), 186–200 (2012).

[420] Taguchi, N., Ishihara, N., Jofuku, A., Oka, T., and Mihara, K. Mitotic phosphorylation of dynamin-related gtpase drp1 participates in mitochondrial fission. *J Biol Chem* **282**(15), 11521–11529 (2007).

[421] Cho, B., Cho, H. M., Kim, H. J., Jeong, J., Park, S. K., Hwang, E. M., Park, J.-Y., Kim, W. R., Kim, H., and Sun, W. Cdk5-dependent inhibitory phosphorylation of drp1 during neuronal maturation. *Exp Mol Med* **46**(7), e105 (2014).

[422] Qi, X., Disatnik, M.-H., Shen, N., Sobel, R. A., and Mochly-Rosen, D. Aberrant mitochondrial fission in neurons induced by protein kinase cδ under oxidative stress conditions in vivo. *Mol Biol Cell* **22**(2), 256–265 (2011).

[423] Yu, T., Jhun, B. S., and Yoon, Y. High-glucose stimulation increases reactive oxygen species production through the calcium and mitogen-activated protein kinase-mediated activation of mitochondrial fission. *Antioxidants & redox signaling* **14**(3), 425–437 (2011).

[424] Cereghetti, G. M., Stangherlin, A., de Brito, O. M., Chang, C. R., Blackstone, C., Bernardi, P., and Scorrano, L. Dephosphorylation by calcineurin regulates translocation of drp1 to mitochondria. *Proc Natl Acad Sci USA* **105**(41), 15803–15808 (2008).

[425] Braschi, E., Zunino, R., and McBride, H. M. Mapl is a new mitochondrial sumo e3 ligase that regulates mitochondrial fission. *EMBO Rep* **10**(7), 748–754 (2009).

[426] Figueroa-Romero, C., Iiguez-Lluh, J. A., Stadler, J., Chang, C.-R., Arnoult, D., Keller, P. J., Hong, Y., Blackstone, C., and Feldman, E. L. Sumoylation of the mitochondrial fission protein drp1 occurs at multiple nonconsensus sites within the b domain and is linked to its activity cycle. *FASEB J* **23**(11), 3917–3927 (2009).

[427] Gawlowski, T., Suarez, J., Scott, B., Torres-Gonzalez, M., Wang, H., Schwappacher, R., Han, X., Yates, J. R., Hoshijima, M., and Dillmann, W. Modulation of dynamin-related protein 1 (drp1) function by increased o-linked--n-acetylglucosamine modification (o-glcnac) in cardiac myocytes. *J Biol Chem* **287**(35), 30024–30034 (2012).

[428] Wasiak, S., Zunino, R., and McBride, H. M. Bax/bak promote sumoylation of drp1 and its stable association with mitochondria during apoptotic cell death. *J Cell Biol* **177**(3), 439–450 (2007).

[429] Yonashiro, R., Ishido, S., Kyo, S., Fukuda, T., Goto, E., Matsuki, Y., Ohmura-Hoshino, M., Sada, K., Hotta, H., Yamamura, H., Inatome, R., and Yanagi, S. A novel mitochondrial ubiquitin ligase plays a critical role in mitochondrial dynamics. *EMBO J* **25**(15), 3618–3626 (2006).

[430] Nagashima, S., Tokuyama, T., Yonashiro, R., Inatome, R., and Yanagi, S. Roles of mitochondrial ubiquitin ligase mitol/march5 in mitochondrial dynamics and diseases. *J Biochem* (2014).

[431] Santo-Domingo, J., Giacomello, M., Poburko, D., Scorrano, L., and Demaurex, N. OPA1 promotes ph flashes that spread between contiguous mitochondria without matrix protein exchange. *EMBO J* **32**(13), 1927–1940 (2013).

[432] Lee, H. and Yoon, Y. Transient contraction of mitochondria induces depolarization through the inner membrane dynamin OPA1. *J Biol Chem* (2014).

[433] de Brito, O. M. and Scorrano, L. Mitofusin 2 tethers endoplasmic reticulum to mitochondria. *Nature* **456**, 605–610 (2008).

[434] Pich, S., Bach, D., Briones, P., Liesa, M., Camps, M., Testar, X., Palacn, M., and Zorzano, A. The charcotmarietooth type 2a gene product, mfn2, up-regulates fuel oxidation through expression of oxphos system. *Hum Mol Genet* **14**(11), 1405–1415 (2005).

[435] Ryu, S.-W., Choi, K., Park, J.-H., Park, Y.-M., Kim, S., and Choi, C. Mitofusin 1 inhibits an apoptosis-associated amino-terminal conformational change in bax, but not its mitochondrial translocation, in a gtpase-dependent manner. *Cancer Lett* **323**(1), 62 – 68 (2012).

[436] Frank, S., Gaume, B., Bergmann-Leitner, E. S., Leitner, W. W., Robert, E. G., Catez, F., Smith, C. L., and Youle, R. J. The role of dynamin-related protein 1, a mediator of mitochondrial fission, in apoptosis. *Dev Cell* **1**(4), 515–525 (2001).

[437] Pfleger, J., He, M., and Abdellatif, M. Mitochondrial complex ii is a source of the reserve respiratory capacity that is regulated by metabolic sensors and promotes cell survival. *Cell death & disease* **6**(7), e1835 (2015).

[438] Hinkle, P. C. P/O ratios of mitochondrial oxidative phosphorylation. *Biochimica et Biophysica Acta (BBA)-Bioenergetics* **1706**(1), 1–11 (2005).

[439] Lee, C., Gu, Q., Xiong, Y., Mitchell, R., and Ernster, L. P/O ratios reassessed: mitochondrial P/O ratios consistently exceed 1.5 with succinate and 2.5 with nad-linked substrates. *The FASEB Journal* **10**(2), 345–350 (1996).

[440] Sriskanthadevan, S., Jeyaraju, D. V., Chung, T. E., Prabha, S., Xu, W., Skrtic, M., Jhas, B., Hurren, R., Gronda, M., Wang, X., et al. Aml cells have low spare reserve capacity in their respiratory chain that renders them susceptible to oxidative metabolic stress. *Blood* **125**(13), 2120–2130 (2015).

[441] Nicholls, D. G. Mitochondrial ion circuits. *Essays in biochemistry* **47**, 25–35 (2010).

[442] Jin, K., Musso, G., Vlasblom, J., Jessulat, M., Deineko, V., Negroni, J., Mosca, R., Malty, R., Nguyen-Tran, D.-H., Aoki, H., et al. Yeast mitochondrial protein–protein interactions reveal diverse complexes and disease-relevant functional relationships. *Journal of proteome research* **14**(2), 1220–1237 (2015).

[443] Cherry, J. M., Hong, E. L., Amundsen, C., Balakrishnan, R., Binkley, G., Chan, E. T., Christie, K. R., Costanzo, M. C., Dwight, S. S., Engel, S. R., et al. Saccharomyces genome database: the genomics resource of budding yeast. *Nucleic acids research* , D700–D705 (2011).

[444] Phillips, R., Kondev, J., Theriot, J., and Garcia, H. *Physical biology of the cell*. Garland Science, (2012).

[445] Herrmann, J. M., Woellhaf, M. W., and Bonnefoy, N. Control of protein synthesis in yeast mitochondria: the concept of translational activators. *Biochimica et Biophysica Acta (BBA)-Molecular Cell Research* **1833**(2), 286–294 (2013).

[446] Osman, C., Noriega, T. R., Okreglak, V., Fung, J. C., and Walter, P. Integrity of the yeast mitochondrial genome, but not its distribution and inheritance, relies on mitochondrial fission and fusion. *Proceedings of the National Academy of Sciences* **112**(9), E947–E956 (2015).

[447] Myers, M. W. and Bosmann, H. B. Mitochondrial protein content and enzyme activity of reuber hepatoma h-35. *Cancer research* **34**(8), 1989–1994 (1974).

[448] Brandt, F., Etchells, S. A., Ortiz, J. O., Elcock, A. H., Hartl, F. U., and Baumeister, W. The native 3d organization of bacterial polysomes. *cell* **136**(2), 261–271 (2009).

[449] Dill, K. A., Ghosh, K., and Schmit, J. D. Physical limits of cells and proteomes. *Proceedings of the National Academy of Sciences* **108**(44), 17876–17882 (2011).

[450] Lane, N. and Martin, W. F. Mitochondria, complexity, and evolutionary deficit spending. *Proceedings of the National Academy of Sciences* **113**(6), E666 (2016).

[451] Flamholz, A., Phillips, R., and Milo, R. The quantified cell. *Molecular biology of the cell* **25**(22), 3497–3500 (2014).

[452] Shmookler, R. R. and Goldstein, S. Mitochondrial DNA in mortal and immortal human cells. genome number, integrity, and methylation. *The Journal of biological chemistry* **258**(15), 9078–9085 (1983).

[453] Scott, D. W. On optimal and data-based histograms. *Biometrika* **66**(3), 605–610 (1979).

[454] Gardiner, C. W. *Stochastic methods*. Springer-Verlag, Berlin–Heidelberg–New York–Tokyo, (1985).

[455] Gillespie, D. T. and Seitaridou, E. *Simple Brownian diffusion: an introduction to the standard theoretical models*. Oxford University Press, (2012).

[456] Lotka, A. J. Contribution to the theory of periodic reactions. *The Journal of Physical Chemistry* **14**(3), 271–274 (1910).

[457] Getz, W. M. Stochastic equivalents of the linear and lotka-volterra systems of equationsa general birth-and-death process formulation. *Mathematical Biosciences* **29**(3), 235–257 (1976).

[458] Grima, R., Thomas, P., and Straube, A. V. How accurate are the nonlinear chemical fokker-planck and chemical langevin equations? *The Journal of chemical physics* **135**(8), 084103 (2011).

[459] Moyal, J. Stochastic processes and statistical physics. *Journal of the Royal Statistical Society. Series B (Methodological)* **11**(2), 150–210 (1949).

[460] Kramers, H. A. Brownian motion in a field of force and the diffusion model of chemical reactions. *Physica* **7**(4), 284–304 (1940).

[461] Nowak, M. A. *Evolutionary dynamics*. Harvard University Press, (2006).

[462] Eisenberg, B. R. Quantitative ultrastructure of mammalian skeletal muscle. *Comprehensive physiology* (1983).